Design and Numerical Analysis of Line- and Point-Supported CLT Floor Systems: Static and Dynamic Performance of Panel-to-Panel Connections

N.J.I. Schaeffer

TU Delft

Design and Numerical Analysis of Line- and Point-Supported CLT Floor Systems: Static and Dynamic Performance of Panel-to-Panel Connections

From System-Level Analysis to Connection Design

by

Student Name	Student Number
Noah Schaeffer	4912209

University supervisors:	Prof.dr.ir. J.W.G. van de Kuilen
	Dr.ir. H.R. Schipper
	Dr.ir. M. Mirra
Company supervisor:	Ir. A. van Lier
Project Duration:	November 2024 - June 2025
Faculty:	Faculty of Civil Engineering, Delft

TU Delft

LÜNING
Ingenieurs in houtconstructies

Preface

This thesis marks the final step of my Master's degree in Civil Engineering at Delft University of Technology and was carried out in collaboration with Lüning. It reflects several months of intensive work, learning and development that began in November and will conclude with my final presentation in June.

The topic of timber engineering has always fascinated me—not only due to its potential for sustainable construction, but also because of the natural aesthetic and warmth that timber brings to buildings. With this work, I hoped to contribute to the growing field of timber construction by bridging the gap between theoretical modelling and practical design. In particular, I aimed to provide engineers with early-stage tools for designing point-supported CLT floor systems, a concept that offers architectural freedom and structural efficiency.

This project would not have been possible without the guidance and encouragement of several key people. I would like to express my deep gratitude to Prof. dr. ir. J.W.G. van de Kuilen, Dr. ir. H.R. Schipper and Dr. ir. M. Mirra for their academic supervision and valuable feedback throughout this process. I also appreciate the support from Ir. A. van Lier at Lüning, whose practical insights helped shape the project in a real-world context.

In particular, I would like to thank Michele Mirra and Arthur van Lier, who were closely involved in my project and consistently supported me. Their technical expertise, open-minded thinking and constructive criticism were crucial for navigating both the theoretical and applied aspects of this research. I truly appreciated their time and engagement.

I would also like to thank my girlfriend for her continuous support throughout the thesis period. Her encouragement, patience and occasional help with time-consuming calculations contributed meaningfully to the overall progress and completion of this work. I am well aware that I wasn't always the most relaxed or fun person to be around during this period and I am incredibly grateful for her understanding and support.

Lastly, I want to thank my friends, many of whom were also finishing their own Master's theses. Studying together and sharing the ups and downs of this journey provided motivation, perspective and some much-needed laughs along the way.

Writing this thesis has been a rewarding experience, not only for the technical knowledge gained, but also for the personal growth that came with tackling a complex and multifaceted problem. I hope the results of this study will be of use to fellow engineers who share a passion for sustainable, forward-thinking design.

Noah Schaeffer
Delft, June 2025

Abstract

Point-supported Cross-Laminated Timber (CLT) floor systems offer architectural flexibility and material efficiency, enabling biaxial load transfer while minimizing reliance on traditional post-and-beam structures. However, the structural integrity of such systems is highly dependent on the design and performance of panel-to-panel and panel-to-column connections. This study examines these panel-to-panel connections through a comprehensive numerical modelling approach, evaluating both static and dynamic behaviour to inform early-stage design decisions.

To assess static behaviour, a bending moment estimation formula is developed, allowing engineers to approximate internal forces in panel joints without requiring extensive finite element simulations. This facilitates efficient preliminary design calculations for structural connections, emphasizing the crucial role of rotational stiffness at line hinges. The analysis demonstrates that actual bending moments transferred can be significantly lower than those assuming rigid continuity, particularly for connections with moderate to low stiffness. A unified reduction factor, derived from parametric studies, enables practical and reliable estimation of bending moments across various floor configurations.

For dynamic behaviour, vibrational performance is analysed using parametric simulations based on the HIVOSS methodology, revealing the interaction between connection stiffness, flexural stiffness and stiffness ratios on modal response characteristics. The findings underscore the importance of ensuring adequate connection stiffness to maintain floor vibration comfort and serviceability. Design graphs constructed from these simulations provide engineers with intuitive tools to evaluate vibrational performance and assess serviceability thresholds prior to detailed modelling.

The proposed splice plate connection with inclined screws is subjected to analytical and numerical validation using Python-based mechanical models and RFEM finite element (FE) simulations. Key design rules were established to optimize screw length and panel height. While the current models adequately support early-stage design, further refinement, particularly in modelling compressive force dispersion within lamellas could improve accuracy in predicting bending capacity.

A comparative case study between point-supported and conventional beam-supported CLT floor systems highlights architectural and structural trade-offs. The point-supported system offers increased free height and simplified structural layouts by eliminating continuous beams, which benefits architectural integration. However, these advantages come with increased timber volumes and more complex point and panel-to-panel connections requiring detailed engineering. Both systems can satisfy strength and serviceability demands, but the choice depends on project-specific priorities such as spatial efficiency, material availability and construction complexity.

The findings contribute to the development of design guidelines that bridge the gap between theoretical feasibility and practical implementation. By providing engineers with simplified estimation tools and validated numerical insights, this research aims to facilitate the broader adoption of point-supported CLT floors in modern day timber construction.

This research contributes practical design guidelines bridging theoretical modelling and real-world application. By providing simplified estimation tools, validated numerical insights and design aids for both static and dynamic performance, the study facilitates the broader adoption of point-supported CLT floors in modern timber construction.

Contents

Chapter 1: Introduction

1.1 Research Context

Cross-laminated timber (CLT) has emerged as a prominent structural material in the field of sustainable construction. Its increasing application in mid- and high-rise buildings is driven by benefits such as high strength-to-weight ratio, prefabrication potential and a reduced carbon footprint. Among recent innovations, point-supported CLT floor systems offer considerable advantages over traditional systems such as post-and-beam configurations and wall-supported layouts. These conventional approaches typically use CLT as a single-span material, relying on continuous or line-supported arrangements where floor panels are supported along their edges by beams or walls. This often limits architectural flexibility, reduces usable floor height and complicates the integration of building services. In contrast, point-supported systems take advantage of the biaxial load-bearing capabilities of CLT, enabling two-way action across panels. This allows for increased free height, more flexible architectural layouts, easier routing of installations and more efficient material usage by minimizing the need for extensive supporting elements.

1.2 Research Problem

In timber structures, the design of connections is always a critical aspect of the structural system. Connections often govern the dimensions of structural elements such as columns, beams and floor thicknesses. Their mechanical behaviour has a significant influence on overall system performance and is therefore a primary focus in timber design. In point-supported CLT floor systems, this importance becomes even more pronounced. The column-to-panel connection must safely transfer concentrated loads from the floor into the column while permitting necessary deformations or rotations arising from load redistribution. It forms a fundamental component of structural integrity and must accommodate both vertical loads and possible in-plane actions.

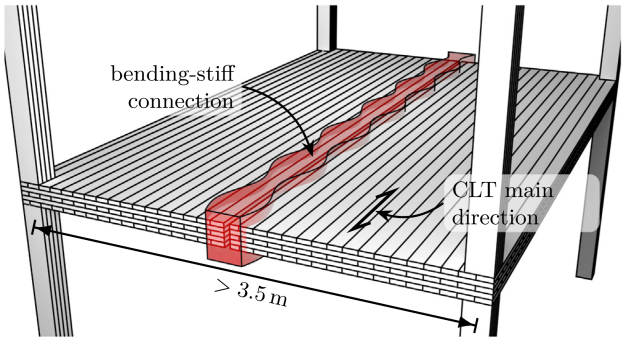

Figure 1.1: CLT panels connected in the secondary direction enable wider column spacing and biaxial action [58]

Further considerations arise from practical constraints: due to transportation limitations, CLT panels are generally restricted to a maximum width of approximately $3.5m$. However, structural grids in modern buildings, especially those favouring open layouts or wide column spacing, often exceed this width. As a result, floor assemblies must consist of multiple CLT panels joined on site, see Figure 1.1.

This creates a critical need for robust and efficient panel-to-panel connection solutions. These joints must bridge the gaps between panels while enabling biaxial load transfer, allowing the floor to act as a continuous two-way spanning system. This behaviour is essential in point-supported floors, where panels are supported only at discrete locations and bending occurs in both principal directions. Consequently, both the column-to-panel and panel-to-panel connections are decisive for the structural performance and design feasibility of point-supported CLT systems. Yet, design guidelines and practical detailing strategies for such panel-to-panel joints remain underdeveloped and require further research.

1.3 Research Objective

The objective of this research is to investigate and evaluate panel-to-panel connections suitable for use in point-supported CLT floor systems. This involves proposing a viable connection detail and assessing its structural performance through analytical models and numerical simulations.

The broader aim is to support efficient design strategies during the preliminary design phase, where quick assessments and decisions are often made. The proposed detail itself is developed to a level of definition that allows application in detailed engineering stages as well. The insights from this research aim to bridge the current gap between conceptual feasibility and practical implementation, supporting the wider application of point-supported CLT floor systems in real building projects.

1.4 Research Scope

This study focuses primarily on the structural aspects of panel-to-panel connections within point-supported CLT floor systems. These connections are investigated with the goal of enabling effective biaxial load transfer across CLT panels and ensuring that the floor system meets key serviceability requirements, particularly in terms of vibration behaviour and stiffness. The research is centred on the preliminary design stage, where simplified methods and design guidelines can assist in early decision-making regarding layout, vibration performance and structural feasibility. While the proposed panel-to-panel connection is developed further to allow evaluation at a detailed engineering level, the overall approach remains focused on early-phase design guidance.

Although panel-to-column connections are acknowledged and discussed where relevant, this thesis does not seek to propose new solutions in that area. Several engineered connection types for panel-to-column interfaces have already been developed and successfully applied in practice, providing sufficient structural performance and design guidance. Examples include solutions presented in [48, 41], which outline effective detailing strategies and associated design rules. While continued innovation in this area remains possible, the availability of proven systems allows this research to focus instead on panel-to-panel connections—where design approaches are still evolving and comprehensive guidelines are currently lacking.

Furthermore, this study is limited to the out-of-plane structural performance of CLT floor systems, with particular attention to serviceability aspects such as stiffness and vibration behaviour. Broader structural topics such as lateral stability, in-plane diaphragm action and seismic performance are not addressed. Likewise, long-term effects typical in timber construction, such as creep, moisture-related deformations, shrinkage and fatigue, are beyond the scope of this research. While fire safety considerations are briefly discussed in the literature review, detailed fire performance assessments of the proposed connection are not part of the analysis. The focus is restricted to flat CLT floor panels supported by discrete columns.

1.5 Research Questions

The central question of this research is:

> How can panel-to-panel connections in point-supported CLT floor systems be effectively designed and modelled to ensure adequate structural performance and serviceability?

To address this main question, the following sub-questions are posed:

1. How can the stiffness and strength of a proposed panel-to-panel connection be accurately modelled and evaluated?
2. To what extent can simplified estimation formulas for bending moments in line hinges, representing panel-to-panel joints, be formulated, and how accurately do they compare to results from numerical models?
3. How can design graphs be developed that estimate whether point-supported CLT floor systems meet vibration requirements in the preliminary design stage?
4. How does the proposed connection perform in a real-world case study compared to a traditional post-and-beam CLT floor system in terms of structural efficiency and vibration

behaviour?

1.6 Research Method

This research proposes and evaluates a panel-to-panel connection detail for use in point-supported CLT floor systems. The proposed connection is analytically modelled to determine its stiffness and strength, with a focus on meeting structural and serviceability requirements. To extend the analysis, a simplified estimation formula is developed to predict the bending moments in the line hinges. This formula is based on results from numerical models and offers an efficient way to approximate the internal forces in panel-to-panel connections. Additionally, the vibration performance of the floor system is assessed using established guidelines, resulting in design graphs that provide a clear method for evaluating whether the system meets required serviceability criteria for user comfort.

A real-world case study, originally designed with a traditional post-and-beam CLT system, serves to validate the theoretical findings and illustrate the practical application of the proposed connection in actual construction projects. This comparison between a point-supported CLT floor system and a traditional post-and-beam layout highlights the structural and functional benefits of the new design approach.

The research is structured into several chapters, each addressing a key aspect of the investigation. Chapter 2 provides a comprehensive literature review, covering relevant topics such as panel-to-column connections, CLT panel behaviour, inclined screw connections, vibration performance and an overview of fire safety considerations. In Chapter 3, the proposed panel-to-panel connection is introduced and a mechanical model is developed to evaluate its stiffness and strength. These mechanical models are implemented in Python, enabling customized calculations based on specific connection parameters. Chapter 4 broadens the focus to integrate panel-to-panel connections into a floor system model using line hinges and presents a simplified formula for estimating bending moments in panel joints. Chapter 5 further extends the line hinge model to assess the system's vibration performance, implementing this in the creation of practical design graphs. For these calculations, the RFEM [15] software is used, which is a powerful finite element analysis (FEA) tool for evaluating structural systems. Additionally, Grasshopper, a visual programming language for Rhinoceros 3D, is utilized to create a flexible calculation framework that enables the automation of a large number of simulations and optimizations. Chapter 6 applies the developed design approach to a real-life case study, comparing the proposed point-supported CLT floor system to a traditional post-and-beam layout in terms of structural efficiency and vibration behaviour. Finally, Chapter 7 summarizes the key findings, discusses the limitations of the study, and outlines implications for future research and practice.

Chapter 2: Literature Study

2.1 Introduction

This chapter provides the theoretical foundation for the design and analysis of point-supported CLT floor systems. It focuses on key structural behaviours and connection detailing, with particular attention to the equations and theory relevant to modelling and performance evaluation.

The literature is structured in three main parts. First, the structural behaviour of CLT panels is reviewed, including their anisotropic properties and capacity for two-way spanning. Second, the column-to-panel connection is discussed, highlighting the forces involved and established detailing strategies that enable point support. Although not developed further in this thesis, these connections are essential for the functioning of the system. Third, panel-to-panel connections are examined, with a focus on inclined screw fasteners. Their stiffness and strength characteristics are reviewed, as they form a key part of the proposed connection detail and are essential for enabling biaxial load transfer. The chapter also includes a discussion on floor vibration performance, based on established serviceability criteria, and concludes with a brief overview of fire safety considerations.

2.2 CLT Panel behaviour

CLT consists of multiple layers of timber boards, arranged orthogonally to each other and bonded with structural adhesives under pressure. This cross-layering enhances dimensional stability and enables load transfer in both principal directions. A key advantage of CLT is its high level of prefabrication: panels are produced off-site which allows for any dimension and shape needed. In the longitudinal direction, boards are joined using finger joints, enabling the production of panels in lengths much greater than the size of individual boards. The production process must comply with the requirements set out in NEN-EN 16351 [22], while manufacturer-specific properties are documented in a European Technical Assessment (ETA).

Timber is an orthotropic material, meaning its mechanical properties vary with direction relative to the grain. In CLT panels, strength and stiffness depend on the orientation of stresses relative to the board directions. As timber is a natural material, its properties vary significantly between boards and panels. To ensure structural reliability, boards are strength-graded, which can be done either visually or machine—based on measurable properties and then sorted into standard strength classes [35]. The strength of a CLT panel is derived from the properties of its individual lamellae but may be increased using a system strength factor k_{sys} when multiple layers are stressed in parallel, allowing local defects to be statistically compensated across the panel [40]. To cover general material uncertainty, partial safety factors are applied, with Eurocode prescribing $\gamma_M = 1.25$ for CLT and $\gamma_M = 1.20$ for laminated veneer lumber (LVL) [23]. Additionally, timber is susceptible to long-term deformation under sustained load, known as creep.

The mechanical behaviour of CLT in bending and shear is influenced by its layered, orthotropic structure. During bending, the outer layers with grain in the longitudinal direction carry most of the load, while the perpendicular layers contribute little to bending stiffness. For shear, all layers are involved, but the transverse layers are especially sensitive to rolling shear. This type of deformation happens in the plane of the panel, but across the grain, and leads to lower shear strength and stiffness. Rolling shear can have a significant effect on how the panel performs, particularly in short spans or when shear forces are high. Figure 2.1 illustrates the typical stress distribution in a CLT panel under bending, highlighting the dominance of bending stresses in the outer layers and the concentration of shear stresses at the interfaces. These behaviours must be carefully considered in design. For a more detailed treatment of CLT mechanics, including analytical models and calculation methods, the CLT Handbook [27] offers comprehensive guidance.

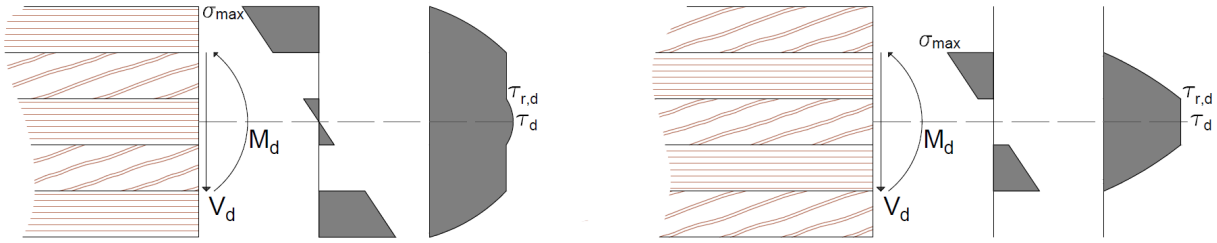

Figure 2.1: Stresses in major (L) and minor (R) direction in CLT panel

The design strength of timber elements is determined using partial safety factor design according to Eurocode 5, and is calculated using Equation 2.1. This equation adjusts the characteristic strength of timber to reflect service conditions, variability in material behaviour and safety requirements.

$$f_d = k_{mod} \Pi k_i \frac{f_k}{\gamma_M} \tag{2.1}$$

with
- k_{mod} factor taking into account load duration and moisture content
- Πk_i product of additional applicable factors (e.g. $k_{c,90}$, k_v, k_h and k_{sys})
- f_k characteristic strength

2.3 Column-to-panel

The column-to-panel connection in point-supported CLT floor systems is crucial for load transfer, with key forces including shear, bearing pressure, and bending moments. These forces impact the design and performance of the connection. Additionally, torsional stresses, although less common, can occur and may affect the connection's behaviour. This section will cover these forces, with a focus on their relevance to point-supported floor systems.

2.3.1 Shear force

Rolling shear strength is often the governing design criterion in point-supported CLT floor systems. To evaluate rolling shear stresses, formulas proposed by Mestek [43] are commonly used, see Table 2.1. The coefficient k_A (see Tab. 2.3) accounts for increased rolling shear stress near the edges of point supports located at the corners of a CLT panel. The factors $k_{R,x}$ and $k_{R,y}$ (see Tab. 2.2) reflect the influence of the number of layers in the CLT panel, as a more layers increases the effective shear-carrying capacity.

Table 2.1: Determination of rolling shear stresses [43]

System		Point support in center of CLT slab	Point support in corner of CLT slab
Shear force	x-direction	$V_{xz} \approx 0.33 \cdot n^{-0.1} \cdot F$	$V_{xz} \approx 0.67 \times n^{-0.1} \times F$
	y-direction	$V_{yz} \approx 0.5 \times F - V_{xz}$	$V_{yz} \approx F - V_{xz}$
Tributary width	x-direction	$b_{ef,x} = b_{A,x} + d \cdot \tan(35°)$	$b_{ef,x} = b_{A,x} + \frac{d}{2} \cdot \tan(35°)$
	y-direction	$b_{ef,y} = b_{ef,x}$	$b_{ef,y} = b_{ef,x}$
Rolling shear stress	x-direction	$\tau_{R,xz} = \frac{V_{xz}/b_{ef,x}}{k_{R,x} \cdot (d_x + d_y)}$	$\tau_{R,xz} = \frac{V_{xz}/b_{ef,x}}{k_{R,x} \cdot (d_x + d_y)} \cdot k_A$
	y-direction	$\tau_{R,yz} = \frac{V_{yz}/b_{ef,y}}{k_{R,y} \cdot (d_x + d_y)}$	$\tau_{R,yz} = \frac{V_{yz}/b_{ef,y}}{k_{R,y} \cdot (d_x + d_y)} \cdot k_A$

Table 2.2

Number of layers	5	7	9	11
$k_{R,x}$	2.00	2.50	3.33	3.89
$k_{R,x}$	1.00	2.00	2.50	3.33

Table 2.3

$\frac{b_{A,x}}{d}$ **or** $\frac{b_{A,y}}{d}$	≤ 1.0	≤ 1.5	≤ 2.0
k_A	1.35	1.50	1.65

According to Mestek, the shear force distribution in CLT floors is primarily influenced by the number of layers and the thickness ratio between layers in the primary and secondary directions. Floor thickness and the $\frac{L}{B}$ ratio have negligible impact. Figure 2.2 illustrates the effective support width for point supports placed at the corner or centre of a panel. Shear load propagation can be estimated using a 45° angle along the grain and 15° across the grain, but Mestek proposes a simplified method using a single 35° angle to the vertical, being on the conservative side. This simplification may be less accurate when double layers with the same grain direction are present.

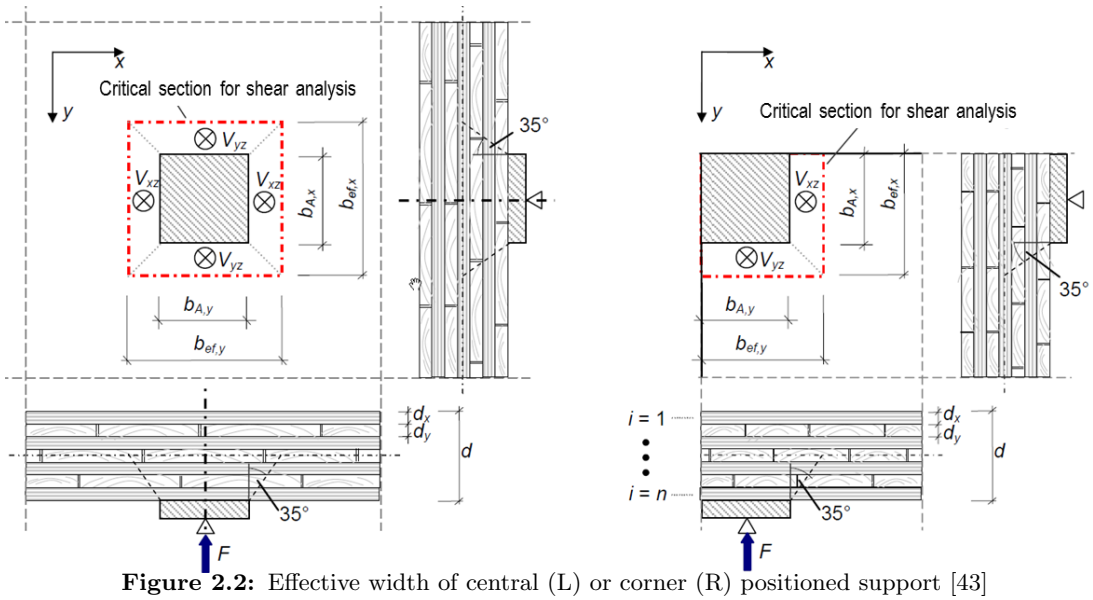

Figure 2.2: Effective width of central (L) or corner (R) positioned support [43]

According to Mestek [43], the design shear strength can be increased with factor $k_{R,90}$ to account for the compression perpendicular to the grain effect. Although not stated by Mestek, a possible explanation for the beneficial effect of compression perpendicular to the grain on shear strength is that it confines the wood structure, increasing friction and interlocking between fibres. This reduces the risk of shear crack formation, particularly in rolling shear-prone layers. Depending on the grain direction of each layer, shear verification must be performed using either the design longitudinal shear strength $f_{v,k}$ or the design rolling shear strength $f_{r,k}$. Using this factor and a panel specific characteristic shear strength f_k, the design shear strength can be determined using Equation 2.2.

$$f_{v/r,d} = k_{R,90} \times \Pi k_i \times \frac{f_{v/r,k}}{\gamma_M} \tag{2.2}$$

with

$$k_{R,90} = \min \begin{cases} 1 + 0.35 \times \sigma_{c,90} \\ 1.2 \end{cases}$$

Due to the combined action inherent to two axis bending, the Eurocode 5 draft states a combined shear check as shown in Equation 2.3. For comparison also see Equation 2.7. The design strengths relevant for this verification can be found in the Eurocode 5 draft [23].

$$\left(\frac{\tau_{xy,d}}{f_{v,xy,d}}\right)^2 + \left(\frac{\tau_{xz,d}}{f_{v,xz,d}}\right)^2 \leq 1 \tag{2.3}$$

2.3.2 Bearing pressure

For compression perpendicular to the grain, a model proposed by Brandner [11] uses two dispersion angles $\alpha_L = 45°$ for propagation parallel to the grain and $\alpha_T = 15°$ for perpendicular. These angles are used to determine the effective loaded area $A_{c,ef}$, as illustrated in Figure 2.3.

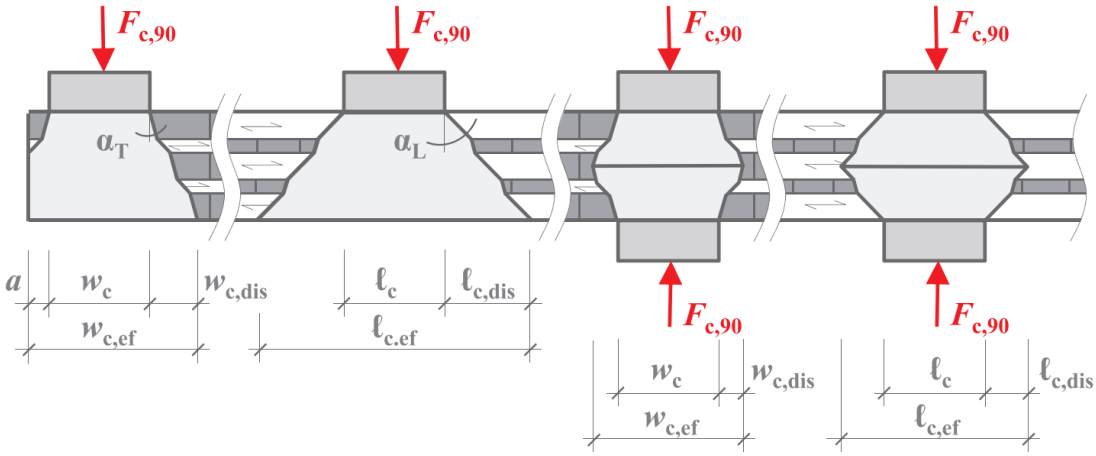

Figure 2.3: Load introduction in a CLT plate [11]

In the draft of Eurocode 5 [23], the equations proposed by Brandner are adopted, see Equation 2.4. Unlike the value specified in the Eurocode, Brandner suggests an upper limit of 5 for $k_{c,90}$.

$$\sigma_{c,90,d} \leq k_{mat} k_{c,90} f_{c,90,d} \tag{2.4}$$

where

$$k_{c,90} = \sqrt{\frac{A_{c,ef}}{A_c}} = \sqrt{\frac{l_{c,ef} w_{c,ef}}{l_c w_c}} \leq 4$$

with
- $k_{c,90}$ factor accounting for spreading of compressive stresses
- k_{mat} factor accounting for material behaviour and compressive deformation
- $f_{c,90,d}$ design compressive strength $[N/mm^2]$

Reinforcement for compression perpendicular to the grain can be achieved using screws, which help redistribute the load into stronger grain directions. This method increases the effective bearing capacity and can be particularly useful near point supports or in highly loaded zones.

2.3.3 Bending moments

The introduction of concentrated vertical loads at column positions within CLT slabs presents a significant challenge in terms of local bending stress, particularly when openings are present to avoid compression perpendicular to the grain. In the presence of an opening, finite-element (FE) models often return unreliable results due to local stress singularities. Openings may interrupt load-carrying boards, locally amplifying the bending stress in the remaining section, or may leave adjacent boards intact, significantly reducing the local concentration.

To address this variability, Muster [48] conducted both experimental and numerical investigations. A stress concentration factor k_{SC} was introduced to quantify the increase in bending stress caused by the opening, relative to the stress without an opening. This factor was determined through strain measurements during testing. The results of these experiments were adjusted and optimized by three-dimensional FE simulations that provided a more consistent representation of the stress distribution. Regression analyses resulted in parametric equations for k_{SC}, which depend on the support width d_{sup}, opening width d_{op} and slab thickness t_{CLT}. The following equation was derived with separate parameters for interior and edge column configurations:

$$k_{SC} = k_{0,SC} + d_{op} \times k_{op,SC} + d_{sup} \times k_{sup,SC} + t_{CLT} \times k_{t,SC}$$

Table 2.4: Stress concentration factors [48]

	$k_{0,SC}$	$k_{op,SC}$	$k_{sup,SC}$	$k_{t,SC}$
Interior column	1.05	0.0025	-0.0001	0.00025
Edge column	1.10	0.0050	-0.00033	0.00050

In the numerical model, modelled without an opening, the CLT floor is simulated as an orthotropic plate. The floor is modelled with appropriate support and loading conditions to represent interior and edge column scenarios. To realistically represent the structural behaviour, the support is modelled with a finite surface area rather than as a point. This ensures that the bending moment is distributed more uniformly over the support region, avoiding unrealistically high stress concentrations. Based on this model without an opening, the bending stress at the support can be calculated. By applying the stress concentration factor, the increased stress due to an opening can then be estimated, allowing the effective bending strength to be assessed. This effect is depicted in Figure 2.4 and calculated using Equation 2.5.

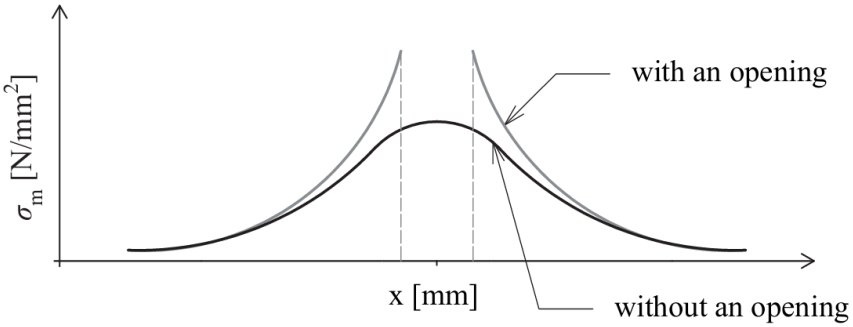

Figure 2.4: Bending stress concentration around an opening at a column-slab connection [48]

$$\sigma_{m,ef} = \sigma_{m,no} \cdot k_{SC} \tag{2.5}$$

with
$\sigma_{m,ef}$ bending stress at the support with an opening $[N/mm^2]$
$\sigma_{m,no}$ bending stress without an opening $[N/mm^2]$

A key outcome of this research was the confirmation of a system effect in CLT, where the bending strength increases locally at point supports. Experimental investigations showed that the 5-percentile tensile stress at failure was approximately 19% higher than the 5-percentile tensile strength. To account for this effect, Muster [48] introduced a system coefficient $k_{sys} = 1.10$ for these regions. At point supports, only a limited area of the CLT slab is subjected to maximum stress. Bogensperger et al. [9] demonstrated that this localized loading condition can lead to an increase in apparent bending strength. This phenomenon, often referred to as a volume effect, arises because only a small portion of the material is exposed to high bending moments under concentrated loads. Consequently, an increase in bending strength can be expected, which justifies the introduction of the system strength factor k_{sys}. The factor has been adopted in NEN-EN 16351 [22]:

$$k_{sys,x} = \min(0.975 + 0.025 n_{lay,x}; 1.1)$$
$$k_{sys,y} = \min(\frac{4350 + h_{CLT}}{4500}; 1.1)$$

2.3.4 Torsional stresses

Closely related to the shear stresses are torsional stresses, Flaig and Blaß [26] distinguish three different failure modes:

- Mode I: shear failure parallel to the grain in the gross section
- Mode II: shear failure perpendicular to the grain in the net cross section
- Mode III: shear failure within the crossing-areas between orthogonally bonded lamellae

This third failure mode is due to torsional stresses, which becomes critical in point-supported CLT floor systems. The concentrated loads lead to rotation and twisting, which exploit the weak

cross-area shear stiffness of CLT. These stresses can cause delamination or shear failure between layers, a vulnerability not as pronounced in line-supported systems. Based on the equilibrium method, Boggian et al. [10] derived a formula to calculate the torsional stresses based on the lamellae proportions and internal stresses:

$$\tau_T = 3 \times \frac{\tau_{xy} \times t_{max}}{b_l} \tag{2.6}$$

with
- b_l width of laminations [mm]
- t_{max} maximum lamella thickness [mm]
- τ_{xy} shear stress in the panel, depending on the number of layers $[N/mm^2]$

This formula is more unfavourable compared to the one prescribed in the building code. That formula is also derived, but is derived for the case of a three layer panel. Normally these stresses in the panel are relatively small and often not governing. However, due to the panels being point-supported, in-plane stresses develop. These stresses are the highest around the supports. The following design rule is stated in the draft of Eurocode 5 [23]:

$$\frac{\tau_{tor,d}}{f_{v,d}} + \left(\frac{\tau_{xy,d}}{f_{v,xy,d}}\right)^2 + \left(\frac{\tau_{xz,d}}{f_{v,xz,d}}\right)^2 \leq 1 \tag{2.7}$$

2.4 Inclined screw connection

In this report panel-to-panel connections will be investigated and in particular a splice plate connection. The connection of this splice plate to the CLT panel is executed using an angled screw connection. In the new prEN 1995-1-1 standard [23] a calculation method is included for inclined screw connections. This section will focus on multiple calculation methods that are suitable for estimating the strength and stiffness of an inclined screwed connection.

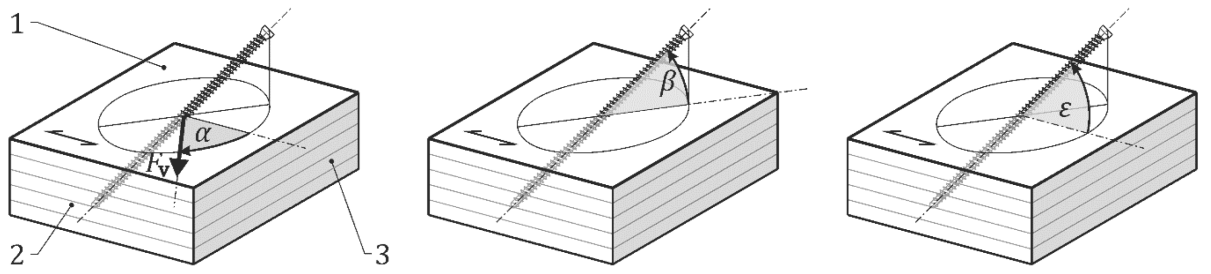

(a) In the wide face

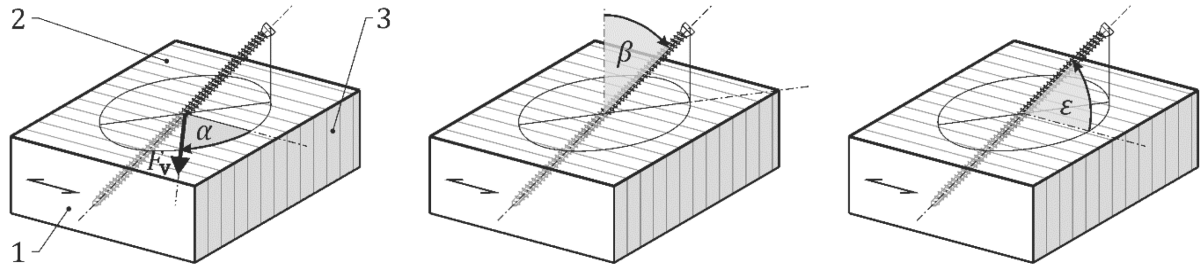

(b) In the narrow face

Figure 2.5: Definition of angles α, β and ε [23]

First, some assumptions, or definitions, should be made to prevent any miscommunications. Clearly stated assumptions make it possible to compare different approaches, methods, or outcomes. If two different researches lead to different results, knowing the assumptions behind

each helps explain why. The inclination of the screw is divided into three angles, as stated in prEN 1995-1-1 [23], see also Figure 2.5:

- α angle between acting force and grain direction
- β angle between fastener axis and surface of the wide face
- ε angle between fastener axis and grain direction

The structural performance of a timber connection is influenced by multiple elements, each with their own strength and stiffness properties. This complexity makes it difficult to directly compare applied stresses and strengths in a straightforward way. Multiple mechanical models have been developed to predict the structural behaviour of connections. However, one of the key challenges in implementing these models is accounting for the varying characteristic properties of the individual components and the different possible failure modes. To ensure a reliable connection design, the complete system should be considered. [33]

2.4.1 Inclined screws - stiffness

Tomasi, Crosatti and Piazza (2010)

Tomasi et al. [61] investigated the strength and stiffness of inclined screws subjected to shear tension. Based on the work done by Bejtka and Blaß [8] (see section 2.4.2) equation 2.8 is derived.

$$K_{ser} = K_{\perp} \times \cos\alpha \times (\cos\alpha - \mu \sin\alpha) + K_{\parallel} \times \sin\alpha \times (\sin\alpha + \mu \cos\alpha) \tag{2.8}$$

with

$\mu = 0.25$	friction coefficient between the members [-]
$K_{\perp}$	connector stiffness for lateral loading [N/mm]
$K_{\parallel}$	connector stiffness for axial loading [N/mm]
α	angle between screw and the normal to the shear plane ($\alpha = 90° - \beta$) [°]

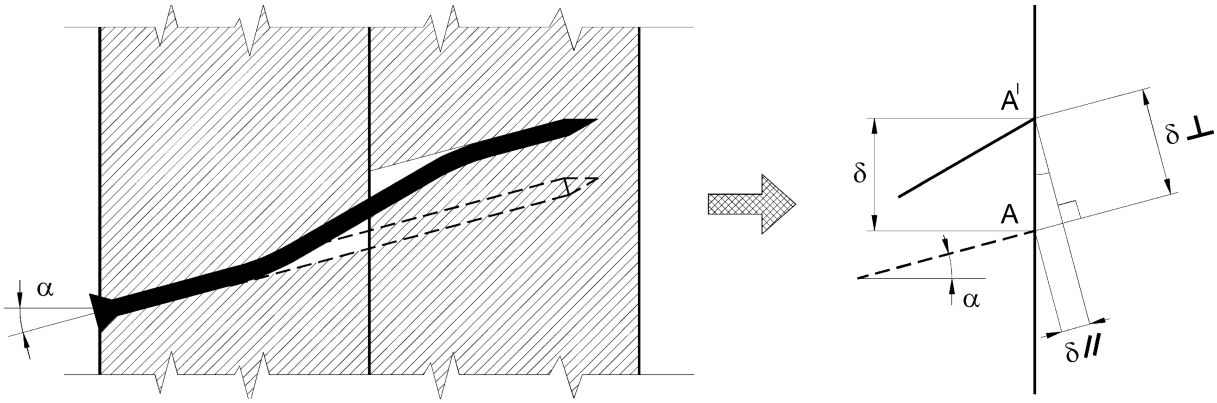

Figure 2.6: Components of displacement on the shear plane [61]

Tomasi et al. [61] propose equation 2.9 to calculate the lateral stiffness of a fastener. This equation is stated in the EN 1995-1-1 [21] for screws in timber-to-timber connections.

$$K_{\perp} = \frac{\rho_m^{1.5} \times d}{23} \tag{2.9}$$

with

d	screw diameter [mm]
ρ_m	mean density of the timber member (if $\rho_{m1} \neq \rho_{m2}$, $\rho_m = \sqrt{\rho_{m1}\rho_{m2}}$) [kg/$m^3$]

The axial stiffness of a screwed connection in two (timber) members should be calculated as a series of two springs, see equation 2.10. This calculation assumes a simultaneous pull-out of both threaded parts of the screws in both timber members, Tomasi et al. refer to this as "double

stiffness model" [61].

$$K_{\parallel} = \frac{1}{\frac{1}{K_{ser,ax,1}} + \frac{1}{K_{ser,ax,2}}} \tag{2.10}$$

Tomasi et al. [61] suggest that individual axial stiffness values should be determined experimentally. However, nowadays the calculation of the axial stiffnesses of a screw is often provided in the associated technical documentation.

De Santis and Fragiacomo (2021)

De Santis and Fragiacomo [12] employ an elastic beam on an elastic foundation model to derive an exact solution to predict the slip modulus of timber-to-timber connections. Equation 2.11 is used in combination with eighteen boundary conditions, six for every layer, can be used to find an analytical solution.

$$K_{s,an} = \frac{EA \times u_2' \times (l_1 + l_2) \times \sin\theta}{\delta} + \frac{EI \times \nu_2''' \times (l_1 + l_2) \times \cos\theta}{\delta} \tag{2.11}$$

In this formulation the angle θ is formulated as the angle between screw and the normal to the shear plane ($\theta = 90° - \beta$).

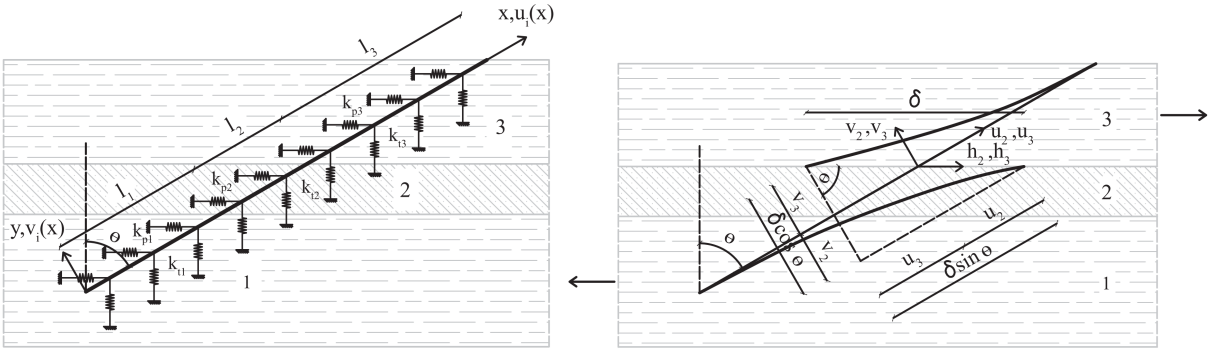

Figure 2.7: Beam on elastic foundation model [12]

De Santis and Fragiacomo [12] derive a closed form expression based on interpolation for the most relevant parameters, see equation 2.12. Through this approach the complex analytical model is rewritten to a form suitable for implementation in codes of practice. If no interlayer is present, $l_2 = 0$ and the exponential term with "dd" as the base becomes 1.0 and thus disappears from the equation.

θ [°]	aa	bb	cc	dd	ee
0	1.11	0.103	1.10	0.852	0.0814
30	1.04	0.598	0.676	0.965	0.274
45	1.05	0.695	0.657	0.988	0.325
60	1.07	0.755	0.608	0.993	0.266
75	1.13	0.846	0.489	0.996	0.106

$$K_{s,\text{int}} = \frac{ee \times \varphi^{cc}}{\frac{1}{\rho_1^{aa} l_1^{bb}} + \frac{1}{\rho_3^{aa} l_3^{bb}}} \times dd^{\left(\frac{l_2}{\varphi^{0.55}}\right)} \tag{2.12}$$

with
- φ screw diameter [mm]
- ρ_i mean density of the timber members within range 400-750 [kg/m^3]
- l_i screw length in timber member within range 50-200 [mm]

De Santis and Fragiacomo [12] use experimental studies from multiple authors to validate the proposed analytical model and its closed form, see Figure 2.8 for the results. These formulas have been shown to accurately capture the influence of key parameters, such as densities, screw penetration lengths and screw diameter, on the slip modulus. The model underestimates the test results, the neglected frictional effect is mentioned as a possible explanation.

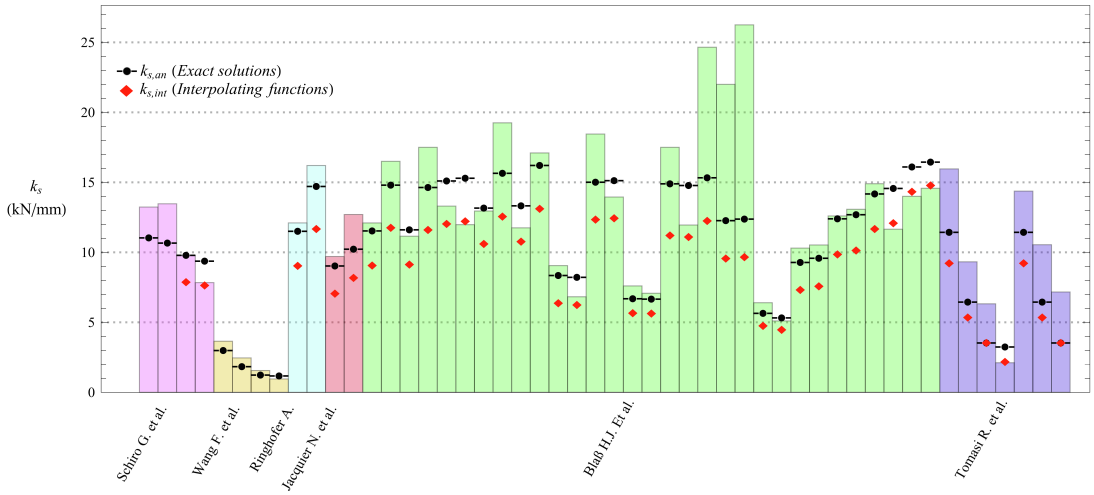

Figure 2.8: Comparison between experimental mean (bars) and predicted stiffness values [12]

Eurocode 5: prEN 1995-1-1 Draft (2023)

At the moment of writing the building code for designing with timber is being updated and extended. A draft version has already been released and most of the content will be in the final version. According to this prEN 1995-1-1:2023 [23] the slip modulus of a connection with inclined fasteners subjected to shear tension can be calculated using equation 2.13.

$$K_{SLS} = K_{SLS,v} \times \sin\varepsilon \times (\sin\varepsilon - \mu\cos\varepsilon) + \frac{1}{2} K_{SLS,ax} \times \cos\varepsilon \times (\cos\varepsilon + \mu\sin\varepsilon) \tag{2.13}$$

with
- $\mu = 0.25$ friction coefficient between the members [-]
- $K_{SLS,v}$ lateral slip modulus per fastener per shear plane [N/mm]
- $K_{SLS,ax}$ axial slip modulus per fastener per connected member [N/mm]

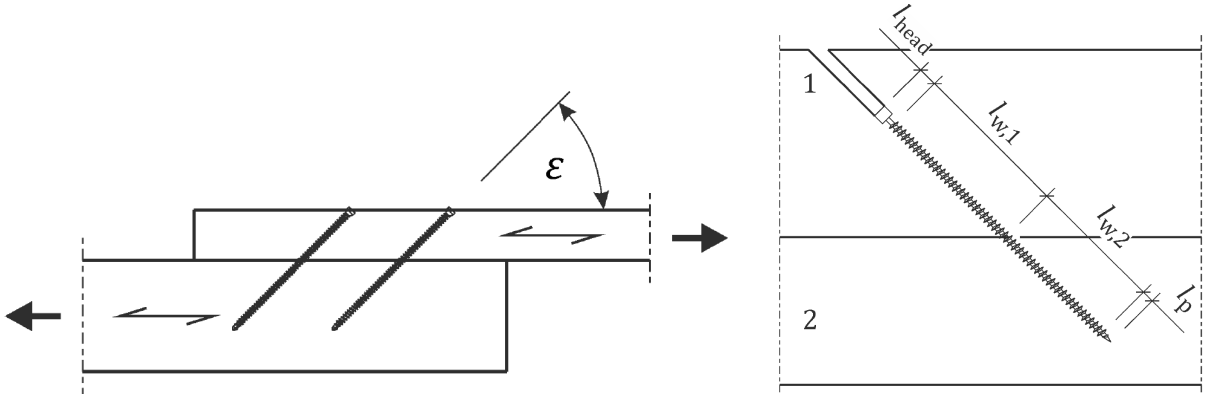

(a) Inclined fastener **(b)** Withdrawal length in two members

Figure 2.9: Connection with inclined fasteners [23]

The axial and lateral slip moduli of screws can be calculated using the following formulations:

$$K_{SLS,v} = 60 \times (0.7d)^{1.7} \tag{2.14}$$

$$K_{SLS,ax} = 160 \times (\frac{\rho_{mean}}{420})^{0.85} \times d^{0.9} l_w^{0.6} \tag{2.15}$$

with
- $\mu = 0.25$ friction coefficient between the members
- d diameter of the screw [mm]
- l_w withdrawal length [mm]
- ρ_{mean} mean density $[kg/m^3]$

The origin of the $\frac{1}{2}$-term in equation 2.13 is not completely clear, however, the equation has a similarity to the equation that has been derived by Tomasi (see equation 2.8). In the formula used in the building code, the connection is assumed to consist of two equal timber members with equal penetration lengths and thus equal axial slip moduli. This means $K_{sls,ax,1} = K_{sls,ax,2}$, hence the $\frac{1}{2}$ in equation 2.13:

$$\frac{1}{K_{sls,ax}} = \frac{1}{K_{sls,ax,1}} + \frac{1}{K_{sls,ax,2}} \quad \rightarrow \quad \frac{1}{K_{sls,ax}} = \frac{2}{K_{sls,ax,1}} \quad \rightarrow \quad K_{sls,ax} = \frac{1}{2} K_{sls,ax,1}$$

For a connection consisting of two different timber members and/or different penetration lengths, the $\frac{1}{2}$-term should be left out.

2.4.2 Inclined screws - strength

EYM: Johansen (1949)

The strength of a dowel connection depends on its failure mode. Johansen first derived closed-form expressions for these possible failure types in 1949 [34]. The European Yield Model (EYM) is based on plasticity principles and identifies failure modes based on relative strength and stiffness of the fastener and the timber members. The possible failure types are shown in Figure 2.10 and divided into three distinct failure mode types:

- Mode I: No plastic hinges in the dowel
- Mode II: One plastic hinge in the dowel
- Mode III: Two plastic hinges in the dowel

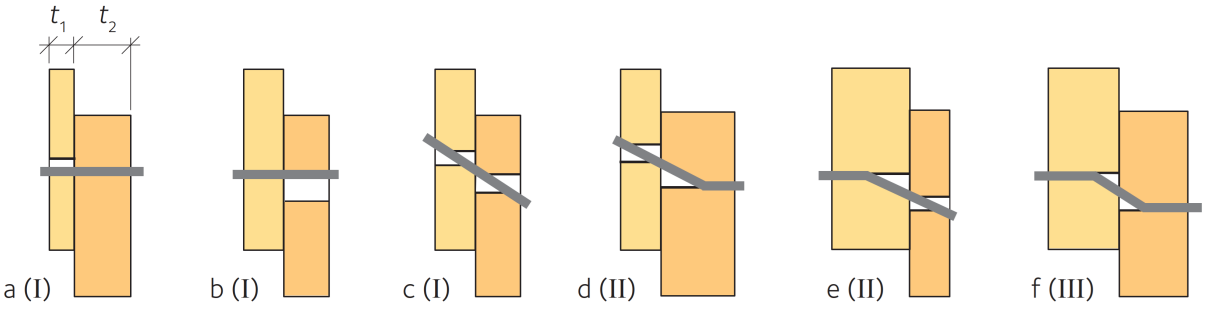

Figure 2.10: Possible failure modes in timber-to-timber joints [29]

The model considers a force balance between embedding failure of the timber elements and plastic yielding of the fastener. By assuming perfect plastic behaviour in both the wood and the dowel, equations 2.16 are derived describing the different failure modes.

$$F_{D,k} = min \begin{cases} (a) & f_{h,1,k} t_1 d \\ (b) & f_{h,2,k} t_2 d \\ (c) & \frac{f_{h,1,k} t_1 d}{1+\beta} [\sqrt{\beta + 2\beta^2 [1 + \frac{t_1}{t_2} + (\frac{t_2}{t_1})^2] + \beta^3 (\frac{t_2}{t_1})^2} - \beta(1 + \frac{t_2}{t_1})] \\ (d) & 1,05 \frac{f_{h,1,k} t_1 d}{2+\beta} [\sqrt{2\beta(1+\beta) + \frac{4\beta(2+\beta) M_{y,Rk}}{f_{h,1,k} d t_1^2}} - \beta] \\ (e) & 1,05 \frac{f_{h,1,k} t_2 d}{1+2\beta} [\sqrt{2\beta^2(1+\beta) + \frac{4\beta(1+2\beta) M_{y,Rk}}{f_{h,1,k} d t_2^2}} - \beta] \\ (f) & 1,15 \sqrt{\frac{2\beta}{1+\beta}} \sqrt{2 M_{y,Rk} f_{h,1,k} d} \end{cases} \tag{2.16}$$

where

$$\beta = \frac{f_{h,2,k}}{f_{h,1,k}}$$

with

$f_{h,i,k}$	characteristic embedment strength of member i	$[N/mm^2]$
$t_{h,i}$	embedment depth in member i	[mm]
$M_{y,k}$	characteristic yield moment of fastener	[Nmm]
d	diameter of fastener	[mm]

The EYM does not account for contributions from friction between the timber members or the axial force in the fastener during deformations. Johansen himself demonstrates that these factors most likely influence the behaviour of a dowelled connection. Kuipers and Van der Put [39] studied this rope effect further in 1982 and show a 27% effect on the strength of a dowelled connection with long nails. [57]

Bejtka and Blaß (2002)

Bejtka and Blaß [8] suggest to utilize the withdrawal capacity of screws and contact friction at the timber-to-timber interface, this way the load-carrying capacity can be significantly increased. They note that Johansen's yield theory assumes ideal rigid-plastic behaviour from both the fastener and the timber. However, testing shows non-plastic behaviour of the screws. To solve this problem, Bejtka an Blaß [8] propose a modified withdrawal parameter that depends on the considered failure mode. Including this parameter and the other mentioned parameters (screw angle and friction) an extended design equation is derived, see Figure 2.11a. This modified withdrawal parameter depends on the axial displacement Δ relative to slip δ between the timber members, see Figure 2.11b.

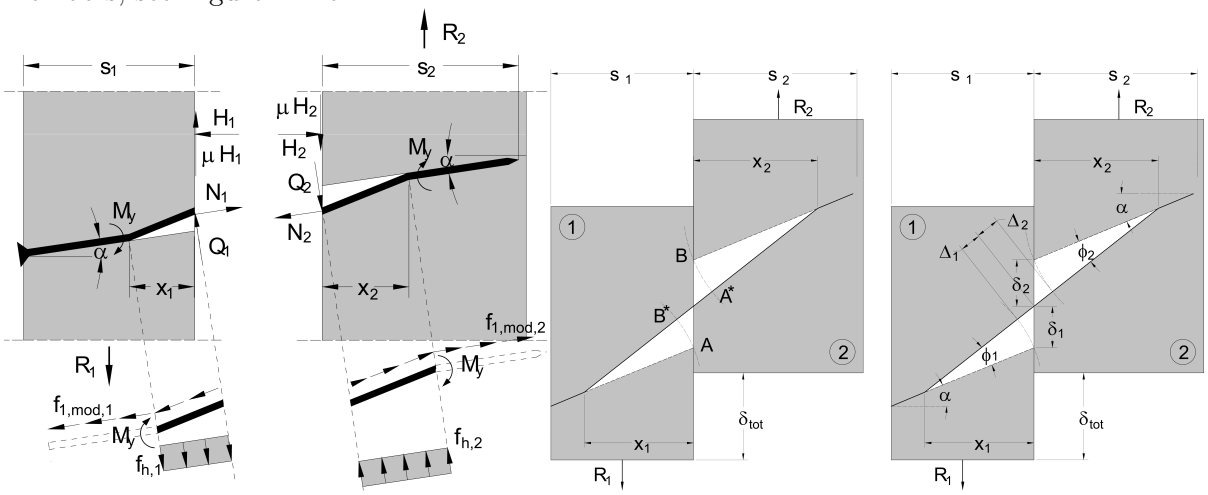

(a) Forces in a timber-to-timber connection with an inclined screw according to failure mode III in EYM [8]

(b) Deformation behaviour in a timber-to-timber connection with an inclined screw [8]

Figure 2.11

They propose an extended EYM including the aforementioned parameters:

$$R_{\mathrm{VM1a,l}} = R_{\mathrm{ax,1al}} \times \sin\alpha + f_{h,1} d s_1 \times \cos\alpha$$

$$R_{\mathrm{VM1a,r}} = R_{\mathrm{ax,1ar}} \times \sin\alpha + f_{h,2} d s_2 \times \cos\alpha$$

$$R_{\mathrm{VM1b}} = R_{\mathrm{ax,1b}} \times (\mu\cos\alpha + \sin\alpha)$$

$$+ \frac{f_{h,1} d s_1}{1+\beta} \times (1 - \mu\tan\alpha) \times \left[\sqrt{\beta + 2\beta^2 \times \left(1 + \frac{s_2}{s_1} + \left(\frac{s_2}{s_1}\right)^2\right) + \beta^3 \times \left(\frac{s_2}{s_1}\right)^2} - \beta\left(1 + \frac{s_2}{s_1}\right) \right]$$

$$R_{\mathrm{VM2a}} = R_{\mathrm{ax,2a}} \times (\mu\cos\alpha + \sin\alpha)$$

$$+ (1 - \mu\tan\alpha) \times \frac{f_{h,1} s_1 d}{2+\beta} \times \left[\sqrt{2\beta(1+\beta) + \frac{4\beta(2+\beta) \times M_y \times \cos^2\alpha}{f_{h,1} d s_1^2}} - \beta \right]$$

$$R_{\text{VM2b}} = R_{\text{ax,2b}} \times (\mu \cos\alpha + \sin\alpha)$$
$$+ (1 - \mu \times \tan\alpha) \times \frac{f_{h,1} \times s_2 \times d}{1 + 2\beta} \times \left[\sqrt{2\beta^2(1+\beta) + \frac{4\beta(2\beta+1) \times M_y \times \cos^2\alpha}{f_{h,1} d s_2^2}} - \beta \right]$$

$$R_{VM3} = R_{ax,3} \times (\mu \cos\alpha + \sin\alpha) + (1 - \mu \tan\alpha) \times \sqrt{\frac{2\beta}{1+\beta}} \times \sqrt{2 M_y d f_{h,1} \times \cos^2\alpha}$$

In this formulation the angle θ is formulated as the angle between screw and the normal to the shear plane ($\theta = 90° - \beta$, with β as defined in Figure 2.5). Using these equations the load-bearing capacity of inclined screws in a timber-to-timber connection can be determined with equation 2.17.

$$R = \min \begin{cases} R_{\text{VM1a,l}} \\ R_{\text{VM1a,r}} \\ R_{\text{VM1b}} \\ R_{\text{VM2a}} \\ R_{\text{VM2b}} \\ R_{VM3} \end{cases} \qquad (2.17) \qquad R_{ax,j} = \min \begin{cases} f_{1,mod,1,j} \times d \times \frac{s_1}{\cos\alpha} \\ f_{1,mod,2,j} \times d \times \frac{s_2}{\cos\alpha} \end{cases} \qquad (2.18)$$

with
- $f_{h,i}$ characteristic embedment strength of member i $[N/mm^2]$
- s_i embedment depth in member i [mm]
- $M_{y,k}$ characteristic yield moment of fastener [Nmm]
- d diameter of fastener [mm]
- j Johansen's failure mode; 1a,l; 1a,r; 1b; 2a; 2b or 3

For angles $\alpha > 30°$ ($\beta < 60°$) the ultimate withdrawal capacity is reached in timber-to-timber connections for all screw diameters. The use of these formulas is possible after determining the embedding strength and the modified withdrawal capacity. Nowadays these parameters can be obtained using the associated technical documentation for a certain screw.

Eurocode 5: prEN 1995-1-1 Draft (2023)

As mentioned before a draft version exists for Eurocode 5 - Design of timber structures. The rules in this document are partly based on the mentioned research and of course on other research. The axial resistance of a screw can be calculated using the following formulas [23]:

$$F_{ax,t,d} = \min(F_{ax,t,d,1}, F_{ax,t,d,2}) \qquad (2.19)$$

with
$$F_{ax,t,d,1} = \frac{k_{mod}}{\gamma_R} \max \begin{cases} F_{pull,k} \\ F_{w,k} \end{cases}$$
$$F_{ax,t,d,2} = \frac{F_{t,k}}{\gamma_R}$$

Equation 2.19 means that the axial resistance of a fastener is governed by the lower of either the withdrawal resistance in the timber member or the tensile strength of the fastener itself. The characteristic tensile strength of the screw itself should be taken as follows [23]:

$$F_{t,k} = 0.9 A_s f_{u,k} \qquad (2.20)$$

with
- A_s Nominal stress area of the inner thread diameter of the screw based $[mm^2]$
- $f_{u,k}$ Characteristic steel strength $[N/mm^2]$

The resistance of the fastener in the timber member is determined by the maximum value of either the head pull-through resistance of the screw head, or the withdrawal resistance along the

screw length. The head pull-through resistance is calculated depending on the material, in this report the calculation for CLT and LVL are relevant:

$$CLT: \quad F_{pull,k} = \begin{cases} f_{head,k} A_{head} & \text{for } A_{head} \leq 4072 \\ 3 f_{c,90,k} A_{head} & \text{for } A_{head} > 4072 \end{cases} \tag{2.21a}$$

$$LVL: \quad F_{pull,k} = \begin{cases} d_{head}^2 \times 70 \times 10^{-6} \times \rho_k^2 & \text{for } \rho_k \leq 730 \\ d_{head}^2 \times (70 - 0.8 d_{head}) & \text{for } \rho_k > 730 \end{cases} \tag{2.21b}$$

with

$$f_{head,k} = 19 e^{-\frac{d_{head}}{50}} (\frac{\rho_k}{350})^{0.8}$$

where

A_{head}	area of fastener head or washer $[mm^2]$
d_{head}	head diameter ($d_{head} \geq 1.8d$) [mm]
ρ_k	characteristic density $[kg/m^3]$
$f_{c,90,k}$	characteristic compressive strength perpendicular to grain $[N/mm^2]$

The withdrawal resistance calculation depends on the fastener type and the material. For this report only the witdrawal strength for screws is relevant and this is calculated using equation 2.22:

$$F_{w,k} = \pi d l_w f_{w,k} \tag{2.22}$$

with

$f_{w,k} = k_{screw} k_w k_{mat} d^{-0,33} (\frac{\rho_k}{350})^{k_\rho}$
$k_{screw} = 7,5$
$k_w = 1,0$ for $30° \leq \varepsilon \leq 90°$
$k_{mat} = 1 + \frac{\ln(n_p)}{12} \leq 1,15$
$k_\rho = \begin{cases} 1,10 \text{ for softwoods and } 15° \leq \varepsilon \leq 90° \\ 1,60 \text{ for hardwoods} \end{cases}$

Using the equations above the axial resistance of a fastener can be determined. The EYM as described in chapter 2.4.2 returns the lateral resistance. In failure modes that involve bending of the dowel (mode c-f), a part of the load is transferred through tension, the rope effect. This means the lateral resistance per shear plane for a single fastener can be calculated by increasing the dowel effect with the rope effect [23]:

$$F_{v,Rk} = F_{D,k} + \min \begin{cases} 0.25 \times F_{ax,t,k} \\ 1.00 \times F_{D,k} \end{cases} \tag{2.23}$$

Designing a connection subjected to shear tension means an interaction of axial and lateral loads. The following design check should be satisfied:

$$(\frac{F_{ax,Ed}}{F_{ax,Rd}})^p + (\frac{F_{v,Ed}}{F_{v,Rd}})^p \leq 1 \tag{2.24}$$

$F_{ax,Rd}$ should be reduced by the rope-effect and exponent p depends on the failure mode:

Failure mode	Unknown	0 plastic hinges (a,b)	1 plastic hinge (d,e)	2 plastic hinges (f)
p	1.0	1.0	1.5	2.0

2.4.3 Timber-to-timber friction

A parameter returning in both the stiffness and strength calculations is the coefficient of friction. Friction is typically neglected in the design of wood connections due to its unpredictable nature and the possibility that it may disappear over time as a result of shrinkage or relaxation in the

timber members [2]. However, it has been shown by multiple authors that including the friction between the two timber members leads to more economical joint designs. If this friction is not included, the deviation from test results is linked to frictional effects ([34],[12]).

The friction coefficient is defined as the ratio between the friction force and the normal force, both acting in the contact surface. A distinction is made between static and kinetic friction, the first is a frictional force that should be overcome to move an object, the second is force that opposes movement of that object. [59]

McKenzie and Karpovich [42] investigated the frictional behaviour of wood against multiple materials among which also itself. It was concluded that the following parameters influence the frictional behaviour:

- Moisture content; a very dominant factor and dry wood typically exhibited higher friction coefficients than wet wood
- Surface roughness; has a more critical effect at low roughness ($< 50\mu m$)
- Sliding speed; friction typically decreases for increased speed, which is even more so for wet wood, see Figure 2.12
- Material density; under identical test conditions, denser and harder wood species showed lower friction coefficients compared to their softer counterparts

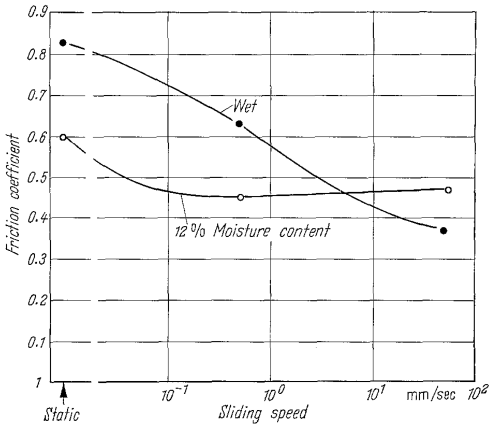

Figure 2.12: Wood sliding on wood [42]

Figure 2.12 seems to go against the statement on higher coefficient of friction for dry wood. McKenzie and Karpovich [42] note that on rough steel, wet wood can deform into surface irregularities, increasing the effective contact area and raising static friction. Further, the conclusion can be drawn that a softer wood surface leads to higher coefficients of friction. McKenzie and Karpovich [42] also mention that friction is influenced by grain orientation, but these influences were small.

In a more recent study Aurand and Blaß [7] investigated the possibility to utilize frictional resistance by treating surfaces. The study by Aurand and Blaß [7] demonstrates that the load-carrying capacity of timber connections with inclined screws can be significantly increased by enhancing shear plane friction through surface modifications. Treatments such as

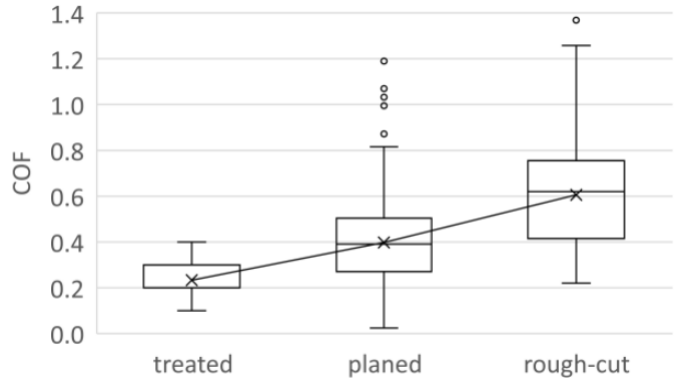

(a) Effect of the surface roughness [7]

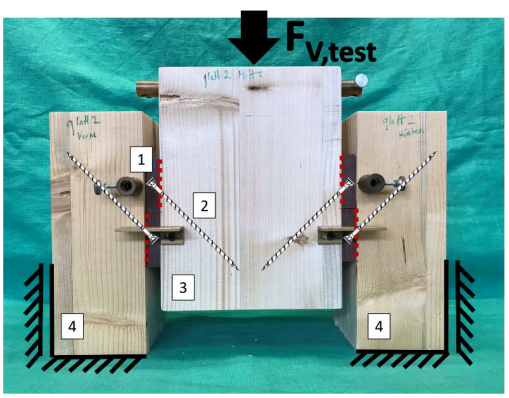

(b) Test setup for push out tests [7]

Figure 2.13

sanding and milling produced much higher coefficients of friction compared to untreated surfaces. Push-out tests, see Figure 2.13b, confirmed that these increased friction levels led to 30–40% higher load capacities.

The research also introduces a validated analytical model that incorporates friction:

$$F_v = n_{ef} \times F_{ax} \times (\cos\alpha + \mu \sin\alpha) \tag{2.25}$$

In this report a coefficient of friction $\mu = 0.25$ will be used, unless stated otherwise. For inclined screws with $\alpha = 45°$ and $\mu = 0.25$, as is assumed in Eurocode 5 [23], this formula simplifies to:

$$F_v = n_{ef} \times \frac{1.25 F_{ax}}{\sqrt{2}}$$

2.5 Vibrations

CLT is beneficial in a lot of designing aspects due to the high stiffness-to-weight ratio and structural efficiency. However, using timber in floor structures also brings an additional challenge in vibrational behaviour. The study of their vibrational behaviour is essential in assessing serviceability limits, comfort levels and dynamic performance. CLT panels exhibit orthotropic properties due to the alternating orientation of their lamellae. This anisotropy influences their dynamic response, particularly the natural frequencies and mode shapes.

On the one hand, vibrations refer to the physical phenomenon of floors oscillating due to external excitation. On the other hand, the perception of these vibrations is subjective and depends on the individual experiencing them. Although floor vibrations can originate from various sources, the most common and troublesome are those generated by occupants during routine activities. To understand the challenge in designing for vibrations, this section will touch onto two subjects. First the influence of and on humans will be described; the excitation due to humans and the human perception of these vibrations. Secondly, more extensively, the vibrational behaviour of CLT floors is introduced. After explaining the relevant aspects of vibrations in floors, relevant design equations will be summarized.

2.5.1 Human induced vibration

Pernica [49] investigated dynamic load factors and found that typical footstep frequencies for rhythmic human activities remain below 4 Hz. Normal walking occurs between 1.6 and 2.2 Hz, while jumping typically ranges from 2.0 to 3.0 Hz. These frequencies are well below the 10 Hz upper limit of the force platform used in their study, which limited the number of measurable harmonics at higher footstep rates. However, the third and fourth harmonics were found to be relatively small and consistent, indicating that dynamic effects are primarily governed by the first and second harmonics [49].

Human sensitivity to vibration is greatest in the frequency range between 4 and 8 Hz, with acceptability thresholds influenced by factors such as building use and activity type [52]. To minimize resonance effects, design practice typically adopts a minimum fundamental, or cut-off, frequency of 8 Hz. For high frequency floors, among which CLT floors, Mohammed et al. [47] even suggest a 14 Hz cut-off frequency in combination with a more probabilistic approach for vibration analysis.

2.5.2 Floor dynamics

The vibrational behaviour of CLT floors is governed by several interacting parameters, including stiffness, mass distribution, damping and boundary conditions. The verification of floor vibrations in design generally focuses on two primary factors: frequency and acceleration, which are essential in determining the floor's dynamic response.

Stiffness
Smith and Chui [53] investigated the dynamic behaviour of joisted, single-span timber floors, focusing on how different stiffness parameters influence vibration performance. They observed that increasing longitudinal stiffness raises the fundamental natural frequency of the floor system. While this increase is typically viewed as beneficial, it was also found to reduce the spacing between adjacent natural frequencies. Closely spaced modes can interact under dynamic excitation, leading to relatively high vibration amplitudes. Therefore, increasing longitudinal stiffness does not always result in improved vibration performance. In contrast, increasing transverse stiffness was found to have a consistently positive effect: it increases the spacing between vibration modes, reduces the likelihood of mode interaction, and improves the overall dynamic response of the floor. [53]

Modal Mass
Modal mass refers to the portion of the total mass of a floor system that actively participates in a specific mode of vibration. The influence of the mass on the natural frequency can most clearly be shown in a single-degree-of-freedom (SDOF) system:

$$f_n = \frac{1}{2\pi}\sqrt{\frac{k}{m}}$$

Increasing the mass causes the structure to vibrate at lower frequencies, which could bring the natural frequency into the perceptible range for humans (4-8 Hz).

On the other hand, increasing the modal mass reduces the root mean square (RMS) acceleration of the system. This is beneficial because lower acceleration means that the structure moves less violently in response to dynamic loads. This means low mass in floors results in greater sensitivity to excitation from human activities, leading to higher vibration amplitudes when impacted by force. Mass is a relatively straightforward parameter to adjust in real-world structures, and its effects can be easily estimated and predicted during design calculations [32].

Damping
Damping is the process of dissipating energy in a vibrating system. It can occur in various forms, including material and structural damping, where the properties of the materials and the structure itself help absorb the vibrational energy. Additionally, damping can be caused by elements like furniture and finishes, such as false floors, which further reduce vibrations. Another type of damping, known as geometrical radiation, occurs when energy is spread through the structure as it propagates. These different mechanisms work together to reduce the intensity and duration of vibrations. [24]

The main effect of damping is reducing vibration amplitudes, which makes the structure move less intensely, improving comfort for occupants. A higher damping ratio leads to quicker vibration decay, preventing excessive movement. The damping ratio depends on the total system, typical values are shown in table 2.5. Contrary to the value specified in this table, prEN 1995-1-1 [23] prescribes a damping ratio of $\zeta = 0.04$ for CLT floors.

Boundary conditions
Huang et al. [31] investigated the vibration performance of a CLT floor through on-site measurements and OpenSees simulations, examining the influence of support conditions. The study found that increasing the stiffness of the supports—such as through larger beams—improves vibration performance by reducing differences between one-way and two-way support scenarios. However, beyond a certain stiffness, additional gains in serviceability were minimal. Reduced support stiffness led to pronounced vibration issues. The results underline the critical role of both support stiffness and spacing in controlling floor vibrations. [31]

Table 2.5: Estimation of damping ratio [24]

Type	**Damping (% of critical damping)**
Structural damping D_1	
Wood	6%
Concrete	2%
Steel	1%
Composite (Steel-Concrete)	1%
Damping due to furniture D_2	
Traditional office for 1 to 3 persons with separation walls	2%
Paperless office	0%
Open plan office	1%
Library	1%
Residential	1%
Schools	0%
Gymnastic rooms	0%
Damping due to finishes D_3	
Ceiling under the floor	1%
Free floating floor	0%
Swimming screed	1%
Total damping $D = D_1 + D_2 + D_3$	

Panel-to-panel connections in CLT floors have a significant influence on vibration performance, yet they have been largely neglected in design practice and research to date. While most studies focus on material properties, damping, and boundary conditions, Milojevic et al. [45] show that inter-panel connections can substantially affect the floor's modal properties. Through experimental data and FEM updating, the connections were effectively modelled as elastic strips, with the strip width identified as the most influential parameter. The findings revealed that, while mode shapes were relatively insensitive, natural frequencies were highly affected by connection stiffness. In particular the elastic modulus was influenced, it was found to be much lower than predicted by static-based expressions. These results underscore the need to account for connection behaviour in vibration assessments and highlight the importance of further research on a broader range of joint types. [45]

Most research into vibrational behaviour has focused on line supported CLT. This report will focus on point-supported CLT, this completely different boundary condition will have its effect on vibrational behaviour. There has been done little investigation into this type of boundary conditions. Some relevant testing will be introduced in the state of the art section 5.2 for nummerical modelling.

2.5.3 Design equations

The main influencing factors for floor vibrations have now been introduced, highlighting the complex and often unpredictable nature of the system. Many parameters interact in ways that are not straightforward, making it difficult to assess vibration behaviour with certainty. Even when the mechanical response of a floor system can be determined accurately, the human perception of vibration remains subjective. Nonetheless, clear guidelines are essential to limit vibration-induced discomfort and ensure occupant satisfaction.

The development of guidelines for vibrations in timber floor systems began in the 1970s and continues to evolve today. Presenting this progression in chronological order helps illustrate the challenges involved and the ways in which different researchers have addressed them. Simovic et al. [52] offer a clear summary of relevant design approaches for human-induced vibrations in CLT

structures. Using their overview, together with the current Eurocode 5 [21], this section outlines the evolution of vibration guidelines leading up to the upcoming standard prEN 1995 [23].

NEN 1995-1-1 (2004)
The current Eurocode 5 [21] provides very limited design rules regarding vibrations. There are three different rating methods proposed:

- *Fundamental frequency*

$$f_1 = \frac{\pi}{2L^2}\sqrt{\frac{(EI)_L}{m}} > 8 \text{ [Hz]} \tag{2.26}$$

  This calculation method is valid for rectangular floors, simply supported along all edges. If the fundamental frequency does not meet this demand, a special investigation should be conducted, it is not specified what kind of verification this is.

- *Unit point load deflection*

$$\frac{w}{F} \leq \text{a [mm/kN]} \tag{2.27}$$

  In this equation w equals the maximum instantaneous deflection caused by force F. The limit a is not specified, but a range of $0.5 - 4.0$mm can be seen in Figure 2.14.

- *Unit impulse velocity response*

$$v \leq b^{f_1\zeta - 1} \text{ [m/(Ns}^2\text{)]} \tag{2.28}$$

  where

$$v = \frac{4(0.4 + 0.6n_{40})}{mBL + 200}$$

  where

$$n_{40} = \left[\left(\left(\frac{40}{f_1}\right)^2 - 1\right)\left(\frac{B}{L}\right)^4 \frac{(EI)_L}{(EI)_B}\right]^{0.25}$$

  This is the peak initial vertical vibration velocity of the floor, measured in m/s, resulting from a unit impulse of 1 Ns applied at the point of highest response. Vibrational components exceeding 40 Hz are not included. The limit b is again not specified, but depends on the limit a, see Figure 2.14.

with

	L, B	floor span and width $[m]$
	m	mass per unit area $[kg/m^2]$
	$(EI)_{L,B}$	equivalent bending stiffness in span or width direction $[Nm^2/m]$
	ζ	damping ratio (recommended $\zeta = 0.01$) [-]
	n_{40}	number of first-order modes with natural frequencies up to 40 Hz [-]

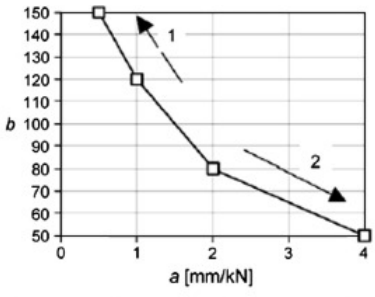

1. Better performance 2. Poorer performance

Figure 2.14: Relationship between a and b [21]

While Eurocode 5 provides a unified basis with its three main criteria, national applications of these guidelines vary significantly across Europe. Zhang et al. [65] highlight that many countries incorporate perception-based comfort evaluation using perception curves. These curves, such as the W_b and W_d curves for vertical and horizontal vibrations respectively, are derived from statistical measures like the one-step root mean square (OS-RMS) values at a defined fractile (e.g. 90%). These descriptors, typically based on weighted velocity or acceleration, cannot be obtained through analytical methods alone and require experimental input.

This dependency calls for collaboration between structural engineers and acousticians. Among the three Eurocode criteria, the unit point load deflection is generally regarded as the most decisive in design, while the relevance of the other two varies by floor system. The current diversity in national approaches, particularly regarding how stiffness and deflection are calculated and limited, emphasises the urgent need for harmonisation and more integrated design methodologies that consider both structural behaviour and occupant perception.

Hamm et al. (2010)
Despite the existence of established design rules aimed at avoiding disturbing floor vibrations, practical issues with timber floor vibrations remain common. In many cases, investigations confirm that existing guidelines are technically satisfied, which indicates that prevailing criteria may be insufficient. This observation, along with the overly conservative nature of existing guidelines, which often result in oversized beams, motivated Hamm et al. [28] to refine the Eurocode-based expression for fundamental frequency. Their revised approach first of all proposed a categorised table to support design decisions based on three floor usage classes, see Table 2.6.

Table 2.6: Design classification of floors according to vibration demands (adapted from Hamm et al. [28])

Demands	**Higher demands**	**Lower demands**	**Without demands**
Description of perception of vibrations	Vibrations are not perceptible or only perceptible when concentrating on them. Vibrations are not annoying.	Vibrations are perceptible but not annoying.	Vibrations are clearly perceptible and sometimes annoying.
Frequency criterion $f_e \geq f_{lim}$	$f_{lim} = 8$ Hz	$f_{lim} = 6$ Hz	-
Stiffness criterion $w_{2kN} \leq w_{lim}$	$w_{lim} = 0.5$ mm	$w_{lim} = 1.0$ mm	-
Acceleration criterion $4.5 \leq f_e \leq f_{lim}$	$a_{lim} = 0.05$ m/s^2	$a_{lim} = 0.10$ m/s^2	-
Demands on construction	Set up of floating screed, heavy screed or light screed on grit fill or not, see table		-

The fundamental frequency calculation from Eurocode 5 (see Eq. 2.26) is adopted for single span beams and specifically for plates an expanded Equation 2.29 accounts for plate behaviour by incorporating transverse stiffness. For comparison, see also Equation 2.32 from the prEN 1995-1-1 standard.

$$f_{plate} = f_{beam} \times \sqrt{1 + \left(\frac{L}{B}\right)^4 \times \frac{(EI)_B}{(EI)_L}} \tag{2.29}$$

Furthermore, they explicitly state an deflection formula (Eq. 2.30) that introduces an effective width term, B_{eff}. This equation uses a $2kN$ point load, as this showed stronger correlation with subjective vibration assessments from their own study than the conventional $1kN$ load. The limit for this deflection can be found in Table 2.6. For comparison, see also Equation 2.33 from the prEN 1995-1-1 standard.

$$w_{2kN} = \frac{2 \times L^3}{48(EI)_L b_{ef}} \tag{2.30}$$

where

$$b_{ef} = \min\left(\frac{L}{1.1} \times \left(\frac{(EI)_T}{(EI)_L}\right)^{0.25}; B\right)$$

Hamm et al. [28] state that the frequency demand for wide spans is very strict, to accommodate these situations a fourth criterion is proposed. A lower bound criterion of $f_1 \geq 4.5Hz$ must still be met, additionally, based on the acceleration of the floor Equation 2.31 is formulated. For comparison, again consider prEN 1995-1-1, see Equation 2.35.

$$a = \frac{F_{dyn}}{M^* 2\zeta} = \frac{0.4F(t)}{0.5L \times 0.5B \times m \times \zeta} \tag{2.31}$$

with
- L, B floor span and width $[m]$
- M^* modal mass of the floor [kg]
- F_{dyn} dynamic force on the floor (0.4-factor applied to account for limited duration and the location not always being at most unfavourable location) [N]
- $F(t)$ harmonic part of force, can be taken as 70 [N]
- ζ damping ratio (recommended $\zeta = 0.01$) [-]

prEN 1995-1-1 (2023)

Updated design rules for the vibration serviceability of timber floors are currently being developed, with a focus on accommodating CLT floor structures. Important proposals were presented by Abeysekera et al. [1] as part of the ongoing revision of the vibration chapter in Eurocode 5.

The vibration criteria table as proposed by Hamm et al. [28] (see Tab. 2.6) is expanded and updated to the version shown in Table 2.7. The values for the upper deflection limit and the response factor deviate from those presented in the original study by Abeysekera et al. [1].

Table 2.7: Floor vibration criteria according to the floor performance level [23]

	Floor performance levels					
Criteria	**I**	**II**	**III**	**IV**	**V**	**VI**
Response factor R	4	8	12	24	36	48
Upper deflection limit $w_{lim,max}$ in mm	0.25	0.5	0.5	1.0	1.5	2.0
Stiffness criteria for all floors:	$w_{1kN} \leq w_{lim}$ mm					
Frequency criteria for all floors:	$f_1 \geq 4.5$ Hz					
Acceleration criteria for resonant vibration design situations ($f_1 < f_{1,\text{lim}}$):	$a_{\text{rms}} \leq 0.005\,R$ m/s^2					
Velocity criteria for all floors:	$v_{\text{rms}} \leq 0.0001\,R$ m/s					

Abeysekera et al. [1] introduce an $k_{e,1}$ factor in the calculation of the fundamental frequency. Equation 2.29 is extended in to Equation 2.32 as prescribed in prEN 1995-1-1 for double span floors. In case of a single span floor $k_{e,1} = k_{e,2} = 1.0$ and the equation simplifies to Equation 2.26.

$$f_1 = k_{e,1} k_{e,2} \frac{\pi}{2L^2} \sqrt{\frac{(EI)_L}{m}} \tag{2.32}$$

where

$$k_{e,2} = \sqrt{1 + \frac{(\frac{L}{B})^4 (EI)_T}{(EI)_L}}$$

with $k_{e,1}$ frequency factor depending on span ratio, see table 2.8

Table 2.8: Factor $k_{e,1}$ for double span floor on rigid supports [23]

$\frac{l_2}{l}$	1.0	0.9	0.8	0.7	0.6	0.5	0.4	0.3	0.2
$k_{e,1}$	1.00	1.09	1.16	1.21	1.25	1.28	1.32	1.36	1.41

The stiffness criterion in the Eurocode is very similar to that proposed by Hamm et al. [28] (see Eq. 2.30), though there are slight differences in formulation. While Hamm et al. [28] uses a $2kN$ point load with a correction factor of $\frac{1}{1.1}$, the prEN 1995-1-1 draft is based on a $1kN$ point load with a factor of 0.95; this discrepancy likely reflects the incorporation of safety margins required in official design standards.

$$w_{1kN} = \frac{FL^3}{48(EI)_L b_{ef}} \tag{2.33}$$

where

$$b_{ef} = \min(0.95L \left(\frac{(EI)_T}{(EI)_L}\right)^{0.25}; B)$$

The velocity criterion has been significantly extended by Abeysekera et al. [1], now supported by a more comprehensive theoretical and experimental foundation compared to earlier formulations. The design calculation is now based on the root mean squared (RMS) velocity, Equation 2.34 can be used to obtain this velocity.

$$v_{rms} = v_{tot,peak}(0.65 - 0.01 f_1)(1.22 - 11.0\zeta)\eta \tag{2.34}$$

where

$$I_{mod,mean} = \frac{42 f_w^{1.43}}{f_1^{1.3}}$$

$$v_{1,peak} = k_{red}\frac{I_{mod,mean}}{M^* + 70}$$

$$k_{imp} = \max(0.48\frac{B}{L}\left(\frac{(EI)_L}{(EI)_T}\right)^{0.25}; 1.0)$$

$$v_{tot,peak} = k_{imp} v_{1,peak}$$

$$\eta = \begin{cases} 1.35 - 0.4k_{imp} & \text{when } 1.0 \leq 1.9 \text{ else } \eta = 0.59 \text{ for joisted floors} \\ 1.35 - 0.4k_{imp} & \text{when } 1.0 \leq 1.7 \text{ else } \eta = 0.59 \text{ for other floors} \end{cases}$$

with

f_w	walking frequency ($f_w \geq 1.5$Hz (residential), $f_w \geq 2.0$Hz (other) and $f_w = 2.5$Hz for paths > 10m) [Hz]
$I_{mod,mean}$	mean modal impulse [Ns]
$v_{1,peak}$	peak velocity response [m/s]
k_{red}	reduction factor $k_{red} = 0.7$
$v_{tot,peak}$	total velocity peak response [m/s]
k_{imp}	factor accounting for higher modes in transient response

Lastly, the acceleration criterion from Hamm et al. [28] (see Eq. 2.31) is extended by Abeysekera et al. [1] to the RMS value of acceleration calculated using Equation 2.35.

$$a_{rms} = \frac{k_{res}\mu_{res}F_{dyn}}{2\sqrt{2}\zeta M^*} \tag{2.35}$$

with

k_{res}	factor to account the higher modes, take $k_{res} = 0.4k_{imp}$
μ_{res}	resonant build-up factor, may be take as $\mu_{res} = 0.4$
F_{dyn}	dynamic force on the floor caused by weight of walking person ($F_{dyn} = 50N$)

The factor μ_{res} accounts for incomplete resonance and the fact that the walker is not always at the most unfavourable location. For unobstructed walking paths over $10m$, $\mu_{res} \geq 0.8$ is reasonable; the maximum value is 1 for full resonance at midspan. Additionally, the factor $\sqrt{2}$ converts the acceleration response from a peak value to a RMS value.

The draft also provides an advanced method, described in Annex G, which offers a more detailed evaluation of floor vibrations. This method uses numerical analysis to determine the modal properties of the floor, allowing multiple vibration modes to be considered instead of just one. It calculates the vibration response to walking using time-history simulations for velocity and harmonic force models for acceleration. The velocity response is assessed by evaluating the RMS velocity over the duration of a single step, for all modes below 25 Hz. Acceleration is assessed by checking for resonance at any walking frequency, using the first four harmonics of walking-induced forces, for all natural frequencies below 15 Hz. While more computationally demanding, this method provides a more accurate prediction of the floor's dynamic behaviour and is especially useful for complex or low-frequency floor systems.

2.5.4 HIVOSS

The Human Induced Vibrations of Steel Structures (HIVOSS) [24] project is one of the foundational European research initiatives underpinning the methodology and recommendations presented in this report. HIVOSS aimed to provide a comprehensive understanding of human-induced vibrations in lightweight steel floor systems and to develop practical design tools for structural engineers. The main goal of the HIVOSS project was to study how steel and composite floors react to vibrations caused by human activities, particularly walking, and to create a reliable method for predicting and evaluating their vibration performance. The report outlines a procedure for determining and evaluating floor responses to excitations due to walking. It balances the complexity of mechanical vibration issues while providing user-friendly design charts for easy application in the design process.

Three key dynamic properties of the floor structure affect how it responds to vibrations:

- f_i eigenfrequency of vibration mode i
- M_i modal mass of vibration mode i
- ζ damping value of the system

To quantify floor vibrations in a way that directly relates to human comfort, a parameter called the One-Step Root Mean Square ($OS-RMS$) value is used. This value represents the effective vibration velocity of a floor during a single footstep and captures the complex, time-varying response into a single, meaningful number. It is calculated by applying a frequency-weighted RMS operation over a short time window that corresponds to the duration of one step. The weighting function $B(f)$ reflects the variable sensitivity of human beings to different vibration frequencies, particularly between 4 and 8 Hz. Unlike long-term averages, this step-specific evaluation better reflects how people actually experience vibrations as they walk. This is important because people feel vibrations step by step, not continuously. To reflect differences among people, $OS-RMS$ values are computed across a range of body weights and walking speeds, based on real-world population data. These individual values are then sorted, and the 90th percentile, known as $OS-RMS_{90}$, is used as a representative measure for comfort assessment. The general expression is:

$$\text{OS-RMS} = \sqrt{\frac{1}{T_s}\int_t^{t+T_s} \left(\dot{x}_B(t)\right)^2 \, dt} \tag{2.36}$$

with
T_s time duration of a single step [s]
$\dot{x}_B(t)$ weighted velocity response of the floor [mm/s]

The design procedure outlined in this report involves calculating the floor's response to human-induced excitation, specifically walking, and comparing it to the required performance limits. This is done using design charts developed from statistical evaluations. Each of the design charts presented in the report is based on a statistical evaluation of 700 combinations of step frequency and body mass, ensuring that the calculations are reliable for various types of walking patterns.

Different vibration modes in a floor structure correspond to different natural frequencies, and these modes can be excited simultaneously when a person walks on the floor. Each mode has its own vibration pattern and contributes to the overall response of the floor. Since more than one mode may be excited at the same time, the floor's total response is a combination of these individual modes. The $OS-RMS_{90}$-value, which quantifies the floor's vibration response, should therefore be calculated as a combined value, taking into account the contributions from multiple frequencies, rather than from just a single mode. This ensures a more accurate assessment of the floor's behaviour under walking-induced vibrations. Below are the steps for using the design charts to determine the structural response and associated $OS-RMS_{90}$-value.

1. Determine the fundamental properties of the floor structure. This includes calculating the natural frequencies (f_i), the associated modal mass (M_i) and finally the damping ratio (ζ).
2. Using a design chart (see for instance App. F) to obtain the $OS-RMS_{90}$-value. This value is found by cross-referencing the frequency and corresponding modal mass in the graph for the damping ratio for the specific floor structure.
3. The total $OS-RMS_{90}$-value should be determined by combining the individual $OS-RMS_{90}$-value for each mode of vibration i. The combined value reflects the floor's overall vibration response.
$$OS-RMS_{90}=\sqrt{\sum_i (OS-RMS_{90})_i^2}$$
4. The calculated $OS-RMS_{90}$-value is then compared to the recommended or required limits for the floor's intended occupancy, see Table 2.9. These limits are based on the perception classes (A to F), which indicate the level of comfort or disturbance caused by the floor vibrations.

Table 2.9: Allocation of classes of perception A to F to threshold values of $OS-RMS_{90}$-values and relation of occupancies of floors to comfort limits [24]

Class	$OS-RMS_{90}$		Usage of the floor structure										
	Lower Limit	Upper Limit	Critical areas	Health	Education	Residential	Office	Meeting rooms	Shop	Senior citizens	Hotels	Industrial	Sports facilities
A	0,0	0,1											
B	0,1	0,2											
C	0,2	0,8											
D	0,8	3,2											
E	3,2	12,8											
F	12,8	51,2											

With: Recommended / Critical / Not recommended

These outcomes have been integrated into this report to guide the design of floors for human-induced vibrations. The project significantly contributed to the harmonization of design practices across Europe and laid the groundwork for the continued evolution of the Eurocode. Abeysekera

et al. [1] state that class D floors (Tab. 2.9) comply with the highest performance level stated in Table 2.7.

Chapter 3: Panel-to-panel connection

3.1 Introduction

The need for panel-to-panel connections has been stated in the introduction of this report. More research has already been done on multiple panel-to-panel connection types. To introduce the splice plate connection, which is the main focus of this report, first a state of the art investigation is performed. This section will introduce three distinct panel-to-panel connections and will argue why the splice plate connection was chosen. After describing these connection types, the assumptions for the splice plate connection will be stated. This will conclude the introduction of the splice plate connection.

After introduction, a simple model is created to determine the stiffness and strength of the panel-to-panel connection. The model consists of three parts. First, a python model is created that takes as input the variables of the connection and returns a rotational and shear stiffness. Secondly a RFEM model is created, incorporating these rotational and shear stiffnesses in the panel-to-panel connection. Lastly, the connection will be checked in a third model, again created in python, for strength of the connection.

3.1.1 State of the art

Finger-joint

Tapia et al. [58] propose a finger-joint inspired connection between CLT panels. The connection uses LVL gusset plates with milled finger-joint-like profiles that are screw-glued to the CLT outer layers, see Figure 3.1a. The connection is created using Computer numerical control (CNC) or robotic milling, forming an interlocking profile across the panel edge. The bending stresses in the CLT panel are transferred through shear stresses at the glued interface, as is shown in Figure 3.1b. Two variants were studied, one with 2D fingers (Variant A) and another with 3D-tapered fingers (Variant B), through a combination of experimental testing and finite element (FE) modelling.

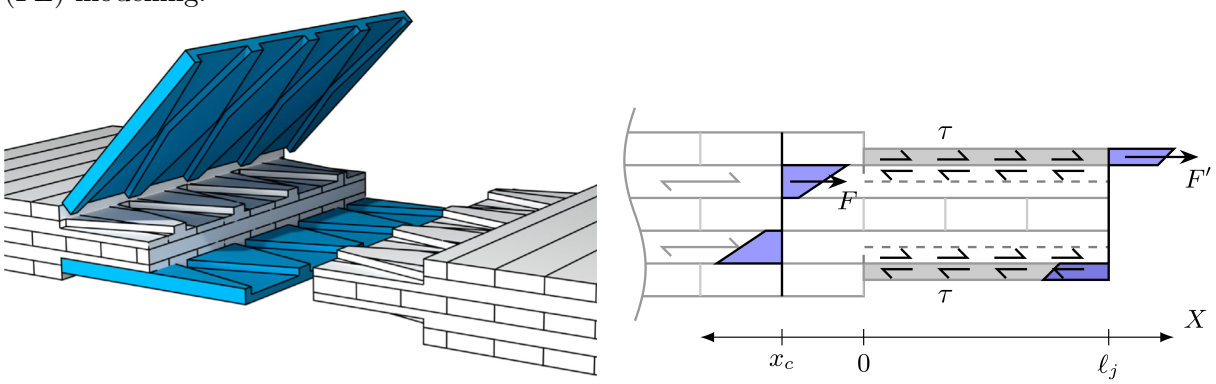

(a) Illustration connection

(b) Schematic illustration of bending stresses

Figure 3.1: Finger jointed connection [58]

Both configurations demonstrated moment capacities comparable to unjointed panels, reaching 96% and 106% of the reference bending strength, respectively. Figure 3.2 illustrates the load-deflection behaviour of the two alternatives under both pure bending and combined shear and bending. In the pure bending tests both alternatives display linear-elastic behaviour up to approximately 80% of the ultimate moment capacity. At very low loading, about 15% of the capacity, audible cracking was noted, but no noticeable degradation was observed. In the combined loading case, visible damage occurred at 69% and 90% of the ultimate load respectively. Alternative A showed a more ductile failure progression, while alternative B failed in a more abrupt and brittle manner. These findings confirm that both connections maintain integrity well into the non-linear range, with configuration A exhibiting greater redundancy and toughness under combined loading. A linear-elastic FE model was developed to simulate the structural

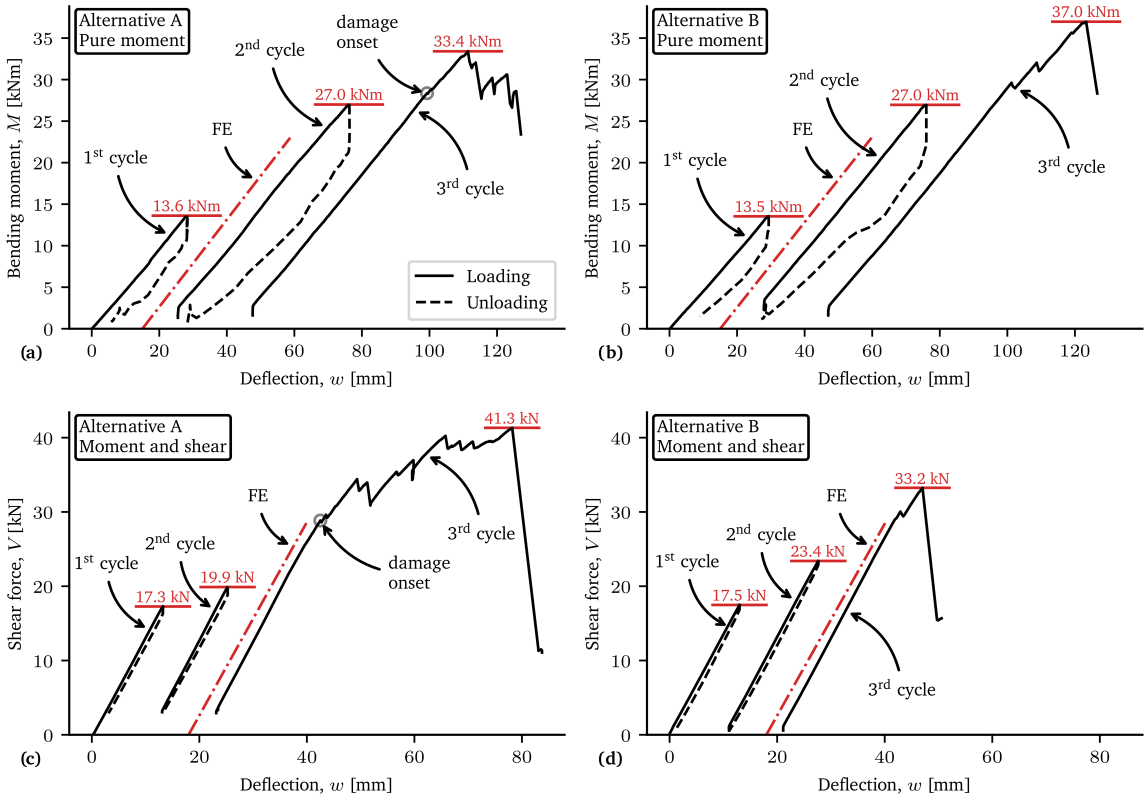

Figure 3.2: Load–deflection curves of the tested connections (note: loading cycles 2 and 3 are shifted along the horizontal axis for clarity) [58]

behaviour of the finger-joint connections under bending and combined loading conditions. The model showed strong agreement with experimental results. [58]

Tapia et al. [58] emphasize the importance of precise manufacturing, particularly for long panels where milling errors can accumulate. The bonding process was found to be demanding due to minimal tolerances, requiring very precise alignment to limit the glueing thickness. For practical applications, Tapia et al. [58] recommend segmenting the LVL connection plates and increasing tolerances. Although the connections performed well structurally, the study also identified the need for further exploration of fire safety, long-term performance and easier on-site assembly solutions.

TC-Fusion

Stieb et al. [54] have developed a timber-concrete connection as shown in Figure 3.3, it is called the TC Fusion connection [51]. Earlier developed solutions often rely on adhesive or screwed connections, the TC Fusion eliminates the need for on-site gluing.

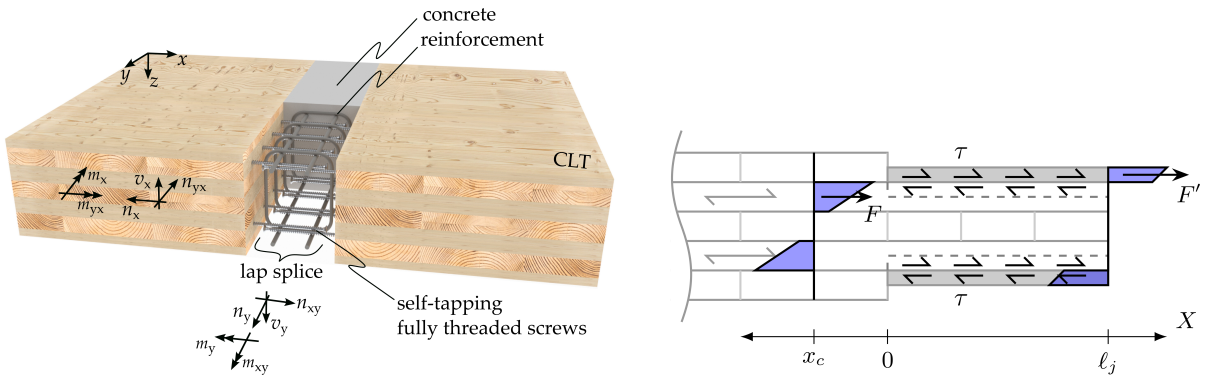

(a) Concept of the connection and forces **(b)** Construction method

Figure 3.3: TC-fusion connection [54]

The force distribution within the proposed timber–concrete–composite edge connection is governed by the interaction between the concrete splice, the self-tapping screws and the cross-laminated timber panels. Under bending, compressive forces are transferred primarily through direct contact between the CLT and the concrete. In the tensile zone, the load is taken up entirely by the self-tapping screws, which are embedded into the narrow face of each adjacent CLT panel. Shear loads in this connection are transferred through shear action on these embedded fasteners. These screws resist axial tension and serve as the primary load-transferring elements across the joint. The cross section and the stress distribution in this section are shown in Figure 3.4. In the concrete part of the connection reinforcement is placed, both longitudinal and stirrups.

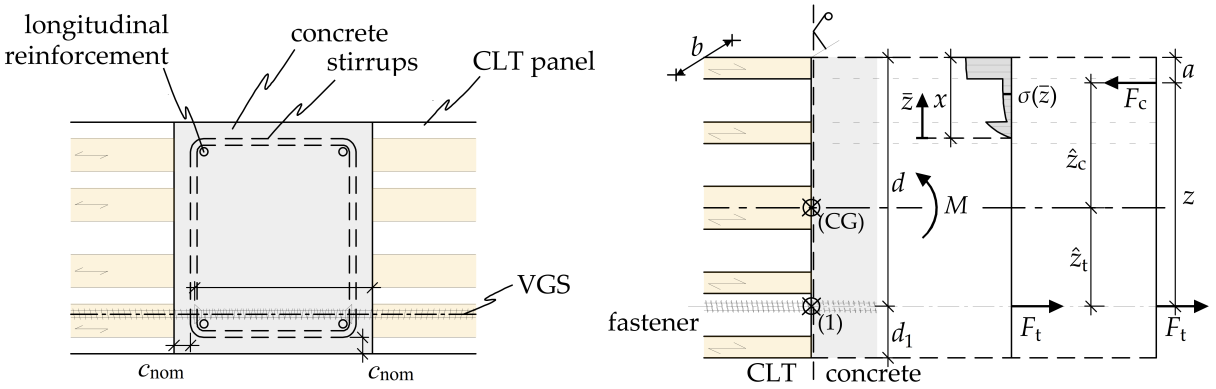

(a) Cross section **(b)** Stress distribution under pure bending

Figure 3.4: [54]

Bending moments acting parallel to the connection are resisted by this longitudinal reinforcement embedded in the concrete. The structural importance of the stirrups is not mentioned specifically, the lack of reference to stirrups in load-transfer discussion indicates they are mainly placed there for crack control. They do not significantly contribute to the load transfer. This configuration creates a composite action where the concrete and CLT resist compressive forces, and the screws carry tension.

The location of F_t is known, this is depending on the location of the fastener in the panel. On the other hand, the location of the compressive force F_c depends on the occurring bending moment. The following equilibrium conditions have to be satisfied:

$$\sum N = 0 \quad \text{and} \quad \sum M = 0$$

The compressive zone depends on the orientation of the layers in the CLT panel, there are three situations that are reasonably likely to occur [54]:

- The height of the compression zone is less than the thickness of the first layer, see Figure 3.1.1, so $x \leq t_1$:

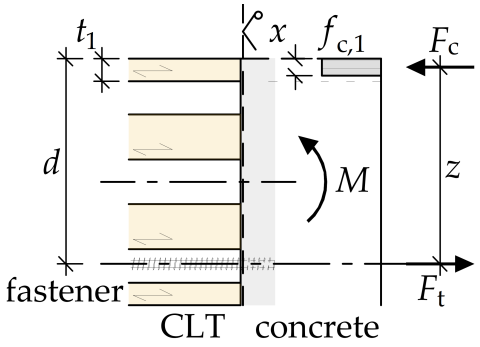

$$x = d - \sqrt{d^2 - \frac{2M}{b f_{c,1}}} \qquad (3.1)$$
$$F_c = x \times f_{c,1} \times b$$

- The first layer is subjected to compression perpendicular to the grain and the compressed zone exceeds the thickness of the first layer, see Figure 3.1.1, so $x > t_1$ and the first layer is in transversal direction:

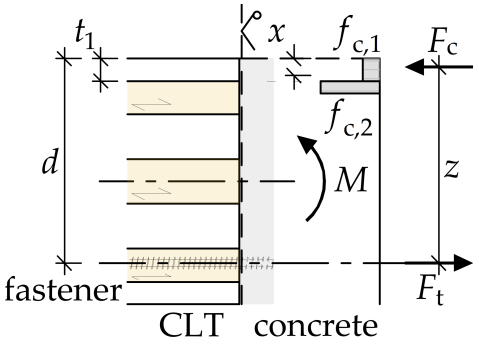

$$x = d - \sqrt{(d-t_1)^2 + \frac{f_{c,1}}{f_{c,2}} t_1(2d - t_1) - \frac{2M}{b f_{c,2}}} \qquad (3.2)$$
$$F_c = (f_{c,1} t_1 + f_{c,2}(x - t_1)) \times b$$

- The first layer is subjected to compression parallel to the grain and the compressed zone exceeds the thickness of the first layer, see Figure 3.1.1, so $x > t_1$ and the first layer is in longitudinal direction. In this equation Stieb et al. [54] suggest the second layer, which would be compressed perpendicular to the grain, should be left out of the equation:

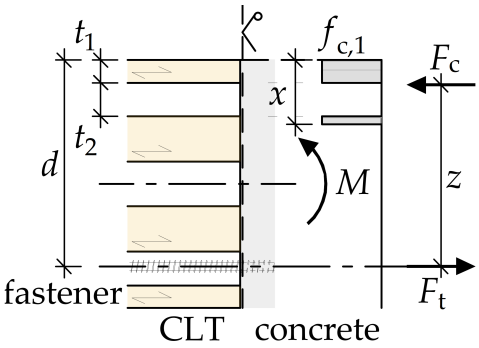

$$x = d - \sqrt{(d-t_1)^2 + 2t_1 t_2 - \frac{2M}{b f_{c,1}}} \qquad (3.3)$$
$$F_c = (x - t_2) \times f_{c,1} \times b$$

Using the above equations to determine F_c, the tensional force is found using equilibrium of forces, so $F_t = F_c$. After determining the forces in the connection, multiple failure mechanisms can be verified. Stieb et al. [54] mention four main failure types:

- Withdrawal of screws in the CLT panel
- Tensile failure of the screws
- Failure of anchorage within the concrete
- Failure of lap splice within concrete

The connection is tested for 4 different connection details, every series has been tested three times. Experimental results show that this connection is capable of transferring bending moments up to 70% of the characteristic bending capacity of the solid CLT element. Stieb et al. [54] mention that this is not an upper limit, by adjusting the connection it could be possible to reach even higher values.

This connection type has developed rapidly and is already being used in practice. A building site is visited in the Netherlands were this connection is being used in the construction of a new office building, see Appendix J. From this site visit and a short interview with the workers on site, small remarks can be made. A positive aspect to the use of concrete according to Stieb et al. [54] is the fact that it is a well-known construction material. However, working with concrete on site considerably limits the construction speed and makes the use of temporary supports, for a longer amount of time, necessary.

Splice plate

A third possible connection can be made by placing a plate at the bottom of the two CLT panels to be connected and connect this splice plate using inclined screws. Zhang et al. [67, 66] performed tests in two phases, phase I a steel plate (see Fig. 3.5a) [67] and in phase II a LVL plate (see Fig. 3.5b) was tested [66]. In phase I it was concluded that the minimum moment

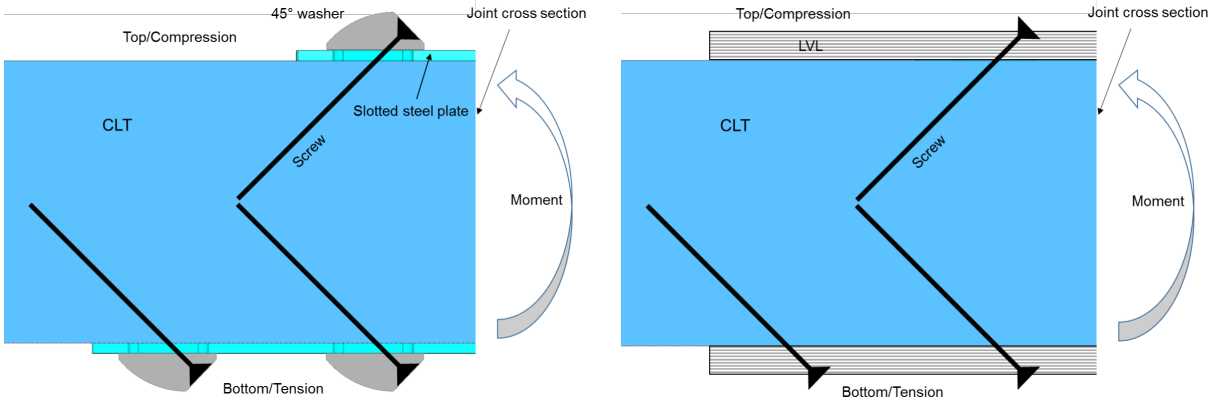

(a) Steel plate connection **(b)** LVL plate connection

Figure 3.5: Moment applied on splice plate connection [66]

capacity of the cross-section reached 3.2 times the design value of the CLT panel. The connected specimens exhibited greater stiffness than the full panels, conservatively the system can be treated as a single continuous CLT plate without connections [67]. It should however be noted that the measured capacity was compared to a 5-layer panel with only two layers in the minor direction. The reached strength is quite favourable compared to this lay-up, so the more interesting value is the absolute bending moment capacity. An average bending moment capacity of $59.9 kNm/m$ was measured in the minor direction of the panel [67].

During phase II the steel was replaced with LVL and the focus shifted more to the rotational stiffness of the connection. The steel connection reached 98% of the stiffness of an intact panel, where the LVL plate reached 92% [66]. Again the same note should be made about the 5-layer panel, this makes it seem like a lot in percentage terms, but the absolute value is quite low. The LVL plate connection resulted in a rotational stiffness of $734 kNm/rad$ [66].

In a publication in 2021 Asselstine et al. [6] presented the results from their experimental investigation and extended the results with nummerical modelling. The splice plate connection is modelled using linear springs, see Figure 3.6, this is valid within the elastic region.

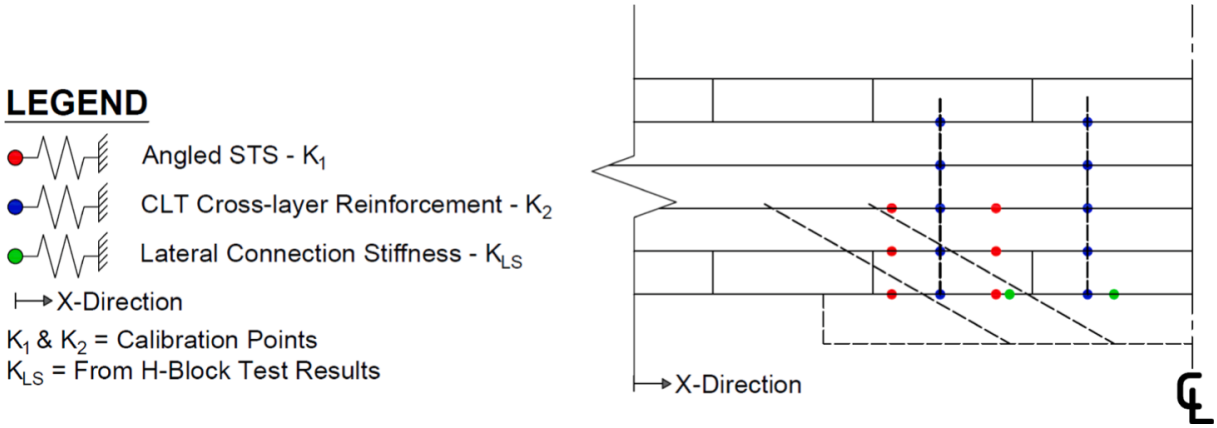

Figure 3.6: Linear spring model as interpretation of the connection [6]

The FE model is calibrated using the performed tests and is used for simulating the splice plate connection. The model confirms that tensile stresses stay within elastic limits under realistic

loads. The numerical model stays close to the test results, A maximum deviation of 5.8% in central deflection and 7.0% in shear-free deflection was observed. [6]

As mentioned before, the testing and model validation is based on a 5-layer panel connection. Asselstine et al. [6] mention that future research needed is on 7- and 9-layer panels to confirm the failure modes. Additionally, it is suggested to investigate a more aesthetical connection by countersinking the splice plate. Lastly, fire safety is mentioned in the study, but only in passing, without emphasizing its importance or exploring its implications in detail. [6]

3.1.2 Proposed connection

Among the various panel-to-panel connections explored before, the splice plate connection emerges as a particularly promising option despite its relatively lower stiffness and strength compared to alternatives. While finger-jointed connection offers high performance, their complexity in production and reliance on glueing processes make them less favourable in terms of manufacturability and sustainability. The TC fusion, on the other hand, has been extensively developed and already implemented in practice; however, it involves concrete, which extends construction times and complicates the overall assembly. In contrast, the splice plate connection stands out for its simplicity, ease of installation, and cost-effectiveness. These qualities make it especially attractive in scenarios where budget and construction efficiency are priorities. Furthermore, its potential for more aesthetically pleasing design solutions adds to its appeal. Of course, numerous other panel-to-panel connections exist, but the three discussed here, are currently seen as the most promising for further development and application.

The proposed and updated splice plate connection is shown in Figure 3.7. It consists of a splice plate countersunk in both CLT panels to simplify finishing work, making it easier to integrate the connection into architectural designs. Additionally, the top of the panel is connected using inclined screws.

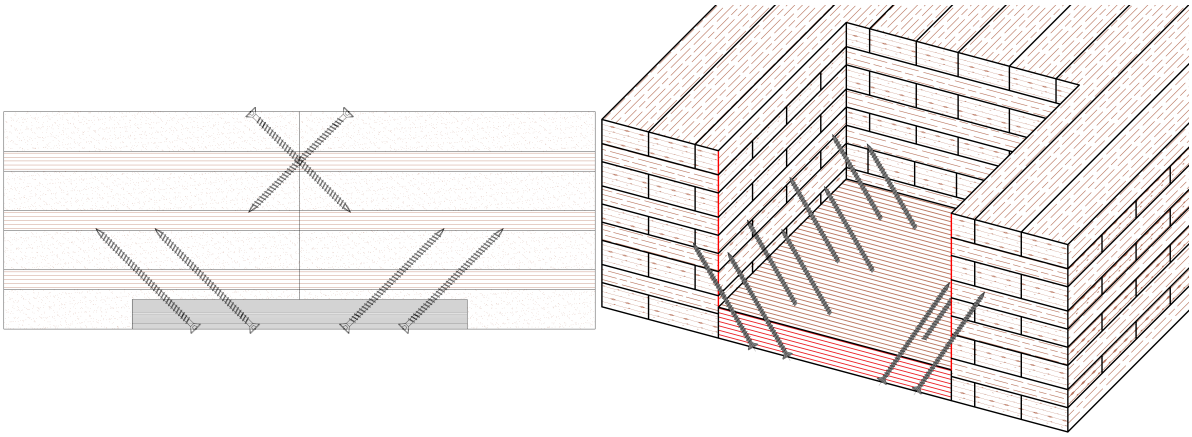

Figure 3.7: LVL splice plate connection and butt-joint

The model makes use of the fact that the connection is mirrored, both rotational stiffness and strength is calculated for one side of the connection. To take into account the other side of the connection the stiffness of the connection, the calculated value is divided by 2 in the model. The rotational stiffness is divided by 2, because the same loss in stiffness on one side, also happens on the other side. The strength of the connection is determined by the weakest link. The same tensional force that the screws on one side of the connection are subjected to, also has to be introduced on the other side.

All calculations are a combination of prescribed formulas in the building code and screw specific relations as prescribed in the relevant European Technical Assessment (ETA). The calculation method for three different possible screw types is included, namely SPAX [17], Würth [13] and

Rothoblaas [16]. The equations for the calculation based on the building code can be found in the literature study in the literature study on inclined screws in paragraph 2.4.

3.1.3 Assumptions

Because the calculations are based on the ETA of three different screw types, some additional assumptions are needed. These assumptions are mostly related to the limitations stated in these ETA's:

- For the performed calculation small rotations are assumed ($\delta < 15mm$). This is also a quite logical assumption, with larger deformations, the connections will most likely have failed, which makes the small angle assumption justified for this model
- $\rho_{k,CLT} \leq 440kg/m^3$
- $\rho_{k,LVL} \leq 750kg/m^3$
- The screws are fully threaded, made of carbon and have a countersunk head
- Screw angles are not defined in line with the building code [23], see Figure 2.5. The angles α and ε are interchanged, so:
  - α angle between grain and screw axis
  - ε angle between load and grain direction

  This is the definition according to the ETA's of the screws that are included in this report.
- The screws are placed at an angle of 45°

Based on this last assumption, it can be stated that in a typical CLT panel with alternating layers, the screw is installed at an angle of 45° to both the wide face of the panel and the grain of the first layer. This means the angle ε (between the screw axis and the grain direction) is 45° in that first layer. Since each subsequent layer has its grain direction rotated 90°, the screw orientation stays the same, and the angle ε remains 45° in all layers. However, while ε stays constant, the angle α (between the acting force and the grain) changes. Starting at the bottom, it is 90° in the first layer, where the grain is perpendicular to the force, and 90° in the next, where the force is parallel to the grain. The installation angle β (between the screw axis and the panel surface) remains constant at 45° throughout.

The ETA's [13, 16, 17] state that it is appropriate to base calculations for screws inserted into the wide face of CLT on the values typically used for solid wood. This should be done by considering the characteristic density of the CLT's outermost lamella, which acts similarly to solid timber in this context. Additionally, where applicable, it's important to factor in the angle at which the load is applied relative to the grain direction of the outer layer, as this can influence the load-bearing behaviour and overall performance of the connection. In cases where screws pass through multiple layers of cross-laminated timber (CLT), it is suggested to consider the contribution of each individual layer when assessing the connection's total performance. The load bearing capacity can be evaluated proportionally accounting for the properties of the layers penetrated by the fastener.

3.2 Stiffness model

The model, both strength and stiffness, is based on the rotational behaviour shown in Figure 3.8. The splice plate develops tensional forces at the shear plane between the LVL and CLT panel. The compressional force is located at the top/bottom of the first lamella orientated in the minor direction of the panel. Whether this compression point is at the top or bottom depends on the direction of the bending moment. In case the bending moment is positive, so tension at the bottom and compression at the top of the panels, the compression point will be a the top of the

first longitudinal layer counting from the top. If there is a negative bending moment, the tension will be at the top of the panel and compression at the bottom, so the compression point will be at the bottom of the first longitudinal layer counting from the bottom. At the compression

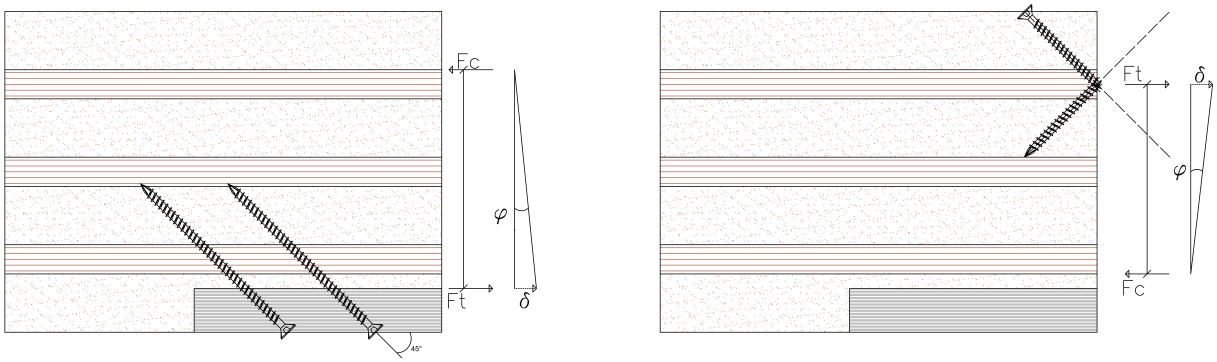

Figure 3.8: Rotational stiffness model plate underneath (L) and aligned with the bottom of (R) the CLT panels

side of the panel no indentation is assumed. The slip at the tension side of the panel is the only contributing factor in δ.

First a stiffness model is created in python to return a rotational stiffness. In this model the splice plate connection provides stiffness for the positive bending moment and the butt-joint for the negative bending moments. After explaining the model and its formula's, a parameter study is performed. Mainly the different screws that can be used are compared and the influence of parameters in the equations. Figure 3.9 shows the spring model that is assumed for this connection. The spring in the LVL plate itself is neglected due to its small effect on the rotational behaviour of the connection. The springs in the splice plate connection are placed in series, so the total spring will be a summation of the reciprocal values. The springs in the butt-joint are placed in parallel, so the total spring is a summation of these values.

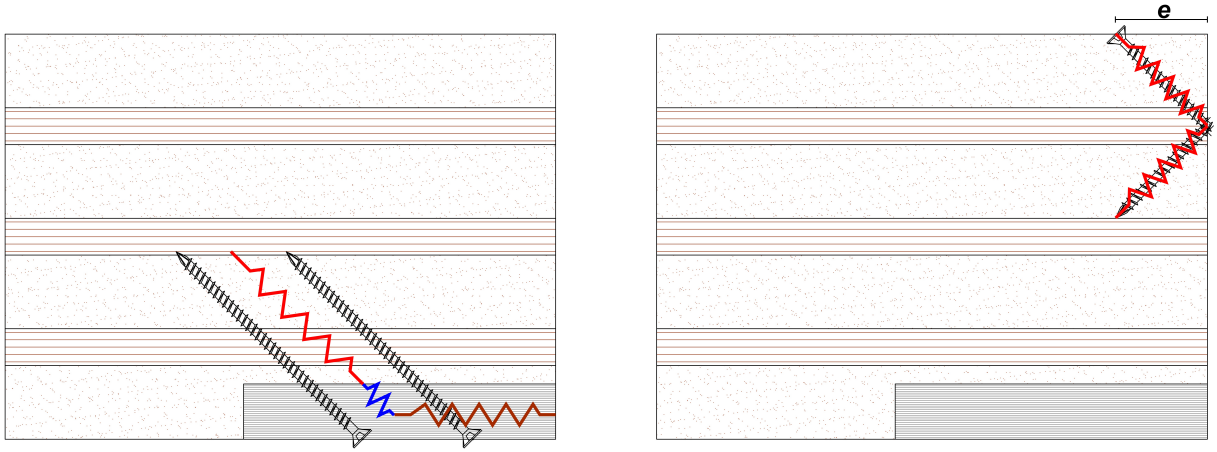

Figure 3.9: Spring model of the connection

3.2.1 Splice plate

The model assumes a splice plate that is aligned with the bottom of the CLT panel. The tensional forces are assumed to be at the shear plane between the splice plate and CLT panel. The compressional force is assumed to seize at the top of the first longitudinal layer in the minor direction of the CLT panel. The axial stiffness calculation according to the ETA's of the three screws is the same [13, 16, 17], see equation 3.4.

This distinction between softwood and hardwood is already very important for the stiffness calculation. Nowadays the use of softwood for LVL is the most common practice, but the

beneficial properties of hardwood for the LVL plate in this connection could lead to the decision for hardwood LVL plates.

$$K_{SLS,ax} = 25 \times d \times l_w \text{ for softwood}$$
$$K_{SLS,ax} = 30 \times d \times l_w \text{ for hardwood} \tag{3.4}$$

The input of the stiffness model consists of two parts. First the timber properties are chosen, these properties are partially predefined, based on the 7- and 9-layer CLT panels as producible by Derix [14] and LVL panels, varying from 21 to 75mm as producible by Metsä Wood [18]. These panels and their lay-up can be seen in Appendix A. While current standard lay-ups are typically optimized for single-span applications, which is now common practice in CLT construction, the panel in this model is subjected to biaxial loading. For such conditions, it is more beneficial to use customized lay-ups with stiffness ratios closer to one. Further explanation on this topic will follow.

Secondly all screw parameters are chosen, the screw connections can be chosen based on the screws deliverable and specified by SPAX, Würth and Rothoblaas. The values to be chosen are the diameter (head and nominal), length, angle and spacing of the screws, for the splice plate the number of screws in a row is also chosen and for the butt-joint the edge distance is also chosen. For the splice plate connection the number of screws is the number of screws in the minor direction of the CLT panel at one side of the connection.

These input variables return a rotational and shear stiffness for the line hinge in the RFEM model. In Appendix H the calculation method is shown based on the case study in chapter 6.

3.2.2 Butt-joint

For the shear forces and possible negative bending moments in the panel-to-panel connection a butt-joint is created. This connection needs less stiffness and also the forces are smaller, hence the decision for a butt-joint. Now the compression point is assumed at the bottom of the first lamella, counting from the bottom, that is orientated in the minor direction of the panel. Tensional forces are at a distance 'e' from the top of the panel, this is under the assumption that the screw is at an angle of 45°. The variables to be chosen for the model have been mentioned above.

3.3 RFEM model

RFEM 6 [15] is used to perform a plate calculation, to determine an accurate mesh size, a mesh sensitivity analysis is performed. Based on this analysis and a maximum relative error of 1%, see appendix B, a mesh size of 0.25m is chosen as appropriate. The calculation time for this mesh size is also very reasonable. However, if a larger maximum relative error of approximately 3% is agreeable, a mesh size of 0.5m could also be applied.

The RFEM model consists of a simple point-supported floor system. All point supports are modelled as idealised nodal supports, representing the vertical load transfer to the structure below. Their actual stiffness and detailing, such as the panel-to-column connection, are not explicitly included in the model. This simplification is acceptable for the current scope, as the focus is on the behaviour of the panel-to-panel connections. However, it should be noted that the internal force distribution across the panels is influenced by how the panel-to-column connection behaves in reality. More detailed support modelling could improve accuracy, particularly when assessing panel performance, but for the line hinge behaviour these effects are considered minor and generally negligible for preliminary design.

The producible width of CLT panels is limited to a maximum of $3.5m$ [14], which forms the starting point for the model. The placement of line hinges in a floor system is a matter of

engineering judgement, requiring an understanding of mechanics and structural behaviour. The optimal location depends on various factors, including, but not limited to, load distribution and support conditions. Engineers must analyse these aspects to determine the best placement that ensures minimal stresses. Since every project has a unique architectural and structural layout, the optimal placement of panels and line hinges is always project-specific. The following design suggestions may be taken into account:

- Hinge location optimisation: When distributing these panels across a floor plan, it is essential to place the line hinges in structurally favourable locations. Normally, these should occur in areas of low bending moment, typically near supports, so that the moment transfer demand across the panel edges is minimised.
- Span efficiency: Maximise panel efficiency by aligning the stiffer direction of the panel with the principal (longer) span direction.
- Fire compartments: Take into account fire compartmentalisation and avoid placing joints over compartment boundaries if this affects fire resistance continuity.

Breaking down a (complex) CLT floor system into simpler mechanical schemes, such as simply supported beams, can be a helpful design strategy. This approach allows engineers to idealise load paths and evaluate bending moments, shear forces, and deflections using simple principles of structural mechanics. Even if actual supports are not physically continuous, grid lines with columns or areas of increased stiffness can often be treated as effective supports during preliminary design. This enables better prediction of structural behaviour, supporting more rational decisions about panel layout and line hinge placement. Such simplifications are especially valuable in early design stages.

The connection between CLT panels is modelled as a bilinear rotational spring, where the stiffness depends on the direction of the bending moment. This non-linear behaviour is captured in RFEM using the φ_x-Diagram option for rotational springs at line hinges. This diagram allows the hinge to result in different rotational stiffnesses for positive and negative bending moments. In this case, it adopts the stiffness of the splice plate connection when the moment is positive and that of the butt-joint connection when the moment is negative. This directional stiffness modelling reflects the actual mechanical performance of the connection more accurately.

As the floor is loaded, the RFEM model evaluates the resulting bending moment at each hinge. Depending on the hinge's position relative to the supports and applied loads, this moment can be either positive or negative. The corresponding stiffness from the bilinear spring is then applied automatically within the analysis. The resulting bending moment, together with the shear force, is used as input for a separate strength model that verifies the connection capacity under design loads. This integrated approach ensures that the actual non-linear and asymmetric behaviour of the connection is reflected in both the global structural model and the detailed strength verification.

While the RFEM model also provides internal forces such as bending moments and shear forces in the panels themselves, its accuracy for verifying the performance of the CLT panel material is limited. A more refined modelling of panel-to-column connections would be needed to reliably assess stresses and deformations within the panels. For this reason, the current model should be regarded as suitable for preliminary design of the line hinge, but not for verifying the CLT floor panels themselves.

3.4 Strength model

Lastly a strength model is created in python to return a rotational strength. The strength of the connection is determined by its weakest link. The model will return the rotational strength, so a maximum allowable bending moment in the line hinge. Also it will return which failure

mechanism occurs first. There are four possible failure mechanisms possible in the splice plate connection:

- The screwed connection in CLT member
- The screwed connection in LVL member
- The screw itself fails
- The LVL plate fails in tension

Information about which failure mechanism is governing, is very useful when designing a connection. If the connection is not strong enough, the input variables can be changed, using the knowledge on which member fails, to create a stronger connection. Figure 3.10 shows the mechanical schematization of the connection, highlighting the locations of compressive and tensile forces at the interface between the CLT panels.

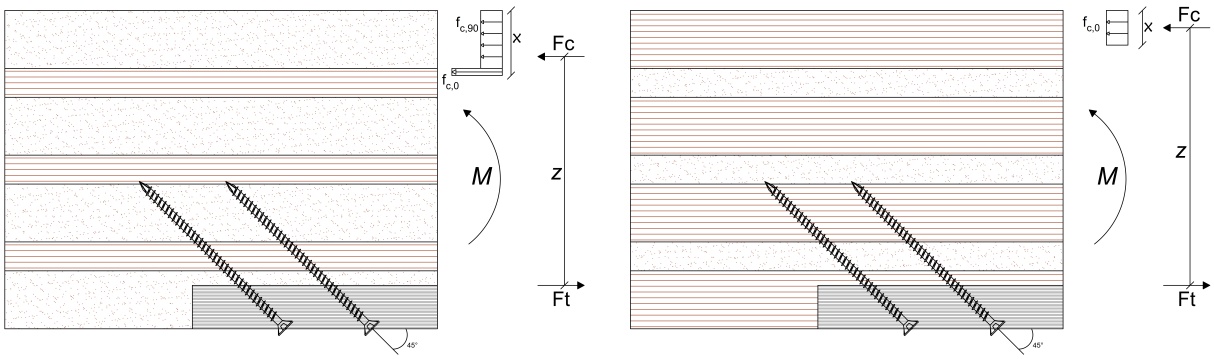

Figure 3.10: Assumed force distribution; (l) $x > t_1$ (r) $x \leq t_1$

Unlike the TC Fusion connection, which is dimensioned based on the compressive strength of the individual lamellae (see paragraph 3.1.1), the design approach for this connection begins with the tensile strength. The tensile force is governed by the inclined screw connection, which is determined by a practical number of screws and returns a specific capacity. Based on this tensile force, the required compressive force can be derived and thus the bending moment capacity. Using the equilibrium of forces the following relation for internal lever arm 'z' can be determined:

$$z = h_{CLT} - t_{LVL} - x_R \tag{3.5}$$

In this equation x_R is the distance from the top of the panel to the location of the compressional force. This distance depends on the force F_t, there are two relevant possibilities, both depicted in Figure 3.10:

- $x \leq t_1$

  $$x_R = \frac{F_t}{2 \times f_c}$$

  With f_c depending on the orientation of this layer. This situation is almost always relevant if the first layer is orientated perpendicular to the panel-to-panel connection, this compressional strength is high and possibly only part of the first lamella is activated.

- $x > t_1$

  $$x_R = \frac{\frac{f_{c,90} t_1^2}{2} + (F_t - f_{c,90} t_1) t_1 + \frac{(F_t - f_{c,90} t_1)^2}{2 f_{c,0}}}{F_t}$$

  This is mostly relevant if the first layer is orientated parallel to the panel-to-panel connection, so it is compressed perpendicular to the grain. The second layer is then activated in compression.

An additional part of the code also checks the design for detailing like minimum spacing, edge and end distances.

The RFEM model will calculate the force distribution in a floor system with a line hinge with a rotational stiffness resulting from the stiffness model under the given loads. The output from this model, specifically the occurring bending moment and shear forces in the line hinge, are the input for this third model. In a new python model the strength of the connection is calculated and checked against the actual forces as calculated in the RFEM model.

3.4.1 Splice plate

In Appendix I the calculation method is shown for the case study in chapter 6, this strength calculation is based on the formulas prescribed in the ETA's for SPAX, Würth and Rothoblaas screws [17, 13, 16]. Equation 2.19 is still used, only the formulas to calculate axial withdrawal resistance and head pull-through capacity are different. The resistance of the screws in the timber members can be determined as follows:

$$\text{SPAX}: \quad F_{ax,\alpha,Rk} = n_{ef} \times (\frac{\rho_k}{350})^{0.8} \times \max \begin{cases} \frac{f_{ax,k} \times d \times l_w}{1{,}2 \times \cos^2 \alpha + \sin^2 \alpha} \\ k_t \times f_{head,k} \times d_h^2 \end{cases} \tag{3.6}$$

$$\text{Würth and Rothoblaas}: \quad F_{ax,\alpha,Rk} = n_{ef} \times (\frac{\rho_k}{\rho_a})^{0.8} \times \max \begin{cases} \frac{k_{ax} \times f_{ax,k} \times d \times l_w}{k_\beta} \\ f_{head,k} \times d_h^2 \end{cases} \tag{3.7}$$

with

n_{ef}	Effective number of screws $n_{ef} = \max(n^{0.9}; 0.9 \times n)$
ρ_k	Characteristic density $[kg/m^3]$
ρ_a	Associated density for $f_{ax,k}$, see table 3.1, $\rho_a = 350$ can be assumed when calculating with $f_{head,k}$, the only exception is for Rothoblaas screws in LVL
$f_{ax,k}$	Characteristic withdrawal parameter $[N/mm^2]$, see table 3.1
$f_{head,k}$	Characteristic head pull-through parameter $[N/mm^2]$, see table 3.2
k_{ax}	Factor taking into angle between screw axis and grain direction $k_{ax} = 1$ for $45° \leq \alpha \leq 90°$ $k_{ax} = a + \frac{b \times \alpha}{45°}$ $a = \begin{cases} 0.5 \text{ for LVL} \\ 0.3 \text{ for CLT} \end{cases} \quad b = \begin{cases} 0.5 \text{ for LVL} \\ 0.7 \text{ for CLT} \end{cases}$ For Würth; $k_{ax} = \frac{1}{1.2 \times \cos^2 \alpha + \sin^2 \alpha}$, if $\alpha \geq 15°$ and $l_{ef} \geq \min \begin{cases} \frac{4d}{\sin \alpha} \\ 20d \end{cases}$
k_β	$k_\beta = 1.0$ for timber $k_\beta = 1.5 \times \cos^2(\beta) + \sin^2(\beta)$ for LVL
k_t	Factor taking into account head side member thickness t_h $k_t = 1$ for $\frac{t_h}{d_h} < 3$ $k_t = 1.3$ for $\frac{t_h}{d_h} \geq 3$
d_h	Diameter screw head or washer [mm]

With equations 3.6 and 3.7, the maximum tension forces can be verified for the screwed connections in the wood members. The performed calculation yields the characteristic axial capacity of the screw, using equation 2.25 which is also suggested for a tension screw connection in the product certificate of the LVL panels [18], the tensional force parallel to the shear plane is calculated. A friction coefficient of $\mu = 0.4$ is assumed based on [18], which specifies this value for untreated Kerto-LVL. Since CLT is similarly unplanned, uncoated and made of the same wood type in this case, the assumption is considered reasonable.

Table 3.1: Characteristic withdrawal parameter for SPAX, Würth and Rothoblaas screws [17, 13, 16]

$f_{ax,k}$	d[mm]	6	7	8	9	10	11	12
SPAX		12.0	12.0	12.0	-	11.5	-	12.0
Würth	$\rho_k \leq 590$ $\rho_a = 350$	11.5	11.5	11.0	11.0	11.0	10.0	10.0
	LVL $590 \leq \rho_k \leq 750$ $\rho_a = 730$	35						
Rothoblaas	LVL $460 \leq \rho_k \leq 550$ $\rho_a = 500$	15.0						
	LVL $590 \leq \rho_k \leq 750$ $\rho_a = 730$	29.0						
	Hardwood $\rho_k \leq 590$ $\rho_a = 350$	$7 \times 10^{-4} \times \rho_k^{1.6} \times d^{-0.34}$						

Table 3.2: Characteristic head pull-through parameter for SPAX, Würth and Rothoblaas screws [17, 13, 16]

$f_{head,k}$	d_h[mm]	≤ 16	≤ 19	≤ 22	≤ 25	≤ 32
SPAX	No washer	$27.0 - d_h$	$11.0 - 0.2(d_h - 16.0)$			
	Washer	$29.0 - d_h$	13.0	$16.0 - 0.5(d_h - 16.0)$		
Würth	$590 \leq \rho_k \leq 750$ $t_{timber} \geq 40$	$40 - 0.5d_h$				-
	Other	13.0			10.0	
Rothoblaas	LVL $\rho_a = 500$	20.0				
	Other	10.5				
$12 \leq t_{timber} \leq 20$		8.0				

Using equation 2.20 the tensional force in the screw itself is verified. This leaves the model with one member still unverified. The LVL plate should also be checked. This is also included in the model with a very simple equation. The LVL member is assumed to be activated completely in tension between the screws over the total height.

$$F_{LVL,k} = s_{screw} \times t_{LVL} \times f_{t,0,k} \tag{3.8}$$

The forces, based on the four failure mechanisms, are now calculated and using the internal lever arm calculation from equation 3.5, the bending strength is calculated.

3.4.2 Butt-joint

The same equations are used for the butt-joint connection, but there is no longer a distinction needed between LVL or CLT. There is a dependency on a new variable 'e', which is the distance from the screw head to the panel edge. This variable determines the screw lengths in the two panels. However, the axial withdrawal capacity of a fully threaded screw is governing compared to the head pull-through resistance. This means the edge distance is calculated in such a way that both screw lengths are equal.

3.5 Parameter study

3.5.1 Stiffness

Splice plate

For the calculations there is a distinction to be made between a calculation based on the ETA of a screw or based on the building code. As mentioned before the stiffness calculations from the

ETA's do not differ for the screws which are covered in this report. The calculation based on the building code does however differ. Besides the difference in calculation method, there are four parameters of interest that need further investigation. First, the influence of the thickness of the LVL plate is investigated, secondly, the comparison between soft and hardwood LVL panels will be made, and third the μ value (see equation 2.13) will be varied. This will always be done for different screw lengths. For this calculation a 7-layer CLT panel, all lamella $t = 40mm$, is assumed and a screw diameter of $10mm$. The softwood LVL panel is assumed as a $39mm$ panel, see A.1, but will be varied later on, ($\rho_{mean} = 510kg/m^3$), and the hardwood LVL panel is assumed as birch plywood $40mm$ ($\rho_{mean} = 680kg/m^3$).

First calculations are performed for $\mu = 0.25$, see Figure 3.11, for both hardwood and softwood. The influence of the screw length is as expected approximately linear, this can be seen in the

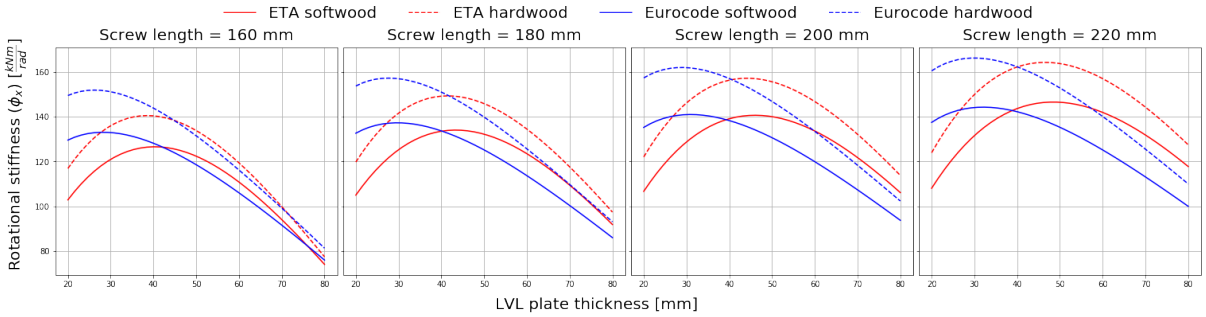

Figure 3.11: Rotational stiffness of a single screw for different LVL thicknesses

increase of the rotational stiffness for longer screws. A thicker LVL panel increases the axial stiffness of the connection, because the summation of the springs becomes more favourable:

$$\frac{1}{K_{tot}} = \frac{1}{K_{CLT}} + \frac{1}{K_{LVL}}$$

On the other hand the internal lever arm of the connection decreases with a larger LVL panel, see Figure 3.7. It depends on the total height of the CLT panel and the thickness of the first lamella that is oriented in the longitudinal direction of the panel. As mentioned before the internal lever arm is between the top of the first layer in the minor direction of the panel and the shear plane of the LVL plate, this leads to the following equation:

$$z_{splice} = h_{CLT} - T - t_{LVL}$$

In this equation T is the summation of lamella thicknesses, counting from the top of the panel, until the first lamella oriented in the minor direction of the panel is reached. These two contributing factors lead to a parabolic function as shown in Figure 3.11. This means there is an optimum value for the thickness of the LVL panel for a certain screw length for every possible lay-up of a CLT panel. The optimum can be found by deriving a solution to the following equation:

$$\frac{d\varphi}{dt_{lvl}} = C_\mu \times (h_{CLT} - T - t_{lvl})^2 \times \left(25d \times \sqrt{2} - \frac{100 \times d \times t_{lvl}}{l}\right)$$

$$-2 \times (h_{CLT} - T - t_{lvl}) \times \left[(1 - C_\mu) \times 60(0.7d)^{1.7} + C_\mu \times \left(\frac{25d \times t_{lvl}\sqrt{2} \times \left(l - t_{lvl}\sqrt{2}\right)}{l}\right)\right] = 0$$

This equation is based on the assumption that the LVL panel is made of softwood, however, as can be seen in Figure 3.11 the maximum of φ_x for both soft- and hardwood is at approximately the same value of t_{LVL}. The equation is to complex for normal use, but it can be simplified

a little. To simplify the equation it is investigated what the influence of the terms is on the equation. The influence of the diameter and friction coefficient turn out to be small, see Figure 3.12.

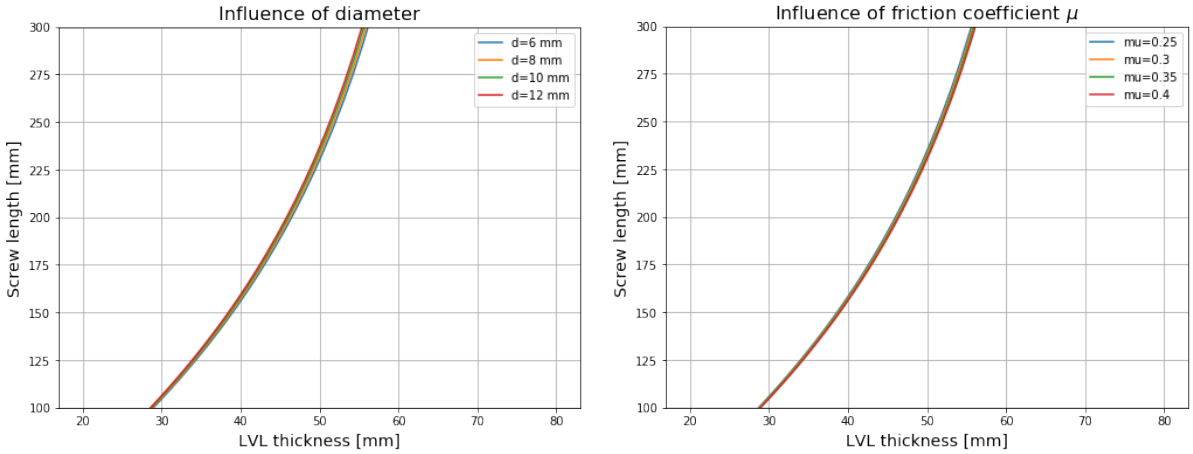

Figure 3.12: 7-layer panel; $H = 280mm$ and $t_1 = 40mm$

The chosen values for diameter and friction coefficient μ were selected to reflect common engineering design conditions. For these common values the diameter and μ have a minimal impact on the outcome of the calculation for the values. This suggests that, within the practical range of values, the optimal screw length for a certain LVL thickness is primarily determined by the panel geometry (H and t_1). To simplify the equation a little, a diameter ($d = 10$) and friction coefficient ($\mu = 0.25$) are assumed, this leads to the following equation:

$$(H - t_1 - t_{lvl}) \times (220.97 - \frac{625 t_{lvl}}{l}) - 1229.93 - 312.5 \times \frac{t_{lvl}\sqrt{2} \times (l - t_{lvl}\sqrt{2})}{l} = 0$$

The solution to this equation is non-linear, to make the results understandable, the equation is solved for a few panel geometries in appendix H. The optimum LVL thickness can be found for certain screw lengths, this is done for relevant 7- and 9-layer panels as producible by Derix, see Figure H.1 and H.2. The use of this Figure is a little counter intuitive because it suggests that for a certain LVL plate thickness there is an optimum screw length. The use of this Figure is actually the other way around, for a predefined LVL thickness an appropriate screw length can be obtained. Increasing the screw length can also increase the stiffness of the connection, but increasing the LVL plate thickness would not increase the stiffness without also increasing the screw length.

As stated before, the optimal combination of t_{lvl} and l_{screw} does not depend significantly on the material of the LVL plate. However, the rotational stiffness does depend on whether the LVL plate is soft- or hardwood. To find the influence of a hardwood splice plate compared to a softwood plate, the ratio between the two values is plotted, this can be seen in Figure 3.13.

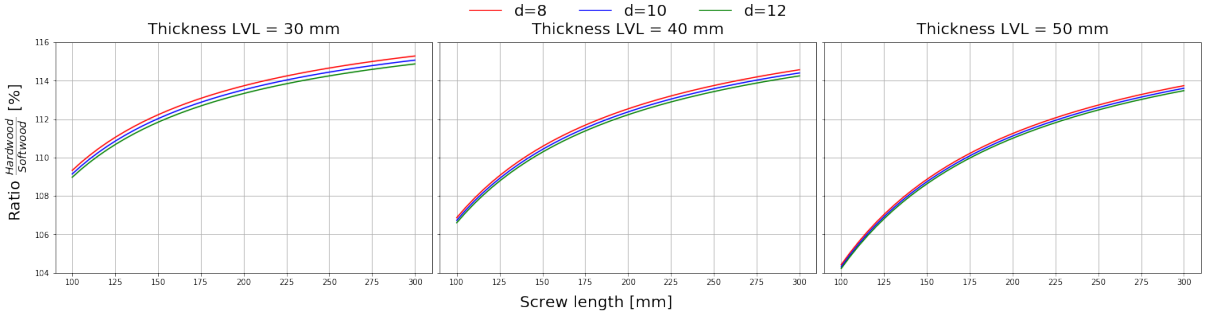

Figure 3.13: Ratio between hard- and softwood

Using hardwood increases the rotational stiffness with a maximum of 15% for the parameter limits of this design. Because of the fact that softwood LVL is more common in use, it is advised to use softwood LVL and only use hardwood in case an additional 15% in stiffness is needed.

To illustrate the effect of the friction coefficient a ratio $\frac{\mu=0.40}{\mu=0.25}$ is calculated. By plotting this ratio for multiple diameters, LVL thicknesses and screw lengths, see Figure 3.14, the effect becomes visible. The effect of a higher friction coefficient increases with thicker LVL panels, but is limited to approximately 10% for the more common designs. It is often very challenging to estimate the friction coefficient in a accurate way, so it is advisable to use a friction coefficient of $\mu = 0.25$ due to the small beneficial effect it has.

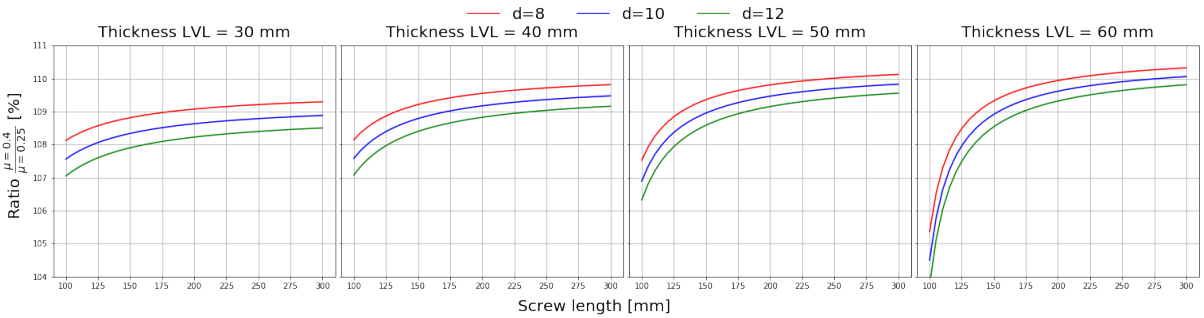

Figure 3.14: Ratio between $\mu = 0.40$ and $\mu = 0.25$

Some parameters have not been mentioned specifically in this study. Mainly the effect of the panel geometry, spacing of the screws and diameter have not been studied on their own. This is due to the fact that their effect is in line with expectations, for instance a bigger diameter increases the stiffness of the connection and so does a smaller spacing.

Butt-joint

The number of parameters for the butt-joint is smaller due to the absence of the LVL plate. The most interesting parameter to study here is the screw length and the distance 'e' from the panel edge. Because the angle of the screws is assumed to be 45°, $e = \frac{L_1}{\sqrt{2}}$, with L_1 as shown in

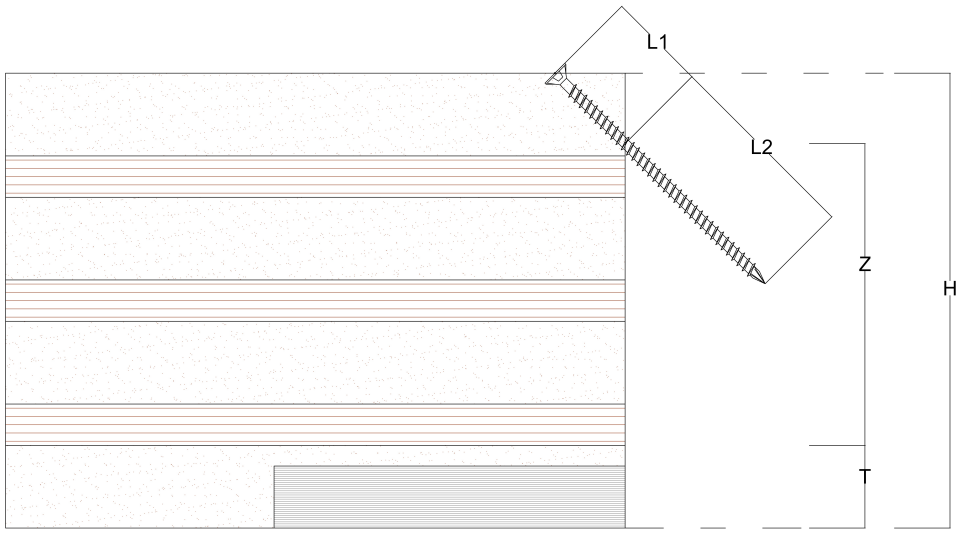

Figure 3.15: Screw lengths related to edge distance

Figure 3.15. For fully threaded screws the axial withdrawal capacity is almost always governing compared to head pull-through when considering the strength of the connection, see also 3.4.1. To take this already into account for the stiffness calculation, $L_1 = L_2$ is assumed, and thus:

$$e = \frac{l_{screw}}{2\sqrt{2}}$$

Now the edge distance is coupled to the screw length, the only variables are screw length and diameter. Like for the splice plate connection, the derivative with respect to l can be taken from the rotational stiffness φ, so:

$$\frac{d\varphi}{dl} = \frac{d}{dl}(\frac{K_r \times z_{butt}^2}{2}) = 0$$
$$l = \frac{2\sqrt{2}}{3} \times (H - T)$$

In this equation T is the summation of lamella thicknesses, counting from the bottom of the panel, until the bottom of the first lamella oriented in the minor direction of the panel is reached. For a specific panel lay-up there is an optimum screw length when considering the rotational stiffness.

3.5.2 Strength

Splice plate

To design this connection it is important to establish important parameters in the model. In other words, now it will be investigated which parameters have the biggest influence on the strength of this connection.

First it can be stated that the tensional strength in the screw and LVL member itself are rarely governing. The connection can also be adjusted quite easily if one of these failure mechanisms becomes governing. The decision can be made to use higher quality timber for the LVL plate or higher strength screws.

Secondly, due to the "max"-term inside the equations, the head-pull through strength is rarely governing. The axial withdrawal strength of the screw is the larger value and determines the capacity in the timber members. The ETA's mention specifically that the axial withdrawal capacity of threaded screws is governing compared to head-pull through capacity. This means that adding washers underneath the screws is expected to add almost no extra capacity to the connection.

Thirdly, and most relevant, is the limitation of the connection depending on the thickness of the LVL plate. Due to the design of this connection, the connection should be dimensioned in such a way that the screw fails first in the LVL member. The LVL member has a fixed thickness that has been determined depending on factors like stiffness, availability and whether it is easy to install. The screw length should be chosen in such a way that the screw in the LVL plate is the governing failure mechanism. If the screw fails first in the CLT member, the screw length should be increased, this way the maximum rotational strength is obtained. Figure 3.16 shows this limitation of the strength of the connection depending on the thickness of the LVL plate. For this calculation a 7-layer CLT panel, all lamella $t = 40mm$, is assumed and a screw diameter of $10mm$. The LVL panel is assumed to be made of softwood.

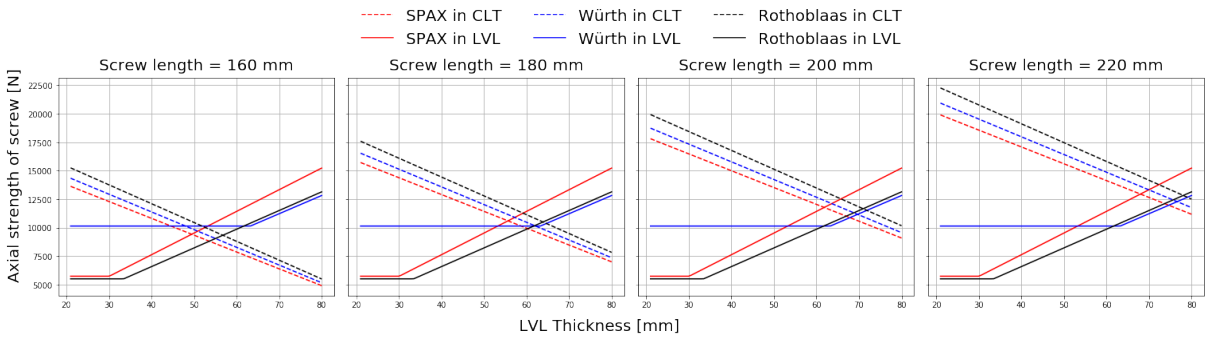

Figure 3.16: Characteristic axial withdrawal strength

The connection is as strong as its weakest link, so the lower value of the screw in the LVL member or in the CLT member determines the strength of the total connection. By using a thicker LVL plate, the maximum tensional strength of the screw becomes larger, but also the internal lever arm becomes smaller. However, the increase of the strength due to a thicker LVL plate is larger than the decrease due to a smaller internal lever arm. This is show in Figure 3.17, where the characteristic bending moment capacity for a single screw is calculated. The length of

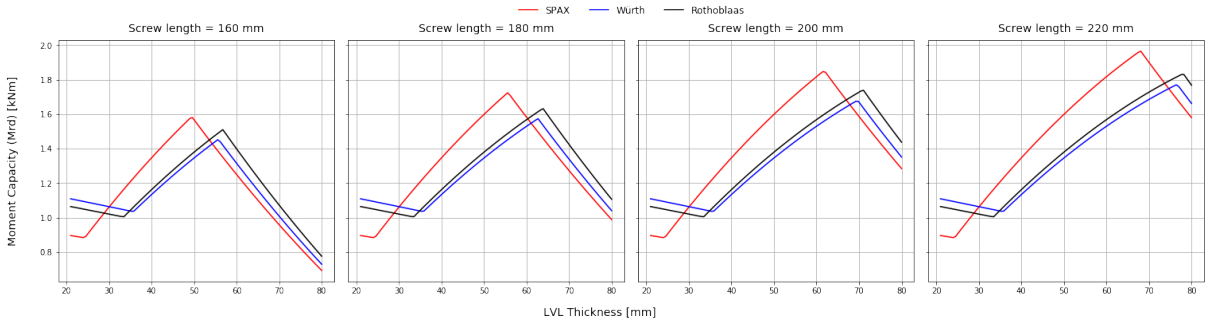

Figure 3.17: Characteristic bending moment capacity

the screw should be chosen in such a way that the screw in the LVL member is the governing failure mechanism. The strength in the CLT panel is determined by the length of the screw in this panel, a larger screw means more length is in this panel and thus the axial withdrawal capacity increases. The tipping point in the bending moment capacity is determined by the screw length, for a certain thickness of the LVL plate, the axial capacity of the screw in the CLT panel becomes governing. When increasing the LVL thickness even further, the length of the screw in the CLT panel decreases and so does the bending moment capacity. The maximum point of the bending moment is actually the point where the axial withdrawal capacity in the CLT panel equals the axial withdrawal capacity in the LVL plate. This equation leads to the following relations, based on the assumptions that the screw angle equals 45° and the CLT panel is made of softwood timber, see table 3.3:

Table 3.3: Requirements for minimum screw lengths

	LVL	*Requirement*
SPAX	Any	$L_{screw} \geq (1 + \frac{\rho_{LVL}}{\rho_{CLT}}^{0.8}) \times t_{lvl}\sqrt{2}$
Würth	$\rho_k \leq 590$	$L_{screw} \geq (1 + \frac{5}{4} \times \frac{\rho_{LVL}}{\rho_{CLT}}^{0.8}) \times t_{lvl}\sqrt{2}$
	$590 \leq \rho_k \leq 750$	$L_{screw} \geq (1 + \frac{28}{f_{ax,k,CLT}} \times (\frac{\rho_{LVL}}{\rho_{CLT}} \times 0.4795)^{0.8}) \times t_{lvl}\sqrt{2}$
Rothoblaas	$460 \leq \rho_k \leq 550$	$L_{screw} \geq (1 + \frac{12.0}{11.7} \times (\frac{\rho_{LVL}}{\rho_{CLT}} \times 0.7)^{0.8}) \times t_{lvl}\sqrt{2}$
	$590 \leq \rho_k \leq 750$	$L_{screw} \geq (1 + \frac{23.7}{11.7} \times (\frac{\rho_{LVL}}{\rho_{CLT}} \times 0.4795)^{0.8}) \times t_{lvl}\sqrt{2}$

Using the minimum required screw lengths as a starting point, a preliminary estimate for the panel height can be made. This quick estimation method is further elaborated in Appendix D, where the relationship between screw length and panel height is explored under a set of conservative, unfavourable assumptions. In particular, the quick method links panel height to the screw failure limit within the LVL panel. While this provides a useful initial guideline, it is important to note that the purpose of this chapter is to develop a more refined and detailed engineering model. Such a model aims to better capture the complexity of the system and provide reliable design data for practical applications.

Next the comparison can be made between a softwood and hardwood LVL panel to connect the CLT panels. The softwood LVL panel is manufactured from pine or spruce ($\rho_k = 480kg/m^3$) and the hardwood LVL panel is assumed as birch plywood ($\rho_k = 630kg/m^3$). It has been stated before that the axial withdrawal capacity is governing for a fully threaded screw. However, due

to the higher density of hardwood panels, the head pull-through capacity does become governing for hardwood in some cases. This effect, amongst others, can be seen in Figure 3.18. The lines

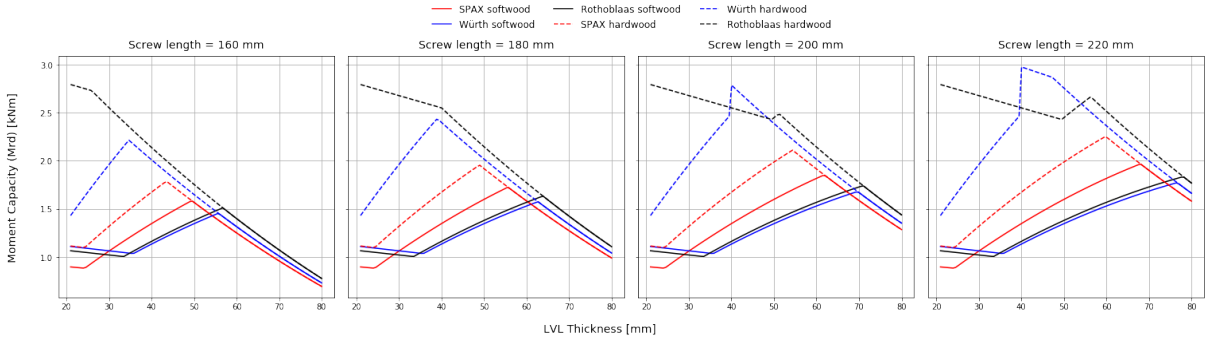

Figure 3.18: Characteristic bending moment capacity hardwood compared to softwood

have some sharp turns due to the limitations of densities for a certain characteristic parameter as given in tables 3.1 and 3.2. The conclusion that can be drawn from these figures, is to find these limits of the design to maximize the strength of the connection within ETA limits.

The influence of the friction coefficient is more clear in the calculation of the bending moment strength. Using the relation in equation 2.25, it can be seen that the influence of μ can be simplified to $\frac{\sqrt{2}}{2}(1+\mu)$ for a 45° angle of the screws. Comparing $\mu = 0,40$ and $\mu = 0,25$, which is an approximate range of realistic values, the effect of increasing μ is limited to 12% increase in bending moment capacity.

Lastly it should be noted that the strength of the connection also increases with a larger diameter and a larger number of screws. This number of screws is increased with a smaller spacing and multiple screws in a row.

Butt-joint

As mentioned before, the head-pull through strength is rarely governing compared to the axial withdrawal strength. For the butt-joint this means the lengths of the screws in both panels should be equal to reach optimum strength, so $e = \frac{l_{screw}}{2\sqrt{2}}$. Taking this assumption as as starting point for the calculation, the optimum screw length can be derived:

$$l = \sqrt{2} \times (H - T)$$

The optimum for the strength of the screw is at a different screw length than for the stiffness. The screw lengths become very large when reaching the optimum length, so it is advisable to check for smaller lengths. Of course a larger diameter and smaller spacing increase the strength.

3.6 Verification

Both the splice plate and butt-joint configurations were verified against experimental data, as presented in Appendix C. The model shows good agreement in terms of strength. For the splice plate, it slightly underestimates capacity due to its elastic assumptions, which does not capture the plastic behaviour observed during testing [30]. In contrast, the butt-joint model slightly overestimates strength, likely because the limited number of tests led to a conservative characteristic value [68].

Rotational stiffness predictions showed greater variability. This is partly due to the model's sensitivity to timber properties and load introduction, and partly due to differing definitions of rotation angle in each test series. The splice plate used horizontal gap measurements, while the butt-joint relied on a geometric conversion method. These differences highlight the need for standardized procedures for rotational stiffness testing. Despite these limitations, the model

provides a reliable basis for strength evaluation and is a practical tool for early-stage stiffness assessments.

3.7 Conclusion and Discussion

This chapter presents a detailed approach to modelling and designing panel-to-panel connections, specifically the proposed connection as shown in Figure 3.7, for CLT structures. The focus of this chapter is on the integration of RFEM and custom Python scripts for evaluating connection strength and stiffness. While significant progress has been made in understanding the behaviour of these connections, certain aspects deserve further exploration and refinement.

A key design rule was established: the screw length should be chosen so that failure occurs in the LVL member, rather than in the CLT or the connection itself. Based on this, a quick estimation method has been developed to approximate the required panel height. This method, detailed in Appendix D, relies on conservative assumptions to ensure safety while enabling efficient early-stage assessments. The minimum screw lengths are determined by key parameters such as the material densities of the CLT and LVL, and the thickness of the LVL layer. These factors influence the screw's embedment strength and withdrawal resistance, which affect the governing failure mode. While useful as a preliminary guideline, this approach should be complemented by a detailed engineering model—such as the one presented in this chapter—for accurate design under complex connection behaviour.

A key point of the study is the evaluation of the splice plate connection and the butt-joint, with emphasis on parameters like screw length, spacing and diameter. Although parameters such as panel geometry and screw diameter were not elaborated on, their effects are generally predictable. For example, a larger screw diameter and reduced screw spacing are expected to increase connection stiffness, which aligns with general mechanical expectations. However, further exploration into the influence of these parameters could provide more detailed design guidelines, especially when dealing with variable or less predictable panel geometries.

The chapter also introduces the use of RFEM for structural analysis, alongside a Python-based model to assess strength and stiffness. The bilinear spring model used to capture the non-linear behaviour of connections under positive and negative bending moments is an accurate approach, providing more reliable predictions for the design of CLT floor systems. While this method is effective, the iterative process of refining models based on the interaction between RFEM and Python remains time-consuming. A potential solution would be the integration of Python and RFEM into a single model, which could streamline the process and reduce design iteration times. Additionally, incorporating a formula to estimate bending moments in a given floor system would help further reduce the process's iterativity, making the overall design more efficient.

An interesting area for improvement lies in the model's current approach to compressive strength in the lamellas. As it stands, the model uses a simplified assumption of compressive strength without considering the dispersion of compressive force within the panel. By accounting for the dispersion of compressive force, a larger area within the panel would be activated in compression, leading to a greater internal lever arm and, consequently, an increase in the bending moment capacity. This aspect could enhance the accuracy and reliability of the model in predicting the true bending capacity of the panel connections.

In conclusion, the proposed model is sufficient for designing the panel-to-panel connection. While further optimisation is possible, this is only necessary if the connection design is already at an advanced stage and refinement is still required. The RFEM model serves well for preliminary design of the line hinge, but lacks the accuracy needed to verify the CLT panel itself, which largely depends on how the panel-to-column connection is modelled. Introducing more general rules for modelling line hinges would significantly reduce the iterativity of the process.

Chapter 4: Moment Estimation in Panel Joints

4.1 Introduction

During preliminary design, quick and reliable estimates of internal forces are essential to guide decision-making without resorting to detailed numerical models. In point-supported CLT floor systems, this is particularly important for dimensioning hinge connections between adjacent panels. This chapter presents a simplified parametric formula to estimate the bending moment at the line hinge, developed through numerical simulations in RFEM 6.

The approach is based on a series of parametrized plate models, from which key influences are identified and an empirical expression is fitted to the results. The aim is to support early-stage design with a practical, structurally informed estimate that avoids time-consuming finite element iterations.

The chapter begins with relevant plate theory, followed by a description of the numerical modelling approach, which is also used in Chapter 5. The development of the formula is then presented, including discussion of rotational stiffness and the final expression. The influence of line support conditions is examined before concluding with a summary of findings.

4.2 Relevant Plate Theory

The deflection of anisotropic plates can be determined using the following equation as defined by Timoshenko and Woinowsky-Krieger[60]:

$$D_x \frac{d^4w}{dx^4} + 2H \frac{d^4w}{dx^2 dy^2} + D_y \frac{d^4w}{dy^4} = q \tag{4.1}$$

with

$$H = D_1 + 2D_{xy}$$
$$D_1 = D_x \nu_y = D_y \nu_x$$

The flexural rigidities, D_x, D_y, D_{xy}, for a CLT panel are calculated using the Classical Lamination Theory. CLT is a specially orthotropic lamina, which means the principal material axes are aligned with the axes of the body [36]. The following stiffness matrix can be constructed for an individual lamella:

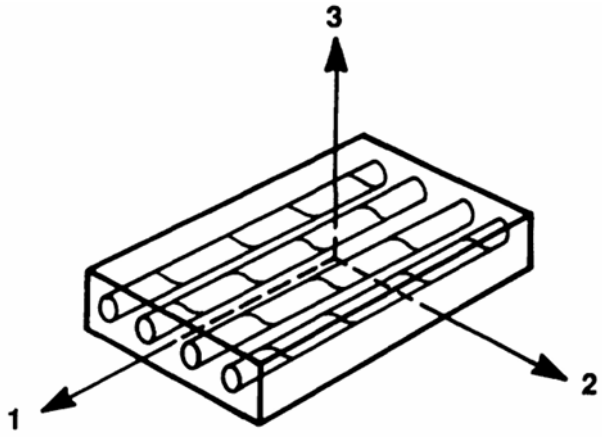

Figure 4.1: Unidirectionally lamina [36]

$$Q_{ij} = \begin{bmatrix} Q_{11} & Q_{12} & 0 \\ Q_{21} & Q_{22} & 0 \\ 0 & 0 & Q_{66} \end{bmatrix}$$

$$Q_{11} = \frac{E_1}{1-\nu_{12}\nu_{21}} \qquad Q_{22} = \frac{E_2}{1-\nu_{12}\nu_{21}}$$

$$Q_{12} = \frac{\nu_{12}E_1}{1-\nu_{12}\nu_{21}} \qquad Q_{66} = G_{12}$$

For $E_2 = 0$ and $\nu_{12} = \nu_{21} = 0$, the matrix can be simplified to:

$$Q_{ij} = \begin{bmatrix} E_1 & 0 & 0 \\ 0 & 0 & 0 \\ 0 & 0 & G_{12} \end{bmatrix}$$

In the structural modelling of CLT, the interaction between longitudinal stresses and transverse strains is commonly disregarded, which corresponds to setting Poisson's ratio to zero. Due to the alternating grain direction of lamellas and the presence of transverse butt joints, CLT

panels exhibit minimal transverse deformation when stressed in the longitudinal direction. This interlocking effect of the layers causes significant strain transfer between orthogonal directions. As a result, standard orthotropic stiffness matrices used in finite element modelling exclude the coupling terms that would otherwise represent Poisson effects. [40]

So $\nu_{12} = \nu_{21} = 0$ and, to simplify the stiffness matrix, the contribution of transverse layers is negligible, so $E_{90} = 0$ is assumed for individual lamella. Using the individual matrices for the lamellae, and using $b_x = b_y$, the bending stiffness for the laminate can be calculated.

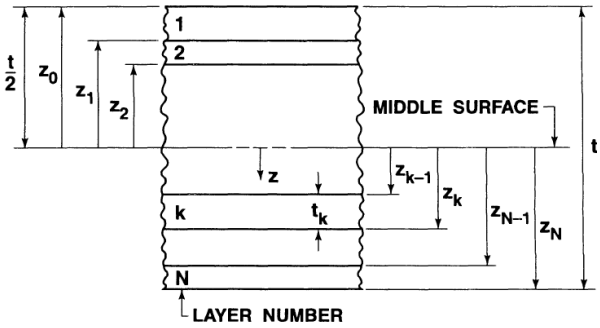

Figure 4.2: Geometry of an N-layered Laminate [36]

$$D_{ij} = \frac{1}{3}\sum_{k=1}^{N}(Q_{ij})_k(z_k^3 - z_{k-1}^3) \tag{4.2}$$

Where z_k is the distance from the middle of the laminate to the bottom of the k$^{\text{th}}$ layer, with a positive z-direction downwards. This is depicted in the figure to the left. This means $z_0 = -\frac{t}{2}$ and $z_N = +\frac{t}{2}$. For a CLT panel the bending stiffness matrix can be written in the following form:

$$D_{ij} = \begin{bmatrix} EI_x & 0 & 0 \\ 0 & EI_y & 0 \\ 0 & 0 & \frac{G_{xy}h_{CLT}^3}{12} \end{bmatrix} \tag{4.3}$$

The equation 4.1 is used in the Kirchhoff theory and assumes a thin plate deforming under pure bending behaviour. The calculations in the RFEM 6 FEA software [15] are based on Mindlin plates, also known as thick plates and include shear deformations. In this section, internal forces such as bending moments are assumed to follow standard sign conventions, with positive moments represented as tension on the bottom face of the panel and negative moments as tension on the top face.

To indicate the bending behaviour of orthotropic plates, it is insightful to consider Kirchhoff plate theory. Timoshenko and Woinowsky-Krieger [60], extending the Navier solution for rectangular plates subjected to uniform loading, derived an expression to estimate the bending moment at the centre of an orthotropic plate with simply supported boundary conditions. The bending moment M_x is given by:

$$M_x = \left(\beta_1 + \beta_2 \frac{E"}{E'_x}\sqrt{\frac{D_x}{D_y}}\right) \times q_0 \frac{a^2}{\epsilon} \tag{4.4}$$

$$M_y = \left(\beta_2 + \beta_1 \frac{E"}{E'_y}\sqrt{\frac{D_y}{D_x}}\right) \times q_0 b^2 \tag{4.5}$$

where

$$\epsilon = \frac{a}{b}\sqrt[4]{\frac{D_y}{D_x}} \tag{4.6}$$

with

M_x	Bending moment at the centre of the plate $[Nm]$
q_0	Applied uniform load $[N/m^2]$
a, b	Spans in x- and y-directions $[m]$
β_1, β_2	Constants depending on ϵ
$E'_x, E"$	Stiffness moduli $[Nm^2]$
D_x, D_y	Flexural rigidities of the plate $[Nm]$

This formulation captures how both the plate geometry and its material anisotropy influence the resulting bending moment. The coefficients β_1 and β_2, which are numerical factors obtained from solutions under simply supported boundary conditions, reflect the combined effects of the support configuration and the plate's deformation behaviour. Their values depend explicitly on the dimensionless parameter ϵ, which incorporates the geometric aspect ratio $\frac{a}{b}$ and the relative flexural rigidity in the two orthogonal directions. This parameter governs how the plate deforms under uniform load and thereby has a significant impact on the distribution of internal moments. As ϵ varies, the relative contribution of the two terms in the bending moment expression changes, with β_1 and β_2 adjusting accordingly, becoming equal when $\epsilon = 1$ and tending toward $\beta_1 \to 0$, $\beta_2 \to \frac{1}{8}$ as $\epsilon \to \infty$. A more detailed exploration of this limiting case is provided in Appendix B.1.1.

The term $\frac{E''}{E'_x}\sqrt{\frac{D_x}{D_y}}$ captures the effect of stiffness anisotropy between the principal directions. A stiffer response in the x-direction, achieved by increasing D_x or decreasing D_y, raises the bending moment by providing greater resistance to bending along that axis.

The scaling factor $\frac{a^2}{\epsilon}$ governs how the plate's size and orthotropic properties influence the central bending moment. While a larger span a increases the moment quadratically, a higher ϵ, which corresponds to plates that are either longer in the x-direction or more flexible in the y-direction, alters the load distribution. In such cases, a larger share of the bending moment is carried in the stiffer x-direction, leading to a more directional response. This reduces the relative contribution of the y-direction and shifts the moment distribution.

Altogether, this formulation illustrates the key parameters governing the bending behaviour of orthotropic plates and how they interact; namely, the geometry, material anisotropy and stiffness distribution across principal directions. While these expressions (Eq.4.4, Eq.4.5) are derived assuming simply supported boundary conditions, the identified relationships remain valuable for understanding and predicting the mechanical response of plates under varying conditions. Even in cases with alternative boundary constraints, such as clamped or point-supported configurations, the same influencing factors continue to play a central role.

When extending this understanding to point-supported floors, one may expect qualitative similarities in how geometry and stiffness influence the load-bearing behaviour. The introduction of discrete supports, such as point supports, alters the load transfer mechanism within the plate by localising reaction forces. This localisation changes how the plate bends, potentially increasing local bending effects and stress concentrations near the supports. As a result, while the overall form of the bending moment expression remains valid, the influence of boundary conditions becomes more pronounced. These changes are expected to primarily affect the values of the coefficients β_1 and β_2, which contain the response associated with support conditions and deformation behaviour. Therefore, for point-supported systems, these coefficients would need to be re-evaluated or modified to reflect the altered boundary constraints and associated mechanical response.

4.3 Numerical Modelling Approach

4.3.1 Modelling Assumptions

In a floor design any number of parameters can be varied. In this chapter the goal is to create simple design tables and graphs that can help in the preliminary phase of designing a floor system. To this extent some assumptions have to be made that reduce the number of variables in all equations. The assumptions are related to the line hinge, floor direction and CLT panels.

After assuming a maximum panel width of $3.5m$ and length of $16.0m$ for all floor systems, the location of line hinges in continuous floors can still be freely chosen. To streamline design and ensure consistency, this analysis considers symmetrical placement of the line hinges. This results

in two main configurations, as illustrated in Figure 4.3b, depending on the field length L_y.

When $L_y \leq 5.25m$ and $L_A \leq 3.5m$, each field requires only one line hinge, this hinge is placed at distance of $3.5m$ from the support. If $L_y > 5.25m$ and $L_B > 0.875m$, two hinges per field are introduced. In this case, a central panel of $3.5m$ is defined and a hinge is placed on either side of this panel, positioned symmetrically near the supports, where bending moments are smaller. This approach avoids placing hinges at the locations of maximum moment, while maintaining good force distribution and constructibility. The same rule is applied consistently to both single-span and continuous floor systems, ensuring standardised hinge placement and manageable internal forces across various layouts.

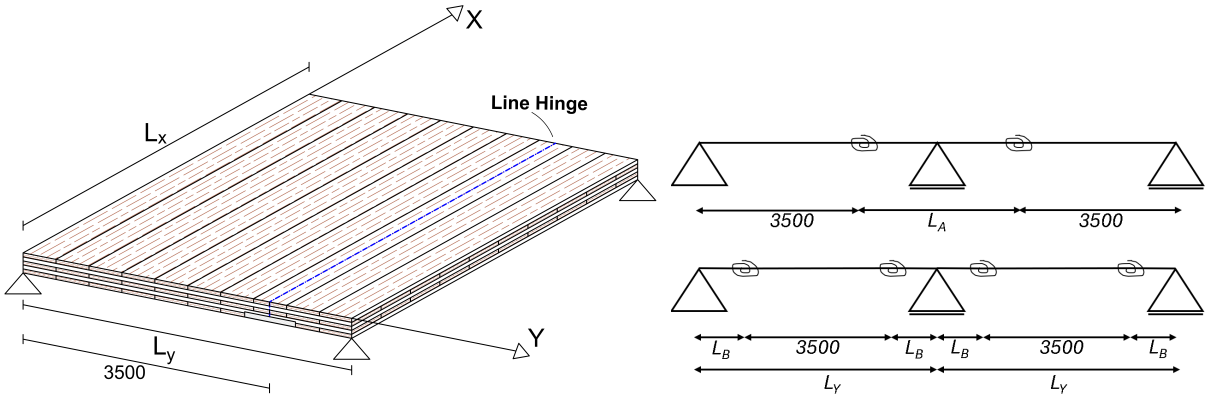

(a) Single span floor system **(b)** Continuous floor system

Figure 4.3

Secondly, the rotational stiffness φ of line hinges in the model is constrained to the interval $1000 \leq \varphi \leq 5000 \frac{kNm}{rad}$. Values below $1000 \frac{kNm}{rad}$ are considered unrealistic for satisfying both ULS and SLS requirements. On the upper end, Stieb et al. [55] evaluated various floor systems and demonstrated that increasing the rotational stiffness up to approximately $5000 \frac{kNm}{rad}$ results in significant improvements in structural performance. However, further increases beyond this threshold have only marginal effects. The proposed connection, as detailed in chapter 3, exhibits stiffness values within this range, which motivates focusing on this interval in the numerical study.

Thirdly, the major stiffness direction of the CLT panel is assumed to align with the longer span, implying that $EI_x \geq EI_y$. In this study, cases where $EI_x = EI_y$ will also be considered to assess more balanced stiffness configurations. The line hinge is positioned along the major direction (the longer span), as illustrated in Figure 4.3a. As a result, the rotational spring acts in the minor direction of the panel, where the bending moments and deflection demands are typically lower. Placing the hinge along this less critical axis reduces the impact on global floor performance while still allowing the study of rotational flexibility.

Lastly, it is assumed that at least two modules are created. This is very beneficial for the modal mass that will be activated when the floor is vibrating, relevant in Chapter 5. This assumption is justified by remembering that the limitation of the floor is in the smaller direction of the span. In the other direction, it is easier and preferable on site to work with larger panels. This will lead to at least two modules, or two spans besides each other, that can be seen as one continuous floor system.

4.3.2 Parametric Model Creation

A parametric model is developed in Grasshopper, a visual programming tool for Rhino commonly used in architectural and structural design, to generate point-supported CLT floor configurations based on adjustable geometric and material parameters. Grasshopper connects to RFEM 6 via the Dlubal plug-in, allowing floor layouts to be generated and visualized directly while structural

analysis is performed in RFEM. This setup enables efficient iteration across many configurations. An overview is shown in Figure 4.4.

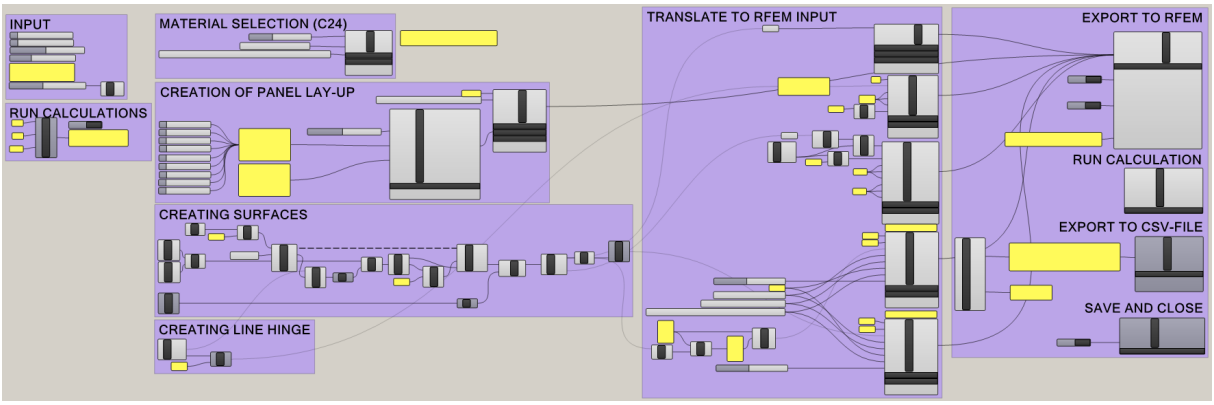

Figure 4.4: Grasshopper model to parametrise a floor system

The spans, L_x and L_y, are varied along with the plate lay-up, inherently changing the bending stiffness values. Two load cases are included: one with a single field loaded and another with both fields loaded, to account for asymmetric loading. The Dlubal plug-in transfers the parametric geometry from Grasshopper to RFEM, where the model is automatically generated and meshed with finite elements of $0.25m \times 0.25m$ (see App. B), based on the defined input.

RFEM then performs static analysis for each generated configuration. The resulting data are exported to Excel, from which key values are extracted using Python. For consistency and comparability, the results are evaluated at a governing section along the line hinge.

4.4 Development of the Formula

In classical plate theory, Timoshenko and Woinowsky-Krieger [60] provide expressions for the bending moments at the centre of a simply supported orthotropic rectangular plate subjected to uniform pressure q_0. These moments, acting in the x- and y-directions, are given in Equations 4.4 and 4.5.

A notable feature of these expressions is that the moment M_x is divided by a parameter ϵ, while M_y lacks any explicit dependence on ϵ. At first glance, this appears to introduce asymmetry between the two directions. However, this is not due to any fundamental physical imbalance between the x- and y-directions, but rather arises from the choice of reference direction in the derivation. Specifically, the x-direction (with span a) is treated as primary and the equation is normalized accordingly. If one were to reverse the coordinate system, swapping $x \leftrightarrow y$ and $a \leftrightarrow b$, the roles of M_x and M_y would also switch and the parameter ϵ would instead appear in the expression for M_y, restoring symmetry.

In this thesis, the bending moment M_y is the primary focus, motivated by the assumptions stated in Section 4.3, which align the dominant span and stiffness properties with the x-direction. Although the bending moment of interest acts in the y-direction, it remains important to incorporate both spans a and b, as well as the orthotropic stiffness ratio $\frac{D_y}{D_x}$, to accurately capture the plate's response. From a structural and modelling perspective, particularly in the case of point-supported plates, it becomes increasingly appropriate to view the bending response in both directions as intrinsically coupled. Unlike simply supported plates, where moments develop predominantly along supported edges, point-supported plates engage bending stiffness more uniformly across both directions. Consequently, the moments M_x and M_y tend to be more closely related and influenced by each other than in simply supported cases.

To reflect this interdependency between bending moments in both directions, a modified bending moment in the y-direction is introduced by incorporating the scaling factor ϵ used in the

x-direction:

$$M_y^{\text{mod}} = M_y \times \epsilon = \left(\beta_2 + \beta_1 \frac{E''}{E_y'} \sqrt{\frac{D_y}{D_x}}\right) \times q_0 \times ab \times \left(\frac{D_y}{D_x}\right)^{\frac{1}{4}} \tag{4.7}$$

This modification reflects the coupled behaviour of the bending moments influenced by the plate's geometry and orthotropic stiffness properties. Additionally, Equation 4.7 indicates that the bending moment is mainly influenced by three factors: the applied load q_0, the plate geometry ab and the plate's stiffness properties expressed through the terms involving E'', E_y' and the flexural rigidities D_x, D_y. The geometric term ab represents the influence of the plate's dimensions and can be written as $L_x L_y$ for consistency with the notation used throughout this study. Similarly, the rigidity ratio $\frac{D_x}{D_y}$, which reflects both material and geometric contributions, can more generally be expressed in terms of the bending stiffnesses EI_x and EI_y. While this substitution does not apply to the anisotropic term $\frac{E''}{E_x'}$, using the ratio $\frac{EI_y}{EI_x}$ captures the dominant flexural behaviour in a format that is more commonly used in engineering practice. For convenience in the parametric study, this stiffness ratio is denoted by $\eta = \frac{EI_y}{EI_x}$.

Using these relations, the bending moment at the line hinge can be expressed as a function of several parameters. To clearly indicate the individual effects of the parameters and to account for unknown differing effects in a point-supported floor system, constants are introduced. The expected form of the function is:

$$M_y(b_{plate} = 3.5) = C_1 q_0 \times C_2 L_x L_y \times C_3 \eta^{\frac{1}{4}} \tag{4.8}$$

with

$M_y(b_{plate} = 3.5m)$	Estimated bending moment in line hinge for $b_{plate} = 3.5m$ $[kNm]$ This hinge location follows Sec. 4.3.1
C_1, C_2, C_3	Numerical coefficients to be calibrated through parametric studies
q_0	Uniformly distributed load $[kN/m^2]$
L_x, L_y	Plate dimensions in x- and y-directions $[m]$
$\eta = \frac{EI_y}{EI_x}$	Stiffness ratio of the plate

This form highlights the dependence of the bending moment on the applied load ($C_1 q_0$), the overall plate area ($C_2 L_x L_y$) and the anisotropic stiffness effect, captured by the fourth-root stiffness ratio in the final term. The coefficient C_3 implicitly includes the influence of the β-factors derived from orthotropic plate theory, which account for sensitivity to both stiffness directionality and geometry. In addition, C_3 includes the anisotropic modulus ratio $\frac{E''}{E_y'}$ as well as the rigidity ratio $\frac{D_y}{D_x}$, both of which influence how bending resistance varies with direction. Together, these terms make C_3 a key parameter in representing the directional stiffness effects that govern the moment distribution in orthotropic plates.

While the constants could theoretically be combined into a single coefficient, separating them clarifies their individual roles and supports a more transparent calibration process. This formulation thus provides a structured foundation for isolating and evaluating each parameter's contribution through targeted numerical and parametric analysis.

4.4.1 Load

Simple mechanics rules for single-span structures indicate a linear relationship between applied load and resulting bending moment, for example, $M = \frac{1}{8} q L^2$ under a uniform load and $M = \frac{1}{4} F L$ under a central point load. While point-supported floor systems exhibit more complex behaviour, a similar linear dependency on the load may still be expected. To investigate this, a floor system is analysed under uniformly distributed loads of 1, 2 and 3 kN/m^2. The resulting bending moments along a segment of a line hinge are compared in Figure 4.5. By normalizing the results, dividing all bending moment values by their corresponding applied loads, it becomes evident that

the distributions overlap perfectly. This confirms a linear structural response to load magnitude, validating the use of a proportionality constant $C_1 = 1.0$ in the bending moment formulation.

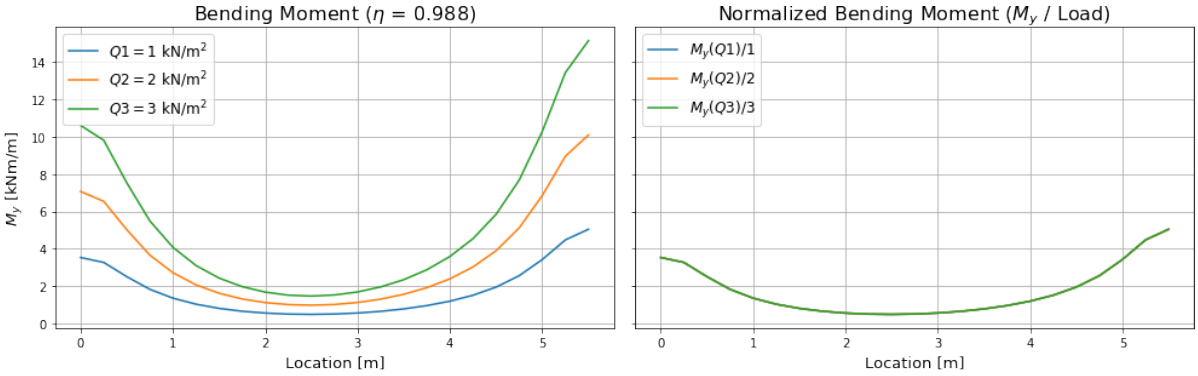

Figure 4.5: Comparison of loads along a line hinge segment

4.4.2 Combined Influence of Span and Stiffness Ratio

To capture the maximum bending moment in point-supported floor systems, the parametric expression in Equation 4.8 was proposed. Here, $C_1 = 1.0$ is based on the linearity between applied load and bending response. However, the remaining terms C_2 and C_3 cannot be directly isolated due to their interdependence. Specifically, C_3 captures the influence of anisotropic behaviour through orthotropic plate theory coefficients (i.e., the β-factors), which depend not only on the stiffness ratio $\eta = \frac{EI_y}{EI_x}$, but also on the span ratio (see Eq. 4.6). Therefore, variations in span and stiffness cannot be separated cleanly.

To address this coupling, the terms C_2 and C_3 are combined into a single numerical coefficient C', which represents the joint influence of span geometry and orthotropic stiffness:

$$M_y(b_{plate} = 3.5) = q_0 \times L_x L_y \times C' \times \eta^{1/4} \tag{4.9}$$

This form allows the parametric expression to scale with span size and load, while encapsulating the effects of anisotropy and layout in the single coefficient C'. The process to further optimize this relation is described below.

4.4.3 Influence of Span Geometry

To explore the relation between geometry, stiffness and the resulting maximum bending moment M_y, a series of numerical simulations was conducted. The results are presented in Figure 4.6.

In the left figure, the numerically obtained maximum M_y values are plotted against L_x for various stiffness ratios η. A linear regression is applied to each set of data points, and the corresponding slopes are shown in the legend. As expected, these slopes vary with η, reflecting its influence on the bending response. In the right figure, this dependency is approximated analytically using lines with slope $\eta^{1/4}$, based on the proposed relation:

$$M_y \propto \eta^{1/4} \times L_x \quad \Rightarrow \quad M_y = \eta^{\frac{1}{4}} \times L_x$$

By considering only the slope, the intercepts from the first subplot's linear fits are discarded and the approximate slopes $\eta^{1/4}$ are retained. While this captures the trend well, a noticeable vertical offset remains due to the neglected intercept. To align the empirical and parametric formulations, it is first noted that the approximated lines in the figure should be scaled to pass through the known reference value M_0, corresponding to the maximum moment at $L_x = L_y$. In the numerical simulations, the applied load was normalized with $q_0 = 1.0$, allowing direct calculation of the scaling factor C.

A first modelling assumption would be to scale the expression such that it passes through the

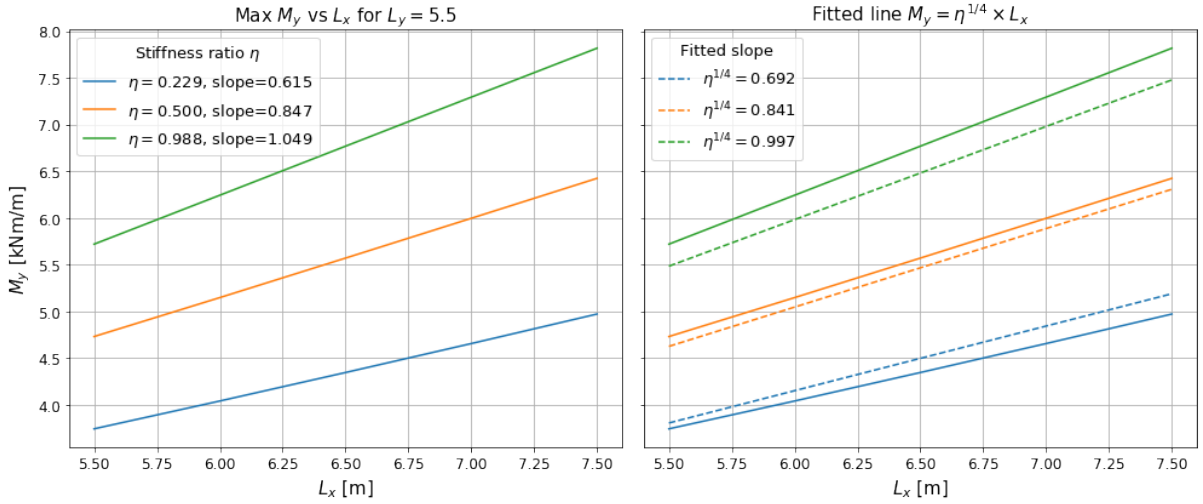

Figure 4.6: Relation between span L_x and maximum bending moment M_y for different stiffness ratios η

reference point. This approach leads to a form with $b = 0$ in the linear form $M_y = a \cdot L_x + b$. This assumption is justified by imposing $M_y \to 0$, which is encapsulated in the definition of M_0: when $L_x \to 0$, the corresponding reference span $L_y \to 0$ as well, thus the moment vanishes with the domain. A vertical scaling factor C is introduced to adjust the slope of the expression according to geometry and boundary conditions, resulting in:

$$M_y = C \times \eta^{1/4} \times L_x \quad \Rightarrow \quad M_0 = C \times \eta^{1/4} \times L_y \quad \Rightarrow \quad C = \frac{M_0}{\eta^{1/4} \times L_y}$$

Alternatively, the intercept can be retained explicitly as an additive term, so $b \neq 0$. In this form C captures the vertical offset directly, which means it is no longer a scaling factor, but an additive shift. This leads to the following form with an additive shift:

$$M_y = \eta^{1/4} \times L_x + C \quad \Rightarrow \quad M_0 = \eta^{1/4} \times L_y + C \quad \Rightarrow \quad C = M_0 - \eta^{1/4} \times L_y$$

Both formulations provide a means to resolve the vertical discrepancy observed when using only the slope $\eta^{1/4}$. Each approach is justifiable: assuming $M_y = 0$ when $L_x = 0$ supports the use of a zero-intercept model, while introducing an additive offset allows for a better fit when the data suggest a non-zero initial moment. In Figure 4.7, both adjusted lines are compared against the numerical results to assess which representation aligns more closely with the observed behaviour.

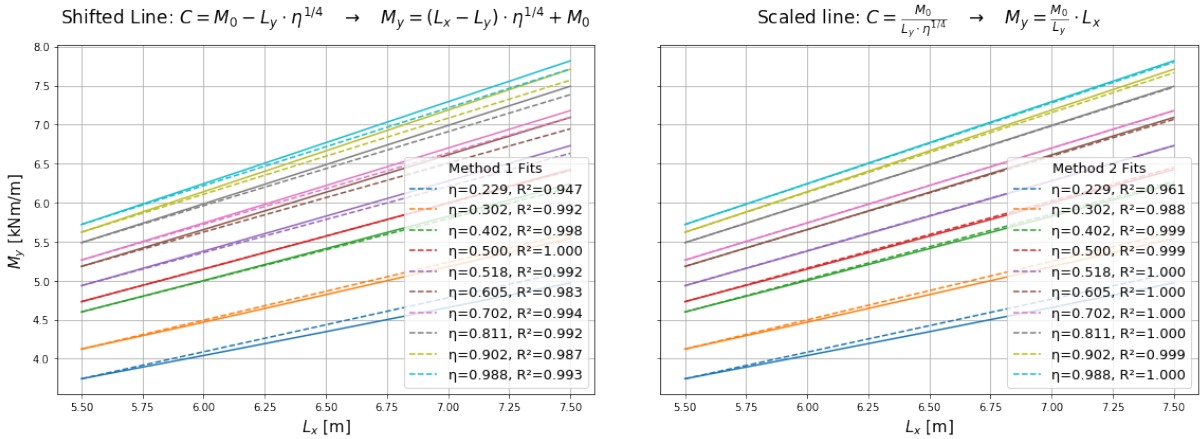

Figure 4.7: Scaled or shifted lines for different stiffness ratios η

Both estimations provide a good approximation, but the scaled line, with a mean value or $R^2 = 0.9945$ for the plotted stiffness ratios, returns a slightly better fit. Based on this performance,

the scaled parametric form is adopted as the preferred model and used to update the expression in Equation 4.9. Recall that the bending moment is normalized by the applied load $q_0 = 1$ in the numerical calculations, making a direct calculation of the scaling factor C possible.

Additionally, L_y was kept constant in the calculation and the plot. The identification of C' now follows from the fact that both these parameters were absorbed into the scaling coefficient C. To recover the general form, these constants must be divided out:

$$\frac{M_y}{q_0} = C \times \eta^{1/4} \times L_x \quad \Rightarrow \quad \frac{M_y}{q_0} = \left(C \times \frac{1}{L_y}\right) \times \eta^{1/4} \times L_x L_y \quad \Rightarrow \quad C' = \frac{C}{L_y} = \frac{M_0}{L_y^2 \times \eta^{1/4}}$$

Inserting this result into the original formulation leads to the final form:

$$\frac{M_y}{q_0} = L_x L_y \times \eta^{1/4} \times \left(\frac{M_0}{L_y^2 \times \eta^{1/4}}\right) \quad \Rightarrow \quad M_y = q_0 \times \frac{L_x}{L_y} \times M_0$$

This compact formulation expresses the maximum bending moment as a product of the applied load q_0, the span ratio L_x/L_y and the calibrated reference moment M_0, defined from the square panel case $L_x = L_y$.

4.4.4 Influence of Bending Stiffness Ratio

To investigate the influence of the anisotropic stiffness ratio $\eta = \frac{EI_y}{EI_x}$ on the bending moment response of point-supported plates, two numerical experiments were performed. The results are summarized in Figure 4.8.

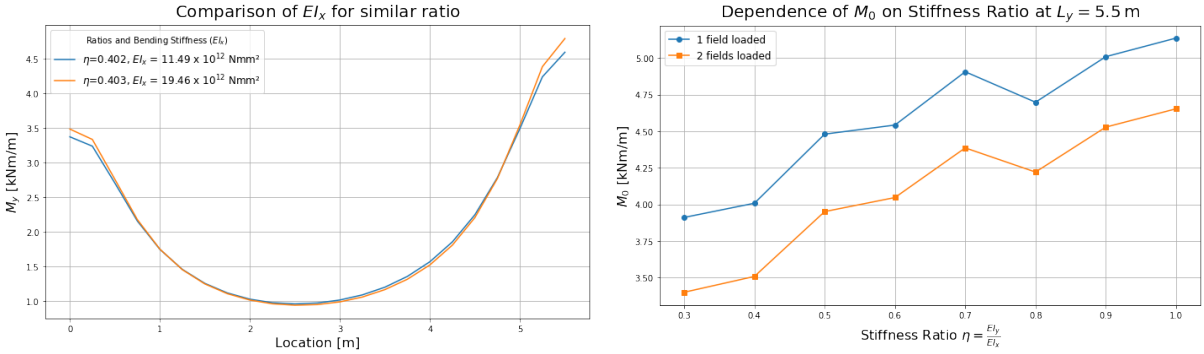

(a) Bending moments at fixed η, varying EI_x, EI_y

(b) Relation between η and M_0 for $L_y = 5.5m$

Figure 4.8: Numerical evaluation of the influence of stiffness ratio η on bending moment response

In Figure 4.8a, plates with significantly different absolute bending stiffnesses (EI_x, EI_y) but nearly identical stiffness ratios η are compared. The resulting bending moment distributions show very close agreement, indicating that it is the relative stiffness, rather than the absolute stiffness values, that primarily governs the moment response. This observation supports the simplification of the moment formulation by focusing on the stiffness ratio η rather than treating EI_x and EI_y separately.

Figure 4.8b presents the relationship between the stiffness ratio η and the maximum bending moment M_y along the line hinge, for plates with fixed $L_y = 5.5\,\text{m}$. The data show a general trend with increasing or decreasing η, but also reveal that the relationship is not smooth or easily predictable. Simple expressions such as $\eta^{1/4}$, which are commonly used in classical plate theory, fail to capture the full variability seen in the numerical results. This suggests that the interplay between geometry and anisotropic stiffness—reflected through the complex β-factors in analytical solutions—is more nuanced than a fixed exponent model can accommodate.

To account for this complexity, the moment formulation is recast using a numerically calibrated

factor C_η, which effectively captures the combined influence of geometry and stiffness. Rather than splitting the expression into multiple coefficients (e.g., C_2 for geometry and C_3 for stiffness), a more compact form is proposed:

$$M_y(b_{plate} = 3.5) = \frac{L_x}{L_y} \cdot q_0 \cdot C_\eta \tag{4.10}$$

Here, C_η is obtained directly from simulations for each configuration and is equivalent to the previously defined reference moment M_0, which corresponds to the maximum bending moment at $y = 3.5\,\text{m}$ in a plate with square dimensions ($L_x = L_y$) and a specific stiffness ratio η. This formulation provides a practical and flexible approximation of the moment response while maintaining fidelity to the underlying mechanics.

4.5 Rotational Stiffness

In the early design stages, the rotational stiffness of floor hinges is often uncertain, as connection details have not yet been finalized. The previously derived bending moment estimation assumes infinitely stiff rotational continuity, representing a fully continuous plate. However, real connections exhibit finite rotational stiffness, which reduces the actual bending moment transferred to the hinge. This reduction becomes more pronounced for flexible connections and diminishes as stiffness increases. The proposed connection in Chapter 3 has relatively low stiffness, which significantly reduces the bending moment transferred to the hinge. This sensitivity can be beneficial, as it leads to lower internal forces and potentially allows for smaller or more economical connection detailing. To avoid unnecessary over-dimensioning of both the connection and the floor system, it is therefore important to account for the rotational stiffness when estimating bending moments.

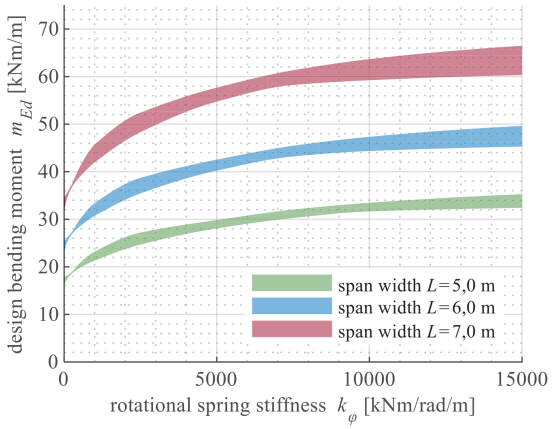

Figure 4.9: Influence of rotational spring stiffness on bending moment [55]

In structural systems where plates are supported by point supports and connected through rotationally flexible line hinges, the stiffness of these hinges plays a critical role in the resulting bending moment distribution. Stieb et al.[55] demonstrated a non-linear relationship between stiffness and moment, ranging from pinned to rigid behaviour (Figure 4.9). This trend has also been observed and confirmed through numerical modelling in this study. While Stieb et al. [55] concluded that increasing stiffness above $5000\frac{kNm}{rad}$ has limited effect, the range between 1000 and $5000\frac{kNm}{rad}$ remains relevant here.

To investigate the effect of rotational stiffness, a series of numerical simulations were conducted with varying spring stiffness values. Unlike the model presented in Chapter 3, the rotational spring used here is linear, responding equally to both positive and negative bending moments. The most relevant comparisons can be made based on the normalized bending moment, expressed as a percentage of the moment at infinite stiffness. Figure 4.10 illustrates the influence of this spring in a continuous floor system spanning two fields, composed of two modules. Load cases LC2 and LC3 correspond to loading in one field and both fields, respectively. The influence of rotational stiffness shows a consistent trend with the findings of Stieb et al. [55]. The influence of the stiffness depends a little on the stiffness ratio of the plate itself, but this effect is limited.

To ensure that a single reduction factor can be applied in the estimation of bending moments, it is important to assess whether the span in the x-direction (L_x) significantly influences the development of the normalized bending moment. This is evaluated by fixing $L_y = 5.5m$ and

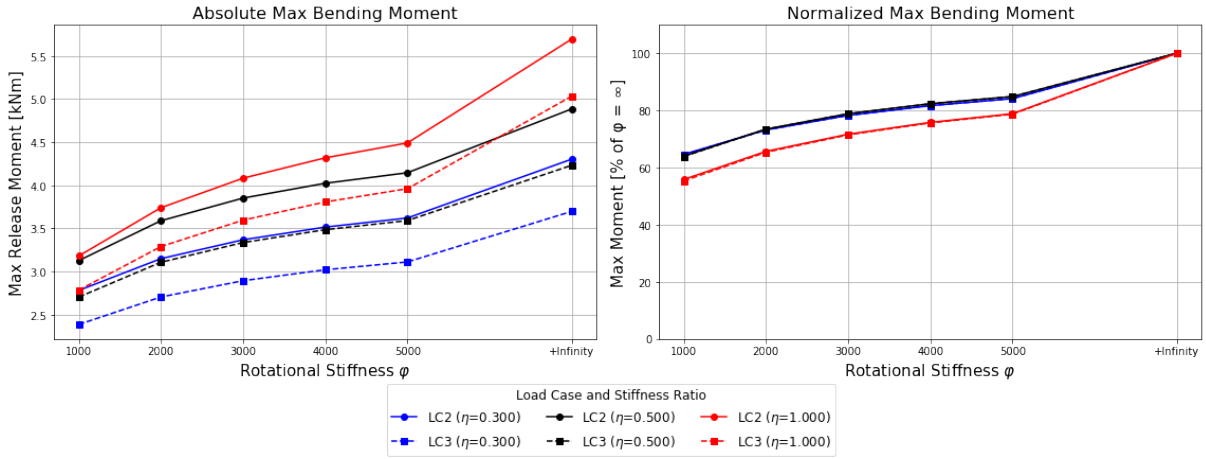

Figure 4.10: Effect of rotational stiffness φ on bending moment ($L_x = L_y = 5.5m$, 2 Modules)

comparing three different spans in the x-direction. The results, shown in Figure 4.11, indicate that the normalized bending moment evolves similarly for all three cases, regardless of the L_x value. This suggests that the effect of span length in the x-direction is minimal. Consequently, the use of a single reduction factor in the moment estimation is justified. Since the estimation formula already accounts for the span ratio and uses M_0 (the maximum bending moment for $L_x = L_y$), this result supports applying a unified reduction factor without requiring additional adjustment for the L_x/L_y ratio.

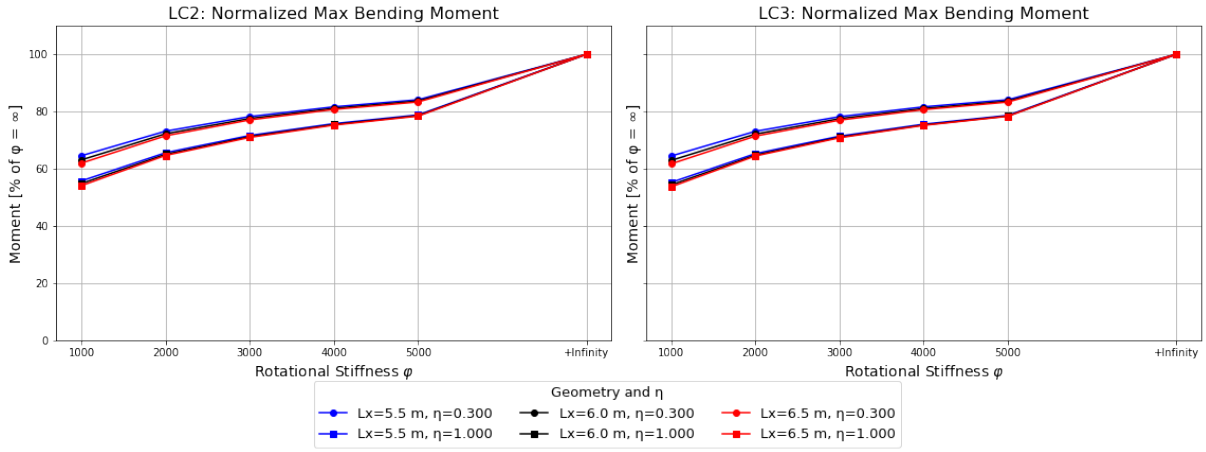

Figure 4.11: Comparison of Normalized Bending Moments vs. φ for three span lengths ($L_y = 5.5m$, 2 Modules)

Due to the assumptions stated in Section 4.3.1, the location of the line hinge can vary. Figure 4.12 presents the normalized bending moments for three different spans. The trend for the case with $L_x = L_y = 5.0m$ (left plot) differs notably from the other two cases. This deviation results from the design assumption that for $L_y \leq 5.25m$, only one hinge is placed per span, whereas for longer spans ($L_y > 5.25m$), two hinges are used. This change in hinge count influences both moment distribution and system stiffness.

In the single-hinge configuration, the $3.5m$ plates connect directly to a continuous central panel. When both spans are loaded simultaneously (LC3), bending moments from either side interact at the middle support. The hinges on both sides become critical, and the system's rotational behaviour becomes highly sensitive to the stiffness φ, which governs how much moment can be transferred into the central plate. In contrast, under LC2 (one field loaded), the moment demand and interaction at the central support are lower. As a result, only one side of the system engages significantly in moment transfer, which reduces the influence of hinge flexibility on the overall behaviour.

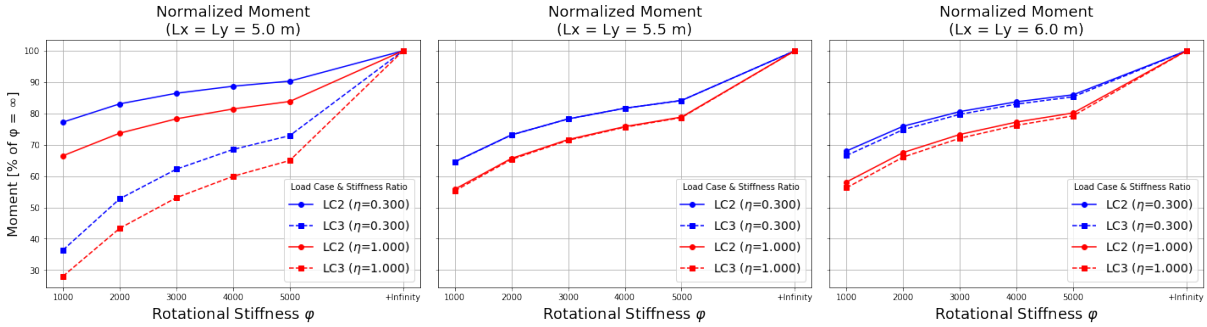

Figure 4.12: Comparison of Normalized Bending Moments vs. φ for three span lengths ($L_x = L_y$, 2 Modules)

The final variable of interest is the number of modules in the floor system. To assess its influence, the normalized bending moments are evaluated for both $L_y = 5.5m$ and $L_y = 5.0m$, considering cases with one and two modules. The previously derived C_η-values already indicate only minor differences in bending moments between these configurations. This observation is confirmed in Figure 4.13, where the results for the lowest and highest stiffness values show minimal variation between the one- and two-module cases. Based on this, it can be concluded that a similar reduction factor may be applied for systems with either one or two modules without significant loss of accuracy.

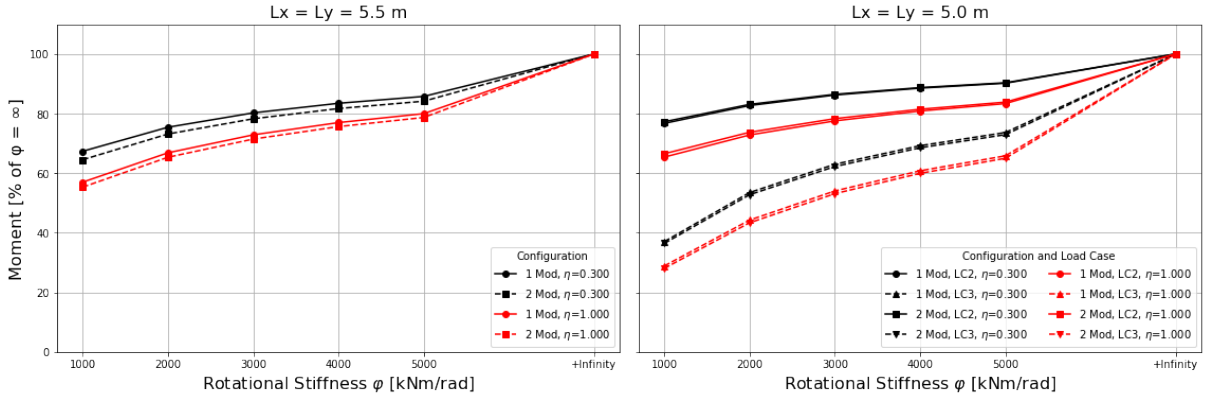

Figure 4.13: Comparison of Normalized Bending Moments vs. φ for 1 and 2 modules

In the early stages of structural design, the rotational stiffness of the panel-to-panel connections is not yet defined, as it is determined through more detailed engineering of the connection in later phases. At this point, assuming fully rigid hinges (i.e., very high φ) provides conservative bending moment estimates that respect safety margins and help prevent unsafe or under dimensioned design outcomes.

However, bending moments are sensitive to the actual rotational stiffness, and this relationship is inherently non-linear. The system's response further depends on hinge layout and the applied load cases. To account for this in early design while maintaining a degree of realism, the following stiffness-based reduction factors are recommended. These factors express the estimated maximum bending moment as a percentage of the fully rigid case:

- $L_y > 5.25m$ $\varphi_{red} = 0.85$
- $L_y \leq 5.25m$ and LC2 $\varphi_{red} = 0.90$
- $L_y \leq 5.25m$ and LC3 $\varphi_{red} = 0.73$

These values are based on an assumed rotational stiffness of $5000 \frac{kNm}{rad}$, which represents an overestimation of the actual stiffness expected from the proposed connection. This intentional overestimation is considered justified for early design, as it supports conservative moment

predictions. Where needed, the reduction factors may be adjusted downward based on lower stiffness values, following the trend illustrated in Figure 4.13.

As connection details are developed and the stiffness is quantified through engineering analysis or testing, these assumptions should be revisited and refined to reflect the actual behaviour of the system.

4.6 Estimation Formula

Equation 4.11 estimates the bending moment at a specific location in a rectangular plate supported at its corners, as illustrated in Figure 4.3a. It is valid for plate geometries and stiffness configurations within the limits of the estimation function:

$$M_y(b_{plate} = 3.5m) = \varphi_{red} \times \frac{L_x}{L_y} \times Q_d \times C_\eta \tag{4.11}$$

where:

M_y	Estimated bending moment in line hinge for $b_{plate} = 3.5m$ $[kNm]$
φ_{red}	reduction factor accounting for finite rotational stiffness
Q_d	design load intensity [kN/m^2]
C_η	coefficient based on span ratio and orthotropy, see Appendix E
EI_x, EI_y	flexural stiffness in x and y directions [kNm^2], with $EI_x \geq EI_y$
L_x, L_y	plate spans [m], with $L_x \geq L_y$

The values of C_η are provided in Appendix E, based on a parametric study. Each entry corresponds to a specific combination of:

- Minor span length L_y
- Orthotropic ratio $\eta = EI_y/EI_x$
- Load configuration (single-field or two-field)

The values of C_η represent the maximum bending moment M_0 in the line hinge for a square plate ($L_x = L_y$), evaluated for a standard plate width $b_{plate} = 3.5m$. The tables in Appendix E are based on this fixed panel width of $3.5m$ and a predefined, structured hinge layout (see Sec. 4.3.1) to ensure clear and consistent trends. While the estimation method remains valid for different plate widths or hinge positions, new C_η values must be generated accordingly, always using square configurations and evaluating the maximum moment at the relevant hinge location. This allows the method to adapt to varied layouts while maintaining its simplicity and consistency.

Interpolation between tabulated values may be used to obtain C_η for intermediate cases. The surrounding values $C_{11}, C_{12}, C_{21}, C_{22}$ are defined as shown in Table 4.1, based on nearby span and stiffness ratio:

Table 4.1: Interpolation values at surrounding grid points

	η_{n-1}	η_{n+1}
$L_{y;n-1}$	C_{11}	C_{12}
$L_{y;n+1}$	C_{21}	C_{22}

The following methods can be used to extract C_η:

- Conservative estimate: Select the highest of the four values (typically C_{22}).
- Linear interpolation in L_y:

$$C_\eta(L_y, \eta) = C_{12} + \frac{L_y - L_{y;n-1}}{L_{y;n+1} - L_{y;n-1}}(C_{22} - C_{12})$$

- Bilinear interpolation in L_y and η:

$$C_\eta(L_y, \eta) = BI_{11}C_{11} + BI_{21}C_{21} + BI_{12}C_{12} + BI_{22}C_{22}$$

with weights:

$$BI_{11} = \frac{(L_{y;n+1} - L_y)(\eta_{n+1} - \eta)}{(L_{y;n+1} - L_{y;n-1})(\eta_{n+1} - \eta_{n-1})}$$
$$BI_{21} = \frac{(L_y - L_{y;n-1})(\eta_{n+1} - \eta)}{(L_{y;n+1} - L_{y;n-1})(\eta_{n+1} - \eta_{n-1})}$$
$$BI_{12} = \frac{(L_{y;n+1} - L_y)(\eta - \eta_{n-1})}{(L_{y;n+1} - L_{y;n-1})(\eta_{n+1} - \eta_{n-1})}$$
$$BI_{22} = \frac{(L_y - L_{y;n-1})(\eta - \eta_{n-1})}{(L_{y;n+1} - L_{y;n-1})(\eta_{n+1} - \eta_{n-1})}$$

Once C_η is determined, the estimated moment can be computed using Equation 4.11. In Chapter 6 this bending moment formula is applied on a real time case-study to show its use in practice.

4.7 Comparison Between Point and Line Supports

To assess the applicability of the bending moment estimation method under different support conditions, a comparison is made between point supports and line supports with finite rotational stiffness. Figure 4.14 shows a plate subjected to an arbitrary distributed load, analysed in RFEM. The top row of the figure presents the moment component m_y, while the bottom row shows m_x. In all plates, a line hinge with a stiffness of 4000$\frac{kNm}{rad}$ is used to include the effect of such a hinge.

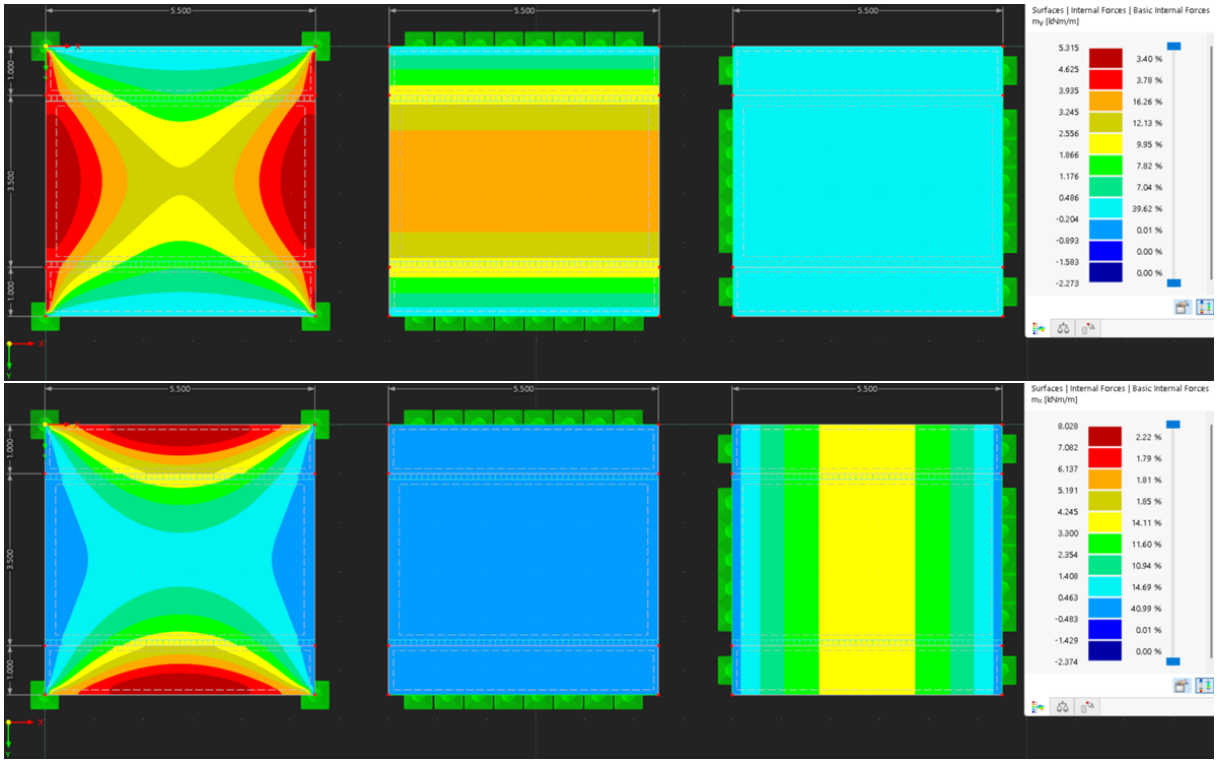

Figure 4.14: Top: Moment component m_y. Bottom: Moment component m_x. Left to right: point supports, line support on left/right edges, line support on top/bottom edges.

From left to right, the support conditions vary: the first column shows a plate supported by discrete point supports; the second features continuous line hinges along the left and right edges of the plate; and the third applies line hinges along the top and bottom edges.

The comparison illustrates that line supports significantly influence the distribution of internal forces in the plate. In the m_y component, where the line hinge is aligned parallel to the x-axis, the hinge reduces moment concentrations along the supported edges. This results in a more even spread of bending moments across the plate, compared to the point-supported case which shows high moment concentrations near the corners.

In the m_x component, the effect of the hinge is less pronounced, which is expected due to the hinge being parallel to the x-axis and thus not directly affecting bending in that direction. However, even here, a more uniform moment distribution is observed with line supports, indicating an overall improved structural response.

This demonstrates that line supports help to minimize peak bending effects by redistributing internal forces, making the system more efficient. Consequently, bending moment estimates developed for point-supported configurations can be conservatively extended to line-supported plates due to their more favourable force distribution.

4.8 Conclusion

This chapter has presented a simplified method to estimate bending moments in line hinges of floor systems, emphasizing the crucial role of rotational stiffness. Early design stages often lack precise connection details, making it necessary to account for finite rotational stiffness effects to avoid overly conservative or unsafe assumptions. The study demonstrated that the actual bending moment transferred to line hinges can be significantly lower than that predicted assuming rigid continuity, especially for connections with moderate to low stiffness.

The proposed estimation formula, developed through parametric studies and interpolation of C_η coefficients, offers a practical and efficient tool for structural engineers to approximate bending moments in line hinges. This approach accounts for key factors such as plate geometry, orthotropic stiffness ratios and rotational stiffness effects. The analysis demonstrated that variations in span length along the x-direction and the number of modules in the floor system have minimal impact on the normalized bending moments, thereby supporting the use of a unified reduction factor applicable across a variety of configurations.

By conducting numerical simulations and comparing results with existing literature [55], the chapter established that a stiffness-based reduction factor effectively captures the non-linear influence of rotational flexibility on bending moments. Although this reduction factor depends on parameters including span length, load case and hinge configuration, it shows limited sensitivity to span ratio and module count. This characteristic enables the practical application of a unified reduction factor, simplifying design calculations without sacrificing accuracy.

Consequently, a practical estimation formula was formulated, integrating design load, span geometry, stiffness ratio and the reduction factor derived from rotational stiffness considerations. Supported by extensive parametric studies, this formula facilitates rapid and reliable bending moment assessments at line hinges, thereby enhancing the efficiency of early-stage structural design. Furthermore, the comparison between point and line supports confirmed that line supports tend to yield more favourable moment distributions, reinforcing the conservative applicability of the formula across different support conditions.

However, several important limitations should be recognized when applying the formula. For span lengths L_y near $5.25m$, the behaviour of the system changes notably due to a significant shift in the hinge location. This shift causes the bending moment response to differ significantly between configurations with $L_y \leq 5.25m$ and those with $L_y > 5.25m$. As a result, interpolation of C_η-values across this threshold is not recommended, since the system's response does not vary smoothly. Instead, it is advisable to use C_η-values corresponding to the closest available span length on either side of this boundary. Although this may introduce some approximation error,

the approach remains sufficiently reliable for preliminary design and early-stage assessments. Furthermore, the formula is calibrated for single-span systems in both directions and continuous spans with up to two fields in the y-direction. For floor systems with more than two spans, bending moments in the y-direction tend to decrease and therefore, the formula may provide conservative estimates for these more extended configurations. More detailed connection design in such cases should rely on updated numerical models to capture the nuanced behaviour more accurately. Finally, the assumption of symmetric linear spring behaviour for the rotational stiffness simplifies the real connection response. As connection design advances and more precise stiffness values become available, the reduction factors and moment estimates should be revisited to maintain accuracy.

In summary, the developed estimation approach balances simplicity and engineering realism, enabling safe and efficient early-stage design of point-supported floor systems with rotationally flexible line hinges. As connection details are refined, further analysis should be conducted to update bending moment predictions accordingly, ensuring that structural designs remain both safe and cost-effective throughout the project.

Chapter 5: Vibration Design Graphs

5.1 Introduction

This chapter presents a design tool aimed at estimating the vibrational performance of point-supported CLT floor panels in the early phases of structural design. Ensuring occupant comfort requires a basic understanding of dynamic behaviour even before detailed modelling is carried out.

The goal is to develop a set of design graphs based on numerical simulations in RFEM 6. These graphs enable designers to quickly assess whether floor configurations with different spans and boundary conditions are likely to satisfy comfort criteria, based on their dynamic response characteristics.

5.2 Relevant Literature

As mentioned in the literature study, vibrational behaviour of CLT floors has been investigated, but almost exclusively line supported panels where investigated. However, some testing has been done on point-supported CLT panels and their behaviour, these relevant tests will be introduced.

Popovski et al. [50] performed an experimental investigation focusing on the dynamic performance of an innovative point-supported CLT floor system specifically developed for an 18-storey wood-hybrid student residence building at the University of British Columbia. The CLT panels were designed to span two or three bays, with lengths of 8m and 12m respectively. The panels were supported by glulam columns arranged on a $2.85m \times 4.0m$ grid. Vibration testing showed that the fundamental natural frequency of the floors was approximately 17Hz, decreasing by 7.1% to 15.8Hz when service openings were introduced. Notably, the variation in material properties across different CLT manufacturers had a negligible effect on the vibrational characteristics, indicating that geometric and structural configuration, in particular the presence of openings, had a greater influence on dynamic performance than material source. [50]

After the development of panel-to-column connections that allowed for larger grid sizes, Kawrza et al. [37] performed an experimental and numerical analysis on a $5.0m \times 5.0m$ grid size. The test specimen consisted of a $16.0m \times 11.0m$ point-supported CLT slab composed of seven interconnected panels with a total thickness of 200mm. The system was supported on twelve columns arranged in the mentioned grid, with inner supports reinforced by star-shaped steel connectors and panel joints connected via epoxy-embedded steel plates. A detailed experimental modal analysis was carried out using a shaker excitation and measurements at 651 uniformly distributed points. Over a two-day measurement campaign, seven vibrational modes were identified, including natural frequencies, damping ratios and mode shapes. The measured fundamental frequency of 10.51Hz demonstrated compliance with the serviceability criteria of Eurocode 5 [21], showing the suitability of such configurations for wide-span timber structures. The initially observed mode shapes were complex due to environmental influences during testing, but these effects were corrected through post-processing. A finite element model of the CLT slab was created and calibrated using the measured modal properties. The study showed that both material properties and boundary conditions need to be included for accurate prediction of dynamic behaviour. It also highlighted that poor parameter choices can strongly affect the agreement between numerical and experimental results, especially at low frequencies. The validated model was then used for parametric studies, which showed how changes in support conditions, spans, and layer configurations influence the dynamic properties of CLT slabs, supporting their suitability for large-scale use. [37]

The point-supported floor system is made possible by reliable panel-to-column connections, as demonstrated by [48, 41]. Another crucial aspect of this system is the panel-to-panel connection. In this regard, Stieb et al. [55] explored various types of connections and examined how their

stiffness influences the fundamental frequency.

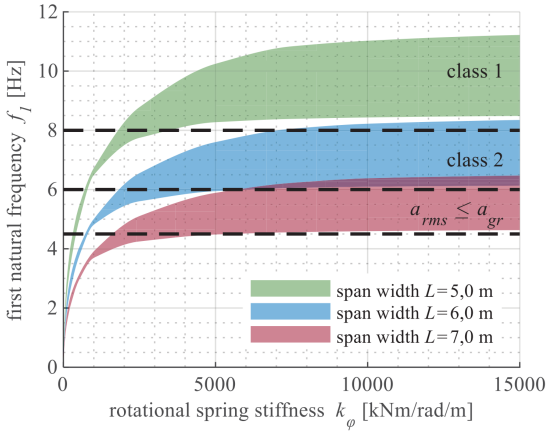

Figure 5.1: Influence of rotational spring stiffness on first natural frequency [55]

Figure 5.1 demonstrates that the rotational stiffness of panel-to-panel connections in point-supported CLT slabs significantly affects both the first natural frequency and the bending moments. However, the benefit of increased stiffness diminishes beyond a certain point. Stieb et al. [55] identified a threshold of approximately $5000 \frac{kNm}{rad \times m}$, above which further stiffening results in minimal improvement. This finding indicates that while a certain degree of rotational stiffness is essential to ensure adequate vibration performance, fully rigid connections are not necessary for effective design. [55]

Felicita et al. [25] compared the current vibration assessment approach for lightweight timber floors, based on the HIVOSS method, as is commonly used in the Netherlands, with the new methods proposed in the draft Eurocode 5 [23]. While the HIVOSS method evaluates comfort based on a statistical distribution of user mass and walking frequency using the $OS - RMS_{90}$ value, the draft Eurocode introduces two approaches: a simplified method and an advanced method. The simplified method (see Sec. 2.5.3) uses analytical estimates based on a single dominant vibration mode and checks floor performance against thresholds for frequency, stiffness, velocity and, where resonance is likely, acceleration. However, this method often classifies floors as non-compliant that would otherwise be acceptable under the HIVOSS approach, particularly due to stricter frequency and stiffness requirements. In contrast, the advanced method, described in Annex G, employs numerical simulations to assess the response across multiple vibration modes. It calculates how much the floor moves, in terms of speed and acceleration, when someone walks on it, by simulating the effect of different walking rhythms and step patterns. This method showed stronger agreement with HIVOSS classifications, but differences in how acceleration and modal mass are treated still affect outcomes. Felicita et al. [25] highlight the need for improved guidance, especially for modal mass estimation in two-way supported floors, and note that the shift to prEC5 could have a notable impact on floor design unless calibrated carefully against existing methods. [25]

5.3 Methodology

For the numerical study presented here, the HIVOSS method is selected due to its established use in Dutch practice, its proven practical reliability and its alignment with the highest comfort performance class, as confirmed by Abeysekera et al. [1]. Furthermore, its strong correspondence with the advanced Eurocode method, as noted by Felicita et al. [25], supports its continued relevance in design applications. While the method is explained in detail below, its basic principles have already been introduced in Section 2.5.4. For clarity, the main steps are briefly summarised here:

- Determine dynamic floor properties: Natural Frequency, Modal Mass, Damping
- Read $OS - RMS_{90}$-value in graph, see Appendix F
- Determine and check floor class, see table 2.9

5.3.1 Parametric Model Creation

To determine the dynamic properties of the floor system, the model incorporates the same assumptions outlined in Section 4.3.1. The earlier developed Grasshopper model (Sec. 4.3.2) is

rewritten to a new format that enables the creation of multiple plate configurations for a modal analysis. This setup enables rapid testing of multiple design scenarios.

The model takes five input variables: L_x, L_y, φ, plate width and the number of modules. Here, L_x and L_y represent the spans of the floor panel in the major and minor directions, respectively, while φ denotes the rotational stiffness of the line hinge. For this analysis, the plate width ($3.5m$) and number of modules (2) are held constant, their influence is examined separately in the parametric study. For the calculation, the following load combination is assumed:

$$Q_{vibration} = Q_{sw} + Q_g + 0.1 \times Q_q \text{ with } Q_g = 2.0\frac{kN}{m^2} \text{ and } Q_q = 3.0\frac{kN}{m^2}$$

The Dlubal RFEM 6 plug-in is used to transfer the parametric geometry from Grasshopper directly into RFEM. Here, the model is automatically constructed and divided in finite element plate elements with a mesh of $0.1m \times 0.1m$ (see App. B), based on the Grasshopper-defined input variables. RFEM performs a modal analysis for each floor configuration, as defined in the Grasshopper model. Frequencies and modal masses of the first ten modes are computed and exported automatically to an Excel file, forming the foundation for vibrational evaluation. This concludes the first step in the HIVOSS method.

5.3.2 Data Processing

After running the Grasshopper model, the natural frequencies and corresponding modal masses for the first ten vibration modes are obtained for each floor configuration.

The first step is to check whether the fundamental frequency exceeds the minimum threshold of $4.5Hz$, as required by the simplified method in the draft Eurocode 5 [23]. The alternative method in Annex G, as well as the HIVOSS method, do not explicitly require this frequency limit. However, considering that the calculation includes permanent loads (in addition to self-weight) and some variable loading, a fundamental frequency of $4.5Hz$ remains a reasonable threshold, particularly since it is close to the typical running frequency.

For floors that meet this threshold, a damping ratio of 4% is assumed, which corresponds with the values presented in the graph in Appendix F. This graph is a contour plot that shows the relationship between two variables: modal mass (on the x-axis) and eigenfrequency (on the y-axis) of the floor. The contours represent different ranges of $OS - RMS_{90}$ values, which are colour-coded based on different comfort classes (see Tab. 2.9) to visualize the interaction between these two parameters. However, due to the contours being closely spaced, it becomes difficult to read the values accurately, especially for a large number of configurations with varying L_x and φ values.

To simplify this process, a parametrized Excel sheet, provided by Lüning, was utilized. This sheet is designed to return the $OS - RMS_{90}$ value for each combination of natural frequency and modal mass. To automate the calculation across all configurations, macros in Excel were employed. Macros are automated sequences of actions programmed using Visual Basic for Applications (VBA), allowing for the efficient execution of repetitive tasks. By using VBA, the sheet processes each combination of frequencies and modal masses, performing the $OS - RMS_{90}$ calculation without the need for manual intervention.

Considering the fact that all floor types are characterized by multiple modes, the total floor response needs to be calculated based on the combined action of these modes. This final value reflects the combined dynamic effect of all significant vibration modes. A single response value per

plate configuration is obtained using a quadratic summation of the individual modal responses:

$$OS - RMS_{90;floor} = \sqrt{\sum_{i=1}^{10} \text{OS-RMS}_{90;i}^2}$$

This approach greatly enhances the speed and automatisation of the calculations, allowing for a large number of floor configurations to be evaluated for their vibrational performance with minimal effort. This concludes the second step of the HIVOSS method.

5.3.3 Acceptance Criteria

According to the HIVOSS method, configurations with an $OS - RMS_{90}$ value between 0.8 and 3.2 are classified as acceptable in terms of vibrational comfort. Values below 0.8 indicate very high performance, while values above 3.2 exceed comfort limits and should be avoided in design. The upper threshold of 3.2 corresponds to comfort class D, which is typically acceptable for standard occupancies such as office and residential buildings. However, more sensitive building types—such as educational institutions, libraries or laboratories, require significantly higher performance. These are associated with stricter comfort classes (e.g. class C or lower), which require lower threshold values to ensure greater vibration control.

This threshold range serves as the primary criterion for evaluating the dynamic suitability of a floor configuration. All $OS - RMS_{90}$-values, determined by unique combinations of span dimensions (L_x, L_y) and rotational stiffness (φ), are verified against these limits. Based on the resulting value, each configuration is classified as either acceptable or not. This binary classification (acceptable or not) is crucial for constructing design graphs that allow for rapid assessment of floor performance during the early stages of architectural and structural design. This evaluation forms the third and final step in applying the HIVOSS method.

5.3.4 Design Graph Construction

To visualize and assess the performance of various floor designs, design graphs are developed based on the calculated $OS - RMS_{90}$ values for different floor configurations, each defined by a combination of span length L_x and rotational stiffness φ. Due to the computational intensity of full simulations, only a limited number of configurations are directly analysed, and the remaining values are estimated using a conditional value forwarding method.

In this method, when a calculated $OS - RMS_{90}$ value at a given φ is below the threshold of 3.2, it is assumed that configurations with larger φ (i.e. higher rotational stiffness) will perform equally well or better. The value is therefore propagated rightward along the φ-axis. Conversely, when a value at a given φ is equal to or exceeds the threshold, it is assumed that configurations with smaller φ (i.e. lower stiffness) will perform similarly poorly or worse. Conversely, if the value is equal to or exceeds the threshold, it is assumed that performance will deteriorate at smaller φ values, so the value is back-filled leftward. Thus, the value is back-filled leftward toward lower φ. In the vertical direction (along increasing span length L), if a value at a certain span exceeds the threshold, the same value is filled downward to larger L values. This reflects the assumption that if a floor fails the comfort limit at a short span, it is expected to also fail at longer spans, due to increased flexibility. This directional filling method allows for conservative extrapolation of performance across the design space, enabling quick classification of floor configurations without recalculating every case.

The process begins with simulations at low stiffness values to establish the minimum requirements for acceptable vibrational comfort. Once a configuration meets the threshold, neighbouring values are filled using the directional method described earlier. Although span length L_x does not always exhibit a linear relationship with comfort performance, $OS\text{-}RMS_{90}$ values typically

remain within a similar range across adjacent spans. However, due to the complex interplay between geometry, stiffness and modal behaviour, each span length is evaluated with at least two stiffness levels to accurately capture the boundary region where performance transitions from acceptable to unacceptable.

A representative subset of directly computed values is shown in Table 5.1, followed by the completed matrix using the conditional filling method in Table 5.2. In this table, configurations that do not meet the fundamental frequency requirement of $4.5Hz$ are assigned an arbitrary $OS\text{-}RMS_{90}$ value of 10.00, clearly marking them as dynamically unsuitable.

Table 5.1: Selected calculated $OS\text{-}RMS_{90}$ values for 9L-290 panel with $L_y = 5.0\,\text{m}$

L_x \ η	∞	5000	3700	3600	2600	2500	1600	1500	1400	1300
5.5	NaN	NaN	NaN	NaN	NaN	NaN	NaN	2.77	2.81	10,
5.8	NaN	NaN	NaN	NaN	NaN	NaN	NaN	2.73	10.00	NaN
6.1	NaN	NaN	NaN	NaN	NaN	NaN	2.68	10.00	NaN	NaN
7.7	NaN	NaN	NaN	NaN	2.62	10.00	NaN	NaN	NaN	NaN
8.3	NaN	NaN	3.00	10.00	NaN	NaN	NaN	NaN	NaN	NaN
8.4	2.99	10.00	NaN	NaN	NaN	NaN	NaN	NaN	NaN	NaN

Table 5.2: Completed table using conditional forwarding

L_x \ η	∞	5000	3700	3600	2600	2500	1600	1500	1400	1300
5.5	2.81	2.81	2.81	2.81	2.81	2.81	2.81	2.81	2.81	10.0
5.8	2.73	2.73	2.73	2.73	2.73	2.73	2.73	2.73	10.00	10.0
6.1	2.68	2.68	2.68	2.68	2.68	2.68	2.68	10.00	10.00	10.0
7.7	2.62	2.62	2.62	2.62	2.62	10.00	10.00	10.00	10.00	10.0
8.3	3.00	3.00	3.00	10.00	10.00	10.00	10.00	10.00	10.00	10.0
8.4	2.99	10.00	10.00	10.00	10.00	10.00	10.00	10.00	10.00	10.0

Using the completed table, a graph is generated in which each floor configuration is represented by a blue circle (○) if it meets the comfort criteria, or a red cross (X) if it exceeds the threshold. This visualisation, shown on the left in Figure 5.2, enables quick identification of acceptable combinations of L_x and φ. To enhance usability, a boundary line is drawn around the region of acceptable configurations. This line indicates the minimum required stiffness for each span length to satisfy the comfort requirements and serves as a practical guide for design. The right-hand side of Figure 5.2 presents this boundary clearly.

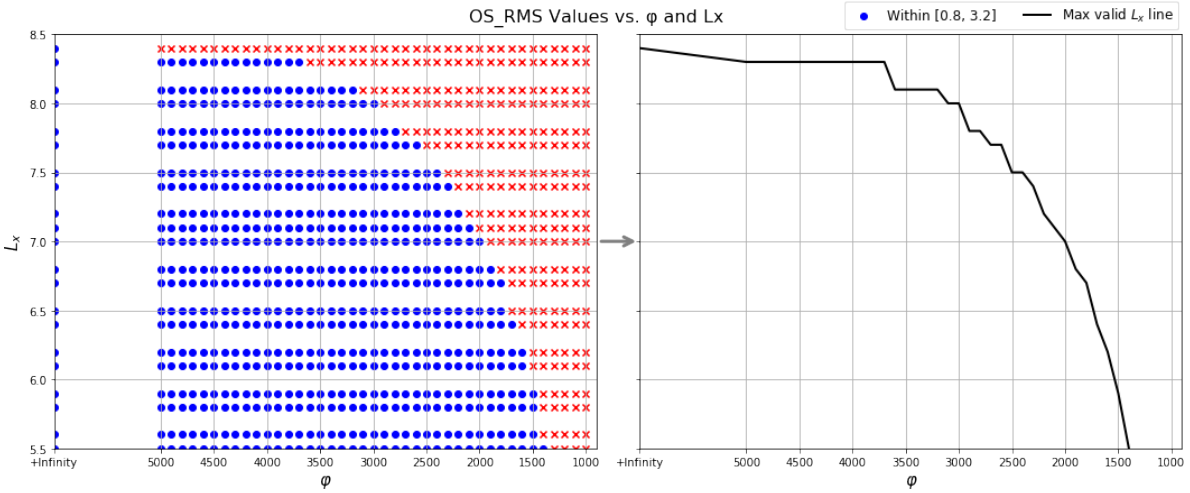

Figure 5.2: (L) Acceptable (•) and unacceptable (x) configurations (R) Design boundary line

Finally, to simplify interpretation and improve clarity for practical use, only the boundary line is retained in the final design graph. This provides a concise and effective tool for estimating the minimum required stiffness for a given span, enabling efficient decision-making during the early stages of structural design. Example boundary lines for specific lamella lay-ups and panel dimensions are included in Appendix F.1. While these figures apply to particular configurations, the underlying method is broadly applicable and can be extended to other cases.

In the upcoming parameter study, the effect of varying individual parameters will be explored. This allows engineers to assess how changes in panel properties, mass and module numbers affect vibrational performance. If a new panel closely resembles one included in the design graph, the study can guide adjustments to bring it within the acceptable comfort range. As a result, the figures serve not only as design tools for specific panels, but also as a comparative reference for adapting similar floor systems to meet vibration requirements.

5.4 Parameter study

The vibrational response of the structure is governed by the interaction between the rotational stiffness of the line hinge, the panel lay-up and the modal characteristics of the system. Modal shapes that primarily deform in a direction perpendicular to the hinge are minimally affected by its rotational stiffness. For example, of the point-supported structure shown in Figure 5.3 the first modal shape (L) forces rotation about the hinge, making it sensitive to the hinge's rotational stiffness. In contrast, the third mode (R) involves deformation that requires little to no rotation about the hinge axis and is therefore largely unaffected by the hinge's stiffness. Although predicting the full dynamic interaction is complex, isolating and evaluating individual parameters such as hinge stiffness can support targeted design improvements when vibrational performance is insufficient.

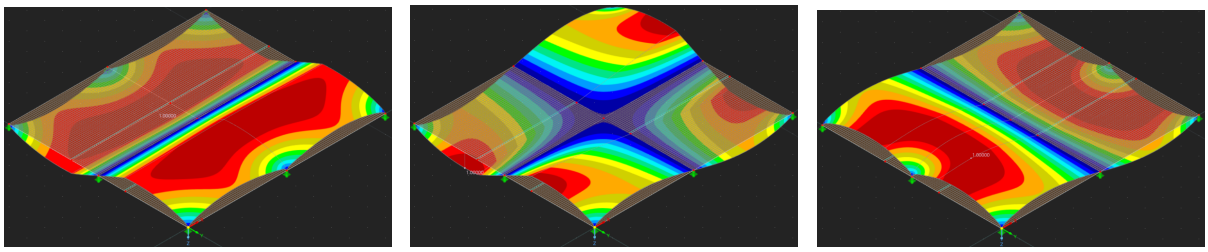

Mode 1 Mode 2 Mode 3

Figure 5.3: First three modal shapes of a point-supported floor system.

Figure 5.4 highlights the relationship between span length (L_x) and three key dynamic parameters: natural frequency (f_1), modal mass (M_1) and the $OS - RMS$ value, which indicates vibrational comfort. As L_x increases, the natural frequency steadily declines, following an approximately linear trend. At $L_x = 7.3m$ the frequency shows a change in trend.

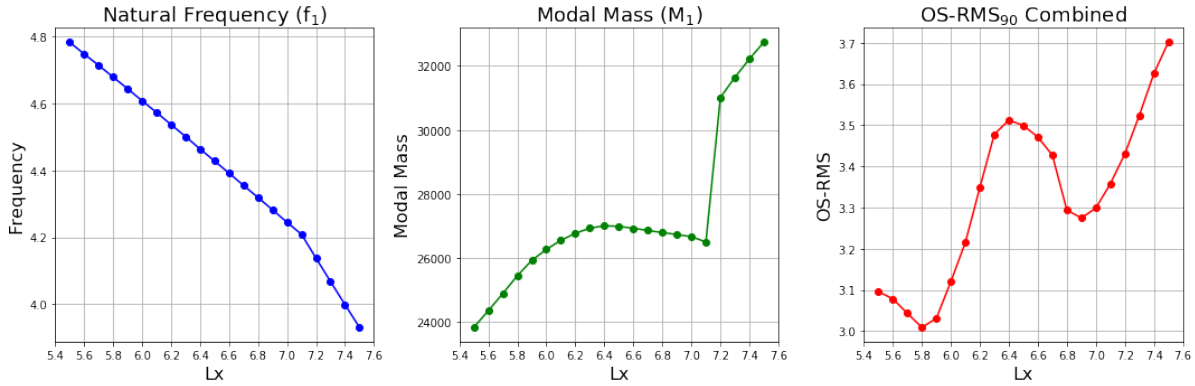

Figure 5.4: Relationship between span length (L_x) and dynamic parameters

The modal mass shows some increase until $L_x = 7.3m$, where a sharp rise occurs. This abrupt transition indicates a shift in the mode shape contributing to the first vibration mode, leading to increased dynamic response. Such a sudden change indicates a fundamental shift in the structural behaviour, which increases the vibrational effects for a certain mode.

Unlike the modal mass and fundamental frequency, the $OS - RMS$ value remains relatively stable across the span range, fluctuating between 3.0 and 3.7. However, a noticeable increase occurs as a result of decreasing frequency and increasing modal mass. Beyond $L_x = 6.0m$, the $OS - RMS$ value exceeds the critical comfort threshold of 3.2, indicating a decline in vibrational performance. These findings confirm that longer spans generally lead to reduced stiffness, greater dynamic mass, and a stronger vibrational response.

Interestingly, this behaviour also highlights why there is no clear, direct relationship between span length and whether a floor satisfies comfort requirements. Intuitively, it might be expected that if a shorter span fails to meet the comfort criteria, a longer one would perform worse. However, this is not always the case. The HIVOSS assessment method incorporates both objective measurements and subjective evaluations of vibration comfort. As a result, the corresponding graph in the HIVOSS framework is non-linear and somewhat complex, which can lead to unexpected shifts in performance classification across span lengths. This complexity underscores the importance of detailed dynamic analysis when evaluating floor designs, rather than relying on span alone as a predictor of vibrational adequacy.

5.4.1 Effect of Permanent Load on Vibration Performance

Figure 5.5 illustrates the effect of permanent load q_g on the vibration response of a floor system with fixed geometry and stiffness. Two cases are compared: one with $q_g = 1.0kN/m^2$ and another with $q_g = 2.0kN/m^2$.

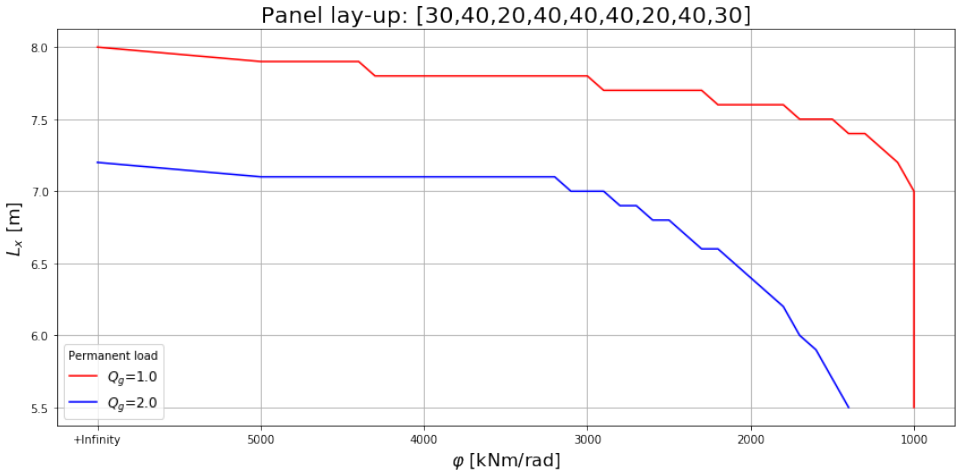

Figure 5.5: Influence of permanent load on vibrational behaviour

Although increased mass is commonly associated with lower accelerations due to greater inertia, the results show that the floor with lower permanent load achieves superior vibration performance. Specifically, longer spans L_x remain within the acceptable vibration limits for the lighter configuration. This is primarily because lower mass leads to higher natural frequencies, shifting the system response away from the resonance-prone excitation range of human walking.

This behaviour is consistent with structural dynamics theory. The natural frequency f of a system is proportional to the square root of the stiffness-to-mass ratio:

$$f = \frac{1}{2\pi}\sqrt{\frac{k}{m}} \text{ with } k \text{ the system stiffness and } m \text{ the modal mass}$$

In this study, the panel lay-up and stiffness remain constant, so reducing q_g directly lowers the

mass without affecting stiffness. This results in a clear increase in natural frequency, thereby improving the dynamic response.

However, these findings also highlight the sensitivity of the results to the underlying assumptions used in generating the design boundaries. For the specific lay-up considered in Figure 5.5, the governing vibration limit for $q_g = 2.0$ was not typically the one based on OS-RMS accelerations. Instead, the critical threshold was often reached when the fundamental frequency dropped below $4.5Hz$, meaning the floor was disqualified before exceeding acceptable RMS acceleration values.

In other lay-ups, however, the situation can differ significantly. It is entirely possible that OS-RMS becomes the governing criterion rather than frequency. In such cases, increasing the natural frequency alone may not be sufficient to achieve compliance. As the modal mass also tends to decrease with a lighter floor, the resulting acceleration response might not improve to the same extent. This underscores the importance of considering both mass and frequency effects simultaneously, particularly when evaluating different structural configurations.

5.4.2 Influence of Module Count on Vibration Properties

The floor system is composed of two spans in the y-direction, while the number of spans in the x-direction is defined by the number of modules. A single module consists of one floor field adding a second module extends the floor by an additional field in the x-direction. Figure 5.6 illustrates the influence of the number of modules on the vibration performance.

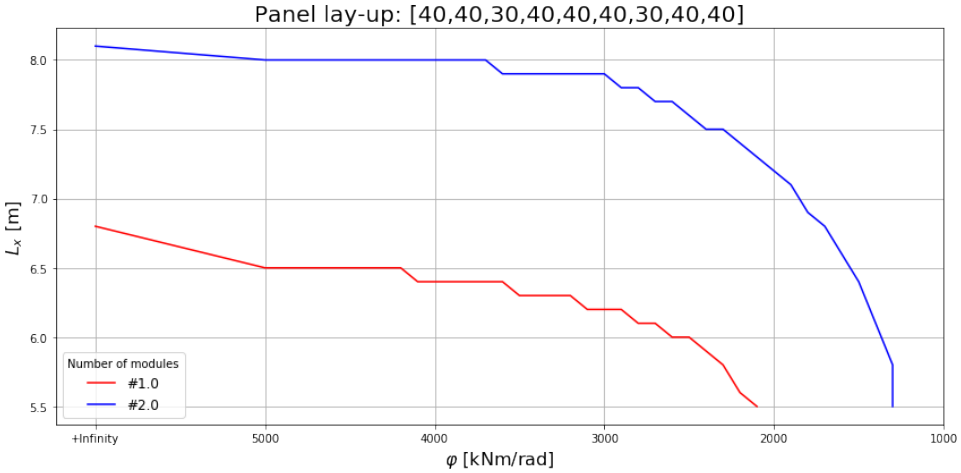

Figure 5.6: Influence of module count on vibrational behaviour

The design boundaries constructed in this thesis are based on a two-module configuration, which serves as the reference case for most analyses. As the number of modules increases, the modal mass contributing to the floor's vibration response changes. Larger configurations engage more mass across a wider area, increasing the total participating mass, which can improve vibration performance. In contrast, smaller configurations, such as a single module, concentrate the structural response in a more localized region. With less mass participating in each mode, these systems typically perform worse in terms of vibrational behaviour.

It is technically possible to meet vibration criteria using only one module; however, this becomes increasingly challenging, especially for larger spans or more flexible support conditions. The panel used in this comparison (Fig 5.6) is already quite thick ($t = 340mm$), resulting in a very high bending stiffness ($EI_x = 23.74 \times 10^{12}\ Nmm^2$). Despite this substantial stiffness, the difference in vibration performance between one and two modules is clearly evident.

Overall, the number of modules has a strong influence on how the floor behaves under vibration. While a very stiff panel can help reduce issues in smaller setups, using more modules generally provides a more reliable way to meet vibration requirements in modular timber floors.

5.4.3 Influence of Stiffness on Vibration Performance

The vibrational performance of the floor depends largely on the stiffness of the panel. In early design stages, it is helpful to estimate suitable panel dimensions. The goal of constructing these graphs is to quickly assess whether a floor is likely to meet vibration requirements. The influence of stiffness can be separated into two aspects: the actual stiffness in a certain direction and the stiffness ratio between directions.

Stiffness

First, the effect of increasing flexural stiffness EI_x on the vibration behaviour of a floor system is examined. The boundary curves in Figure 5.7 represent three different panel lay-ups, each with a constant modal mass ratio $\eta \approx 0.51$, but different values of EI_x.

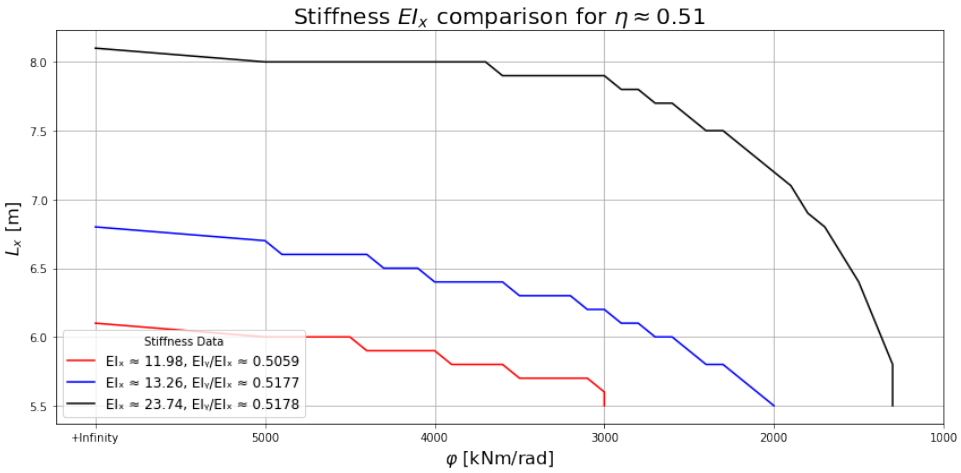

Figure 5.7: Effect of EI_x on vibration performance

As flexural stiffness EI_x increases from approximately $12 \cdot 10^{12} N/mm^2$ to $24 \cdot 10^{12} N/mm^2$, the feasible design region expands significantly. This means that longer spans L_x can still meet the vibration limits, even with lower values of rotational stiffness φ. The trend shows that higher stiffness leads to better dynamic performance by increasing natural frequencies and reducing acceleration levels, which in turn improves comfort.

It is important to note that EI_x is increased while maintaining a fixed stiffness ratio η which means that EI_y increases proportionally as well. In practice, this is usually achieved by increasing the overall panel height, which results in both higher bending stiffness and greater structural mass. As a result, the observed improvement in vibration performance cannot be attributed to increased stiffness alone, the effect of increased mass is also present. Whether this mass effect contributes positively or negatively depends on the specific floor configuration and must be considered in combination with stiffness changes.

Moreover, the shape of the performance boundaries in Figure 5.7 reveals that the influence of rotational stiffness φ becomes more critical as stiffness EI_x increases. While stiffer panels allow for longer spans under favourable hinge conditions (high φ), they also show a steeper drop in performance as φ decreases. This is evident from the sharper decline of the black curve (highest EI_x) compared to the more gradual slopes of the red and blue curves (lower EI_x). The increasing curvature indicates that high-stiffness systems are more vulnerable to variations in rotational support.

This trend aligns with expected modal behaviour. As the flexural stiffness increases, the relative influence of a line hinge becomes more significant in shaping the floor's modal deformation. In such cases, both the natural frequency and the activated modal mass are more sensitive to the boundary condition, making accurate modelling of φ essential. Although higher EI_x generally improves vibration performance, it also increases the system's sensitivity to support

flexibility—emphasising the importance of carefully considering rotational stiffness during design.

Stiffness Ratio

The influence of the stiffness ratio $\eta = \frac{EI_y}{EI_x}$ on floor vibration performance is shown in Figure 5.8. The boundary curves represent floor configurations with similar stiffness $EI_x \approx 15.7 \cdot 10^{12}\,\mathrm{Nmm}^2$, but with varying stiffness ratios. By adjusting EI_y, the stiffness ratio η is changed, which influences the shape of the modal response and overall vibration behaviour.

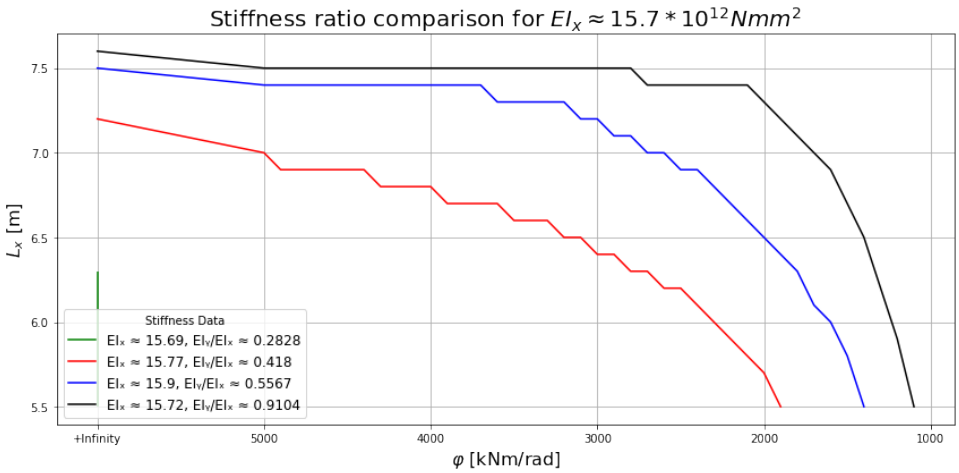

Figure 5.8: Effect of stiffness ratio η on vibration performance

The figure shows that increasing the stiffness ratio, making EI_y relatively larger, shifts the performance boundary upward, allowing for longer spans L_x at the same rotational stiffness φ. This improvement arises because a higher ratio leads to a more favourable modal shape, distributing deformation more uniformly across the plate and activating a larger modal mass. In contrast, a lower stiffness ratio results in more localized deformations, especially in the direction of weaker stiffness, which can reduce modal mass participation and lower natural frequencies.

An important detail in interpreting this result is the role of the line hinge, which is placed parallel to the x-axis and primarily transfers moments in the y-direction. Because of this, its effect is more closely related to EI_y. When EI_y is low, the influence of this hinge becomes more pronounced, leading to greater reductions in effective stiffness. This explains why lower stiffness ratios result in steeper declines in performance as φ decreases, as seen in the figure.

These findings underline the importance of balancing stiffness in both directions. While the absolute flexural stiffness EI_x remains the dominant factor, particularly as it governs the primary span direction L_x, the stiffness ratio $\eta = \frac{EI_y}{EI_x}$ still plays a significant role. It influences the shape of the vibration modes, the efficiency of modal mass participation and the floor's sensitivity to hinge flexibility. A well-chosen stiffness ratio can therefore improve dynamic performance by distributing deformation more uniformly and making the system less vulnerable to changes in boundary conditions.

5.5 Line supports

Line-supported floor systems generally perform better in terms of vibration than point-supported floors. This improvement comes from the continuous support along the edges, which increases stiffness, changes how the floor vibrates and helps spread dynamic loads more evenly.

Line-supported floors show more uniform modal shapes, meaning that vibrations are spread out over the whole plate rather than being concentrated in one area. This leads to better activation of modal mass and reduces the risk of resonance. In contrast, point-supported floors often have more localised vibration modes that are more sensitive to excitation forces and small irregularities.

Another advantage of line supports is that they make the floor less sensitive to local changes in stiffness. Because the support is continuous, local weaknesses are less noticeable in the overall behaviour. Line supports also add rotational stiffness along the edges, which helps reduce twisting and improves the floor's stability under dynamic loads.

Although the vibration design graphs developed in this study are based on point-supported floors, they can also be used for line-supported systems. Since point supports are a more conservative case, using these graphs for line-supported floors gives designs that are both safe and reliable.

In conclusion, line-supported floors offer clear benefits in vibration performance and can be confidently designed using the provided graphs. This makes them still a strong alternative for projects where vibration comfort and reliability are important.

5.6 Conclusion

In this chapter the dynamic performance of floor systems was examined by analysing the influence of connection stiffness, flexural stiffness and stiffness ratio on modal response characteristics. The connection stiffness, represented by a rotational stiffness φ in a line hinge, significantly affects vibration sensitivity. Floors with low stiffness experience notable reductions in natural frequencies and modal mass participation, leading to reduced performances. This sensitivity highlights the importance of ensuring adequate connection stiffness.

The stiffness ratio $\eta = \frac{EI_y}{EI_x}$ emerged as a second key parameter influencing modal shape and deformation distribution. Higher ratios promote more uniform modal shapes and improved modal mass activation, enabling better vibration control even with longer spans or more flexible line hinges. Conversely, lower stiffness ratios cause more deformation in the weaker direction, which increases the influence of line hinges, especially when these hinges are aligned with the stiffer axis. Based on these observations, a stiffness ratio in the range of $\eta = [0.5, 1.0]$ is recommended. See Appendix A.1 for suitable panel lay-ups sorted based on their stiffness ratio.

Additionally, it was observed that the effect of connection stiffness is not absolute, but relative to the stiffness of the floor itself. Stiffer floors are less sensitive to flexible connections, as the relative influence of the hinge decreases. This highlights that performance cannot be predicted by individual parameters. Rather, the vibration behaviour is almost always governed by the interaction between all governing parameters. This complex interplay, combined with the non-linear nature of the HIVOSS performance criterion, makes forward-filling assumptions less reliable near boundary conditions. While these assumptions hold in the overall trend, inaccuracies may arise in edge cases. As a result, some specific configurations may now be excluded as unsuitable, even though they might meet the HIVOSS requirements, these cases are very rare, but such cases are very rare. However, the goal of the developed design graphs is not to capture every acceptable case, but to provide guidance towards reliable solutions.

For the development of the design graphs, it was assumed that performance improves in a consistent way to keep the graphs clear and easy to use. The graphs were made using a mesh size of 0.1×0.1, which is practical for design but can cause small errors, as explained in Appendix B. Therefore, it is recommended not to design exactly on the boundary line, since small inaccuracies may occur.

Finally, it was demonstrated that line supports generally improve vibrational performance by reducing deformation and enhancing modal stability. As such, all design graphs constructed for point-supported systems are also valid—albeit conservatively—for floor systems with line supports. This further increases the applicability of the proposed design method.

Chapter 6: Case study

6.1 Introduction

To illustrate the practical application of the proposed panel-to-panel connection and the preliminary design rules developed in earlier chapters, this case study focuses on a real-life building project. Applying the connection design to a real structure makes it easier to evaluate the structural assumptions and the steps involved in the verification process. It also provides context for assessing the feasibility of implementing a point-supported CLT floor system in real-world construction.

In addition to demonstrating the use of the proposed connection, the case study offers a valuable opportunity to compare a conventional post-and-beam CLT floor system with a newly conceptualized point-supported alternative. By examining the same building under both support configurations, the structural implications, design challenges, and potential benefits of the new system can be assessed directly. This side-by-side comparison forms a solid basis for evaluating the practical and structural relevance of the design approach developed in this thesis.

The building used in this case study is a new office building for a shipbuilding company in the north of the Netherlands. Although construction has not yet begun, the building is scheduled to be realized in the near future. The design features a fully timber structure with a total floor area of over $2500m^2$, using CLT floors supported by beams and columns.

This chapter is structured as follows: Section 6.2 outlines the current floor system used in the building, including panel layout and support conditions. Section 6.3 introduces the conceptual adaptation to a point-supported CLT floor system using the proposed panel-to-panel connection. Section 6.4 presents a structural comparison between the existing and adapted systems. Finally, Section 6.5 discusses the feasibility and implications of implementing this concept in practice.

6.2 Existing Floor System

The existing floor system of the office building is based on a conventional post-and-beam structure with CLT floor panels spanning between beams. The building has a total width of $17.8m$ and a length of $49.0m$. The panels span in the longitudinal direction, across the $17.8m$ width of the building, covering three bays of $6.2m$, $5.4m$ and again $6.2m$. Along the building's length, the structural grid is divided into bays of $5.4m$, with the first and last bays slightly wider at $5.6m$. The CLT panels are designed as single-span elements, transferring vertical loads through bending and shear to the supporting beams. The structural drawing of the floor plan can also be seen in Appendix G.2.

The CLT floor panels are $220mm$ thick and made up of seven layers in a $40 - 20 - 40 - 20 - 40 - 20 - 40$mm layup, with alternating grain directions for structural stability. Each panel is approximately $2.5m$ wide, allowing them to be placed side by side across the $49.0m$ building length. The panels are connected using inclined screw connections, which ensure diaphragm action by providing in-plane stiffness and continuity between adjacent elements.

Support is provided by glulam beams and columns. The beams are either $360 \times 400mm$ or $360 \times 600mm$, both made of GL28c timber. The larger beams are located along the interior lines of support and carry two adjacent CLT panels, while the smaller beams are positioned around the building's perimeter, supporting one side of a panel and thus carrying only half the span load. These beams act as simply supported elements and are supported by continuous glulam columns measuring $360 \times 360mm$ in GL24h timber. In addition to the beam-column frame system, $240mm$ thick CLT walls—constructed with a 7-layer layup—provide stabilization and carry vertical loads where necessary.

The floor system carries both dead and imposed loads. The dead load consists of the self-weight

of the CLT floor, screed, insulation, finishing, and technical installations, as summarized in Table 6.1. A uniformly distributed variable load of 3.30 kN/m^2 is applied in design.

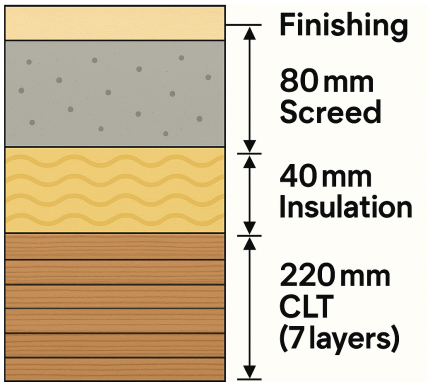

Figure 6.1: Detail of floor layer build-up

Table 6.1: Load assumptions for existing floor system

Load Component	Load (kN/m^2)
Finishing	0.15
Screed floor (d = 80mm)	1.60
Insulation	0.15
CLT floor (d = 220mm)	1.00
Installations	0.20
Total permanent (G_k)	**3.10**
Variable load (Q_k)	**3.30**

6.3 Point Supported Concept

To investigate the potential of the proposed panel-to-panel connection within a real building context, the existing post-and-beam floor layout is reconfigured into a point supported concept. In this system, CLT panels are directly supported on columns without intermediate beams, enabling a structurally efficient and material-saving alternative. The following sections outline the concept design, analytical checks, and verification methods used.

The python models as shown in Appendix H and I are added to show the use of the model. The model is shown by performing an example calculation based on the conclusions from the parameter studies.

6.3.1 System Layout and Structural Modifications

To allow the floor to handle the concentrated loads from the columns, extra space is needed around each column for better load distribution. For this reason, all columns are moved inward by 0.5 meters. This creates more area around each column to safely introduce the load into the floor. The updated structural layout is shown in Appendix G.3. The walls are kept in place, as they are important for the stability of the structure. By shifting the columns inward, a regular grid of 5.4 m × 5.7 m is created.

6.3.2 Preliminary design

In the preliminary design stage, the panel height is the first question mark in the design. To estimate the height and a fitting panel lay-up, a flow chart is provided in Appendix D. Following these steps will guide towards a fitting panel height:

1. First a panel stiffness ratio is assumed to be $\eta \approx 0.5$, this ratio is based on the numerical studies performed in Chapter 5.
2. Using this stiffness ratio, the known loading and the grid size, the bending moment can be estimated. To account for the increased panel thickness under permanent loading, the value is slightly increased in the calculations, this leads to the following design load:

$$Q_d = 1.2 \times 3.5 + 1.5 \times 3.3 = 9.15 kN/m^2$$

Based on the grid size the following C_η-values are determined:

$$C_{\eta;1 \text{ field}} = \frac{4.770 + 5.043}{2} = 4.91 \qquad C_{\eta;2 \text{ field}} = \frac{4.150 + 4.371}{2} = 4.26$$

Using these factors and the governing loading pattern, the following bending moment can be calculated:

$$M_y(b_{plate} = 3.5) = \frac{5.7}{5.4} \times (1.2 \times 3.5 \times 4.26 + 1.5 \times 3.3 \times 4.91) = 44.54 \frac{kNm}{m}$$

Lastly, to account for the finite stiffness of the connection, the bending moment may be reduced. Conservatively a reduction factor of $\varphi_{red} = 0.85$ is applied, so $M_{est} = 0.85 \times 44.54 = 37.86 \frac{kNm}{m}$

The corresponding values for C_η are extracted from Table E.3, which is constructed for a floor system with two modules. In reality, the structure will consist of three modules, but for an early design estimate, this conservative approach is acceptable.

Now a bending moment has been estimated, engineering judgement is needed, a LVL thickness, screw type and spacing needs to be chosen. For this the following connection properties are chosen:

- SPAX screws;
  - 2 per row
  - $10mm$ diameter
  - $80mm$ spacing

  So $n_{ef} = 0.9 \times n_{row} \times \frac{1000}{spacing} = 22.5$
- $t_{LVL} = 51mm$

Using the design rules from Chapter 3 that the connection should designed in such a way that the screw in the LVL plate is the governing failure mechanism, Figure D.1 can be used. For additional information of this quick estimate figure, see Appendix D. The characteristic value can be read from the graph and is estimated as:

$$F_{v,Rk} \approx 9500\ N$$

In this estimation method, the characteristic value of the shear force is used in the internal lever arm calculation. While this choice may appear arbitrary, it has proven effective for quick and practical estimations. Using the design shear force would significantly increase the estimated lever arm, leading to overly conservative results and unnecessarily large panel depths. The partial safety factor $\gamma_M = 1.3$ for connections is included, but the k_{mod} factor is not. This approach is intended for preliminary sizing and should be followed by a full verification using consistent design values in the final structural analysis. The estimated lever arm, taking into account the effective number of fasteners, becomes:

$$z_{est} = \frac{M_{est}}{F_{v,Rk} \times n_{ef}} = \frac{37.86}{\frac{9.50}{1.3} \times 22.5} = 0.230m$$

The estimated total panel height is then calculated by summing the LVL thickness, the estimated lever arm, and the top layer thickness:

$$H_{est} = t_{LVL} + z_{est} + t_1 = 51 + 230 + 30 = 311\,\text{mm}$$

Based on the stiffness ratio of $\eta \approx 0.5$ and the estimated panel height, a fitting panel is chosen from Table A.1:

[30, 30, 40, 40, 30, 40, 40, 30, 30] — Thickness: 310 — Ratio: 0.5106 — EI_x: 18.08

6.3.3 Stiffness Calculation

First the decision is made to use a softwood panel from Metsä Wood, so $\rho_{mean} = 510\frac{kg}{m^3}$ and $\rho_k = 480\frac{kg}{m^3}$. A $51mm$ thick LVL panel is used, this panel is placed in a 9-layer panel with lamella thicknesses mentioned above, $\rho_{mean} = 450\frac{kg}{m^3}$ and $\rho_k = 350\frac{kg}{m^3}$. This panel has a bending stiffness ratio of $\eta = 0.5106$.

Using the SPAX screws, a requirement for the minimum screw length can be found in table 3.3 based on parameter studies. Dimensioning the butt-joint screws on strength leads to quite large screws, so instead of dimensioning the screw based on strength, the optimum length is sought for stiffness.

$$L_{splice} \geq (1 + \frac{\rho_{LVL}}{\rho_{CLT}}^{0,8}) \times t_{lvl}\sqrt{2} \qquad L_{butt} = \frac{2\sqrt{2}}{3} \times (H - T)$$

$$L_{splice} \geq (1 + \frac{480}{350}^{0,8}) \times 51\sqrt{2} \qquad L_{butt} = \frac{2\sqrt{2}}{3} \times (310 - 30)$$

$$L_{splice} \geq 165mm \qquad L_{butt} = 264mm$$

For both the butt-joint connection and the splice plate connection, the same screw length is used to ensure consistency and ease of installation. This eliminates the need for on-site workers to differentiate between screw types, reducing the risk of errors and streamlining the construction process. The values for the screws used in the example model are summarized in table 6.2. The connection is depicted in Appendix G. The rotational stiffness of the splice plate connection returns as $6301\frac{kNm}{rad \cdot m}$ and that of the butt-joint as $4061\frac{kNm}{rad \cdot m}$.

Table 6.2: Screw properties connection

	d_{screw}	L_{screw}	# of screws	spacing
Splice plate	10 mm	260 mm	2	80 mm
Butt-joint	10 mm	260 mm	2 (cross-wise)	200 mm

6.3.4 Vibration requirements

The exact chosen panel is not included in the relevant design graph shown in Appendix F.1. However, a more unfavourable and comparable panel is included:

[20, 20, 40, 40, 40, 40, 40, 20, 20] — Thickness: 280 — Ratio: 0.5177 — EI_x: 13.26

This panel used in this case study has approximately the same stiffness ratio and higher directional stiffness in both directions. For the calculated rotational stiffness of $\varphi = 5000\frac{kNm}{rad}$ the panel in the design graph can reach up to $6.8m$. For a grid of $5.4 \times 5.7m$ the vibrational demands will thus most likely be met.

6.3.5 Finite Element Verification (RFEM)

The stiffness is just as important as the strength of this connection type. To check whether the connection is stiff enough, the system is also checked in SLS for deflections. For this check the k_{def} factor is used, for CLT the factor is 0.8 [23] for timber members in service class 1. The ψ-factor for quasi-permanent action for office buildings equals 0.3 [38]. The deflection check is done using the following load combination [23]:

$$\begin{gathered}(1 + k_{def}) \times (Q_{sw} + Q_G) + (1 + \psi_2 k_{def}) \times Q_Q \\ 1,8 \times (Q_{sw} + Q_G) + 1,24 \times Q_Q\end{gathered} \tag{6.1}$$

As described in the previous chapter, the input for the model is mainly the geometry of the CLT and LVL panel and the screw properties. The calculation is based on the following input:

- CLT panel: 9-layer; [30, 30, 40, 40, 30, 40, 40, 30, 30]
- LVL plate: 17-layers, $t_{LVL} = 51mm$
- Screw properties as summarized in table 6.2

The governing load combinations and the resulting internal forces in the line hinge are shown in Figure 6.2. These results are based on RFEM 6 calculations, incorporating the previously calculated rotational stiffness values for the line hinge.

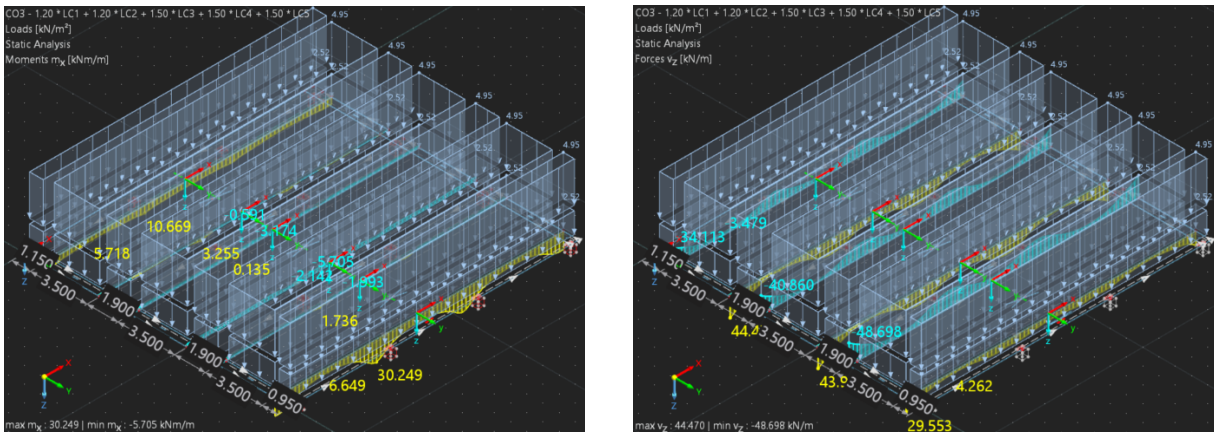

(a) Governing moment m_x in the line hinge

(b) Governing shear force v_z in the line hinge

Figure 6.2: Internal forces in the line hinge under governing load combinations, based on RFEM 6 modelling

6.3.6 Structural Verification

Panel-to-panel connection

Based on the RFEM calculation the following resulting forces are calculated:

- $m_x^+ = 30.2kNm/m$
- $m_x^- = 5.7kNm/m$
- $v_z = 48.7kN/m$

These forces are the input for the third calculation model. From the calculation in Appendix I it can be concluded that the occurring bending moment at the panel-to-panel connection can be transferred in this connection. The following U.C.-values are calculated:

$$U.C. = \frac{m_{x,Ed}^+}{m_{x,Rd}^+} = \frac{30.2}{32.4} = 0.93$$

$$U.C. = \frac{m_{x,Ed}^-}{m_{x,Rd}^-} = \frac{5.7}{12.3} = 0.46$$

$$U.C. = \frac{v_{z,Ed}}{v_{z,Rd}} = \frac{48.7}{61.6} = 0.79$$

Deflection

For timber floor systems, deflection often governs the design and this is no different for the examined point-supported system. From the RFEM calculation, using the SLS load combinations, the deflection is largest under the load case as illustrated in Figure 6.3. The maximum deflection of the system reaches 23.2 mm.

It is important to note that the rotational stiffness of the line hinge has relatively little influence

on the overall deflection of the system. This is because deflection primarily depends on the flexural stiffness and the span length of the supported sections. In this case, the supported section length is quite small, which limits the impact of the hinge's rotational flexibility on vertical displacements. As a result, variations in the line hinge stiffness do not significantly affect the maximum deflection.

Instead, the deflection is predominantly controlled by the bending stiffness of the floor elements themselves and the span length between supports. The line hinge, while important for moment transfer and vibration behaviour, mainly influences rotational constraints and modal response rather than the magnitude of vertical deflections. Therefore, from a deflection perspective, ensuring sufficient flexural stiffness and minimizing unsupported spans are more critical design considerations than hinge rotational stiffness.

The deflection check is done along the diagonal of the floor system, with a deflection demand for floors of $\frac{3}{1000} l_{rep}$[38].

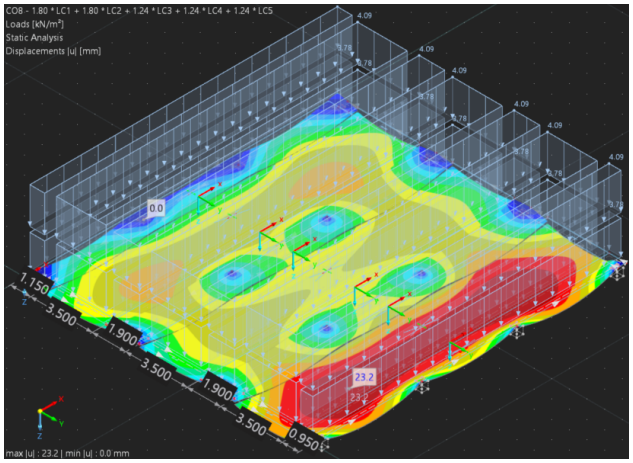

Figure 6.3: Deflection of the floor system

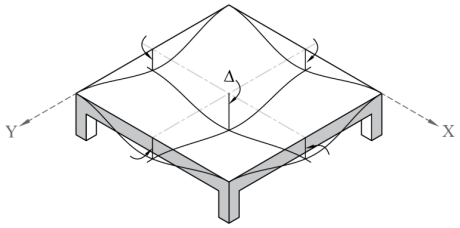

Figure 6.4: Deflection of a point-supported slab [56]

$$\Delta_{max} = \frac{\sqrt{5700^2 + 5400^2}}{333}$$
$$= 23.6 \text{ mm}$$
$$U.C. = \frac{23.2}{23.6} = 0.98 \leq 1$$

6.4 Structural Comparison

The point-supported floor system offers several distinct advantages over the traditional beam-supported floor system. Most notably, the absence of continuous beams beneath the floor panels creates more free height within the building. This architectural benefit allows for cleaner ceiling lines and increased usable vertical space, which can be valuable in residential or commercial applications.

In a beam-supported floor system, beams are required to run continuously or at regular intervals to carry the loads from the floor panels to the supports. This not only reduces the available height below the floor but also introduces complexity during construction. On the other hand, the point-supported system relies on discrete support points, which directly support the floor panels. This concentrated support arrangement simplifies the structural layout by eliminating the need for beams, leading to potentially faster installation and a more straightforward grid and structural design.

However, this freedom and simplicity come at the cost of increased timber usage. Since floor panels must span between isolated points without the intermediate support of beams, they require greater bending stiffness and strength. This typically results in thicker or panels, increasing the overall volume of timber material needed. Consequently, the point-supported system demands a larger cubic meter quantity of timber compared to beam-supported floors, which can be a factor in cost and sustainability considerations.

Regarding connections, the beam-supported floor system requires reliable panel-to-beam con-

nections designed to transfer shear forces and bending moments between the floor elements and the supporting beams. Additionally, beams must be connected securely to their supports, often requiring moment-resisting or shear connections depending on the design. In contrast, the point-supported floor system needs strong panel-to-column connections at discrete points. These connections must be designed to transfer significant bending moments, shear forces and normal loads locally without the benefit of continuous support lines. This can lead to more complex connection details at each support point, requiring careful design to prevent failures.

In terms of structural performance, both systems can be designed to satisfy strength and serviceability requirements effectively. The point-supported system, as demonstrated in the strength verification and deflection checks, can transfer moments and resist shear with utilization ratios comfortably below unity. Deflection is mainly governed by the bending stiffness of the panels themselves and the span length between supports, rather than the rotational stiffness of the connection points.

In summary, the point-supported floor system provides architectural and spatial benefits by eliminating beams and increasing ceiling height, while requiring greater timber volumes and carefully designed point connections. The beam-supported system, although potentially more economical in timber usage, limits free height and necessitates coordinated connections along beams and supports. The choice between these systems should consider the project's architectural goals, material availability and construction complexity.

6.5 Conclusion and Discussion

The point-supported floor system offers significant architectural and spatial benefits by eliminating beams, resulting in increased free height and a cleaner structural layout. It can also simplify on-site construction due to fewer components and more streamlined installation. However, this system typically requires a higher volume of timber and more sophisticated connection detailing, which adds to material and engineering demands.

It is recommended to adopt the point-supported system where spatial efficiency and architectural integration are priorities. However, due to its concentrated support strategy and sensitivity to stiffness and connection performance, it demands more detailed structural engineering compared to traditional post-and-beam systems. Early and precise detailing are essential to fully realize its benefits.

Chapter 7: Conclusion and Discussion

This chapter concludes the findings from this research, reflecting on the implications of the proposed panel-to-panel connection in point-supported CLT floor systems. To provide a structured evaluation, the sub questions formulated in the Introduction (see Sec. 1.5) will be addressed. Finally the main research question will be answered.

While Chapter 3 focused primarily on modelling the specific panel-to-panel connection considered in this thesis, the subsequent chapters broadened the scope. In these chapters (see Ch. 4 and 5) the connection was no longer treated as a specific detail, but idealised as a line hinge with a defined rotational stiffness. This simplification enabled a more flexible and broadly applicable understanding of the structural behaviour, making the findings relevant not only to the proposed connection but also to other connection types with similar stiffness characteristics.

The conclusions from the analytical estimation and vibration analysis offer insights that are applicable beyond the specific cases studied. In both chapters (4,5), methods were developed that are broadly applicable to point-supported CLT floor systems with various inter-panel connections. While the resulting tables and graphs may be case- and assumption-specific, the underlying approaches provide useful tools for wider design applications. The following section reflects on the effectiveness and practical integration of the connection model, while acknowledging its limitations.

7.1 Conclusion

1. *How can the stiffness and strength of a proposed panel-to-panel connection be accurately modelled and evaluated?*

   The proposed connection, a splice plate connection, was analysed through both analytical modelling and FEM in RFEM and Python. A bilinear spring model was developed to assess rotational stiffness, while strength evaluations considered various failure mechanisms, including screw withdrawal, tensile failure and LVL plate tension capacity. By integrating prescribed formulas from building codes and screw-specific relations from ETAs, the analysis provided accurate predictions of connection behaviour. Validation against experimental results confirmed that the mechanical model captured the primary elastic response, although some plastic effects were observed in testing.

   The proposed connection, a splice plate connection, was analysed through both analytical modelling using Python and FEM simulations in RFEM. A spring model was developed to assess rotational stiffness, which is implemented as a bilinear rotational spring in RFEM, where the stiffness varies depending on the bending moment direction. This approach accounts for the differing stiffness values under positive and negative bending, reflecting the real mechanical behaviour of the connection more precisely.

   The strength evaluations considered various failure mechanisms, including screw withdrawal, tensile failure and LVL plate tension capacity. By integrating prescribed formulas from building codes and screw-specific relations from ETAs, the analysis provided accurate predictions of connection behaviour. Validation against experimental results confirmed that the mechanical model accurately captured the primary elastic response, although some plastic effects were observed during testing.

2. *To what extent can simplified estimation formulas for bending moments in line hinges, representing panel-to-panel joints, be formulated, and how accurately do they compare to results from numerical models?*

   A bending moment estimation formula was derived from parametric numerical studies using RFEM and Grasshopper. By analysing the effects of span dimensions, stiffness ratios and

applied loads, an empirical equation was formulated to estimate the moment at line hinges within point-supported CLT floors. To capture the complex influence of varying stiffness ratios on bending moment behaviour, C_η-values were introduced as empirical coefficients. These values account for the interaction between stiffness in the major and minor directions of the CLT panels, ensuring a more accurate reflection of load distribution effects.

To reflect the finite rotational stiffness of the panel-to-panel connection, a reduction factor is introduced. The resulting formula showed strong agreement with FEM across a range of panel configurations, offering engineers an efficient early-stage design tool for assessing moment transfer. While it simplifies calculations, its applicability is currently limited to single- and two-span configurations. Additionally, the developed function is conservatively applicable to floors with line supports.

3. *How can design graphs be developed that estimate whether point-supported CLT floor systems meet vibration requirements in the preliminary design stage?*

   Design graphs for estimating vibration compliance of point-supported CLT floors were developed using parametric RFEM modal analysis combined with the HIVOSS methodology, which considers natural frequencies, modal masses and comfort thresholds. By varying key parameters such as the rotational stiffness of panel-to-panel connections and the stiffness ratio $\eta = \frac{EI_y}{EI_x}$, the graphs outline acceptable vibration limits for different spans and connection stiffnesses, providing engineers a practical early-stage assessment tool.

   To ensure usability, performance improvements were assumed to be consistent across parameter ranges with a mesh size of 0.1×0.1, though non-linear interactions and boundary effects mean designs should avoid being exactly on limit lines (see Appendix B). Additionally, these graphs are conservatively applicable to floors with line supports, broadening their relevance.

4. *How does the proposed connection perform in a real-world case study compared to a traditional post-and-beam CLT floor system in terms of structural efficiency and vibration behaviour?*

   The splice plate connection was applied to an upcoming office building project as a practical example of the point-supported CLT floor system. Compared to a traditional post-and-beam system, the point-supported floor eliminates continuous beams, increasing free height and enabling a cleaner, more flexible ceiling design. However, these benefits come at the cost of increased timber volume, as panels must span between discrete points requiring greater thickness and strength. Additionally, connections must be carefully designed, both panel-to-column and panel-to-panel, to transfer bending moments, shear and normal loads locally, demanding more detailed engineering than typical connections in a post-and-beam structure.

   Preliminary bending moment and stiffness estimation methods showed promising biaxial load distribution and acceptable vibration performance. Subsequent calculations have confirmed that all structural demands are met. Nonetheless, the system remains vulnerable due to its reliance on discrete connection points and the sensitivity to connection performance and stiffness. Checks on torsional stresses and fire safety are also necessary before practical implementation.

   In summary, the point-supported system offers significant architectural and spatial benefits but requires higher timber use and more intensive connection detailing. Its successful adoption depends on careful engineering and optimization, making it especially suitable where spatial efficiency and architectural integration are priorities.

7.1.1 Main research question

How can panel-to-panel connections in point-supported CLT floor systems be effectively designed and modelled to ensure adequate structural performance and serviceability?

Panel-to-panel connections in point-supported CLT floor systems must be carefully designed and modelled to ensure both structural performance and serviceability. This research demonstrates that an integrated approach combining mechanical modelling, FEA and empirical estimation forms an effective methodology for connection design. The splice plate connection analysed here shows the ability to transfer biaxial loads with variable rotational stiffness under different bending conditions, supported by strength assessments that confirm reliable load-bearing capacity.

A key contribution of this work is the development of practical design tools that support engineers throughout the early stages of the design process. Central to this is a structured flowchart methodology (see App. D) that guides the selection of appropriate panel geometry and connection detailing based on fundamental structural parameters. The process begins by choosing an optimal stiffness ratio for the panels, which balances bending moment demands and vibration performance. Following this, bending moments are estimated considering the panel layout and loading, with adjustments for connection stiffness.

Subsequent steps involve determining the internal forces acting within the panel-to-panel connection, based on the mechanical model developed in this research. This model simplifies the force distribution by identifying a governing failure mechanism and provides a framework for estimating the tensile force required in the connection. Once the tensile force is known, it is combined with the estimated bending moment to determine the internal lever arm of the connection. This lever arm reflects the vertical distance between the zones of compression and tension and is used to estimate the minimum required panel height. This step enables a quick evaluation of the structural depth needed to safely resist the applied moments, offering a practical tool for early-stage design.

Finally, with known panel properties and connection rotational stiffness, design graphs developed through parametric vibration analyses enable rapid assessment of the floor's vibrational serviceability. These tools allow engineers to confirm whether preliminary designs meet comfort criteria before engaging in detailed modelling, promoting efficient and reliable design workflows.

This combined approach bridges the gap between complex numerical models and practical design needs, making the design of point-supported CLT floor systems more accessible and systematic. While this research establishes a robust framework, it recognizes that detailed engineering and optimization remain essential, especially given the sensitivity of these systems to connection behaviour. Experimental validation and real-world application will be necessary to fully confirm the assumptions and refine the design methodology further.

In summary, the effective design and modelling of panel-to-panel connections in point-supported CLT floors require a multi-step process incorporating stiffness ratio selection, connection force estimation and vibration assessment using design graphs. This approach supports early-stage decision-making while providing a pathway for detailed engineering verification, thus ensuring adequate structural performance and serviceability.

7.2 Discussion

7.2.1 Splice Plate Model

The proposed splice plate connection provides an effective solution for panel-to-panel joints in point-supported CLT floor systems, enabling efficient biaxial load transfer. The current mechanical model assumes linear-elastic material behaviour, which may not fully capture the actual response under ultimate loading. Incorporating non-linear timber and fastener behaviour, such as plastic deformations, would improve stiffness and strength predictions, especially at

ultimate limit states.

A key limitation is that the splice plate requires a compression point before it can develop rotational resistance. While CLT panels are placed with precision, small misalignments can cause initial deflection before full moment transfer occurs. This behaviour is not captured in the simplified model but may affect serviceability, particularly in long-span applications.

Additionally, as each new splice plate is installed, panels are tensioned toward one another, potentially inducing horizontal forces between supports. Over the floor area, this could slightly draw columns inward, a secondary effect not accounted for in current assumptions. In summary, the model offers valuable design guidance, but refinements, such as non-linear modelling, installation tolerance effects and system-wide interactions, are needed to ensure accurate performance predictions and safe implementation in practice.

7.2.2 Estimation Formulas for Bending Moments in Line Hinges

The bending moment estimation formula presents an efficient method for assessing internal forces at panel joints, supporting early-stage design decisions. However, its validity is constrained by specific geometric and loading conditions, meaning caution is required when applying it beyond defined parameter ranges. Expanding the parameter space through additional studies would improve adaptability, allowing engineers to incorporate multi-span floor systems or semi-rigid hinge configurations in design. Furthermore, integrating the formula into design software or spreadsheets would increase its accessibility and practical usage. Doing so could streamline calculations and provide engineers with a standardized tool for assessing moment behaviour across various structural layouts.

7.2.3 Design Graphs for Vibrations

The vibration assessment methodology leverages predefined design graphs to enable rapid preliminary evaluations. These graphs offer valuable guidance during early design phases but rely on assumptions about panel lay-ups, support conditions and boundary conditions. While the approach is systematic and repeatable, allowing engineers to generate graphs for other configurations, its current form does not capture all real-world complexities. For example, linear springs are used to represent connection behaviour in the vibrational analysis, whereas the proposed splice plate connection, like most panel-to-panel joints, behaves more like a bilinear spring. This non-linearity is not accounted for and may lead to slight underestimation of dynamic displacements.

Further extending the methodology to include point loads, variable support stiffness or multi-span configurations would improve its relevance for diverse structural layouts. Finally, integrating the design graphs into a parametric digital tool would enhance usability, enabling designers to adjust floor parameters dynamically and instantly assess vibrational performance.

7.2.4 Comparison through a Case Study

The case study applied the splice plate connection to an office building project, offering a preliminary indication of its architectural and structural feasibility. While results suggest spatial efficiency due to the absence of beams, the scope of the study remains limited. No detailed modelling of the critical panel-to-column connections was performed, which are essential to the actual load path and system behaviour.

Moreover, the comparison between the point-supported and traditional post-and-beam systems is primarily qualitative. A more robust and weighted comparison, including structural performance, cost, material use and construction complexity, is needed to evaluate the compromises involved. Without such an analysis, it is difficult to determine whether the benefits truly outweigh the potential drawbacks.

Chapter 8: Recommendations

8.1 Connection design

The rotational stiffness of panel-to-panel connections plays a crucial role in both bending moment transfer and vibration performance. Designers should select connections that provide adequate stiffness without excessive reinforcement, as overly rigid connections may lead to inefficient stress distribution or diminishing returns in vibration control. In an early stage of design, the developed design graphs can be used to estimate a fitting rotational stiffness.

The developed bending moment estimation formula allows designers to approximate moment transfer at line hinges efficiently. When designing single- and two-span systems, incorporating this formula ensures quite accurate predictions in load distributions. However, caution should be exercised when applying the formula to multi-span layouts, where additional refinement may be required.

Vibrational behaviour significantly impacts comfort levels in CLT floors. The design graphs generated from numerical studies provide a fast preliminary assessment, allowing designers to evaluate whether a floor layout satisfies comfort thresholds before conducting detailed simulations. These graphs should be referenced when selecting panel stiffness values, particularly in office and residential spaces where user perception of vibrations is critical.

For practical implementation, designers should ensure that panel-to-panel connections are not only structurally efficient but also easy to install and cost-effective. Simplified fastening strategies—such as pre-drilled splice plates or optimized screw angles—can streamline assembly without compromising strength. Coordination with manufacturers early in the design process can further enhance constructibility and avoid unnecessary complexity in execution.

8.2 Future research

8.2.1 Splice Plate Modelling

To confirm the assumptions made in numerical studies, experimental validation through full-scale testing is essential. The proposed connection used in a point-supported floor system should be tested under realistic loading conditions to evaluate strength, stiffness and serviceability performance. The fact that the connection consists of both a splice plate and a butt joint suggests that stiffness is significantly increased, though this has yet to be verified experimentally. Testing would provide critical benchmarks to assess how stiffness variations impact load transfer, vibration behaviour and long-term performance.

Beyond structural verification, the practical implementation of the splice plate connection could be optimized further by investigating different connection layouts, materials and fastening techniques. The influence of support stiffness and multi-span configurations should be studied to ensure applicability across diverse projects. Currently, a significant panel height is needed to achieve the internal lever arm required for moment resistance. It could be interesting to investigate other possibilities of increasing this lever arm, without the need for an increased thickness of the CLT panel. For instance by using the screed layer, which is common practice to use for other aspects, as compression point. Exploring such hybrid solutions could lead to more efficient designs.

It is important to note that this research does not include a fire safety analysis. Fire safety is a key concern in timber engineering and as point-supported CLT floors gain wider use, the role of connections in fire performance must be thoroughly evaluated. Given the current developments in this field, future studies should assess the fire resistance of the splice plate connection, including fastener performance at high temperatures and charring effects on CLT panels. While this research provides a strong foundation for structural design, fire safety remains a critical aspect

requiring further investigation before practical implementation.

8.2.2 Estimation Formulas for Bending Moments in Line Hinges

Further research could improve the applicability of the moment estimation formula by extending its use to multi-span configurations and refining its representation of semi-rigid hinge behaviour. While the current formulation provides reliable predictions within single- and two-span systems, more complex layouts introduce additional load redistribution effects that require further investigation. Establishing a generalized approach for multi-span systems would enhance the formula's practicality across a wider range of structural applications.

Additionally, alternative hinge detailing, such as semi-rigid or elastically flexible connections could be explored to provide greater design flexibility. By refining the mechanical representation of rotational stiffness variations, designers could better adapt connection solutions to meet both serviceability and strength requirements. A key aspect of this refinement would be deriving a predictive relation for the C_η factor, which currently acts as an empirical coefficient capturing the interaction between stiffness variations. Identifying a systematic method to predict C_η values based on geometry, material properties and load conditions would significantly improve the formula's reliability across different panel configurations.

Integrating these refinements into automated design tools, such as structural software or parametric spreadsheets, would further enhance usability. A digital implementation allowing engineers to input key parameters and instantly assess bending moment behaviour would streamline the early-stage design process, ensuring efficient decision-making. These advancements would support more accurate, adaptable and accessible methodologies for designing point-supported CLT floors.

8.2.3 Design Graphs for Vibrations

Future advancements in vibration design tools could significantly improve the assessment and optimization of point-supported CLT floor systems, particularly by incorporating a broader range of load cases and support conditions. While the current analysis relies on predefined design graphs, their applicability is limited by specific assumptions regarding panel lay-ups, spans, and boundary conditions. Expanding this database to account for multi-span configurations, point loads and variable support stiffness would enhance flexibility, allowing engineers to evaluate a wider range of real-world scenarios.

Beyond expanding the database, the introduction of a digital parametric tool would transform the usability of vibration design methodologies. A computational interface allowing engineers to input span length, stiffness parameters, floor mass and boundary conditions could generate instant design feedback, eliminating the need for manual graph selection. This tool could provide real-time adjustments, dynamically visualizing comfort thresholds and vibration sensitivity based on project-specific inputs.

Ultimately, these enhancements would make vibration analysis more accessible and precise, supporting optimized floor designs that meet serviceability requirements while maintaining architectural flexibility. As computational capabilities evolve, integrating automated analysis techniques within structural software would further bridge the gap between early-stage design assumptions and detailed performance validation.

References

[1] I. K. Abeysekera, P Hamm, T. Toratti, and A. Lawrence. Development of a floor vibration design method for Eurocode 5. In *INTER Meeting 51*, pages 445–458, Tallinn, 2018.

[2] American Wood Council. General Dowel Equations for Calculating Lateral Connection Values. Technical report, American Wood Council, Leesburg, 2015. URL: https://awc.org/publications/tr-12-general-dowel-equations-for-calculating-lateral-connection-values.

[3] APA. ANSI 117-2020, Amercian National Standard: Standard Specification for Structural Glued Laminated Timber of Softwood Species, 5 2020. URL: https://www.apawood.org/publication-search?q=ansi-117.

[4] APA. Kalesnikoff Cross-Laminated Timber. Technical report, PR-L332, Tacoma, 2022.

[5] APA. Nordic X-Lam. Technical report, PR-L306, Tacoma, 2025.

[6] Julian Asselstine, Frank Lam, and Chao Zhang. New edge connection technology for cross laminated timber (CLT) floor slabs promoting two-way action. *Engineering Structures*, 233, 4 2021. doi:10.1016/j.engstruct.2020.111777.

[7] Simon Aurand and Hans Joachim Blaß. Connections with inclined screws and increased shear plane friction. In *Proceedings - meeting 54 : 16-19 August 2021, online meeting / INTER, International Network on Timber Engineering Research. Ed.: R. Görlacher*, pages 147–168, 2021. doi:10.5445/IR/1000139615.

[8] I. Bejtka and H.J. Blaß. Joints with inclined screws. In *Proceedings from meeting thirty-five of the international council for building research studies and documentation, CIB, Working Commission W18 – Timber Structure*, Kyoto, 2002. doi:10.5445/IR/13752002.

[9] Thomas Bogensperger and Robert A. Jöbstl. Concentrated load introduction in CLT elements perpendicular to plane. In *INTER meeting 48*, pages 163–178, Sibenik, 2015. URL: https://graz.elsevierpure.com/files/86261161/INTER_Bogensperger_Joebstl_V3.pdf.

[10] Francesco Boggian, Mauro Andreolli, and Roberto Tomasi. Cross Laminated Timber (CLT) Beams Loaded in Plane: Testing Stiffness and Shear Strength. *Frontiers in Built Environment*, 5, 5 2019. doi:10.3389/fbuil.2019.00058.

[11] R. Brandner. Cross laminated timber (CLT) in compression perpendicular to plane: Testing, properties, design and recommendations for harmonizing design provisions for structural timber products. *Engineering Structures*, 171:944–960, 9 2018. doi:10.1016/j.engstruct.2018.02.076.

[12] Yuri De Santis and Massimo Fragiacomo. Timber-to-timber and steel-to-timber screw connections: Derivation of the slip modulus via beam on elastic foundation model. *Engineering Structures*, 244:112798, 10 2021. doi:10.1016/j.engstruct.2021.112798.

[13] Deutsches Institut für Bautechnik. Würth self-tapping screws. Technical report, ETA-11/0190 of 23 July 2018, 7 2018. URL: https://www.wuerth.it/progettisti/wp-content/uploads/allegati/carpenteria-legno/certificazioni/ETA_11_0190_EN.pdf.

[14] Deutsches Institut für Bautechnik. Derix X-LAM. Technical report, ETA-11/0189

of 11 September 2019, 9 2019. URL: https://derix.de/media/free-documents/European_technical_assessment_X-LAM.pdf.

[15] Dlubal Software GmbH. RFEM 6 - Structural Analysis and Design Software, 2024. URL: https://www.dlubal.com/en/products/rfem-fea-software/rfem/what-is-rfem.

[16] ETA-Danmark A/S. Rotho Blaas Self-tapping screws and threaded rods. Technical report, ETA-11/0030 of 2019/10/08, 10 2019. URL: https://www.rothoblaas.com/ftp/ETA_11_0030_RB_screws_2019.pdf.

[17] ETA-Danmark A/S. SPAX self-tapping screws. Technical report, ETA-12/0114 of 2020/01/07, 1 2020. URL: https://downloads.spax.com/index.php.

[18] Eurofins. Product Certificate Kerto-S and Kerto-Q. Technical report, ETA-13/0504, 12 2020. URL: www.sertifikaattihaku.fi.

[19] European Committee for Standardization (CEN). ISO 6891: Timber structures - Joints made with mechanical fasteners - General principles for the determination of strength and deformation characteristics, 1983.

[20] European Committee for Standardization (CEN). NEN-EN 1990, Basis of structural design, 4 2002.

[21] European Committee for Standardization (CEN). NEN-EN 1995-1-1, Design of timber structures - Part 1-1: General - Common rules and rules for buildings, 2004.

[22] European Committee for Standardization (CEN). NEN-EN 16351:2021, Timber structures - Cross laminated timber - Requirements, 3 2021.

[23] European Committee for Standardization (CEN). prEN 1995-1-1, Design of timber structures - Part 1-1: General rules and rules for buildings, 9 2023.

[24] M. Feldmann, Ch. Heinemeyer, Chr. Butz, E. Caetano, A. Cunha, F. Galanti, A. Goldack, O. Hechler, S. Hicks, A. Keil, M. Lukic, R. Obiala, M. Schlaich, G. Sedlacek, A. Smith, and P. Waarts. *Design of floor structures for human induced vibrations*. JRC-Scientific and Technical Report, 2009. doi:10.2788/4640.

[25] Maria Felicita, Rudi Roijakkers, Ruxandra Cojocaru, and Geert Ravenshorst. Comfort assessment of timber floor vibrations. In *INTER Meeting 57*, pages 445–460, Padova, 2024.

[26] M Flaig and H J Blaß. Shear strength and shear stiffness of CLT-beams loaded in plane. In *CIB-W18*, Karslruhe, 8 2013. Karlsruhe Institute of Technology, KIT Holzbau und Baukonstruktionen.

[27] Anders Gustafsson, Roberto Crocetti, Alar Just, Pierre Landel, Jörgen Olsson, Anna Pousette, Magnus Silfverhielm, and Birgit Östman. *The CLT Handbook*. Swedish Wood, Stockholm, 2019. URL: https://www.swedishwood.com/siteassets/5-publikationer/pdfer/clt-handbook-2019-eng-m-svensk-standard-2019-2022.pdf.

[28] Patricia Hamm, Antje Richter, and Stefan Winter. Floor vibrations – new results. In *World Conference on Timber Engineering*, Trentino, 2010.

[29] Helena Lidelöw. Design of timber joints. In Patrice Godonou, editor, *Design of timber structures*, volume 1, chapter 4, pages 87–114. Swedish Wood, Stockholm, 2022.

URL: https://www.swedishwood.com/siteassets/5-publikationer/pdfer/sw-design-of-timber-structures-vol1-2022.pdf.

[30] A. Hosseini, M. Shahnewaz, J. Zhou, and T. Tannert. Structural performance of CLT moment connections in the minor strength axis. *Engineering Structures*, 328:119788, 4 2025. doi:10.1016/j.engstruct.2025.119788.

[31] Haoyu Huang, Yan Gao, and Wen-Shao Chang. Human-induced vibration of cross-laminated timber (CLT) floor under different boundary conditions. *Engineering Structures*, 204:110016, 2 2020. doi:10.1016/j.engstruct.2019.110016.

[32] Kirsi Jarnerö. *Vibrations in timber floors: Dynamic properties and human perception*. PhD thesis, Linnaeus University, Växjö, 2014. URL: https://www.diva-portal.org/smash/get/diva2:782513/FULLTEXT01.pdf.

[33] Robert Jockwer, Gerhard Fink, and Jochen Kohler. Assessment of existing safety formats for timber connections - How probabilistic approaches can influence connection design in timber engineering. In *International Conference on Connections in Timber Engineering – From Research to Standards*, pages 16–31, Graz, 9 2017. Verlag der Technischen Universität Graz. doi:10.3929/ethz-b-000228387.

[34] K.W. Johansen. Theory of Timber Connections. *International Association of Bridge and Structural Engineering*, Volume 9:249–262, 1949. doi:10.5169/seals-9703.

[35] Marie Johansson. Structural properties of sawn timber and engineered wood products. In Patrice Godonou, editor, *Design of timber structures*, volume 1, chapter 2, pages 23–53. Swedish Wood, 2022. URL: https://www.swedishwood.com/siteassets/5-publikationer/pdfer/sw-design-of-timber-structures-vol1-2022.pdf.

[36] Robert M. Jones. *Mechanics of Composite Materials*. Taylor & Francis, Philadelphia, second edition edition, 1998. URL: https://isbnsearch.org/isbn/9781560327127.

[37] Michael Kawrza, Thomas Furtmüller, Christoph Adam, and Roland Maderebner. Parameter identification for a point-supported cross laminated timber slab based on experimental and numerical modal analysis. *European Journal of Wood and Wood Products*, 79(2):317–333, 3 2021. doi:10.1007/s00107-020-01641-7.

[38] Koninklijk Nederlands Normalisatie-instituut (NEN). National Annex to NEN-EN 1990+A1:2006+A1:2006/C2:2019 Eurocode: Basis of structural design, 11 2019.

[39] T.A.C.M. Kuipers, J.; Van Der Put. Betrachtungen zum Bruchmechanismus von Nagelverbindugen. In J. Elbeck and G. Steck, editors, *Ingenieurholzbau in Forschung und Praxis*, pages 99–106. Bruderverlag, Karlsruhe, 1982.

[40] Markus Wallner-Novak, Manfred Augustin, Josef Koppelhuber, and Kurt Pock. *Cross-Laminated Timber Structural Design Volume 2*, volume 2. proHolz Austria, Vienna, 2018.

[41] Bernhard Maurer and Roland Maderebner. Cross Laminated Timber under Concentrated Compression Loads - Methods of Reinforcement. *Engineering Structures*, 245:112534, 10 2021. doi:10.1016/j.engstruct.2021.112534.

[42] W. M. McKenzie and H. Karpovich. The frictional behaviour of wood. *Wood Science and Technology*, 2(2):139–152, 1968. doi:10.1007/BF00394962.

[43] Peter Mestek. *Punktgestützte Flächentragwerke aus Brettsperrholz (BSP) – Schubbemessung unter Berücksichtigung von Schubverstärkungen*. PhD thesis, Technischen Universität München, München, 10 2011. URL: https://mediatum.ub.tum.de/1079875.

[44] Metsä Wood. DoP Metsä Wood structural Birch Plywood. Technical report, MW/PW/411-001/CPR/DOP, Espoo, 12 2019.

[45] Marija Milojević, Vitomir Racic, Marija Nefovska-Danilović, Suzana Ereiz, and Ivan Duvnjak. Characterization of inter-panel connections in CLT floors using finite element model updating. *Journal of Building Engineering*, 97:110682, 11 2024. doi:10.1016/j.jobe.2024.110682.

[46] R. D. Mindlin. Influence of Rotatory Inertia and Shear on Flexural Motions of Isotropic, Elastic Plates. *Journal of Applied Mechanics*, 18(1):31–38, 3 1951. doi:10.1115/1.4010217.

[47] A.S. Mohammed, A. Pavic, and V. Racic. Improved model for human induced vibrations of high-frequency floors. *Engineering Structures*, 168:950–966, 8 2018. doi:10.1016/j.engstruct.2018.04.093.

[48] Marcel Muster. *Column-Slab Connection In Timber Flat Slabs*. PhD thesis, ETH Zurich, Zurich, 2020. doi:10.3929/ethz-b-000461541.

[49] G. Pernica. Dynamic Load Factors for Pedestrian Movements and Rhythmic Exercises. *Canadian Acoustics*, 18(2):3–18, 1990. URL: https://jcaa.caa-aca.ca/index.php/jcaa/article/view/618.

[50] Marjan Popovski, Zhiyong Chen, and Bernhard Gafner. Structural behaviour of point-supported CLT floor systems. In *Proc. 14th World Conference on Timber Engineering (WCTE2016)*, Vienna, 2016.

[51] Rothoblaas. TC Fusion and the CLT Floor Revolution: TC fusion. URL: https://www.rothoblaas.com/products/new-products/tc-fusion.

[52] Nađa Simović, Ivan Glišović, and Marija Todorović. Design of cross-laminated timber (CLT) floors for human-induced vibrations. *Gradjevinski materijali i konstrukcije*, 66(1):69–78, 2023. doi:10.5937/GRMK2301069S.

[53] Ian Smith and Ying Hei Chui. Design of lightweight wooden floors to avoid human discomfort. *Canadian Journal of Civil Engineering*, 15(2):254–262, 4 1988. doi:10.1139/l88-033.

[54] Thomas Stieb, Roland Maderebner, and Philipp Dietsch. A Timber–Concrete–Composite Edge Connection for Two-Way Spanning Cross-Laminated Timber Slabs—Experimental Investigations and Analytical Approach. *Buildings*, 13(12):3004, 12 2023. doi:10.3390/buildings13123004.

[55] Thomas Stieb, Bernhard Maurer, Maximilian Bestler, Philipp Dietsch, and Roland Maderebner. Solutions for edge connections to build two-way spanning cross laminated timber slabs. In *World Conference on Timber Engineering (WCTE 2023)*, pages 1322–1329, As, Norway, 2023. World Conference on Timber Engineering (WCTE 2023). doi:10.52202/069179-0180.

[56] StructurePoint. Two-Way Flat Plate Concrete Floor System Analysis and Design (ACI 318-14), 2023. URL: https://structurepoint.org/publication/html/Two-Way-Flat-Plate-Concrete-Floor-System-Analysis-and-Design-ACI-318-14-v550.

[57] Staffan Svensson and Jørgen Munch-Andersen. Theory of timber connections with slender dowel type fasteners. *Wood Material Science & Engineering*, 13(1):7–15, 1 2018. doi:10.1080/17480272.2016.1226382.

[58] Cristóbal Tapia, Marian Claus, and Simon Aicher. A finger-joint based edge connection for the weak direction of CLT plates. *Construction and Building Materials*, 340:127645, 7 2022. doi:10.1016/j.conbuildmat.2022.127645.

[59] The Editors of Encyclopaedia Britannica. coefficient of friction, 2024. URL: https://www.britannica.com/science/coefficient-of-friction.

[60] S. Timoshenko and S. Woinowsky-Krieger. *Theory of Plates and Shells*. McGraw-Hill Book Company, New York, second edition edition, 1959. URL: https://isbnsearch.org/isbn/9780070647794.

[61] Roberto Tomasi, Alessandro Crosatti, and Maurizio Piazza. Theoretical and experimental analysis of timber-to-timber joints connected with inclined screws. *Construction and Building Materials*, 24(9):1560–1571, 9 2010. doi:10.1016/j.conbuildmat.2010.03.007.

[62] Ebenezer Ussher, Kaveh Arjomandi, and Ian Smith. Explicit Vibration Formulas Applicable to Timber Plates with Free and Simply Supported Edges. *Structural Engineering International*, 28(4):506–517, 10 2018. doi:10.1080/10168664.2018.1461535.

[63] C. M. Wang. Natural Frequencies Formula for Simply Supported Mindlin Plates. *Journal of Vibration and Acoustics*, 116(4):536–540, 10 1994. doi:10.1115/1.2930460.

[64] C.M. Wang, J.N. Reddy, and K.H. Lee. *Shear deformable beams and plates: Relationships with classical solutions*. Elsevier, Oxford, 2000.

[65] Binsheng Zhang, Birgit Rasmussen, André Jorissen, and Annette Harte. Comparison of vibrational comfort assessment criteria for design of timber floors among the European countries. *Engineering Structures*, 52:592–607, 7 2013. doi:10.1016/j.engstruct.2013.03.028.

[66] Chao Zhang, Julian Asselstine, George Lee, and Frank Lam. Connection and performance of two-way CLT plates Phase II, 3 2019. URL: https://team.sites.olt.ubc.ca/files/2019/04/TEAM-Report-2018-07-Phase-II-Connection-and-performance-of-Two-way-CLT-Plate.pdf.

[67] Chao Zhang, George Lee, and Frank Lam. Connection and performance of two-way CLT plates, 4 2018. URL: https://team.forestry.ubc.ca/files/2018/05/TEAM-Report-2017-08-Connection-and-performance-of-Two-way-CLT-Plate.pdf.

[68] Sigong Zhang and Ying Hei Chui. Characterizing flexural behaviour of panel-to-panel connections in cross-laminated timber floor systems. *Structures*, 28:2047–2055, 12 2020. doi:10.1016/j.istruc.2020.10.040.

Appendices

Appendix A: Timber elements

Nominal thickness mm	Number of plies	Lay-up
21	7	
21	7	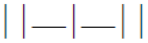
24	8	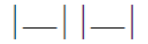
27	9	
30	10	
33	11	
39	13	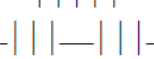
45	15	
51	17	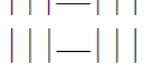
57	19	
63	21	
69	23	
75	25	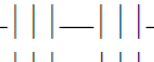

Figure A.1: Lay-up of Kerto-Q-products [18]

Table A.3.2: Characteristic shear strength $f_{v,k}$ calculated with the gross cross section (for mechanical actions in plane of the cross laminated timber)

Element Thickness in mm	Number of layers	Thickness of individual layers in mm (written in **bold** characters for longitudinal layers)											$f_{v,k}$ [1)] in N/mm²
60	3	**20**	20	**20**									**2.7**
80	3	**30**	20	**30**									**2.0**
90	3	**30**	30	**30**									**2.6**
100	3	**40**	20	**40**									**1.6**
110	3	**40**	30	**40**									**2.1**
120	3	**40**	40	**40**									**2.2**
100	5	**20**	20	**20**	20	**20**							**3.2**
110	5	**20**	20	**30**	20	**20**							**2.9**
120	5	**20**	30	**20**	30	**20**							**3.4**
130	5	**30**	20	**30**	20	**30**							**2.5**
140	5	**40**	20	**20**	20	**40**							**2.3**
150	5	**30**	30	**30**	30	**30**							**3.1**
160	5	**40**	20	**40**	20	**40**							**2.0**
170	5	**40**	30	**30**	30	**40**							**2.8**
180	5	**40**	30	**40**	30	**40**							**2.6**
200	5	**40**	40	**40**	40	**40**							**2.7**
140	7	**20**	20	**20**	20	**20**	20	**20**					**3.4**
160	7	**30**	20	**20**	20	**20**	20	**30**					**3.0**
180	7	**30**	20	**30**	20	**30**	20	**30**					**2.7**
200	7	**30**	30	**30**	20	**30**	30	**30**					**3.2**
220	7	**40**	20	**40**	20	**40**	20	**40**					**2.2**
240	7	**40**	20	**40**	40	**40**	20	**40**					**2.7**
260	7	**40**	30	**40**	40	**40**	30	**40**					**2.8**
280	7	**40**	40	**40**	40	**40**	40	**40**					**2.9**
230	9	**30**	20	**30**	20	**30**	20	**30**	20	**30**			**2.8**
250	9	**40**	20	**30**	20	**30**	20	**30**	20	**40**			**2.6**
270	9	**30**	30	**30**	30	**30**	30	**30**	30	**30**			**3.5**
280	9	**40**	20	**40**	20	**40**	20	**40**	20	**40**			**2.3**
290	9	**40**	30	**30**	30	**30**	30	**30**	30	**40**			**3.2**
310	9	**40**	30	**40**	30	**30**	30	**40**	30	**40**			**3.0**
320	9	**40**	30	**40**	30	**40**	30	**40**	30	**40**			**2.9**
360	9	**40**	40	**40**	40	**40**	40	**40**	40	**40**			**3.0**
370	11	**40**	20	**40**	30	**40**	30	**40**	30	**40**	20	**40**	**2.8**
390	11	**40**	30	**40**	30	**40**	30	**40**	30	**40**	30	**40**	**3.0**
190	7	**30**	**30**	20	**30**	20	**30**	**30**					**1.7**
210	7	**30**	**30**	30	**30**	30	**30**	**30**					**2.2**
230	7	**30**	**30**	40	**30**	40	**30**	**30**					**2.0**
240	7	**40**	**40**	20	**40**	20	**40**	**40**					**1.3**
260	7	**40**	**40**	30	**40**	30	**40**	**40**					**1.8**
280	7	**40**	**40**	40	**40**	40	**40**	**40**					**1.9**
240	9	**30**	**30**	20	**30**	20	**30**	20	**30**	**30**			**2.0**
270	9	**30**	**30**	30	**30**	30	**30**	30	**30**	**30**			**2.6**

A.1 Optimized panel lay-ups

Lay-up	Thickness	Ratio	EI_x
[30, 30, 20, 30, 20, 30, 20, 30, 30]	240	0.5000	8.45
[40, 40, 30, 40, 30, 40, 30, 40, 40]	330	0.5023	21.93
[20, 20, 40, 40, 30, 40, 40, 20, 20]	270	0.5059	11.98
[30, 30, 40, 40, 30, 40, 40, 30, 30]	310	0.5106	18.08
[20, 20, 40, 40, 40, 40, 40, 20, 20]	280	0.5177	13.26
[40, 40, 30, 40, 40, 40, 30, 40, 40]	340	0.5178	23.74
[30, 30, 40, 40, 40, 40, 40, 30, 30]	320	0.5221	19.73
[30, 30, 20, 30, 30, 30, 20, 30, 30]	250	0.5228	9.41
[30, 30, 30, 40, 30, 40, 30, 30, 30]	290	0.5406	14.51
[20, 20, 30, 40, 20, 40, 30, 20, 20]	240	0.5484	8.18
[30, 30, 20, 40, 20, 40, 20, 30, 30]	260	0.5516	10.38
[30, 30, 30, 40, 40, 40, 30, 30, 30]	300	0.5567	15.90
[20, 20, 30, 40, 30, 40, 30, 20, 20]	250	0.5667	9.14
[30, 40, 20, 20, 20, 20, 20, 40, 30]	240	0.5738	8.05
[30, 30, 20, 40, 30, 40, 20, 30, 30]	270	0.5755	11.45
[20, 20, 30, 40, 40, 40, 30, 20, 20]	260	0.5840	10.17
[30, 40, 40, 20, 30, 20, 40, 40, 30]	290	0.5960	14.01
[30, 40, 20, 20, 30, 20, 20, 40, 30]	250	0.5975	8.97
[30, 30, 20, 40, 40, 40, 20, 30, 30]	280	0.5981	12.59
[30, 40, 30, 20, 30, 20, 30, 40, 30]	270	0.5999	11.28
[30, 40, 40, 30, 20, 30, 40, 40, 30]	300	0.6102	15.37
[30, 40, 30, 30, 20, 30, 30, 40, 30]	280	0.6208	12.42
[30, 40, 40, 30, 30, 30, 40, 40, 30]	310	0.6211	16.85
[30, 40, 20, 30, 20, 30, 20, 40, 30]	260	0.6274	9.90
[30, 40, 40, 40, 20, 40, 40, 40, 30]	320	0.6358	18.36
[30, 40, 30, 30, 30, 30, 30, 40, 30]	290	0.6374	13.65
[30, 40, 40, 40, 30, 40, 40, 40, 30]	330	0.6478	19.99
[30, 40, 20, 30, 30, 30, 20, 40, 30]	270	0.6517	10.92
[20, 30, 40, 20, 20, 20, 40, 30, 20]	240	0.6536	7.66
[20, 30, 40, 20, 30, 20, 40, 30, 20]	250	0.6582	8.64
[30, 40, 30, 40, 20, 40, 30, 40, 30]	300	0.6585	14.92
[30, 40, 40, 40, 40, 40, 40, 40, 30]	340	0.6592	21.71
[20, 30, 40, 30, 20, 30, 40, 30, 20]	260	0.6707	9.64
[20, 20, 20, 40, 40, 40, 20, 20, 20]	240	0.6744	7.57
[30, 40, 30, 40, 30, 40, 30, 40, 30]	310	0.6760	16.29
[20, 30, 40, 30, 30, 30, 40, 30, 20]	270	0.6784	10.75
[30, 40, 30, 40, 40, 40, 30, 40, 30]	320	0.6926	17.75
[20, 30, 40, 40, 20, 40, 40, 30, 20]	280	0.6928	11.89
[20, 30, 40, 40, 30, 40, 40, 30, 20]	290	0.7033	13.13
[20, 30, 40, 40, 40, 40, 40, 30, 20]	300	0.7132	14.45
[20, 30, 30, 30, 20, 30, 30, 30, 20]	240	0.7143	7.39
[20, 30, 30, 30, 30, 30, 30, 30, 20]	250	0.7290	8.28
[20, 30, 30, 40, 20, 40, 30, 30, 20]	260	0.7520	9.20
[20, 30, 30, 40, 30, 40, 30, 30, 20]	270	0.7693	10.20
[20, 30, 30, 40, 40, 40, 30, 30, 20]	280	0.7853	11.27
[20, 30, 20, 40, 20, 40, 20, 30, 20]	240	0.8247	6.94
[20, 30, 20, 40, 30, 40, 20, 30, 20]	250	0.8524	7.73
[20, 40, 40, 20, 30, 20, 40, 40, 20]	270	0.8613	9.69
[20, 40, 40, 30, 20, 30, 40, 40, 20]	280	0.8730	10.74
[20, 30, 20, 40, 40, 40, 20, 30, 20]	260	0.8778	8.58
[20, 40, 40, 30, 30, 30, 40, 40, 20]	290	0.8797	11.89
[20, 40, 30, 20, 20, 20, 30, 40, 20]	240	0.8824	6.73
[20, 40, 40, 40, 20, 40, 40, 40, 20]	300	0.8929	13.08
[20, 40, 30, 20, 30, 20, 30, 40, 20]	250	0.8951	7.56
[20, 40, 40, 40, 30, 40, 40, 40, 20]	310	0.9020	14.36
[20, 40, 40, 40, 40, 40, 40, 40, 20]	320	0.9104	15.72
[20, 40, 30, 30, 20, 30, 30, 40, 20]	260	0.9171	8.40
[20, 40, 30, 30, 30, 30, 30, 40, 20]	270	0.9318	9.34
[20, 40, 30, 40, 20, 40, 30, 40, 20]	280	0.9544	10.30
[20, 40, 20, 30, 20, 30, 20, 40, 20]	240	0.9614	6.46
[20, 40, 30, 40, 30, 40, 30, 40, 20]	290	0.9711	11.34
[20, 40, 30, 40, 40, 40, 30, 40, 20]	300	0.9865	12.46
[20, 40, 20, 30, 30, 30, 20, 40, 20]	250	0.9882	7.20
[20, 40, 20, 40, 20, 40, 20, 40, 20]	260	1.0249	7.96
[20, 40, 20, 40, 30, 40, 20, 40, 20]	270	1.0531	8.79
[20, 40, 20, 40, 40, 40, 20, 40, 20]	280	1.0788	9.68

Appendix B: Mesh sensitivity analysis

To ensure the reliability of numerical simulations, a sensitivity analysis is performed. The objective is to evaluate how the choice of mesh size influences the calculated results. In this study, a mesh sensitivity analysis is conducted for both static and dynamic calculations.

B.1 Static analysis

B.1.1 Plate theory

First it should be noted that RFEM 6 [15] uses Mindlin's plate theory [46] by default, which includes shear deformation. Including shear deflection leads to quite complex formulations for orthotropic plates. Wang et al. [64] related the Mindlin equations to the classical plate theory as formulated by Kirchhoff. For simply supported rectangular plates the relation simplifies to the following:

$$w^{\mathbb{M}} = w^{\mathbb{K}} + \frac{\mathfrak{M}^{\mathbb{K}}}{\kappa^2 G h} \tag{B.1}$$

with
- κ shear correction factor commonly assumed as $\kappa^2 = \frac{5}{6}$
- G shear modulus $[N/mm^2]$
- h total plate thickness [mm]

In this equation for the static equilibrium of plates, based on the Kirchhoff and Mindlin plate theories, the moment sum (or Marcus moment) is denoted as $\mathfrak{M}$. The superscripts $\mathbb{M}$ and $\mathbb{K}$ refer to the Kirchhoff and Mindlin plate theories respectively. A clear 'bending' and 'shear' deformation part can be distinguished.

For the mesh sensitivity analysis, the RFEM settings are adjusted to use the Kirchhoff model for calculations instead of the Mindlin model. By selecting the Kirchhoff model, shear deformation is not considered in the analysis, eliminating the need for shear deformation calculations during calibration. This simplification allows for a more focused evaluation of the mesh without the need for complex calculations.

The Kirchhoff plate solution for simply supported orthotropic plates under uniformly distributed loading has been introduced in section 4.2. A particularly insightful case arises when examining the limit as ϵ tends to ∞. In this scenario, where the plate becomes much longer in the x-direction relative to the y-direction, or where the stiffness properties between the principal directions differ significantly, the constants approach limiting values:

$$\beta_1 \to 0, \quad \beta_2 \to \frac{1}{8}.$$

Under these conditions, the bending moment formula derived by Timoshenko and Woinowsky-Krieger [60] (see Eq 4.4) simplifies to:

$$M_x \approx \frac{1}{8}\frac{E''}{E'_x}\sqrt{\frac{D_x}{D_y}}\, q_0 \frac{a^2}{\epsilon}$$

Recalling that

$$\epsilon = \frac{a}{b}\sqrt[4]{\frac{D_y}{D_x}}$$

ϵ can be substituted into the expression for M_x:

$$M_x \approx \frac{1}{8}\frac{E''}{E'_x}\sqrt{\frac{D_x}{D_y}}\, q_0 \frac{a^2}{\frac{a}{b}\sqrt[4]{\frac{D_y}{D_x}}} = \frac{1}{8} q_0 ab \frac{E''}{E'_x}\left(\frac{D_x}{D_y}\right)^{\frac{1}{2}-\frac{1}{4}} = \frac{1}{8} q_0 ab \frac{E''}{E'_x}\left(\frac{D_x}{D_y}\right)^{\frac{1}{4}}$$

If the case is considered where the material is isotropic or the stiffness ratios approach unity, then:

$$\frac{E''}{E'_x} \approx 1, \quad \frac{D_x}{D_y} \approx 1,$$

Which further reduces the bending moment to:

$$M_x \approx \frac{1}{8} q_0 ab.$$

For a plate with equal spans $a = b = L$, this becomes the classical formula for the maximum bending moment in a simply supported, uniformly loaded beam:

$$M_x \approx \frac{1}{8} q_0 L^2.$$

This shows that as $\epsilon \to \infty$, the orthotropic plate behaves increasingly like a single-span beam in the x-direction and the complex plate bending moment formula simplifies to the familiar beam bending moment expression.

B.1.2 Exact calculation

For a simply supported plate under uniform distributed loading, Navier's solution is expressed in the form rewritten by Timoshenko and Woinowsky-Krieger [60]:

$$w = \frac{16 q_0}{\pi^6} \sum_{m=1,3,5,\ldots}^{\infty} \sum_{n=1,3,5,\ldots}^{\infty} \frac{\sin \frac{m\pi x}{a} \sin \frac{n\pi y}{b}}{mn\left(\frac{m^4}{a^4} D_x + \frac{2m^2 n^2}{a^2 b^2} H + \frac{n^4}{b^4} D_y\right)} \tag{B.2}$$

with

	a, b	Plate lengths in the x- and y-directions, respectively (see Figure B.1a) [mm]
	D_x, D_y, H	Flexural rigidities as defined in Equation 4.1 [Nmm]
	x, y	Coordinates of interest, for plate centre: $x = \frac{a}{2}, y = \frac{b}{2}$ [mm]
	q_0	Uniformly distributed load [N/mm^2]

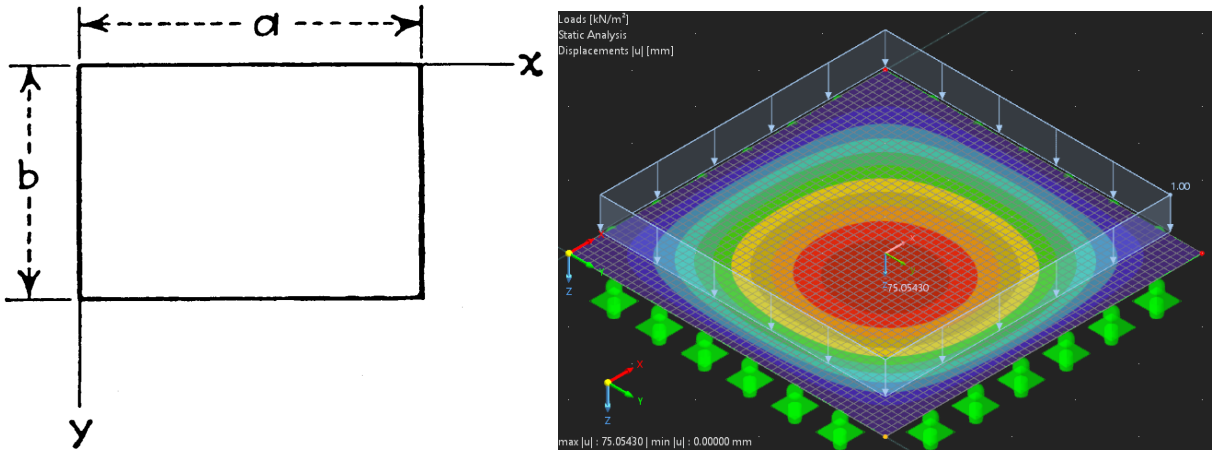

(a) Coordinate axes used [60] **(b)** Deformation under uniform load

Figure B.1: Plate geometry and deformation under uniform load

This exact solution assumes linear elastic, orthotropic behaviour with simply supported boundary conditions on all edges. The deflection is computed by evaluating the double series up to $m = n = 10$, ensuring convergence to a highly accurate value.

The calculations in RFEM use, solely for this mesh sensitivity analysis, the Kirchhoff-Love plate theory, consistent with the assumptions underlying the Navier solution. Consequently, the deflection computed from Equation B.2 represents a very accurate, near-exact reference value for

the plate's behaviour. This high accuracy allows the Navier solution to serve as a benchmark to calibrate and validate the mesh sensitivity in RFEM simulations effectively.

Three different panel configurations with lamella thicknesses of 10mm are modelled for square plates ($a = b$), subjected to a uniform load of $1.0kN/m^2$. The mesh sensitivity analysis compares the relative error of RFEM results against the Navier reference solution for multiple mesh sizes, as shown in Figure B.2.

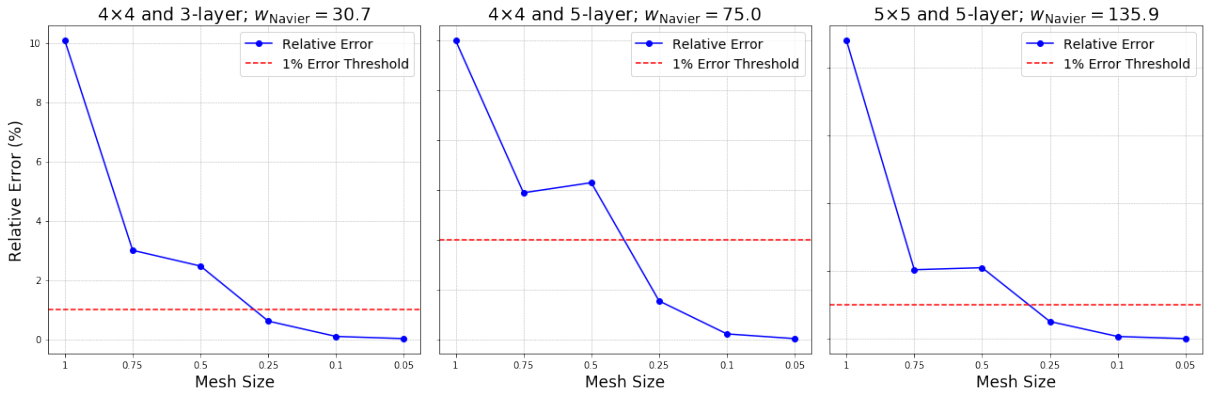

Figure B.2: Relative error in maximum deflection compared to the Navier reference solution for different CLT panel configurations under uniform loading.

The plots illustrate the relative error for the three configurations: (a) 4×4 and 3-layer, (b) 4×4 and 5-layer, and (c) 5×5 and 5-layer panels. An error threshold of 1% is used to determine an acceptable mesh size. For this criterion, a mesh with element size 0.25×0.25 mm is sufficient to ensure reliable results in RFEM.

B.1.3 Mesh Sensitivity using numerical calculation

The static analysis focuses on the distribution of shear force and bending moment along a critical line hinge region within the floor system. In finite element models of floor structures with point supports, localised stress singularities arise at these support locations, causing theoretically infinite stresses and unreliable local numerical results [60]. Consequently, direct evaluation of the response exactly at the supports is not recommended.

Instead of assessing sensitivity at a single point, this study evaluates the force and moment distributions along the entire length of the line hinge. This approach provides a better understanding of how the structure behaves overall and avoids mistakes that can happen if only a single point is considered. By looking at the full curves, it can be seen whether the mesh properly represents the real physical behaviour instead of focusing only on peak values.

The Navier solution is employed to calibrate the mesh for plate deflections, providing a near-exact benchmark for plate behaviour. However, the system studied in this report focusses on point-supported plates instead of the simply supported edges assumed in the classical Navier solution. Therefore, Navier's solution cannot be directly applied to this case. Therefore, to visualize and quantify mesh convergence effects in the FEM, a mesh sensitivity analysis is conducted by comparing results for larger mesh sizes against those obtained from the finest mesh of size $0.05 \times 0.05m^2$. This reference mesh is treated as a very close approximation for the line hinge segment being studied. It allows to estimate the error practically since there is no exact analytical solution for this more complex case. The 0.05×0.05 mesh size was already shown to be very accurate in the exact Navier plate calculation, so it can be trusted as an accurate reference.

The floor system modelled consists of three panels arranged in the minor direction, spanning two lengths of $5.25\,m$ each. Along the longitudinal direction, a total length of $3 \times 6 = 18.0\,m$ is considered. The system is subjected to a chequerboard load pattern, where alternating panels

carry loads to simulate non-uniform occupancy or variable live loads. The applied loads are:

$$Q_{sw} = 0.27 \times 4.20 = 1.13 \frac{kN}{m^2} \quad ; \quad Q_g = 1.0 \frac{kN}{m^2} \quad ; \quad Q_q = 3.0 \frac{kN}{m^2}$$

This loading configuration results in the force distributions shown in Figure B.3, which corresponds to a mesh size of $0.25 \times 0.25\,m^2$. The governing line hinge section is clearly identifiable, and multiple mesh sizes are applied to this floor structure to assess convergence.

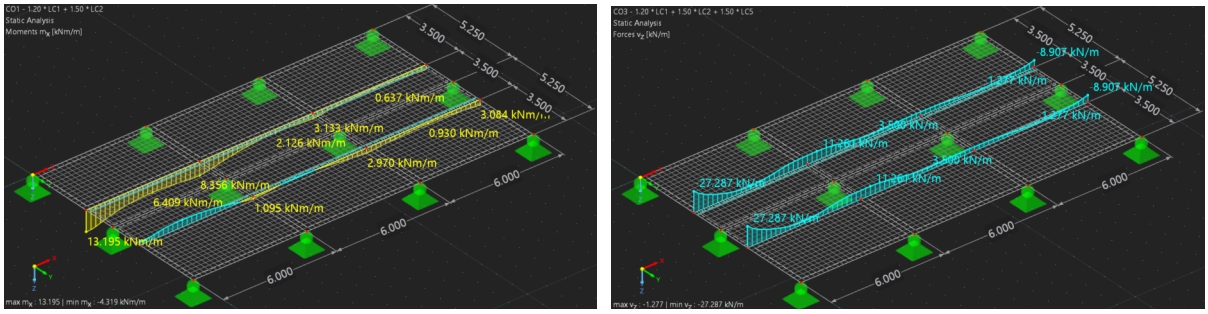

(a) Bending moment m_x **(b)** Shear force v_z

Figure B.3: Line hinge force distributions for mesh size $0.25 \times 0.25\,m^2$

Figure B.4 shows both the distribution of bending moment (m_x) and shear force (v_z) along a $6m$ segment of the line hinge (top), as well as the corresponding relative errors compared to the finest mesh ($0.05 \times 0.05\,m^2$) (bottom). The error is computed point-wise by interpolating the coarser mesh results to align with the reference mesh locations.

Some fluctuations in the relative error can be observed, especially near peaks or inflection points. These are mainly caused by interpolation effects and the limited ability of coarse meshes to represent smooth variations. Despite this, a relative error within roughly 5% is considered acceptable for engineering design. From the figure, it can be seen that a mesh size of $0.25 \times 0.25 m^2$ returns sufficiently accurate results while maintaining reasonable computational cost.

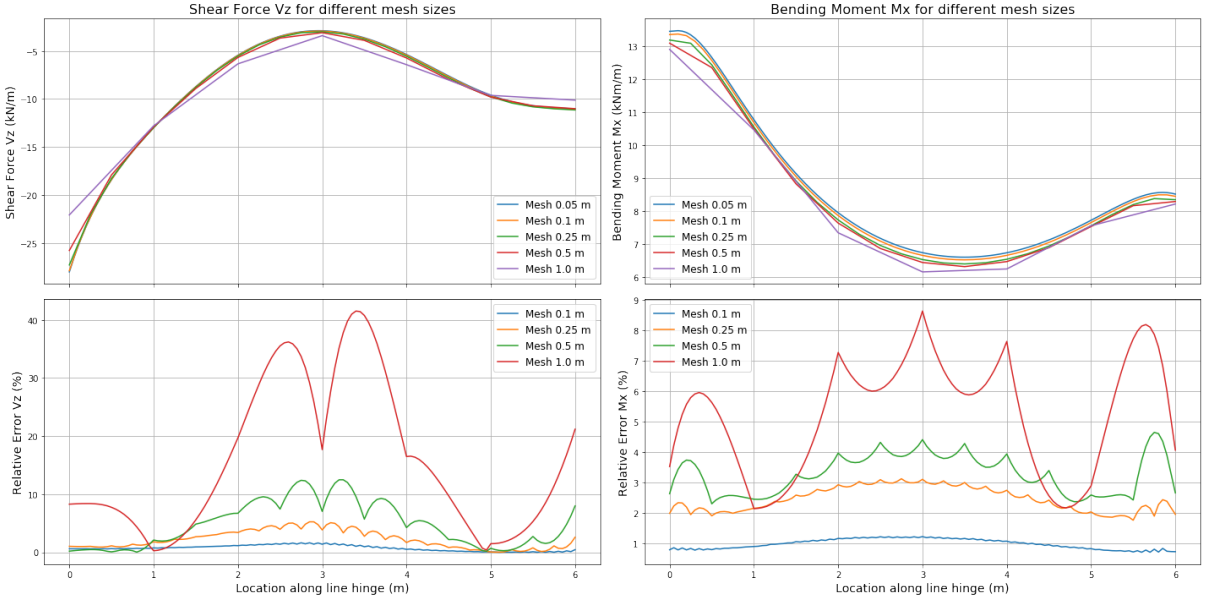

Figure B.4: Relative error of force calculations compared to a fine mesh ($0.05 \times 0.05\,m^2$)

B.1.4 Mesh static analysis

The mesh sensitivity analysis, supported by both numerical and exact calculations, indicates that a mesh size of $0.25 \times 0.25 m^2$ is optimal for static analysis. The Navier-based exact solution for plate deflection confirms that this mesh yields a relative error below 1%, ensuring high accuracy

in capturing global behaviour. In the more complex floor system, numerical results for bending moments and shear forces also show relative errors within 5% when compared to a very fine mesh. This confirms that the chosen mesh size accurately captures both deflection and internal force distributions. Hence, $0.25 \times 0.25m^2$ provides a robust and efficient mesh resolution for engineering design.

B.2 Dynamic analysis

B.2.1 Analytical Plate Frequency Model

As described in Section 5.3, the dynamic analysis and resulting design figures are based on the first 10 mode shapes. A sensitivity study focused solely on the fundamental frequency would therefore be insufficient. Unlike in the static analysis, where RFEM 6 allows the user to select between Mindlin and Kirchhoff plate theories, this selection has no effect on the modal analysis. In RFEM 6, the Mindlin plate theory is always applied for dynamic calculations, as it includes shear deformation and better captures real-world behaviour. According to the software developers, this choice ensures a more realistic representation of structural mass and stiffness, which is especially important for accurate vibration analysis.

Kirchhoff–Love plates

In the vibration analysis of plates, modal shapes describe the distinct deformation patterns that occur at specific natural frequencies. Each mode shape is characterized by two integers, m and n, representing the number of half sine waves along the x- and y-directions, respectively. Figure B.5 illustrates the physical meaning of mode shapes, showing some of the possibilities of deformation forms.

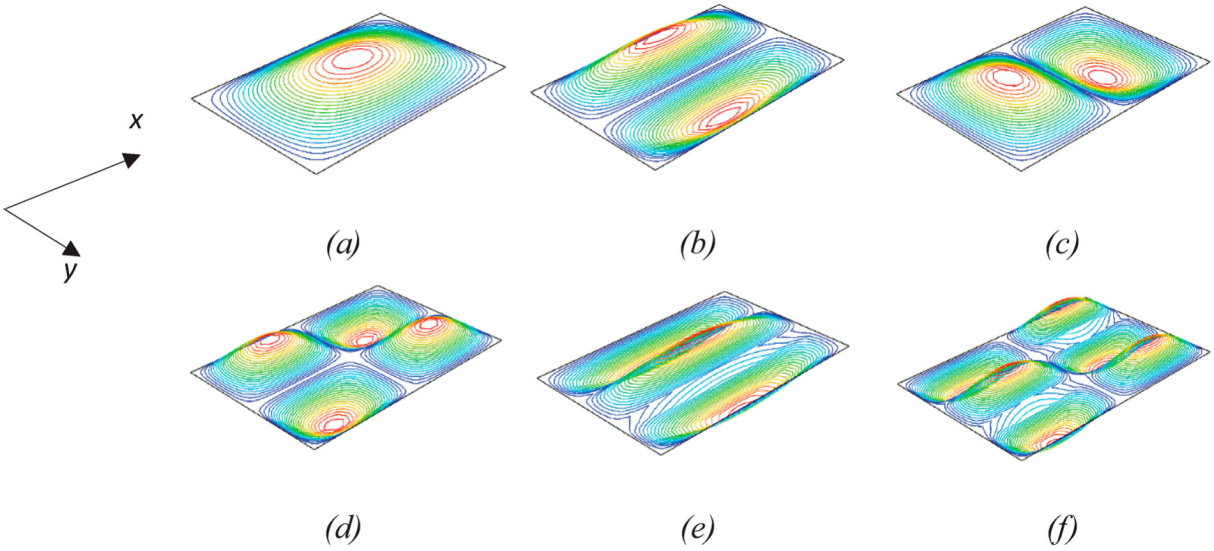

Figure B.5: Mode shapes of a three-ply simply supported CLT plate for the following numbers of half-sinewaves (m,n) in the x- and y-directions, respectively: (a) 1,1; (b) 1,2; (c) 2,1; (d) 2,2; (e) 1,3 (f) 2,3 [62]

For isotropic plates, the modal behaviour is symmetric due to uniform stiffness in all directions. In contrast, orthotropic plates have direction-dependent stiffnesses, leading to asymmetrical modal behaviour. This causes both the shape and frequency of each (m, n) mode to change. To characterize the vibration response of orthotropic plates, the natural angular frequency ω_{mn} is expressed as a function of plate properties and modal indices. This frequency depends on the material stiffness in both directions, the mass distribution, geometry and the chosen mode shape (m, n).

For orthotropic Kirchhoff plates with simply supported edges, an analytical expression for ω_{mn}

can be derived, as shown in [62]:

$$\omega_{m,n} = \left(\frac{\pi}{a}\right)^2 \times \sqrt{\frac{D_x}{\rho h} \times \left[m^4 + n^4 \times \left(\frac{a}{b}\right)^4 \times \frac{D_y}{D_x} + 2 \times (mn)^2 \times \left(\frac{a}{b}\right)^2 \times \frac{H}{D_x}\right]} \tag{B.3}$$

with

m, n	mode numbers in the x- and y-directions respectively
a, b	dimensions of the plate [m]
h	total plate thickness [m]
ρ	density of the plate $[kg/m^3]$
D_x, D_y	flexural rigidities in x- and y-direction [Nm]
H	coupling stiffness [Nm]

This expression originates from classical plate theory (Kirchhoff–Love), extended with orthotropic bending stiffness in both x and y directions and includes coupling stiffness H.

Mindlin Correction for Shear Deformation

To account for transverse shear deformation, particularly important in thick plates or in lower vibration modes, the dimensionless frequency parameter requires correction. Kirchhoff plate theory assumes that cross-sections stay perpendicular to the mid-surface after bending, meaning shear deformation is ignored. This works well for thin plates but can overestimate natural frequencies in thicker ones.

Mindlin plate theory, on the other hand, extends the classical approach by including first-order shear deformation and rotary inertia effects [46]. This theory introduces a shear correction factor κ, making it more accurate for thick plates or where shear flexibility plays a role. Modern FE software packages, such as RFEM 6, often employ Mindlin theory by default, even in modal analysis, to ensure a closer approximation to real physical behaviour.

To adjust the frequency predicted by Kirchhoff plate theory for shear deformation effects, a corrected dimensionless frequency λ_{mn} is calculated from the uncorrected value $\bar{\lambda}_{mn}$ (originating from Kirchhoff theory), as shown in [63]:

$$\lambda_{mn} = \frac{36\kappa^2(1-\nu)}{\beta^4}\left(\left[1 + \frac{\beta^2\sqrt{\bar{\lambda}_{mn}}}{12}\left(1 + \frac{2}{(1-\nu)\kappa^2}\right)\right] - \sqrt{\left[1 + \frac{\beta^2\sqrt{\bar{\lambda}_{mn}}}{12}\left(1 + \frac{2}{(1-\nu)\kappa^2}\right)\right]^2 - \frac{\beta^4\bar{\lambda}_{mn}}{18(1-\nu)\kappa^2}}\right) \tag{B.4}$$

with

$\beta = \frac{h}{b}$	Relative thickness
$\chi = \frac{a}{b}$	Aspect ratio
$\bar{\lambda}_{mn} = \pi^4\left(n^2 + \frac{m^2}{\chi^2}\right)^2$	frequency factor corresponding to classical thin plate
κ	Shear correction factor (typically $\frac{5}{6}$)
ν	Poisson's ratio

This corrected expression for λ_{mn} captures the influence of shear deformation, aligning better with Mindlin-type results and improving the validity of analytical predictions, particularly when comparing to finite element outcomes or design criteria that rely on more realistic assumptions.

B.2.2 Exact calculation

This formulation provides an efficient way to estimate natural frequencies for orthotropic, laminated plates using a reduced-order analytical model. It is particularly useful in early-stage

design, sensitivity analyses, and as a validation tool for numerical results.

Figure B.6 compares the natural frequencies obtained from the Mindlin plate theory with those from finite element mesh results for the first ten modes. The comparison shows good agreement for the first two modes, with errors of approximately 2 and 5%. For modes up to $(m, n) = (2, 2)$, deviations generally remain below 15%. However, for higher modes, the deviations increase noticeably.

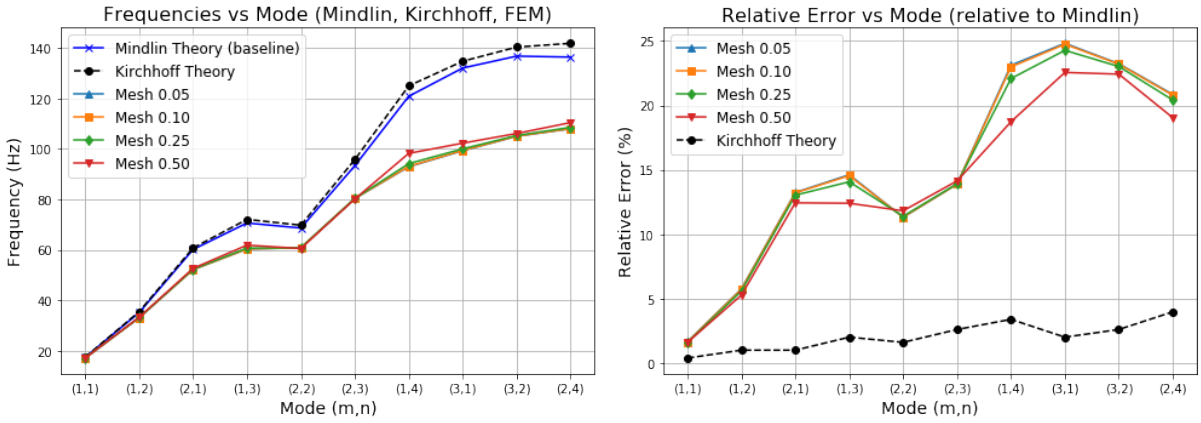

Figure B.6: Frequencies for multiple mode shapes

The primary reason for these deviations is that higher modes are more sensitive to complex stiffness interactions and coupling effects that are simplified or neglected in the analytical model. In particular, while the Mindlin theory accounts for transverse shear deformation and orthotropic stiffness components D_x, D_y and H, it does not fully capture higher-order coupling effects or geometric non-linearities that become significant in more complex vibration shapes.

Mindlin theory provides a reliable baseline for frequency estimation and mesh sensitivity assessment in modal analysis. However, for detailed evaluation, particularly of higher vibration modes, numerical methods such as FEA are necessary. Therefore, calibrating mesh sizes solely based on exact analytical calculations is not ideal and alternative approaches should be considered.

B.2.3 Mesh Sensitivity using numerical calculation

A mesh sensitivity analysis was conducted on a arbitrary design graph to evaluate the influence of mesh size on the stiffness requirements for vibration control. Three mesh sizes (0.05, 0.10 and 0.25) were used to generate corresponding design graphs, as shown in Figure B.7.

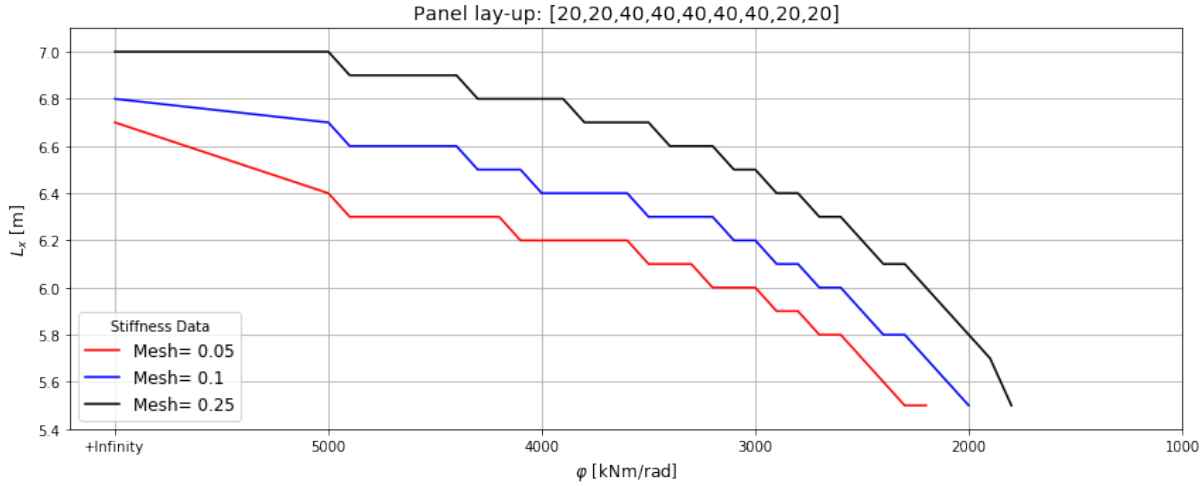

Figure B.7: Mesh comparison for a design graph

The results indicate some variation between meshes, especially when comparing stiffness values

horizontally for a given L_x. Differences in required stiffness to meet vibration criteria can reach up to $\pm 1000\,\text{kNm/rad}$, which is a significant variation.

Considering the increased computational cost of the finest mesh (0.05×0.05), the design graphs are constructed using the 0.10×0.10 mesh size, which offers a good balance between accuracy and efficiency. For broader parameter studies, where capturing overall trends is more important than exact values, the coarser 0.25×0.25 mesh is sometimes used to save computation time.

It is important to note that vibration design should not be performed exactly at the limit lines shown in the graphs. A suitable safety margin should always be maintained to account for model uncertainties, material variability and possible dynamic effects not fully captured by the analysis.

Appendix C: Model verification

C.1 Introduction

To validate the accuracy of the proposed connection models, verification is performed using experimental data from two independent studies. The splice plate connection is verified against test results presented by Hosseini et al. [30], which investigate the rotational behaviour of splice plate connections in CLT systems. For the butt-joint connection, experimental data from Zhang and Chui [68] are used, offering a relevant basis for assessing the mechanical response of such joints under loading. These two experimental setups provide valuable benchmarks for evaluating both the stiffness and strength predictions from the Python and RFEM models introduced in this report.

To ensure a fair and meaningful comparison between model output and experimental data, the test results are converted to characteristic values using the procedure outlined in Annex D of NEN-EN 1990 [20]. The characteristic value is determined using Equation C.1, which adjusts the mean value of the test results based on the number of tests performed and the coefficient of variation. This correction accounts for the statistical uncertainty present in small sample sizes and allows for a more consistent comparison between experimentally obtained values and those predicted by the model.

$$X_{k(n)} = m_x \times (1 - k_n V_x) \tag{C.1}$$

with

m_x the mean value of the tests

V_x the coefficient of variation

k_n correction factor depending on the number of tests, see Table C.1

Table C.1: Values of k_n for the 5% characteristic value [20]

n	3	4	5	6	8	10	20	30	∞
k_n	3.37	2.63	2.33	2.18	2.00	1.92	1.76	1.73	1.64

C.2 Splice plate

C.2.1 Materials and method

Hosseini et al. [30] investigated four connection types under out-of-plane loading, under which the splice plate connection subject of this report. The splice plate configuration corresponds to the S1 series, which utilized screwed plywood splines to connect CLT panels. No material properties are reported, so these values are all taken from manufacturer data sheets.

The CLT used was a 7-layer system with a total thickness of $245mm$, each lamella was $35mm$ thick, manufactured by Kalesnikoff. The panels were of grade V2M6, composed of No.1/No.2 SPF lumber in both longitudinal and transverse directions, $\rho_k = 420\frac{kg}{m^3}$ for this CLT grade [4]. At the joint interface, the bottommost layer (7th layer) of the CLT panels was removed to allow for the installation of the spline plates. The splice plates themselves were made from Baltic birch plywood, grade B, with each plate measuring $400mm$ in length and $600mm$ in width and a thickness of $2 \times 19 = 38mm$. A manufacturer is not mentioned, but using a deceleration of performance of Metsä Wood structural birch plywood [44], the densities can be taken as $\rho_m = 680\frac{kg}{m^3}$ and $\rho_k = 630\frac{kg}{m^3}$.

The mechanical connection was achieved using twelve fully-threaded STS inserted at an angle of 45° at each side of the panel. Fully threaded ASSY plus VG screws Ø8×160 mm are used to connect the timber elements. Because the screws are manufactured by Würth, the equations as specified for strength and stiffness for Würth screws are used. The only difference to the equation mentioned in chapter 3.4 is $f_{head,k} = 23,0\frac{N}{mm^2}$, the ETA specifies this head pull-through

parameter for "ASSY" screws specifically [13]. Pre-drilled holes were used to guide the screws, ensuring proper alignment and embedment depth. A visual schematic and photographs of the setup are provided in Figure C.1.

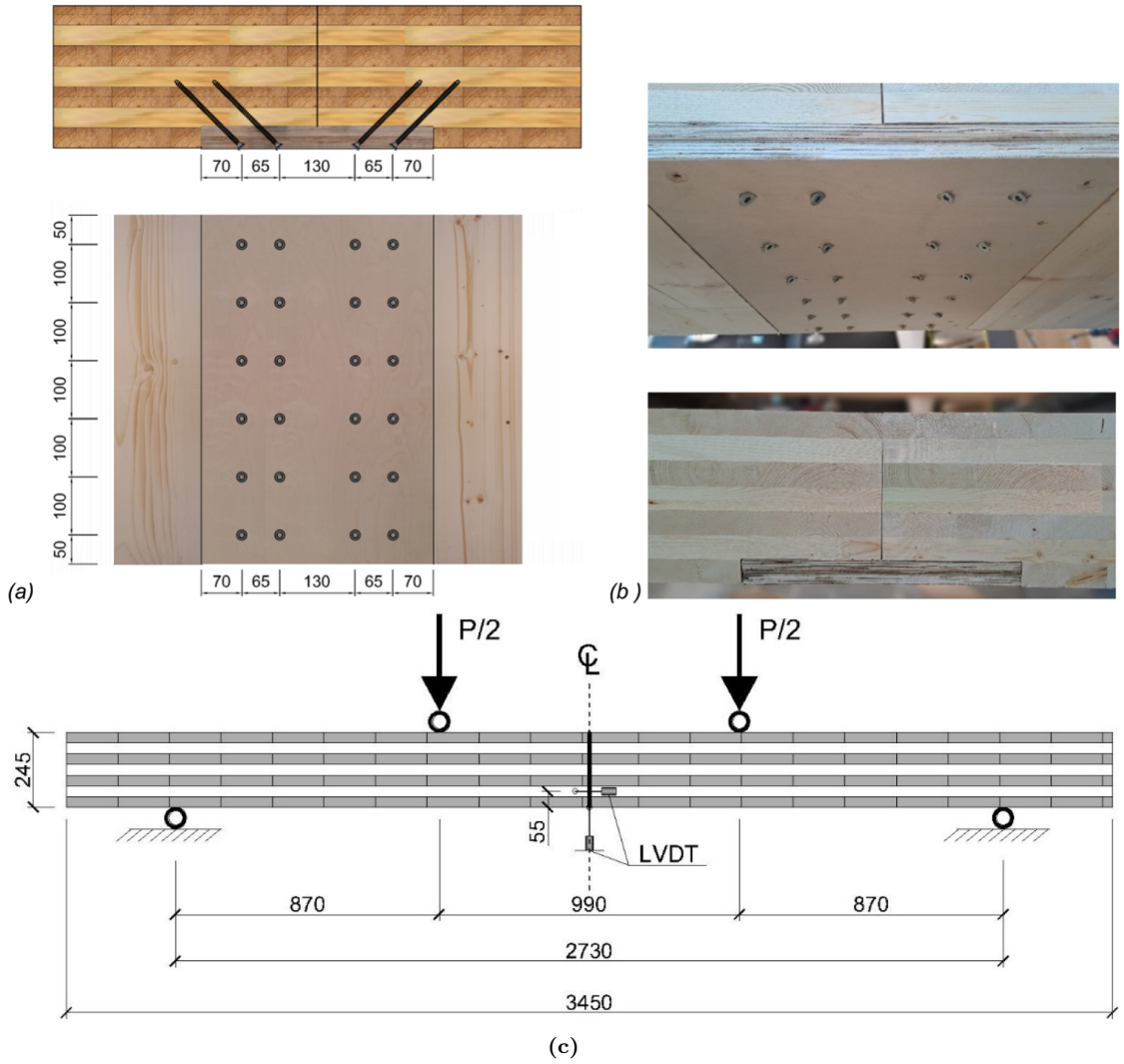

Figure C.1: Spline connection with inclined STS: (a) schematic (b) photos side and bottom (c) Schematic view of 4-point bending test [30]

Two mechanical tests were conducted to evaluate the structural response: a four-point bending test and a three-point bending test. The four-point bending test was designed to induce a constant moment region at the splice connection without introducing shear. The total panel length was 3450mm with a clear span of 2730mm between supports. Loads were applied at two lines located 870mm in distance from both supports. Mid-span deflections and gap openings at the connection line were captured using linear variable differential transformers (LVDTs). Each specimen was loaded to 40% of its expected capacity, unloaded to 10%, then loaded to failure. Failure was defined as a load drop to 80% of the peak. Key performance indicators included bending moment capacity, rotational stiffness, deflection at failure, and ductility.

In addition to the four-point bending test, a three-point bending test was conducted to assess the structural behaviour of the connection under simultaneous bending moment and out-of-plane shear force. However, it is important to note that in the context of the present numerical model, the splice plate is assumed to contribute only to the transfer of bending moments. The numerical evaluation isolates the rotational stiffness and moment capacity provided by the splice plate, while shear resistance is attributed to the bearing capacity of the butt-joint.

C.2.2 Results and comparison

The four-point bending test results for the S1 series demonstrated a ductile load-bearing response characterized by three distinct behavioural phases, see figure C.2. Initially, the specimens exhibited a linear elastic response up to approximately 70% of the peak load, with an average mid-span deflection of $22mm$. This was followed by a non-linear phase with gradually reduced stiffness. After reaching peak capacity, the specimens exhibited a gradual reduction in load-carrying capacity, without abrupt failure, reflecting a continued deformation response beyond the maximum load.

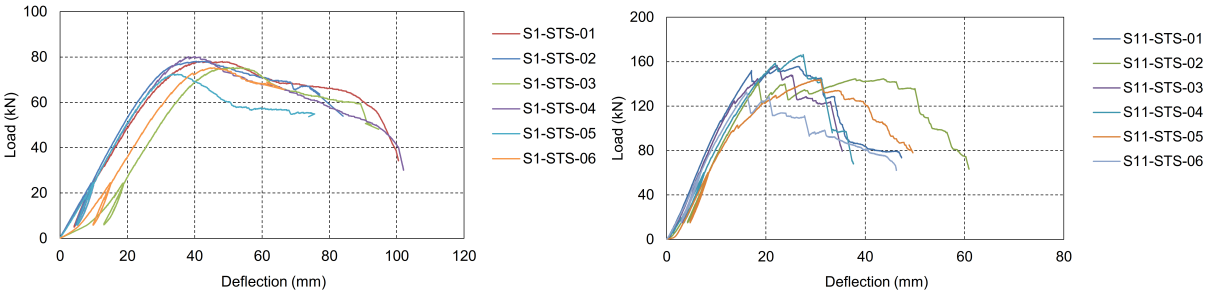

Figure C.2: Load-deflection curves for S1 series: (a) four-point bending, (b) three-point bending [30]

Two primary failure modes were observed across the tested specimens, see figure C.3. In some cases, tension-induced cracking in the plywood spline led to a sudden reduction in load-carrying capacity, while in others, partial withdrawal of the inclined screws caused a more gradual decline in performance. The gap opening at the connection was observed to be either symmetrical or localised respectively.

Figure C.3: Failure modes for S1: (a) plywood tension failure; (b) screw withdrawal [30]

The average bending moment capacity for the S1 series was reported as $33.3kNm$ and the corresponding rotational stiffness, evaluated within the service load range, was approximately $3555\frac{kNm}{rad}$. A total of six specimens were tested to failure under four-point bending, and the results are summarized in table C.2. While the strength values exhibited relatively low coefficients of variation, the stiffness measurements showed significantly higher variability. This difference can be attributed to the nature of timber and the connection system: strength-related failures are typically governed by distinct, well-defined mechanisms, making them less sensitive to minor inconsistencies in material properties or installation. In contrast, stiffness is more susceptible to variations in local wood characteristics, screw embedment quality, and seating conditions, all of which contribute to the observed spread in stiffness values.

Table C.2: Results from testing [30]

	C_φ [kNm/rad]	M_{ult} [kNm]
Mean	3555	33.3
Max	5644	34.9
Min	2347	31.5
CoV	34%	4%
$X_{k(6)}$	920	30.4

To compute the internal lever arm z for the stiffness model, the horizontal gap opening measured at the bottom of the connection ($\delta_{gap} = 5.2mm$) was used. The slip force in the screws was calculated using the following relations:

$$F_s = K_{sls,r} \times \delta_{gap} \quad \rightarrow \quad F_c = F_s \quad \rightarrow \quad h_c = \frac{F_c}{f_{c,90}} \quad \rightarrow \quad z = t_{CLT} - t_{LVL} - \frac{h_c}{2}$$

In the model, this compressive force was conservatively assumed to act at the bottom of the first lamella, reflecting a lower-bound estimate for the lever arm.

The connection properties, specifically the screws, CLT panel, and LVL spline, determine the input parameters for the numerical model described in Section C.5. The model calculates a rotational stiffness of $1484\frac{kNm}{rad}$, which compares reasonably well to the experimentally derived stiffness of $920\frac{kNm}{rad}$. Although the calculated value lies above the characteristic test result, it still falls below the lowest measured stiffness in the S1 series. Given the limited number of specimens and the high coefficient of variation, typical for timber stiffness tests, the characteristic value likely underestimates the actual performance. Stiffness is also difficult to measure precisely due to local slip, embedment behaviour, and timber anisotropy. Part of the discrepancy may also arise from differences in timber properties. In the ETA method used for stiffness prediction, only screw geometry is considered, while test results reflect a broader range of variables such as timber species and local fibre orientation. Since ETA equations are calibrated across multiple timber types, variations in the CLT used for the tests may explain the deviation.

In addition to stiffness, the strength prediction of the connection was verified. Experimental results from the four-point bending tests indicate a characteristic bending moment capacity of $30.4kNm$. The model, using characteristic material values, returns a lower maximum moment capacity of $22.0kNm$.

In addition to stiffness, the strength prediction of the connection was verified. Experimental results from the four-point bending tests indicate a characteristic bending moment capacity of $30.4kNm$. The numerical model, utilizing mean material properties to better represent actual behaviour, predicts a lower maximum moment capacity of $22.0kNm$. This discrepancy can be attributed to several factors. Firstly, the ETA method, upon which the model is based, primarily considers elastic behaviour and does not fully capture the ductile performance exhibited by the screwed spline samples. As mentioned before, these samples demonstrated a linear response up to approximately 70% of the peak load (around 55kN) [30], corresponding to a bending moment of approximately $21.3kNm$, which closely aligns with the model's prediction. Beyond this point, the specimens exhibited non-linear behaviour, indicating that the model effectively captures the initial elastic response but does not account for the additional capacity provided by plastic deformations in the actual connection. Secondly, while mean values are used in the model, the actual density and strength of the timber in the tested specimens may exceed these assumed averages, leading to higher observed capacities.

C.3 Butt-joint

C.3.1 Materials and method

To verify the mechanical behaviour of the butt-joint connection, experimental results from Zhang and Chui [68] are used. Their study focused on evaluating the structural response of panel-to-panel joints in CLT floor systems under flexural loading. Only the test configuration that includes a butt-joint directly between two CLT panels is considered here for comparison. No measured material properties were reported, so the values are all taken from manufacturer data sheets.

The tested CLT specimens consisted of two panels joined at mid-span with a butt-joint, forming

a continuous span supported at both ends. Each panel was fabricated from five-layer CLT with a total thickness of $175mm$, they were manufactured by Nordic Structures [5]. In line with ANSI 177 [3] the 'Specific gravity for fastener design' is provided by the manufacturer, the use of this density is comparable to ρ_k, using SPF timber the characteristic density may be taken as $\rho_k = 420kg/m^3$. A mean density is not stated in the product report [5], so conservatively $\rho_m = \rho_k$ for the verification. The connection is created using fully threaded Rothoblaas screws [16], two screw types are tested; Ø9×160 and Ø9×200.

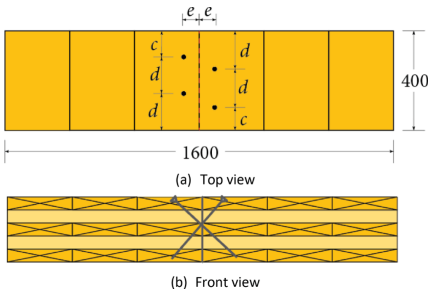

(a) BJ specimen configuration with 150 mm screw spacing (c=100 mm,d= 150 mm,e =50mm)

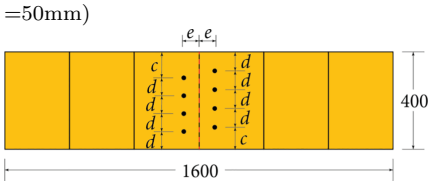

(b) Top view of BJ specimen configuration with 75 mm STS spacing (c =100 mm, d = 150 mm,e = 50 mm)

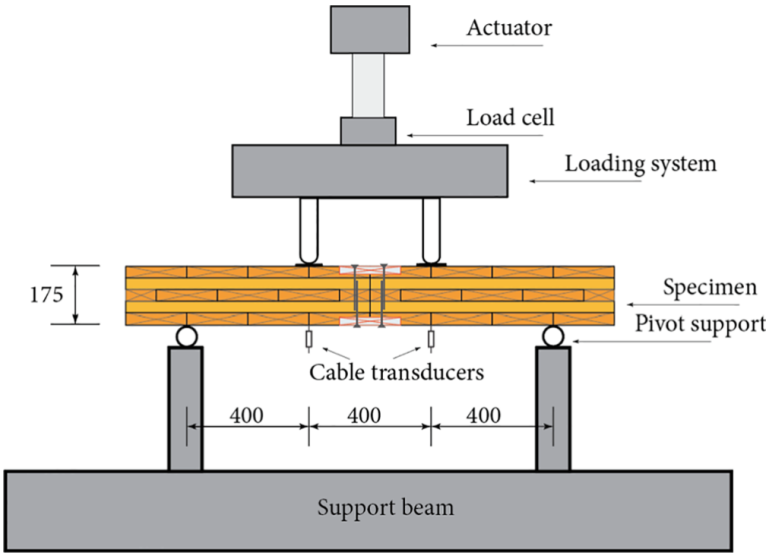

(c) Test set-up

Figure C.4: Schematic views of the butt-joint connection (a and b) and test setup (c) [68]

In this test setup, the butt joint is not utilized in the same way as in the connection design analysed in this report. As shown in Figure 3.8, the butt joint in the connection serves primarily to transfer a negative bending moment. In contrast, the experimental configuration, while geometrically similar (see Figure C.4 for comparison), is subjected to a positive bending moment. Although the physical layout remains the same, the direction of the internal lever arm is reversed in the test setup. This change is expected to result in reduced rotational stiffness and a lower maximum bending moment. Figure C.5 illustrates the specimen naming convention, which reflects the key parameters used as input for the verification model.

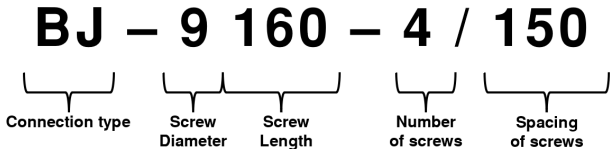

Figure C.5: Break down of the specimen codes

The test setup consisted of a four point bending test to apply a pure flexural moment with negligible shear. On a simply supported beam with a span of $1200mm$ concentrated loads were applied at $\frac{L}{3}$ and $\frac{2L}{3}$ using a hydraulic actuator. Displacement was measured using LVDTs positioned near mid-span and load was recorded throughout the test using a calibrated load cell.

C.3.2 Results and comparison

The butt-joint specimens in this study exhibited distinct ductile failure behaviour. The behaviour was governed by relative rotation and joint opening, consistent with the assumptions of the butt-joint model used in this report, see figure C.6. The failure modes were consistent across the

tested series and primarily involved screw head pull-through and localized crushing of the CLT panel near the connection. No failure in the screws was observed after testing until failure.

(a) Typical failure modes for BJ specimens **(b)** Joint top pressing (BJ-9200-8/75 #1)

Figure C.6: Failure types observed in the tests [68]

The rotational stiffness and ultimate moment capacity were derived from moment-rotation curves. The stiffness values were calculated from the slope of the curve between 10% and 40% of the maximum moment. The results of these tests are summarized in table C.3. In table C.4 the characteristic values of the connections are calculated to use in the model verification. The specimen BJ-9200-4/150 is left out of the model verification, because of the small number of tests and the high coefficient of variation, this test is not usable.

Table C.3: Flexural stiffness and strength properties of different connection types [68]

Specimen series	Rotational stiffness [kNm/rad]					Ultimate moment [kNm]				
	#1	#2	#3	mean	CoV(%)	#1	#2	#3	mean	CoV(%)
BJ-9160-4/150	48.7	52.0	53.9	51.5	5	2.1	2.1	2.3	2.2	5
BJ-9200-4/150	45.2	21.2	34.8	33.7	36	2.0	1.1	1.9	1.7	28
BJ-9200-8/75	53.7	58.0	47.9	53.2	10	4.0	4.0	3.1	3.7	14

Table C.4: Characteristic values

	C_φ [kNm/rad]	M_{ult} [kNm]
BJ-9160-4/150	42.8	1.83
BJ-9200-8/75	35.3	1.95

The model, see paragraph C.5, returns a rotational stiffness of $11.5\frac{kNm}{rad}$ for BJ-9160-4/150, which is quite low compared to the tested characteristic value of $42.8\frac{kNm}{rad}$. This discrepancy is not unexpected, as stiffness is particularly difficult to model in timber connections. It strongly depends on the development of tensile force at the interface, which in turn determines the position of the compressive force at the top of the panel. This directly influences the internal lever arm, which is a critical factor in the calculation of rotational stiffness. Even small variations in these internal force distributions can significantly affect the outcome, making precise modelling of stiffness inherently sensitive. For BJ-9200-8/75, the model predicts a stiffness of $25.5\frac{kNm}{rad}$ which compares more favourably with the tested value of $35.3\frac{kNm}{rad}$.

In terms of strength, the model returns a rotational capacity of $1.88kNm$ for BJ-9160-4/150, which is slightly higher than the tested characteristic value of $1.83kNm$. BJ-9200-8/75 returns a rotational strength of $2.69kNm$, again higher than the tested characteristic value of $1.95kNm$. Notably, the model predictions for strength remain below the minimum individual test results for both series. However, because the characteristic values from the experiments are based on a small number of tests, they are significantly reduced according to Annex D of NEN-EN 1990 [38]. This statistical adjustment, while necessary, ensures a good base for comparison with

model predictions, but it may also lead to a characteristic value that underestimates the actual performance observed in testing.

Overall, the comparison indicates that the model aligns reasonably well with the experimental results. The strength predictions are conservative and fall on the safe side, while the stiffness differences are explained by known modelling challenges. Therefore, the model can be considered both validated and suitable for design applications involving similar butt-joint configurations.

C.4 Discussion

C.4.1 Elastic vs. Plastic-Like Behaviour

The numerical model developed in this study adopts an elastic approach, which inherently limits its ability to predict the non-linear or ductile behaviour often observed in experimental testing. In the S1 test series, for instance, the specimens exhibited a three-phase load–displacement response: an initial linear elastic phase up to approximately 70% of the peak load, followed by a gradual reduction in stiffness and plastic-like deformation before failure. Notably, the bending moment at this 70% load level (21.3,kNm) closely matches the model's predicted strength of $22.0kNm$, suggesting that the model reliably captures the connection's elastic behaviour. Beyond this range, physical mechanisms such as wood crushing, see figure C.6b, which are non-linear, dominate the response and fall outside the scope of the elastic model.

C.4.2 Rotational Measurement Methods

Rotational stiffness in timber connections is a critical parameter but is notoriously difficult to measure and model due to the complexity of the rotational response and lack of standardized procedures. Currently, there is no universally accepted standard solely dedicated to the measurement of rotational stiffness in timber connections. Existing guidelines such as ISO 6891 [19] provide general test protocols for mechanical fasteners, but they do not prescribe a specific method for determining rotational angles. In practice, different studies and test setups apply their own approaches to measure this rotational angle.

For instance, in the S1 test series, the rotation angle was calculated based on the gap opening at the bottom of the connection, measured with horizontal LVDTs, and divided by the panel depth, following the method used by Hosseini [30]. This definition captures the relative rotation between the two CLT elements but is sensitive to local deformation and eccentricities.

In contrast, Zhang and Chui [68] determine the angle using a geometric conversion method.

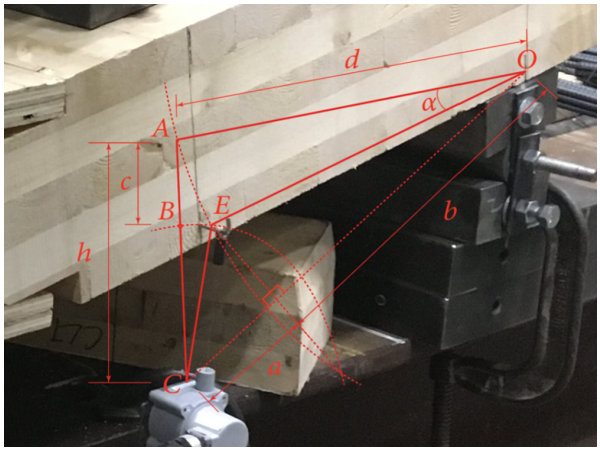

Figure C.7: Conversion of deflection to rotation [68]

Figure C.7 illustrates how the vertical deflection measured by a cable transducer is converted into a rotation angle. Initially, the transducer string extends along line AC. After loading, it shifts to a new position, CE, as the joint rotates. Since CE equals CB, the vertical deflection c is the change in string position from AC to CE. The lever arm, defined by points AO and EO, is the fixed distance between the point of rotation and the transducer. Using basic geometry, this deflection is translated into a rotation angle α. This enables the construction of moment–rotation curves used to evaluate the rotational stiffness and moment capacity of the connection.

The existence of different rotational definitions complicates direct comparison between test setups and model validation. A harmonized and standardized method for measuring joint rotation is

necessary to unify data interpretation, improve reproducibility, and enhance the reliability of numerical models.

C.4.3 Model Suitability

The comparison between model predictions and experimental results for both the splice plate and butt-joint configurations reveals a clear and interpretable trend. For strength, the model underestimates the capacity in the splice plate connection, while it slightly overestimates strength in the butt-joint series. The lower prediction for the splice plate can be attributed to the model's elastic assumptions, which do not capture the plastic deformation observed in tests. In contrast, the apparent overestimation in the butt-joint is likely a result of the limited number of tests, which leads to a statistically conservative characteristic value. Despite these differences, all predicted strengths remain within reasonable margins of the tested results, confirming the model's reliability for strength evaluation.

Rotational stiffness, on the other hand, is much harder to verify and model accurately. Both test series showed a high degree of variation and were based on a small number of samples, making direct comparisons less reliable. Timber connections are particularly sensitive to factors such as the material properties of the wood and the way loads are introduced, among others, which adds complexity to both testing and modelling. These factors make stiffness predictions inherently more uncertain than strength predictions.

In conclusion, while the model shows acceptable agreement with experimental data, particularly for strength, it would benefit from further refinement and validation. Additional testing across a wider range of configurations and specimens is essential to reduce statistical uncertainty and better understand the variability in connection behaviour.

C.5 Python calculation

In [1]:
```
%run Background_functions.ipynb
```

SPLICE PLATE CONNECTION

In [2]:
```
# Define the properties from CLT and LVL
t_LVL = 36
t_lamella = [35, 35, 35, 35, 35, 35, 35]
o_lamella = [0, 90, 0, 90, 0, 90, 0]
h_CLT_splice = np.sum(t_lamella)

rho_LVL = 680
rho_CLT = 420
fc90 = 5.3
fc0 = 11.5
width_panel = 600

# Define screw properties
d_screw = 8
d_head = 15
l_screw = 160
n_screw = 2
a_screw = np.deg2rad(45)
s_screw = 100

# Define outcome experimental study
K_splice = characteristic_value(3555, 34, 6)
M_ed_splice = characteristic_value(33.3, 4, 6)
```

In [3]:
```
draw_clt_panel(t_lamella, o_lamella)
```

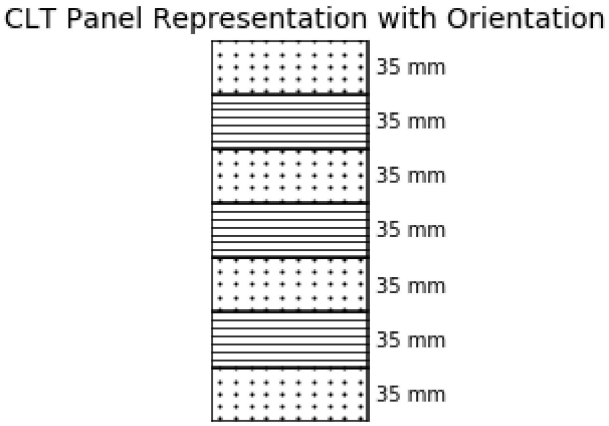

Stiffness

In [4]:
```
# ROTATIONAL STIFFNESS - splice plate
# Determining screw lengths and correction for head
l_screw_LVL = t_LVL / np.sin(a_screw)
l_screw_CLT = l_screw - l_screw_LVL

# Ksls_v calculation prEN 1995-1-1; 11.3.7.2
Ksls_v = 60 * (0.7 * d_screw)**1.7

# Ksls,ax calculation ETA-11/0190 (Würth schroeven)
Ksls_ax_LVL = 30 * d_screw * l_screw_LVL
Ksls_ax_CLT = 25 * d_screw * l_screw_CLT
Ksls_ax = 1 / (1 / Ksls_ax_LVL + 1 / Ksls_ax_CLT)

# Ksls calculation prEN 1995-1-1; 11.3.7.4
mu = 0.4
Ksls_r = Ksls_v * np.sin(a_screw) * (np.sin(a_screw) - mu * np.cos(a_screw)) + \
         Ksls_ax * np.cos(a_screw) * (np.cos(a_screw) + mu * np.sin(a_screw))

# Working with angles:
delta = 5.2
Fs = delta * Ksls_r
hc_stiff = Fs / fc90 / 1000
z_stiff = h_CLT_splice - t_LVL - hc_stiff / 2
theta = delta / z_stiff
Ms = Fs * z_stiff

# Rotational stiffness divided by two because of symmetry
Ms_tot = n_screw * width_panel / s_screw * Ms
C_phix = (Ms_tot / theta / 10**6) / 2
```

In [5]:
```
# INTERMEDIATE RESULTS
print(
f"The lateral stiffness of a single screw is calculated as {Ksls_v:.0f} N/mm \n"
f"The axial stiffness in the CLT member is calculated as {Ksls_ax_CLT:.0f} N/mm \n"
f"The axial stiffness in the LVL member is calculated as {Ksls_ax_LVL:.0f} N/mm \n"
f"The total axial stiffness 1 / (1/K_LVL + 1/K_CLT) equals {Ksls_ax:.0f} N/mm \n"
f"The stifness of the combined system equals {Ksls_r:.0f} N/mm \n"
f"So M = {z_stiff:.0f} × {Ksls_r:.0f} = {Ms:.0f} Nmm per screw")
```

```
The lateral stiffness of a single screw is calculated as 1122 N/mm
The axial stiffness in the CLT member is calculated as 21818 N/mm
The axial stiffness in the LVL member is calculated as 12219 N/mm
The total axial stiffness 1 / (1/K_LVL + 1/K_CLT) equals 7832 N/mm
The stifness of the combined system equals 5819 N/mm
So M = 206 × 5819 = 6238040 Nmm per screw
```

In [6]:
```
# RESULTS
print(
f"Selected splice plate connection properties: \n"
f"  Diameter: {d_screw} mm \n"
f"  Length: {l_screw} mm\n"
f"  Number of screws in a row: {n_screw} with a spacing of {s_screw} mm \n"
f"  Angle: {np.rad2deg(a_screw):.0f}° (converted to radians: {a_screw:.4f}) \n"
f"  LVL plate: {t_LVL} mm LVL \n"
f"  Gives a rotational stiffness of {C_phix:.0f} kNm/rad \n")

print(
f"Timber properties: \n"
f"  \u03C1 CLT: {rho_CLT} kg/m^3 \n"
f"  \u03C1 LVL: {rho_LVL} kg/m^3 \n")

print(
f"Rotational stiffness according to experimental study equals {K_splice:.0f} kNm/ra
```

```
Selected splice plate connection properties:
  Diameter: 8 mm
  Length: 160 mm
  Number of screws in a row: 2 with a spacing of 100 mm
  Angle: 45° (converted to radians: 0.7854)
  LVL plate: 36 mm LVL
  Gives a rotational stiffness of 1484 kNm/rad

Timber properties:
  ρ CLT: 420 kg/m^3
  ρ LVL: 680 kg/m^3

Rotational stiffness according to experimental study equals 920 kNm/rad
```

Strength

In [7]:
```
k_ax = 1.0

# Screws in CLT member
k_beta_CLT = 1.0
rho_a_CLT = 350
f_ax_CLT = 11.0
F_ax_Rk_CLT = k_ax * f_ax_CLT * d_screw * l_screw_CLT / k_beta_CLT * \
              (rho_CLT / rho_a_CLT)**0.8

# Screws in LVL member
k_beta_LVL = 1.5 * np.cos(a_screw)**2 + np.sin(a_screw)**2
f_head_LVL = 23.0
f_ax_LVL = 35.0
rho_a_LVL = 730
F_ax_LVL = k_ax * f_ax_LVL * d_screw * l_screw_LVL / k_beta_LVL * \
           (rho_LVL / rho_a_LVL)**0.8
F_head_LVL = f_head_LVL * d_head**2 * (rho_LVL / rho_a_LVL)**0.8
F_ax_Rk_LVL = max(F_ax_LVL, F_head_LVL)

# Failure of LVL plate or screw
    # characteristic tensile strength of ASSY plus VG
Ft_k = 22.0 * 10**3
    # tensional strength LVL
Ft_LVL = s_screw * t_LVL * 26

# Slip modulus per screw, taking into account friction between the members
mu = 0.4

# Forces at shear plane
Ft_Rk_LVL = F_ax_Rk_LVL * (np.cos(a_screw) + mu * np.sin(a_screw))
Ft_Rk_CLT = F_ax_Rk_CLT * (np.cos(a_screw) + mu * np.sin(a_screw))
Ft_Rk_screw = Ft_k * (np.cos(a_screw) + mu * np.sin(a_screw))

# Example values and their associated failure mechanisms
value1, value2, value3, value4 = Ft_Rk_LVL, Ft_Rk_CLT, Ft_LVL, Ft_Rk_screw
mechanisms = ["Failure in the LVL member",
              "Failure in the CLT member",
              "Failure of the LVL member itself",
              "Tension failure of the screw"]

# Find the governing value and its mechanism
values = [value1, value2, value3, value4]
min_value = min(values)
governing_mechanism = mechanisms[values.index(min_value)]
```

In [8]:
```
# INTERMEDIATE RESULTS
print(f"The axial withdrawal capacity in the CLT member equals {F_ax_Rk_CLT:.0f}N")
print(f"The axial withdrawal capacity in the LVL member equals {F_ax_LVL:.0f}N")
print(f"The head pull-through capacity in the LVL member equals {F_head_LVL:.0f}N")
print(f"The max tensional force in the screw equals {Ft_k:.0f}N")
print(f"These forces have to be corrected for the angle of the screw")
print(f"The max tensional force in the LVL member itself equals {Ft_LVL:.0f}N")
```

```
The axial withdrawal capacity in the CLT member equals 11107N
The axial withdrawal capacity in the LVL member equals 10775N
The head pull-through capacity in the LVL member equals 4889N
The max tensional force in the screw equals 22000N
These forces have to be corrected for the angle of the screw
The max tensional force in the LVL member itself equals 93600N
```

In [9]:
```
Ft = min_value
n_panel = n_screw * 600 / s_screw
n_ef = max(n_panel**0.9, 0.9 * n_panel)


Ft_tot = n_ef * Ft
Mrd = Mrd_calc(Ft_tot, t_lamella, o_lamella, fc0, fc90, t_LVL, panel_width=600)[0]

# RESULTS
print(f"The governing mechanism returns a max tensional force of {Ft:.0f}N \n"
      f"The failure mechanism is: {governing_mechanism}.")
print(f"The allowable bending moment at the connection is {Mrd:.1f}kNm")
print(f"Maximum moment according to experimental study equals {M_ed_splice:.1f}kNm")
```

```
The governing mechanism returns a max tensional force of 10667N
The failure mechanism is: Failure in the LVL member.
The allowable bending moment at the connection is 22.0kNm
Maximum moment according to experimental study equals 30.4kNm
```

BUTT-JOINT CONNECTION

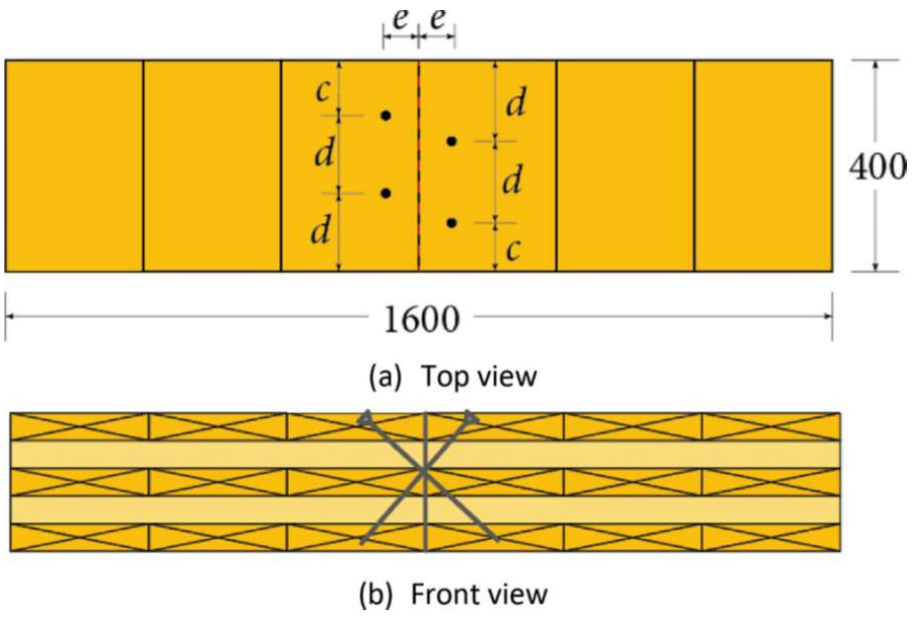

(a) Top view

(b) Front view

In [10]:
```
# Define the properties from CLT
t_lamella_bj = [35, 35, 35, 35, 35]
o_lamella_bj = [0, 90, 0, 90, 0]
h_CLT_butt = np.sum(t_lamella_bj)
rho_CLT = 420
```

In [11]:
```
# BJ-9160-4/150
# Values from experiment
c = 100
d1 = 150
e = 50

# Define screw properties
d_screw_v = 9
l_screw_v1 = 160
s_screw_v1 = d1
n_screw_v1 = 4
a_screw_v = np.deg2rad(45)

# Define outcome experimental study
K_butt1 = characteristic_value(51.5, 5, 3)
M_butt1 = characteristic_value(2.2, 5, 3)
```

In [12]:
```
# BJ-9200-8/75
# Values from experiment
c = 100
d2 = 75
e = 50

# Define screw properties
d_screw_v = 9
l_screw_v2 = 200
s_screw_v2 = d2
n_screw_v2 = 8
a_screw_v = np.deg2rad(45)

# Define outcome experimental study
K_butt2 = characteristic_value(53.2, 10, 3)
M_butt2 = characteristic_value(3.7, 14, 3)
```

Stiffness

In [13]:
```
# ROTATIONAL STIFFNESS - butt-joint
z_butt = e - t_lamella_bj[0]
delta = 10
theta = delta / z_butt
l1 = e / np.sin(a_screw_v)

# BJ-9160-4/150
l2 = l_screw_v1 - l1

Ksls_ax_1 = 25 * d_screw_v * l1
Ksls_ax_2 = 25 * d_screw_v * l2
Ksls_ax_butt1 = Ksls_ax_1 + Ksls_ax_2

# The force in each screw
Fs = Ksls_ax_butt1 * np.sin(a_screw_v) * z_butt * theta
Ms = Fs * z_butt

# Rotational stiffness
C_phix_butt1 = (n_screw_v1 * Ms / theta / 10**6) / 2

print(f"Selected shear connection properties in test BJ-9160-4/150: \n"
      f"  Diameter: {d_screw_v} mm \n"
      f"  Length: {l_screw_v1} mm\n"
      f"  Spacing of screws: {s_screw_v1:.0f} mm \n"
      f"  Gives a rotational stiffness of {C_phix_butt1:.1f} kNm/rad \n")
print(
f"Rotational stiffness according to experimental study equals {K_butt1:.1f} kNm/rad
print()

# BJ-9200-8/75
l3 = l_screw_v2 - l1

Ksls_ax_1 = 25 * d_screw * l1
Ksls_ax_3 = 25 * d_screw * l3
Ksls_ax_butt2 = Ksls_ax_1 + Ksls_ax_3

# The force in each screw
Fs = Ksls_ax_butt2 * np.sin(a_screw_v) * z_butt * theta
Ms = Fs * z_butt

# Rotational stiffness
C_phix_butt2 = (n_screw_v2 * Ms / theta / 10**6) / 2

print(f"Selected shear connection properties in test BJ-9200-8/75: \n"
      f"  Diameter: {d_screw_v} mm \n"
      f"  Length: {l_screw_v2} mm\n"
      f"  Spacing of screws: {s_screw_v2:.0f} mm \n"
      f"  Gives a rotational stiffness of {C_phix_butt2:.1f} kNm/rad \n")
print(
f"Rotational stiffness according to experimental study equals {K_butt2:.1f} kNm/rad
```

```
Selected shear connection properties in test BJ-9160-4/150:
  Diameter: 9 mm
  Length: 160 mm
  Spacing of screws: 150 mm
  Gives a rotational stiffness of 11.5 kNm/rad

Rotational stiffness according to experimental study equals 42.8 kNm/rad

Selected shear connection properties in test BJ-9200-8/75:
  Diameter: 9 mm
  Length: 200 mm
  Spacing of screws: 75 mm
  Gives a rotational stiffness of 25.5 kNm/rad

Rotational stiffness according to experimental study equals 35.3 kNm/rad
```

Strength

In [14]:
```
k_ax = 1.0
k_beta = 1.0
rho_a = 350
f_axk = 11.7

# Failure of LVL plate or screw
    # characteristic tensile strength of Rothoblaas screws
Ft_k = 25.4 * 10**3

# BJ-9160-4/150
n1 = 4
l_gov1 = min(l1, l2)
F_ax_CLT = k_ax * f_axk * d_screw_v * l_gov1 / k_beta * \
           (rho_CLT / rho_a_CLT)**0.8

Ft1 = min(F_ax_CLT, Ft_k) * np.sqrt(2) / 2
Ft_tot1 = n1 * Ft1 * 2
z_bottom = h_CLT_butt - e
Mrd1_calc = Mrd_calc(Ft_tot1, t_lamella_bj, o_lamella_bj,
                     9.0, 5.3, z_bottom, panel_width=400)[0]
Mrd1 = Mrd1_calc / 10**6

# BJ-9200-8/75
n2 = 8
l_gov2 = min(l1, l3)
F_ax_CLT = k_ax * f_axk * d_screw_v * l_gov2 / k_beta * \
           (rho_CLT / rho_a_CLT)**0.8

Ft2 = min(F_ax_CLT, Ft_k) * np.sqrt(2) / 2
Ft_tot2 = n2 * Ft2 * 2
z_bottom = h_CLT_butt - e
Mrd2_calc = Mrd_calc(Ft_tot2, t_lamella_bj, o_lamella_bj,
                     9.0, 5.3, z_bottom, panel_width=400)[0]
Mrd2 = Mrd2_calc / 10**6
```

In [15]:
```
print(f"Selected shear connection properties in test BJ-9160-4/150: \n"
      f"  Diameter: {d_screw_v} mm \n"
      f"  Length: {l_screw_v1} mm\n"
      f"  Spacing of screws: {s_screw_v1:.0f} mm \n"
      f"  Gives a rotational strength of {Mrd1:.2f} kNm \n")

print(
f"Rotational strength according to experimental study equals {M_butt1:.2f} kNm")
print()

print(f"Selected shear connection properties in test BJ-9200-8/75: \n"
      f"  Diameter: {d_screw_v} mm \n"
      f"  Length: {l_screw_v2} mm\n"
      f"  Spacing of screws: {s_screw_v2:.0f} mm \n"
      f"  Gives a rotational strength of {Mrd2:.2f} kNm \n")

print(
f"Rotational strength according to experimental study equals {M_butt2:.2f} kNm")
```

```
Selected shear connection properties in test BJ-9160-4/150:
  Diameter: 9 mm
  Length: 160 mm
  Spacing of screws: 150 mm
  Gives a rotational strength of 1.88 kNm

Rotational strength according to experimental study equals 1.83 kNm

Selected shear connection properties in test BJ-9200-8/75:
  Diameter: 9 mm
  Length: 200 mm
  Spacing of screws: 75 mm
  Gives a rotational strength of 2.69 kNm

Rotational strength according to experimental study equals 1.95 kNm
```

In [16]:
```
#
```

Appendix D: Quick Estimate panel height

To provide a quick method suggest a suitable panel height for a point-supported structural system, the flowchart from Section D can be used.

First, a stiffness ratio for the panel should be chosen. In Chapter 5 an optimum interval of [0.5, 1.0] is advised. A lower stiffness ratio results in relatively smaller bending moments in the line hinge. A higher ratio increases the chance that a floor system will meet vibrational demands.

Secondly, based on this stiffness ratio, the known grid size and loading, the bending moment can be estimated. Chapter 4 explains the use of this formula and introduces the effect of individual parameters. The estimated bending moment may be reduced with a factor φ_{red} to account for finite stiffness.

Thirdly, the tensional force in the connection should be determined. Based on the design rule proposed in Chapter 3 and some basic assumptions, the calculation process for the tensional force in the connection can be simplified. The design rule (see Sec. 3.7) states that the connection should be designed in such a way that axial withdrawal failure in the LVL panel is the governing failure mechanism. Now, using $\mu = 0.4$ [18], and Equation 2.25, the following equation can be formulated:

$$F_v = n_{ef} \times \frac{1.4 \times F_{ax,LVL}}{\sqrt{2}}$$

For the three screw types $F_{ax,LVL}$ is calculated for multiple LVL plate thicknesses, see Figure D.1. This is under the assumption that $F_{ax,CLT} \geq F_{ax,LVL}$ and $\mu = 0.4$. In this step some engineering judgment is needed, a LVL thickness, screw type and spacing should be chosen to determine the tensional force in this connection.

The fourth step is to use this tensional force and estimated bending moment to estimate the internal lever arm of the connection. The model determines this internal lever arm by using the compressive strengths of the individual lamella's. However, to simplify this relation, the simplified model as used for the rotational stiffness (see Fig. 3.8) can be used. This means the compressional force is located at the top of the first lamella orientated in the minor direction of the panel. The tensional force relates to the bending moment capacity by multiplication with the internal lever arm, thus the following equation can be formulated:

$$z_{est} = \frac{M_{est}}{F_t} = \frac{M_{est}}{\frac{F_{v,Rk}}{1.3} \times n_{ef}}$$

The estimation uses the characteristic shear force to calculate the internal lever arm for practicality, avoiding overly conservative results. A partial safety factor $\gamma_M = 1.3$ is applied for connections, while the k_{mod} factor is not included. For a different connection type the tensional force is thus calculated in a different manner. However, the internal lever arm is estimated in the same way.

It is also possible to do this step for any other connection type. The information needed to estimate the internal lever arm is the location of a compression and tensional force. For instance, in the case of the TC Fusion connection (see Sec. 3.1.1) the tensional force is at the location of the glued-in rod and the compressional force is located in the first lamella or the second, depending on the magnitude of the tensional force. An unfavourable assumption should be made for this compression point to eliminate the uncertainty of this location.

Now the internal lever arm is determined based on some quick calculations, it is possible to estimate the panel height. For the modelled connection in this thesis, the tensional force is located at the shear plane between the LVL panel and the CLT panel. The compressional point is at the bottom of the first lamella with thickness t_1. This leads to the following estimated panel height:

$$H_{CLT,\ est} = z_{est} + t_{LVL} + t_1$$

Again, this step can be done for any other panel-to-panel connection. The t_{LVL} value is, in physical terms, the distance from the bottom of the CLT panel to the location of the tensional force. The lamella thickness t_1 is the distance from the top of the panel to the compression point.

Based on this estimated panel height and the stiffness ratio η assumed at the beginning of this flowchart, a fitting panel should be chosen. In Table A.1 some relevant panel lay-ups are provided.

Now, everything is known of this connection. This allows for the last step; calculation of the rotational stiffness of the panel-to-panel connection. With this stiffness, the known grid dimensions and the panel properties (directional stiffness, stiffness ratio, permanent load and module count), the design graphs in Appendix F.1 can be used. If a specific panel is not present in the graph, the parameter study from Chapter 5 offers guidance to interpret similar panels.

This concludes a quick estimation process that ends with a fitting panel for the floor structure at hand. Now more detailed engineering is needed to optimize and verify other structural aspects of the floor structure. The model in Chapter 3 is deemed appropriate for more detailed engineering.

Flowchart

Optimum stiffness ratio

Choose connection properties

Estimate bending moment

$$H_{CLT,est} = z_{est} + t_{LVL} + t_1$$

With first lamella thickness $t_1 \approx 30$

$$z_{est} = \frac{M_{est}}{\frac{F_{v,Rk}}{1.3} \times n_{ef}}$$

Determine $F_{v,Rk}$

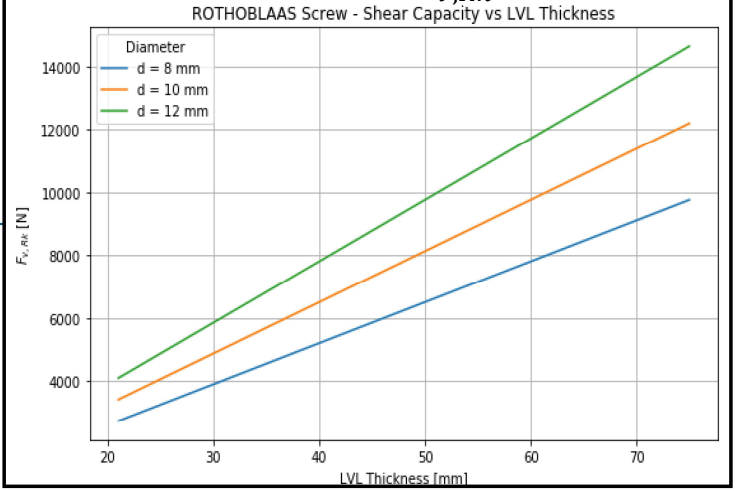

Determine fitting panel

```
Layup: [40, 40, 30, 40, 20, 40, 30, 40, 40] | Thickness: 320 | Ratio: 0.4862 | EIx: 20.210
Layup: [20, 20, 40, 30, 40, 30, 40, 20, 20] | Thickness: 260 | Ratio: 0.4865 | EIx: 10.838
Layup: [40, 40, 20, 30, 40, 30, 20, 40, 40] | Thickness: 300 | Ratio: 0.4868 | EIx: 16.646
Layup: [30, 30, 30, 30, 20, 30, 30, 30, 30] | Thickness: 260 | Ratio: 0.4875 | EIx: 10.831
Layup: [30, 30, 20, 20, 40, 20, 20, 30, 30] | Thickness: 240 | Ratio: 0.4909 | EIx: 8.4993
Layup: [40, 40, 20, 40, 20, 40, 20, 40, 40] | Thickness: 300 | Ratio: 0.4914 | EIx: 16.595
Layup: [40, 40, 40, 40, 30, 40, 40, 40, 40] | Thickness: 350 | Ratio: 0.4915 | EIx: 26.351
Layup: [20, 20, 40, 40, 20, 40, 40, 20, 20] | Thickness: 260 | Ratio: 0.4935 | EIx: 10.787
Layup: [30, 30, 40, 30, 40, 30, 40, 30, 30] | Thickness: 300 | Ratio: 0.4940 | EIx: 16.566
Layup: [30, 30, 40, 40, 20, 40, 40, 30, 30] | Thickness: 300 | Ratio: 0.4987 | EIx: 16.514
Layup: [30, 30, 20, 30, 20, 30, 20, 30, 30] | Thickness: 240 | Ratio: 0.5000 | EIx: 8.448
Layup: [40, 40, 30, 40, 30, 40, 30, 40, 40] | Thickness: 330 | Ratio: 0.5023 | EIx: 21.927
Layup: [30, 30, 30, 30, 30, 30, 30, 30, 30] | Thickness: 270 | Ratio: 0.5031 | EIx: 12.003
Layup: [40, 40, 40, 40, 40, 40, 40, 40, 40] | Thickness: 360 | Ratio: 0.5031 | EIx: 28.453
Layup: [20, 20, 40, 40, 30, 40, 40, 20, 20] | Thickness: 270 | Ratio: 0.5059 | EIx: 11.981
Layup: [30, 30, 40, 40, 30, 40, 40, 30, 30] | Thickness: 310 | Ratio: 0.5106 | EIx: 18.077
Layup: [40, 40, 20, 40, 30, 40, 20, 40, 40] | Thickness: 310 | Ratio: 0.5126 | EIx: 18.053
Layup: [20, 20, 40, 40, 40, 40, 40, 20, 20] | Thickness: 280 | Ratio: 0.5177 | EIx: 13.258
```

Calculate rotational stiffness using model

Check vibrations graph

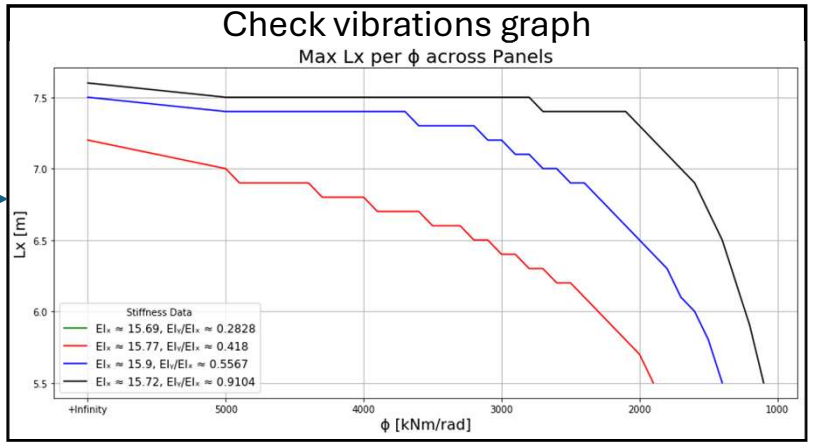

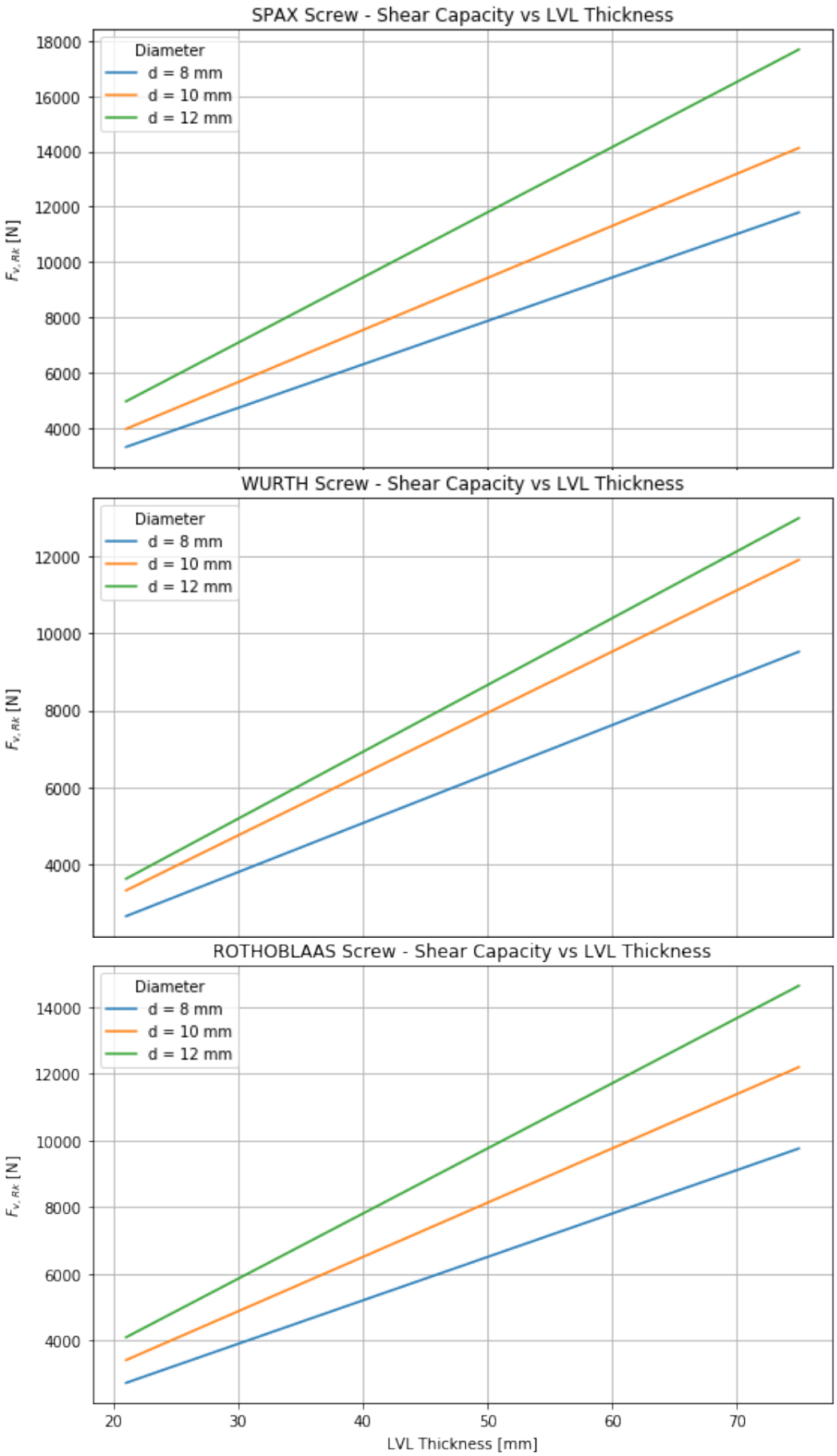

Figure D.1: Characteristic shear capacity ($\mu = 0.4$) for different screw types as a function of LVL thickness.

Appendix E: C_η-values

Table E.1: C_η-values for different L_y and η values in a single span configuration

$L_y \backslash \eta$	0.300	0.400	0.500	0.600	0.700	0.800	0.900	1.000
4.0	2.368	2.255	2.719	2.627	2.986	2.584	2.902	2.985
4.5	3.087	3.160	3.528	3.563	3.859	3.698	3.936	4.049
5.0	3.924	4.094	4.482	4.587	4.911	4.844	5.093	5.249
5.2	4.726	4.479	4.883	5.014	5.352	5.317	5.575	5.748
5.3	4.136	4.208	4.732	4.769	5.179	4.920	5.262	5.404
5.5	4.476	4.588	5.127	5.187	5.614	5.382	5.732	5.890
6.0	5.389	5.599	6.180	6.302	6.771	6.610	6.982	7.181

Table E.2: C_η-values for different L_y and η values in a continuous span configuration - 1 module

Loaded	L_y \ η	0.300	0.400	0.500	0.600	0.700	0.800	0.900	1.000
1 field	4.0	0.935	0.934	1.035	0.964	1.071	1.008	1.026	1.083
2 field		0.972	0.980	1.148	0.992	1.181	1.053	1.068	1.171
1 field	4.5	1.137	1.144	1.207	1.240	1.280	1.260	1.324	1.333
2 field		0.452	0.438	0.514	0.547	0.578	0.534	0.611	0.598
1 field	5.0	2.096	2.156	2.287	2.341	2.445	2.435	2.531	2.582
2 field		1.421	1.488	1.662	1.715	1.838	1.801	1.918	1.965
1 field	5.2	2.470	2.552	2.710	2.777	2.905	2.903	3.013	3.080
2 field		1.779	1.878	2.087	2.157	2.311	2.285	2.418	2.486
1 field	5.3	3.623	3.685	4.145	4.188	4.540	4.309	4.615	4.729
2 field		3.154	3.229	3.657	3.733	4.057	3.870	4.169	4.280
1 field	5.5	3.911	4.008	4.480	4.542	4.906	4.698	5.009	5.136
2 field		3.400	3.508	3.951	4.047	4.386	4.221	4.528	4.653
1 field	6.0	4.680	4.861	5.366	5.478	5.875	5.727	6.051	6.211
2 field		4.052	4.245	4.729	4.878	5.256	5.149	5.476	5.637

Table E.3: C_η-values for different L_y and η values in a continuous span configuration - 2 modules

Loaded	L_y \ η	0.300	0.400	0.500	0.600	0.700	0.800	0.900	1.000
1 field	4.0	0.927	0.922	1.014	0.943	1.047	0.970	0.997	1.045
2 field		0.969	0.953	1.123	0.964	1.161	1.007	1.040	1.129
1 field	4.5	1.196	1.181	1.265	1.312	1.357	1.309	1.406	1.406
2 field		0.608	0.560	0.695	0.743	0.805	0.702	0.844	0.828
1 field	5.0	2.055	2.073	2.204	2.291	2.378	2.335	2.479	2.501
2 field		1.401	1.412	1.617	1.717	1.841	1.742	1.944	1.960
1 field	5.2	2.388	2.421	2.568	2.674	2.774	2.739	2.899	2.930
2 field		1.701	1.726	1.950	2.076	2.217	2.129	2.350	2.378
1 field	5.3	4.168	4.175	4.770	4.912	5.331	4.987	5.482	5.585
2 field		3.600	3.614	4.150	4.319	4.689	4.395	4.869	4.956
1 field	5.5	4.409	4.435	5.043	5.210	5.630	5.305	5.816	5.920
2 field		3.797	3.829	4.371	4.572	4.994	4.669	5.158	5.247
1 field	6.0	5.040	5.118	5.724	5.983	6.403	6.133	6.678	6.788
2 field		4.310	4.393	4.946	5.226	5.603	5.379	5.904	6.001

Appendix F: Hivoss table

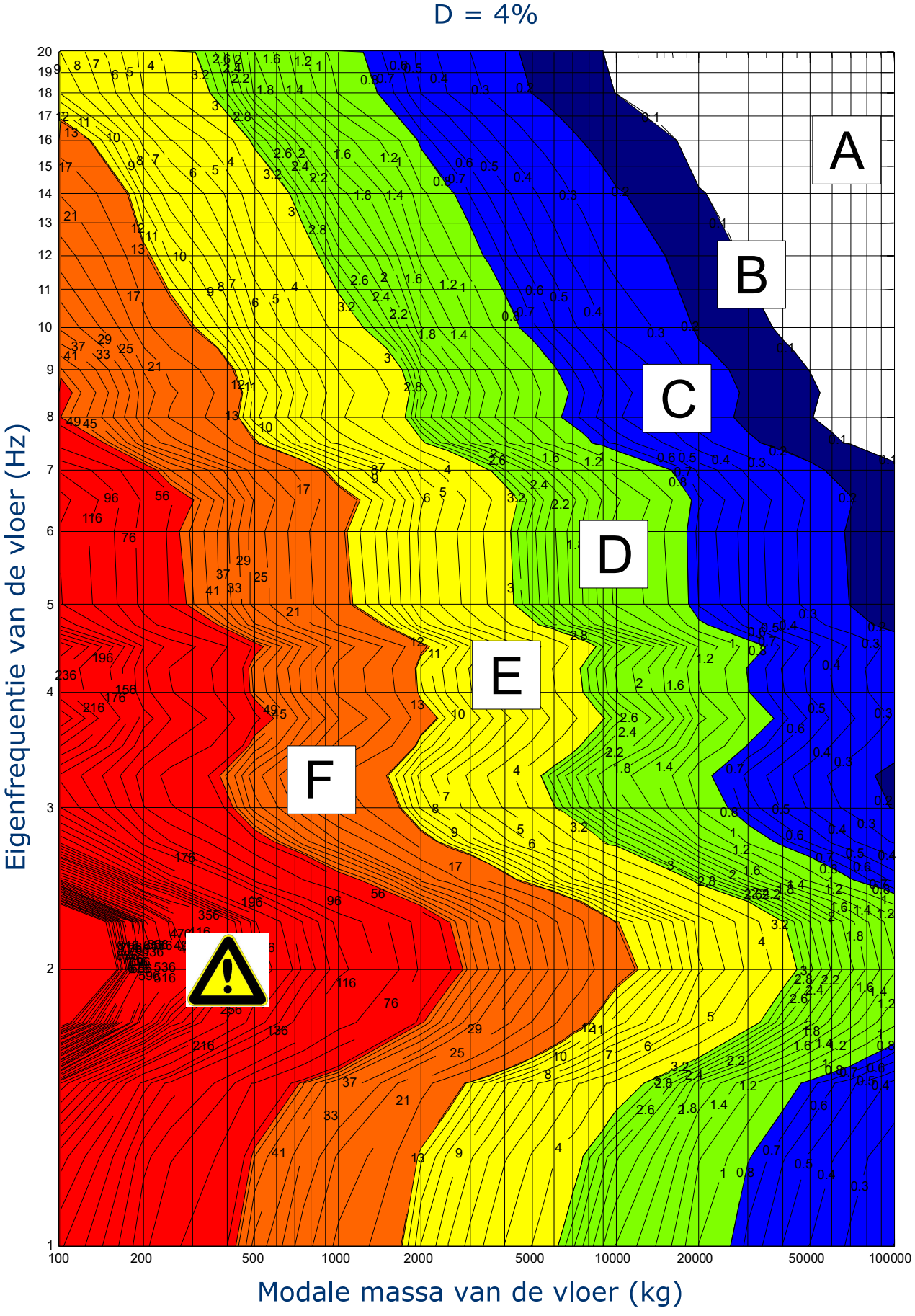

F.1 Design graph

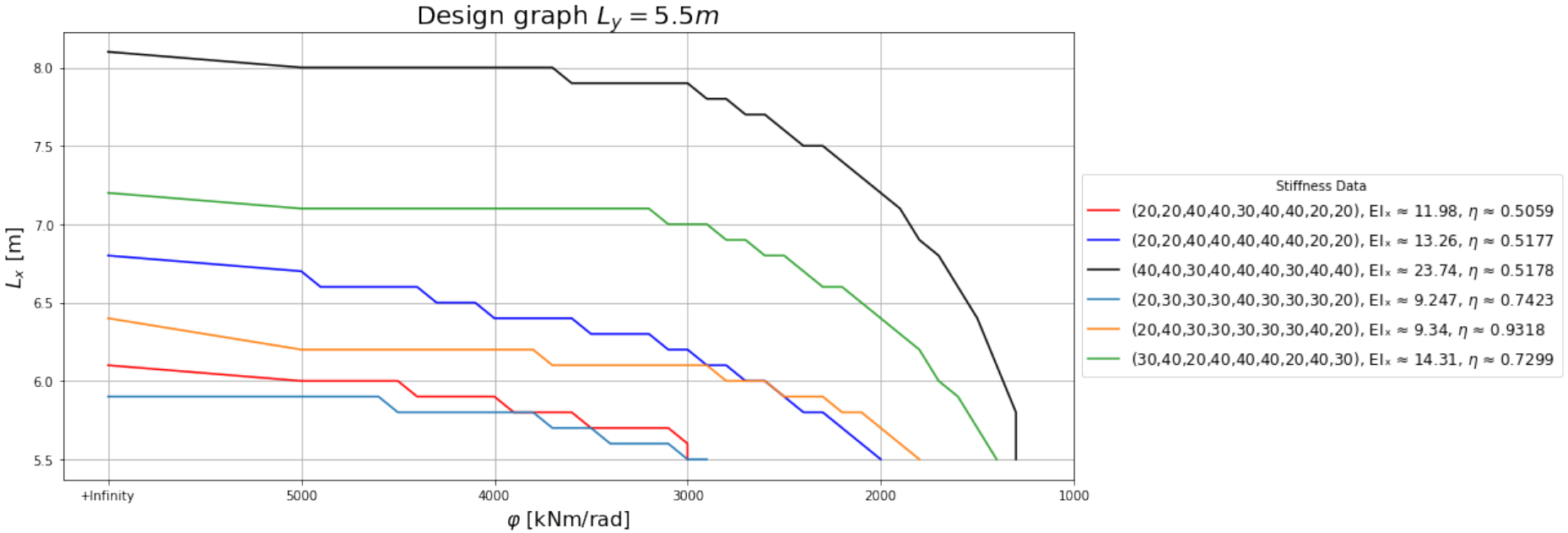

Figure F.1: Floor dimensions meeting Hivoss threshold values

Appendix G: Structural drawings

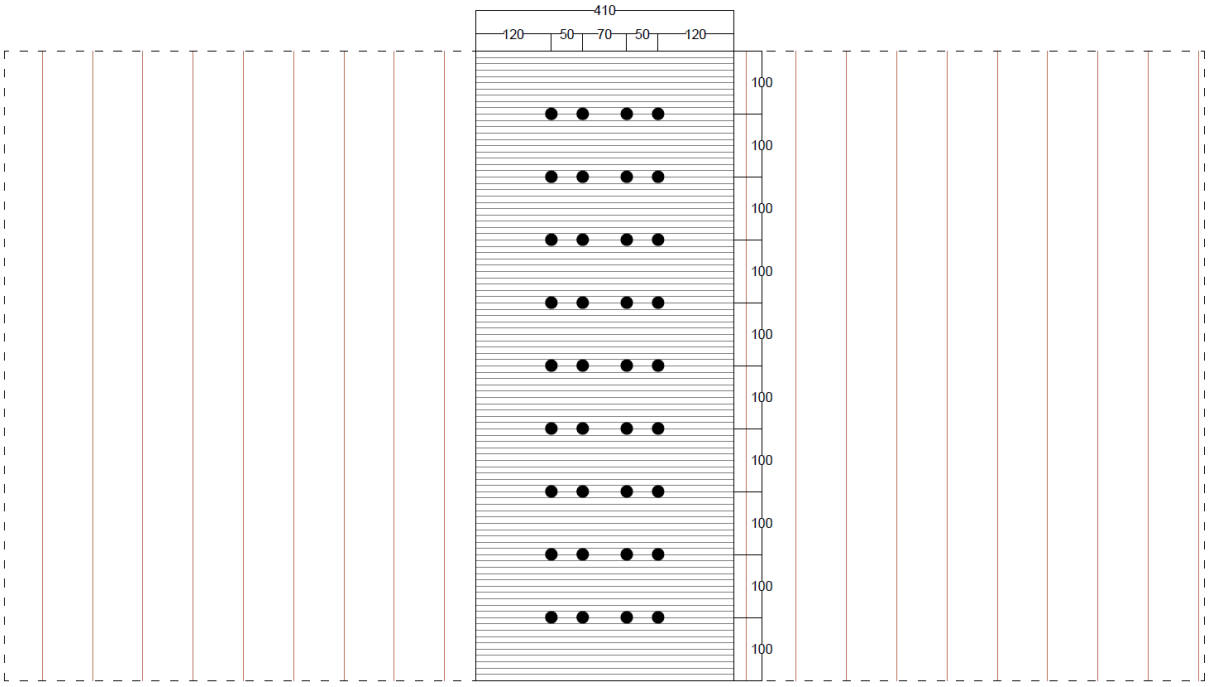

G.1 Post-and-beam system

G.2 Current situation

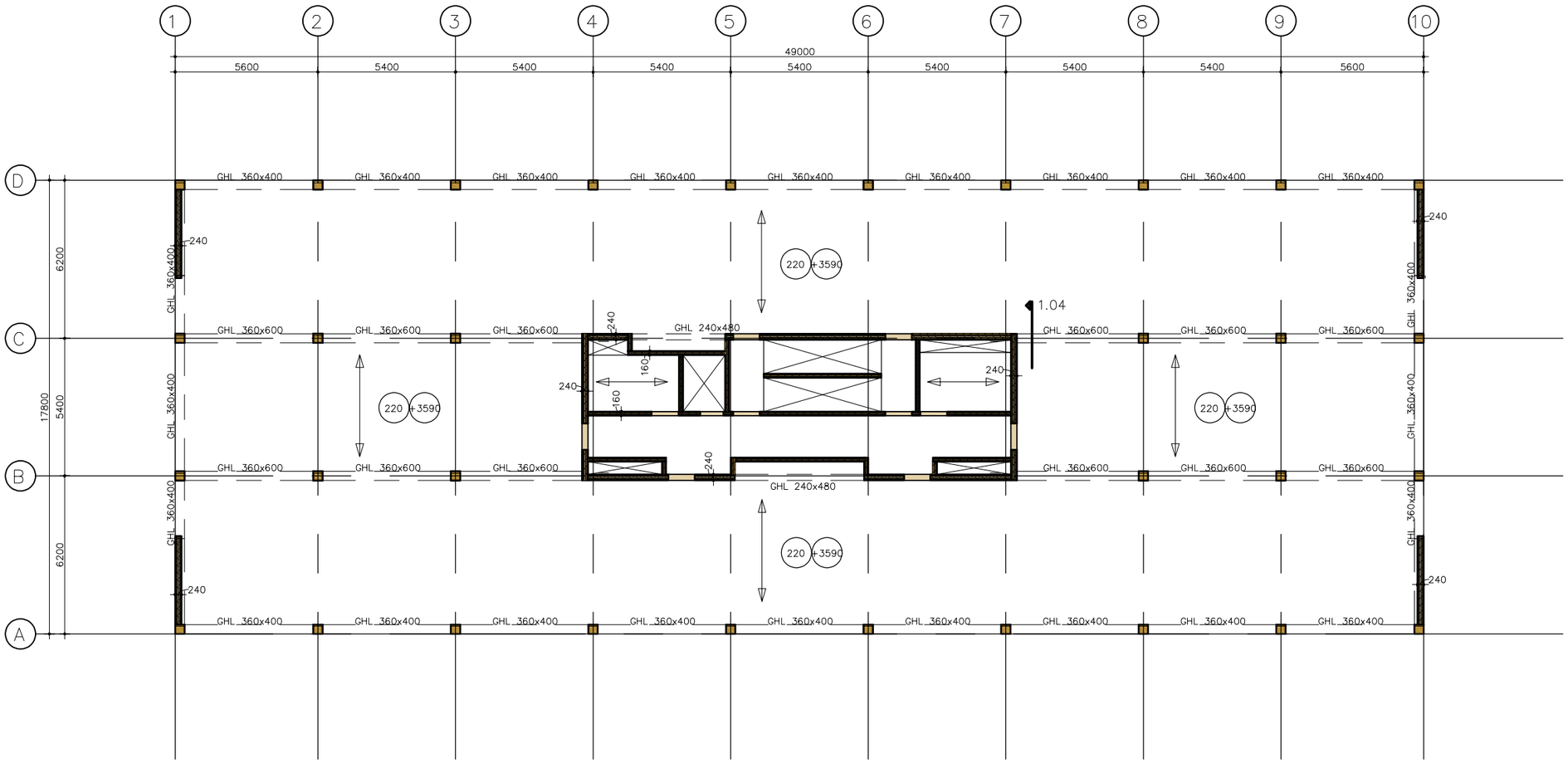

G.3 Point-supported system

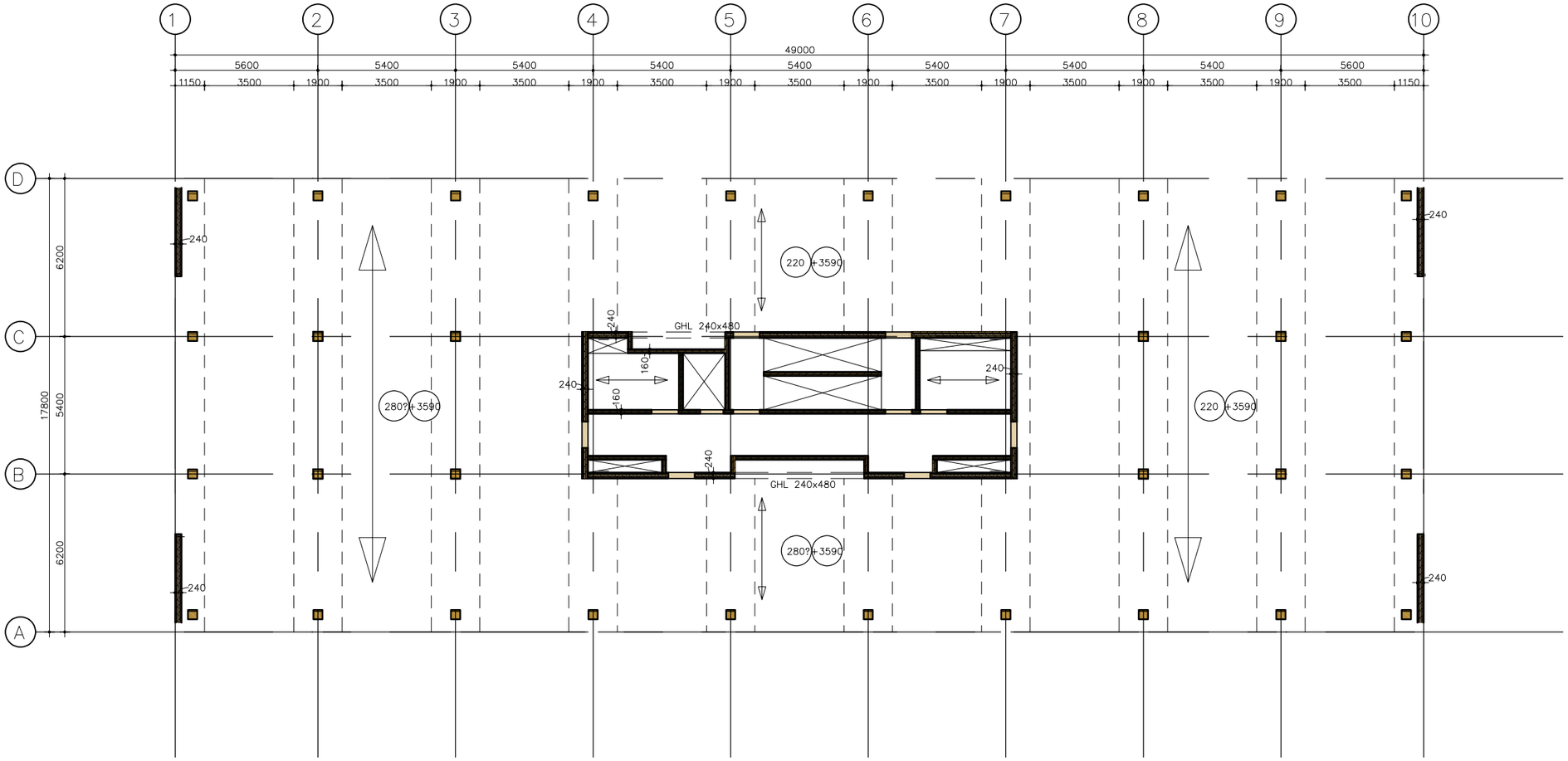

Appendix H: Stiffness model

In [1]:
```
%run Background_functions.ipynb
%run Stiffness_functions.ipynb
```

Connection properties

In [2]:
```
# CLT PROPERTIES
launch_clt_gui()
```

```
CLT Properties Set.
```

In [3]:
```
# LVL PROPERTIES
launch_lvl_gui()
```

```
LVL Properties Set.
```

In [4]:
```
# SPLICE PLATE PROPERTIES
launch_splice_plate_gui()
```

```
Splice plate screws set.
```

In [5]:
```
# BUTT-JOINT PROPERTIES
launch_butt_joint_gui()
```

```
Butt-joint screws set.
```

In [6]:
```
# Define the timber properties from their selections
mu = mu
t_LVL = lvl_thickness_selection['Thickness']
h_CLT = np.sum(t_lamella)

rho_LVL_k, rho_LVL = lvl_density[0], lvl_density[1]
rho_CLT_k, rho_CLT = clt_density[0], clt_density[1]

# Define the screw properties from their selections
Type, d_screw, dh, l_screw, s_screw, n_screw = (
    selected_splice_plate_properties[k] for k in
    ['Type', 'Diameter', 'Head_diameter', 'Length', 'Spacing', 'Number of screws'])

Type_v, d_screw_v, dhv, l_screw_v, s_screw_v, e_screw_v = (
    selected_shear_properties[k] for k in
    ['Type', 'Diameter', 'Head_diameter', 'Length', 'Spacing', 'Distance'])

a_screw = np.deg2rad(45)
```

In [7]:
```
draw_clt_panel(t_lamella, o_lamella)
```

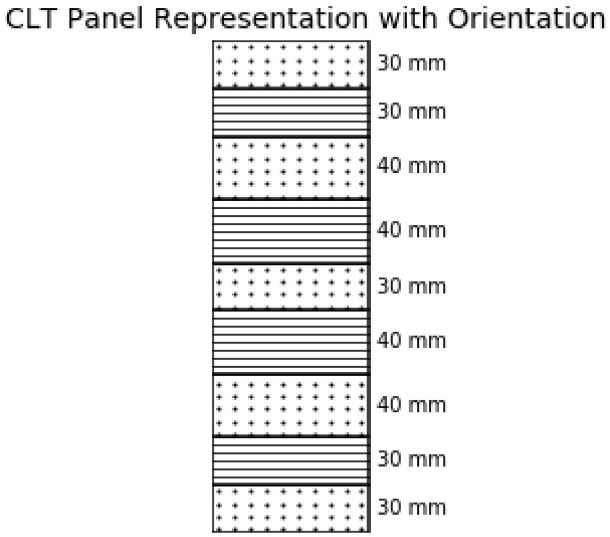

Splice plate calculation

In [8]:
```
# Input
Screw = [d_screw, l_screw, a_screw, s_screw, n_screw]
CLT = [t_lamella, o_lamella, rho_CLT, rho_CLT_k]
LVL = [t_LVL, rho_LVL, rho_LVL_k, lvl_timber]

# Output
C_phix = Splice_stiffness('ETA', Screw, CLT, LVL, mu)[0]
Ksls_r, Ksls_ax, Ksls_v, Ksls_ax_LVL, Ksls_ax_CLT = (
    Splice_stiffness('ETA', Screw, CLT, LVL, mu)[1])
z_splice = Splice_stiffness('ETA', Screw, CLT, LVL, mu)[2]

# INTERMEDIATE RESULTS
print(
f"The lateral stiffness of a single screw is calculated as {Ksls_v:.0f} N/mm \n"
f"The axial stiffness in the CLT member is calculated as {Ksls_ax_CLT:.0f} N/mm \n"
f"The axial stiffness in the LVL member is calculated as {Ksls_ax_LVL:.0f} N/mm \n"
f"The total axial stiffness 1 / (1/K_LVL + 1/K_CLT) equals {Ksls_ax:.0f} N/mm \n"
f"The stifness of the combined system equals {Ksls_r:.0f} N/mm \n")
```

```
The lateral stiffness of a single screw is calculated as 1640 N/mm
The axial stiffness in the CLT member is calculated as 46969 N/mm
The axial stiffness in the LVL member is calculated as 18031 N/mm
The total axial stiffness 1 / (1/K_LVL + 1/K_CLT) equals 13029 N/mm
The stifness of the combined system equals 9612 N/mm
```

Butt-joint calculation

In [9]:
```
# Input
Screw = [d_screw_v, l_screw_v, a_screw, s_screw_v, e_screw_v]
CLT = [t_lamella, o_lamella, rho_CLT, rho_CLT_k]
LVL = [t_LVL, rho_LVL, rho_LVL_k]

# Output
C_phix_r = Butt_stiffness('ETA', Screw, CLT, LVL)[0][0]
C_phix_v = Butt_stiffness('ETA', Screw, CLT, LVL)[0][1]
Ksls_ax, Ksls_ax_1, Ksls_ax_2 = (
    Butt_stiffness('ETA', Screw, CLT, LVL)[1])
z_butt = Butt_stiffness('ETA', Screw, CLT, LVL)[2]

# INTERMEDIATE RESULTS
print(
f"The axial stiffness in the first member is calculated as {Ksls_ax_1:.0f} N/mm \n"
f"The axial stiffness in the second member is calculated as {Ksls_ax_2:.0f} N/mm \n"
f"The total axial stiffness 1 / (1/K_1 + 1/K_2) equals {Ksls_ax:.0f} N/mm \n")
```

```
The axial stiffness in the first member is calculated as 32527 N/mm
The axial stiffness in the second member is calculated as 32473 N/mm
The total axial stiffness 1 / (1/K_1 + 1/K_2) equals 65000 N/mm
```

Results

In [10]:
```
# RESULTS
print(f"Selected splice plate connection properties: \n"
      f"  Diameter: {d_screw} mm \n"
      f"  Length: {l_screw} mm\n"
      f"  Number of screws in a row: {n_screw} spaced {s_screw} mm \n"
      f"  Angle: {np.rad2deg(a_screw):.0f}° (converted to radians: {a_screw:.4f}) \n"
      f"  LVL plate: {t_LVL} mm LVL \n"
      f"  Gives a rotational stiffness of {C_phix:.0f} kNm/rad/m \n")

print(f"Selected shear connection properties: \n"
      f"  Diameter: {d_screw_v} mm \n"
      f"  Length: {l_screw_v} mm\n"
      f"  Spacing of screws: {s_screw_v:.0f} mm \n"
      f"  CLT plate: {h_CLT} mm \n"
      f"  Gives a rotational stiffness of {C_phix_r:.0f} kNm/rad/m \n"
      f"  and shear stiffness of {C_phix_v:.0f} kN/m/m \n")

print(f"Timber properties: \n"
      f"  \u03C1 CLT: {rho_CLT} kg/m^3 \n"
      f"  \u03C1 LVL: {rho_LVL} kg/m^3")
```

```
Selected splice plate connection properties:
  Diameter: 10 mm
  Length: 260 mm
  Number of screws in a row: 2 spaced 80.0 mm
  Angle: 45° (converted to radians: 0.7854)
  LVL plate: 51 mm LVL
  Gives a rotational stiffness of 6301 kNm/rad/m

Selected shear connection properties:
  Diameter: 10 mm
  Length: 260 mm
  Spacing of screws: 200 mm
  CLT plate: 310 mm
  Gives a rotational stiffness of 4061 kNm/rad/m
  and shear stiffness of 16865 kN/m/m

Timber properties:
  ρ CLT: 420 kg/m^3
  ρ LVL: 510 kg/m^3
```

Store results

In [11]:
```
# Store results for strength calculation

# CLT data
CLT_data = {'t_lamella': t_lamella,
            'o_lamella': o_lamella,
            'E': E,
            'clt_density': clt_density,
            'fc': fc}

# Splice plate data to save
splice_connection = selected_splice_plate_properties

# Shear connection data to save
shear_connection = selected_shear_properties

# LVL data
LVL_data = {'lvl_density': lvl_density,
            't_LVL': t_LVL,
            'lvl_timber': lvl_timber,
            'mu': mu}

# Save to file
with open('clt_data.pkl', 'wb') as f:
    pickle.dump(CLT_data, f)
with open('splice_connection.pkl', 'wb') as f:
    pickle.dump(splice_connection, f)
with open('shear_connection.pkl', 'wb') as f:
    pickle.dump(shear_connection, f)
with open('lvl_data.pkl', 'wb') as f:
    pickle.dump(LVL_data, f)
```

In [12]:
```
#
```

In [1]:

```
def Splice_stiffness(Type, Screw, CLT, LVL, mu):
    """
    Returns an array [C_phix, Ksls, z_splice]
        C_phix: rotational stiffness [kNm/rad/m]
        Ksls: array of lateral stiffnesses of a single screw [N/mm]
            Ksls_r: Slip modulus single fastener along shear plane
            Ksls_ax: Axial slip modulus single fastener
            Ksls_v: Lateral slip modulus single fastener
            Ksls_ax_LVL: Axial slip modulus of the fastener in LVL
            Ksls_ax_CLT: Axial slip modulus of the fastener in CLT
        Z_splice: internal lever arm of the connection [mm]

    Parameters:
    Type: The possibilities are 'ETA' and 'Eurocode'
    Screw: array of screw properties [d, l, a, s, n]
        d: screw diameter [mm]
        l: screw length [mm]
        a: angle of the screw (prefered at 45 degrees) [rad]
        s: screw spacing [mm]
        n: number of screws in a row [-]
    CLT: array of CLT properties [t_lamella, o_lamella, rho_CLT, rho_CLT_k]
        t_lamella: array of lamella thicknesses of the used CLT panel [mm]
        o_lamella: array of lamella orientations of the used CLT panel [degree]
        rho_CLT: mean density of the CLT [kg/m^3]
        rho_CLT_k: characteristic density of the CLT [kg/m^3]
    LVL: array of LVL properties [t_LVL, rho_LVL, rho_LVL_k]
        t_LVL: array of lamella thicknesses of the used CLT panel [mm]
        o_lamella: array of lamella orientations of the used CLT panel [degree]
        rho_CLT: mean density of the CLT [kg/m^3]
        rho_CLT_k: characteristic density of the CLT [kg/m^3]
        lvl_timber: timber used for LVL, either 'Softwood' or 'Hardwood'
    mu: the kinetic friction coefficient between the members [-]
    """
    d_screw, l_screw, a_screw, s_screw, n_screw = (
    Screw[0], Screw[1], Screw[2], Screw[3], Screw[4])
    t_lamella, o_lamella, rho_CLT, rho_CLT_k = CLT[0], CLT[1], CLT[2], CLT[3]
    t_LVL, rho_LVL, rho_LVL_k, lvl_timber = LVL[0], LVL[1], LVL[2], LVL[3]

    h_CLT = np.sum(t_lamella)
    z0 = 0
    count = 0
    for i in o_lamella:
        if i == 0:
            z0 += t_lamella[count]
            count += 1
        else:
            break
    z_splice = h_CLT - t_LVL - z0

    # Determining screw lengths
    l_screw_LVL = t_LVL / np.sin(a_screw)
    l_screw_CLT = l_screw - l_screw_LVL

    # Ksls_v calculation prEN 1995-1-1; 11.3.7.2
    Ksls_v = 60 * (0.7 * d_screw)**1.7
```

```
    # Ksls_ax calculation according to calculation type
    if Type == 'ETA':
        # Ksls,ax calculation ETA-11/0190 (Würth schroeven)
        # Ksls,ax calculation ETA-12/0114 (SPAX schroeven)
        # Ksls,ax calculation ETA-11/0030 (Rothoblaas schroeven)
        Ksls_ax_CLT = 25 * d_screw * l_screw_CLT
        Ksls_ax_LVL = 25 * d_screw * l_screw_LVL
        if lvl_timber == 'Hardwood':
            Ksls_ax_LVL = 30 * d_screw * l_screw_LVL
        Ksls_ax = 1 / (1 / Ksls_ax_LVL + 1 / Ksls_ax_CLT)

    elif Type == 'Eurocode':
        Ksls_ax_LVL = 160 * (rho_LVL / 420)**0.85 * d_screw**0.9 * l_screw_LVL**0.6
        Ksls_ax_CLT = 160 * (rho_CLT / 420)**0.85 * d_screw**0.9 * l_screw_CLT**0.6
        Ksls_ax = 1 / (1 / Ksls_ax_LVL + 1 / Ksls_ax_CLT)

    # Ksls calculation prEN 1995-1-1; 11.3.7.4
    Ksls_r = Ksls_v * np.sin(a_screw) * (np.sin(a_screw) - mu * np.cos(a_screw)) + \
             Ksls_ax * np.cos(a_screw) * (np.cos(a_screw) + mu * np.sin(a_screw))
    Ksls = [Ksls_r, Ksls_ax, Ksls_v, Ksls_ax_LVL, Ksls_ax_CLT]

    # Working with angles:
    delta = 1
    theta = delta / z_splice

    # Forces along shear plane due to displacement delta
    Fs = delta * Ksls_r
    Ms = Fs * z_splice

    # Rotational stiffness
    Ms_tot = n_screw * 1000 / s_screw * Ms
    C_phix = (Ms_tot / theta / 10**6) / 2

    return C_phix, Ksls, z_splice
```

In [2]:
```
def Butt_stiffness(Type, Screw, CLT, LVL):
    """
    Returns an array [C_phix_butt, Ksls, z_butt]
        C_phix: array of stiffnesses
            C_phi_r: Rotational stiffness [kNm/rad/m]
            C_phi_v: Shear stiffness [kN/m/m]
        Ksls: array of lateral stiffnesses of a single screw [N/mm]
            Ksls_r: Slip modulus single fastener along shear plane
            Ksls_ax: Axial slip modulus single fastener
            Ksls_v: Lateral slip modulus single fastener
            Ksls_ax_LVL: Axial slip modulus of the fastener in LVL
            Ksls_ax_CLT: Axial slip modulus of the fastener in CLT
        Z_butt: internal lever arm of the connection [mm]

    Parameters:
    Type: The possibilities are 'Würth', 'Spax', 'Rothoblaas' and 'Eurocode'
    Screw: array of screw properties [d, l, a, s, e]
        d: screw diameter [mm]
        l: screw length [mm]
        a: angle of the screw (prefered at 45 degrees) [rad]
        s: screw spacing [mm]
        e: distance from screw head to panel edge [mm]
    CLT: array of CLT properties [t_lamella, o_lamella, rho_CLT, rho_CLT_k]
        t_lamella: array of lamella thicknesses of the used CLT panel [mm]
        o_lamella: array of lamella orientations of the used CLT panel [degree]
        rho_CLT: mean density of the CLT [kg/m^3]
        rho_CLT_k: characteristic density of the CLT [kg/m^3]
    LVL: array of LVL properties [t_LVL, rho_LVL, rho_LVL_k]
        t_LVL: array of lamella thicknesses of the used CLT panel [mm]
        o_lamella: array of lamella orientations of the used CLT panel [degree]
        rho_CLT: mean density of the CLT [kg/m^3]
        rho_CLT_k: characteristic density of the CLT [kg/m^3]
    """
    d_screw, l_screw, a_screw, s_screw, e_screw = (
    Screw[0], Screw[1], Screw[2], Screw[3], Screw[4])
    t_lamella, o_lamella, rho_CLT, rho_CLT_k = CLT[0], CLT[1], CLT[2], CLT[3]
    t_LVL, rho_LVL, rho_LVL_k = LVL[0], LVL[1], LVL[2]

    h_CLT = np.sum(t_lamella)
    z0 = 0
    count = len(t_lamella)
    for i in reversed(o_lamella):
        if i == 0:
            z0 += t_lamella[count-1]
            count -= 1
        else:
            break
    z_butt = h_CLT - z0 - e_screw * np.tan(a_screw)

    # Determining screw lengths
    l_screw_1 = e_screw / np.cos(a_screw)
    l_screw_2 = l_screw - l_screw_1

    # Ksls_ax calculation according to calculation type
    if Type == 'ETA':
        # Ksls,ax calculation ETA-11/0190 (Würth schroeven)
        # Ksls,ax calculation ETA-12/0114 (SPAX schroeven)
```

```
        # Ksls,ax calculation ETA-11/0030 (Rothoblaas schroeven)
        Ksls_ax_1 = 25 * d_screw * l_screw_1
        Ksls_ax_2 = 25 * d_screw * l_screw_2
        Ksls_ax = Ksls_ax_1 + Ksls_ax_2

    elif Type == 'Eurocode':
        Ksls_ax_1 = 160 * (rho_CLT / 420)**0.85 * d_screw**0.9 * l_screw_1**0.6
        Ksls_ax_2 = 160 * (rho_CLT / 420)**0.85 * d_screw**0.9 * l_screw_2**0.6
        Ksls_ax = Ksls_ax_1 + Ksls_ax_2

    # ROTATIONAL STIFFNESS
    # Working with angles:
    delta = 1
    theta = delta / z_butt

    # Forces along shear plane due to displacement delta
    Fs = Ksls_ax * np.sin(a_screw) * z_butt * theta
    Ms = Fs * z_butt
    Ms_tot = 1000 / s_screw * Ms
    C_phix_r = (Ms_tot / theta / 10**6) / 2

    # SHEAR STIFFNESS
    # Ksls_v calculation prEN 1995-1-1; 11.3.7.2
    Kv_factor = 1 - np.rad2deg(a_screw) / 180
    Kv = 60 * (0.7 * d_screw)**1.7 * Kv_factor

    # Ksls calculation prEN 1995-1-1; 11.3.7.4
    C_phix_v = Kv * np.sin(a_screw)**2 + Ksls_ax * np.cos(a_screw)**2 / 2

    C_phix_butt = [C_phix_r, C_phix_v]
    Ksls = [Ksls_ax, Ksls_ax_1, Ksls_ax_2]
    return C_phix_butt, Ksls, z_butt
```

H.1 Parameter study

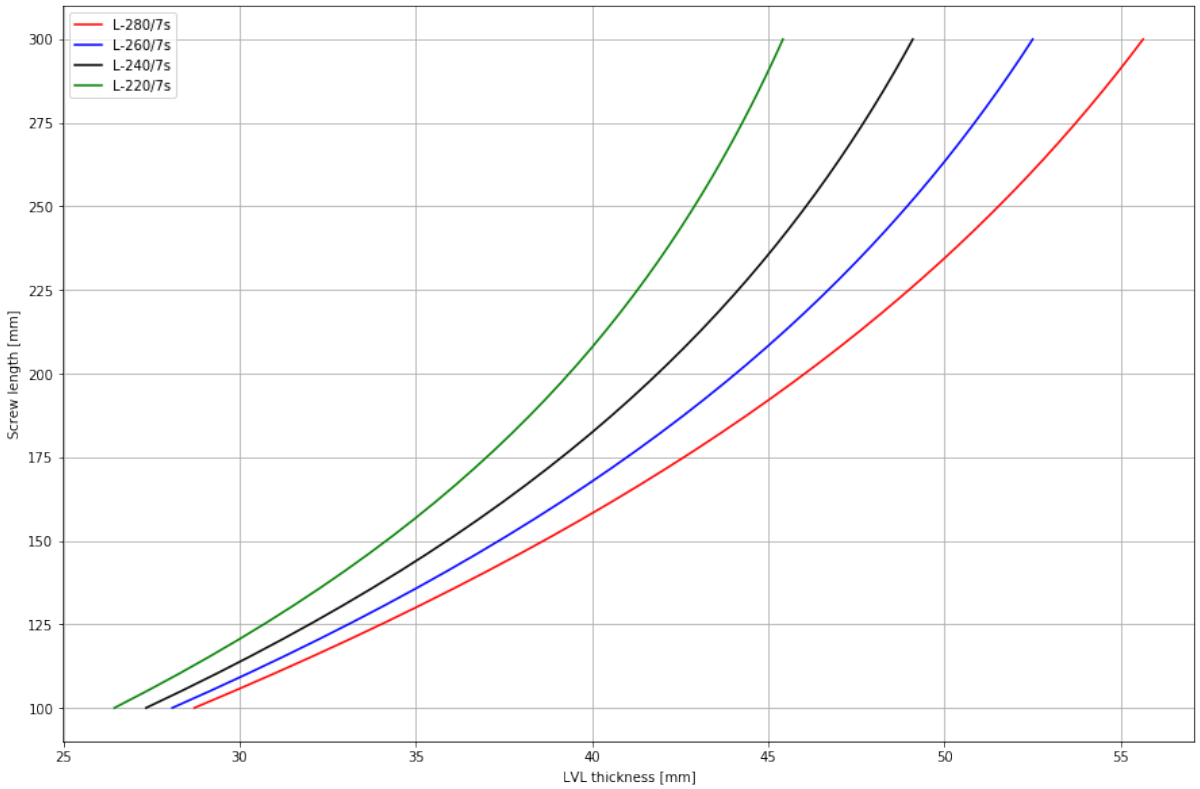

Figure H.1: Optimum screw length for thicknesses of the LVL plate for 7-layer panels

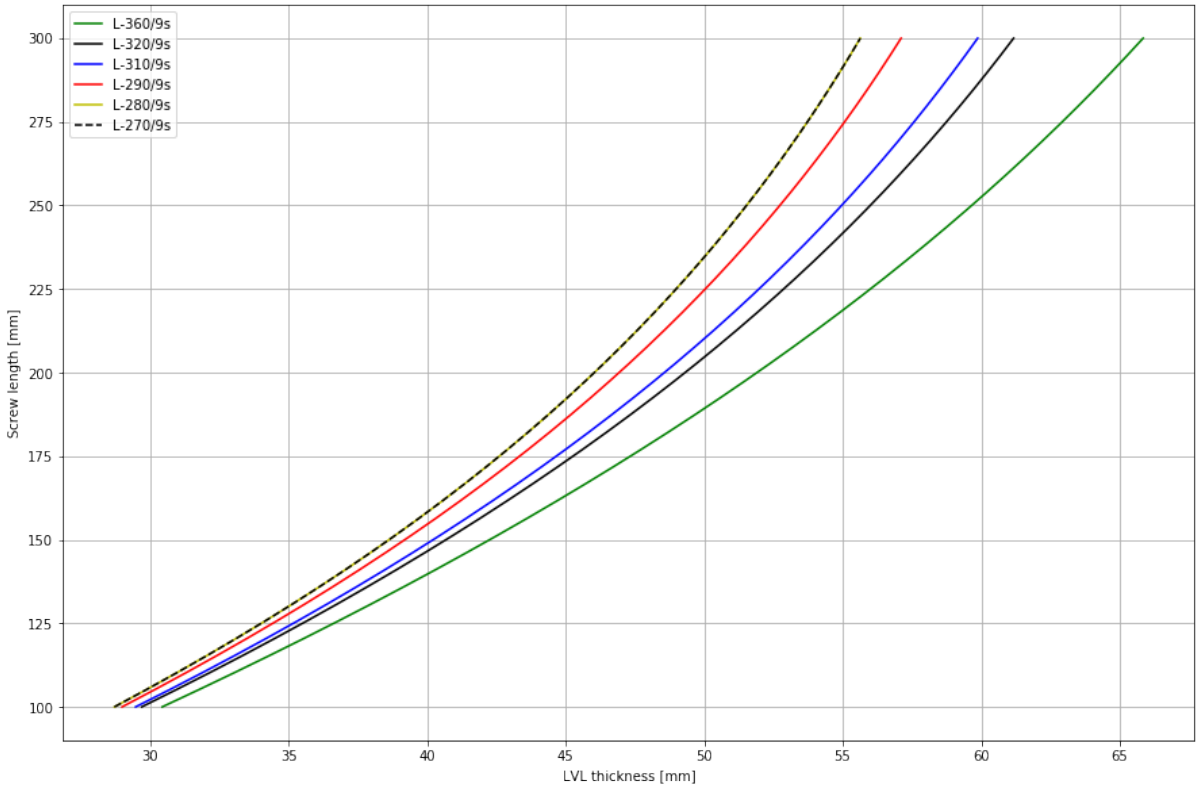

Figure H.2: Optimum screw length for thicknesses of the LVL plate for 9-layer panels

Appendix I- Strength model

In [1]:
```
%run Background_functions.ipynb
%run Strength_functions.ipynb
```

Import connection properties

In [2]:
```
with open('clt_data.pkl', 'rb') as f:
    clt_data = pickle.load(f)
with open('splice_connection.pkl', 'rb') as f:
    splice_connection = pickle.load(f)
with open('shear_connection.pkl', 'rb') as f:
    shear_connection = pickle.load(f)
with open('lvl_data.pkl', 'rb') as f:
    lvl_data = pickle.load(f)

# CLT properties
t_lamella, o_lamella, E, clt_density, fc = (
    clt_data[k] for k in
['t_lamella', 'o_lamella', 'E', 'clt_density', 'fc'])
E0, E90 = E
rho_CLT, rho_CLT_k = clt_density
fc0_k, fc90_k = fc

# LVL properties
lvl_density, t_LVL, lvl_timber, mu = (
    lvl_data[k] for k in
['lvl_density', 't_LVL', 'lvl_timber', 'mu'])
rho_LVL, rho_LVL_k = lvl_density

# Splice plate connection
Type, d_screw, dh, l_screw, s_screw, n_screw = (
    splice_connection[k] for k in
['Type', 'Diameter', 'Head_diameter', 'Length', 'Spacing', 'Number of screws'])

# Butt-joint connection
Type_v, d_screw_v, dhv, l_screw_v, s_screw_v, e_screw = (
    shear_connection[k] for k in
['Type', 'Diameter', 'Head_diameter', 'Length', 'Spacing', 'Distance'])
```

Please provide the line hinge forces and corresponding distances for the connection design

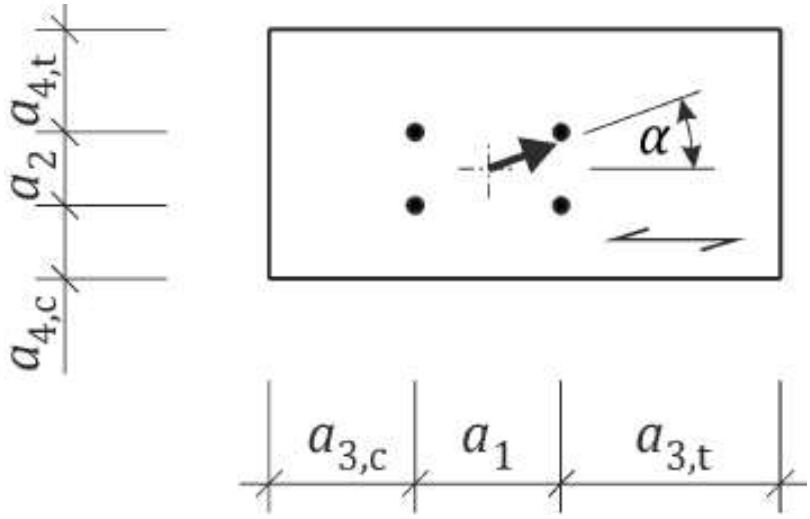

In [3]:
```
# Results RFEM
m_x_pos = 30.249 # kNm/m
m_x_neg = 5.705  # kNm/m
v_z = 48.698     # kN/m

# Factors
kmod = 0.8
gamm_R = 1.3
gamm_M2 = 1.25
gamm_M = 1.25
kmod = 0.8

# Design variables
panel_width = 1000       # per meter width
a_screw = np.deg2rad(45)
alpha = 0 # angle between force and grain direction
beta = a_screw
epsilon = a_screw

# Change values depending on design
a1 = 50
a2 = 100
a3t = 120
a3c = 70
a4t = 100
a4c = 100

# Check design values
designcheck(a1,a2,a3t,a3c,a4t,a4c,d_screw)
```

Calculation splice-plate

In [4]:
```
# Input
Screw_splice = [d_screw, l_screw, s_screw, n_screw, dh]
Screw_butt = [d_screw_v, l_screw_v, s_screw_v, e_screw, dhv]
Screw = [Screw_splice, Screw_butt]
CLT = [t_lamella, o_lamella, rho_CLT, rho_CLT_k]
LVL = [t_LVL, rho_LVL, rho_LVL_k, lvl_timber]

Fax_CLT, Fax_LVL, Fhead_LVL, Ft_screw, Ft_LVL = (
    Ft_calc(Type, Screw, CLT, LVL)[0][k] for k in [0,1,2,3,4])
Ft_Rk_LVL = max(Fax_LVL, Fhead_LVL)

# INTERMEDIATE RESULTS
print(
    f"The following characteristic values are calculated: \n"
    f"The axial withdrawal capacity in the CLT equals {Fax_CLT:.0f}N \n"
    f"The axial withdrawal capacity in the LVL equals {Fax_LVL:.0f}N \n"
    f"The head pull-through capacity in the LVL equals {Fhead_LVL:.0f}N \n"
    f"The tensional strengths; Screw {Ft_screw:.0f}N and LVL {Ft_LVL:.0f}N")

# Fax,t,d calculation prEN 1995-1-1; 11.2.2.1
# Axial forces:
Ft_screw_LVL = kmod / gamm_R * Ft_Rk_LVL
Ft_screw_CLT = kmod / gamm_R * Fax_CLT
Ft_Rd_LVL_member = kmod / gamm_R * Ft_LVL
Ft_screw_d = Ft_screw / gamm_M2

# Forces at shear plane
Ft_Rd_LVL = Ft_screw_LVL * (np.cos(a_screw) + mu * np.sin(a_screw))
Ft_Rd_CLT = Ft_screw_CLT * (np.cos(a_screw) + mu * np.sin(a_screw))
Ft_Rd_screw = Ft_screw_d * (np.cos(a_screw) + mu * np.sin(a_screw))

# Example values and their associated failure mechanisms
value1, value2, value3, value4 = Ft_Rd_LVL, Ft_Rd_CLT, Ft_Rd_LVL_member, Ft_Rd_screw
mechanisms = ["Failure in the LVL member",
              "Failure in the CLT member",
              "Failure of the LVL member itself",
              "Tension failure of the screw"]

# Find the governing value and its mechanism
values = [value1, value2, value3, value4]
min_value = min(values)
governing_mechanism = mechanisms[values.index(min_value)]

# Print the result
print(f" \n"
    f"The values are rewritten to their design values \n"
    f"The governing mechanism returns a tensional force of {min_value:.0f}N \n"
    f"The failure mechanism is {governing_mechanism}.")
```

```
The following characteristic values are calculated:
The axial withdrawal capacity in the CLT equals 22726N
The axial withdrawal capacity in the LVL equals 10190N
The head pull-through capacity in the LVL equals 6013N
The tensional strengths; Screw 28000N and LVL 106080N

The values are rewritten to their design values
The governing mechanism returns a tensional force of 6208N
The failure mechanism is Failure in the LVL member.
```

In [5]:
```python
# BENDING MOMENT RESISTANCE - splice plate
n_1m = panel_width * n_screw / s_screw      # Number of screws in 1m CLT
n_ef = max(n_1m**0.9, 0.9 * n_1m)
Ft_Rd = n_ef * min_value

# Factors for design strength CLT
fc0_d = kmod / gamm_M * fc0_k
fc90_d = kmod / gamm_M * fc90_k

Mrd = Mrd_calc(Ft_Rd, t_lamella, o_lamella, fc0_d, fc90_d, t_LVL)[0] / 10**6

print(f"The allowable tensional force equals {Ft_Rd:.0f}N\n"
      f"The allowable bending moment at the connection is {Mrd:.1f}kNm/m \n"
      f"The occuring bending moment is {m_x_pos}kNm/m according to RFEM \n"
      f"This gives an U.C.-value of {m_x_pos / Mrd:.2f}")
```

```
The allowable tensional force equals 139680N
The allowable bending moment at the connection is 32.4kNm/m
The occuring bending moment is 30.249kNm/m according to RFEM
This gives an U.C.-value of 0.93
```

Calculation Butt-joint

In [6]:
```
# Input
# Characteristic values, depending on screw type
Fax_1, Fax_2, Fhead2, Ft_screw_v = (
    Ft_calc(Type_v, Screw, CLT, LVL)[1][k] for k in [0,1,2,3])


# INTERMEDIATE RESULTS
print(
    f"The following characteristic values are calculated: \n"
    f"Axial withdrawal strength in the CLT member without screw head {Fax_1:.0f}N \n"
    f"Axial withdrawal strength in the CLT member with screw head {Fax_2:.0f}N \n"
    f"Head pull-through strength of the screw in the CLT member {Fhead2:.0f}N \n"
    f"The tensional strength of the screw {Ft_screw_v:.0f}N")

# Fax,t,d calculation prEN 1995-1-1; 11.2.2.1
Ft_Rd_CLThead_v = kmod / gamm_R * max(Fax_2, Fhead2)
Ft_Rd_CLT_v = kmod / gamm_R * Fax_1
Ft_Rd_screw_v = Ft_screw_v / gamm_M2

# Example values and their associated failure mechanisms
value1_v, value2_v, value3_v = Ft_Rd_CLThead_v, Ft_Rd_CLT_v, Ft_Rd_screw_v
mechanisms_v = ["Failure in the CLT member with screw head",
                "Failure in the CLT member without screw head",
                "Tension failure of the screw"]

# Find the governing value and its mechanism
values_v = [value1_v, value2_v, value3_v]
min_value_v = min(values_v)
governing_mechanism_v = mechanisms_v[values_v.index(min_value_v)]

# Print the result
print(f" \n"
    f"The values are rewritten to their design values \n"
    f"The governing mechanism returns a tensional force of {min_value_v:.0f}N \n"
    f"The failure mechanism is {governing_mechanism_v}.")
```

```
The following characteristic values are calculated:
Axial withdrawal strength in the CLT member without screw head 15738N
Axial withdrawal strength in the CLT member with screw head 15712N
Head pull-through strength of the screw in the CLT member 5148N
The tensional strength of the screw 28000N

The values are rewritten to their design values
The governing mechanism returns a tensional force of 9669N
The failure mechanism is Failure in the CLT member with screw head.
```

In [7]:
```
# BENDING MOMENT RESISTANCE - butt-joint
n_1m = panel_width / s_screw_v      # Number of screws in 1m CLT
n_ef = max(n_1m**0.9, 0.9 * n_1m)

# Multiply with 1/sqrt(2) because of the angle
# Multiply with 2 because of the cross-wise arrangement
Ft_Rd_v = n_ef * 2 * min(Ft_Rd_CLT_v, Ft_Rd_screw_v) * np.cos(a_screw)
rev_t_lamella = list(reversed(t_lamella))
rev_o_lamella = list(reversed(o_lamella))
Mrd_v = Mrd_calc(Ft_Rd_v, rev_t_lamella, rev_o_lamella,
                 fc0_d, fc90_d, e_screw)[0] / 10**6

print(
f"The allowable bending moment at the connection is {Mrd_v:.1f} kNm/m, with an \n"
f"occuring bending moment of {m_x_neg} kNm/m, this gives a U.C.-value of "
f"{m_x_neg / Mrd_v:.2f}"
)
```

```
The allowable bending moment at the connection is 12.3 kNm/m, with an
occuring bending moment of 5.705 kNm/m, this gives a U.C.-value of 0.46
```

In [8]:
```
print(
f"The tensile force equals the shear force in the butt-joint this is \n"
f"because of the 45\u00b0 angle of the screws, so: \n"
f"The allowable shear force at the connection is {Ft_Rd_v / 1000:.1f} kN/m, with an \n
f"occuring shear force of {v_z} kNm/m, this gives a U.C.-value of "
f"{v_z / (Ft_Rd_v / 1000):.2f}")
```

```
The tensile force equals the shear force in the butt-joint this is
because of the 45° angle of the screws, so:
The allowable shear force at the connection is 61.6 kN/m, with an
occuring shear force of 48.698 kNm/m, this gives a U.C.-value of 0.79
```

In [9]:
```
#
```

In [1]:

```
def Wurth_strength(Screw, CLT, LVL):
    """
    Returns Ft_Rk_splice and Ft_Rk_butt:
    Ft_Rk_splice = [Fax_CLT, Fax_LVL, Fhead_LVL, Ft_screw, Ft_LVL]:
    An array of characteristic strengths of different splice plate members [N]
        Fax_CLT: Axial withdrawal strength of the screw in the CLT member
        Fax_LVL: Axial withdrawal strength of the screw in the LVL member
        Fhead_LVL: Head pull-through strength of the screw in the LVL member
        Ft_screw: Tensile strength of the screw
        Ft_LVL: Tensile strength of the LVL
    Ft_Rk_butt = [Fax_1, Fax_2, Fhead2]:
    An array of characteristic strengths of different butt-joint members [N]
        Fax_1: Axial withdrawal strength in the CLT member without screw head
        Fax_2: Axial withdrawal strength in the CLT member with screw head
        Fhead2: Head pull-through strength of the screw in the CLT member

    Parameters:
    Screw: two arrays of screw properties for splice plate and butt-joint
    splice plate; [d, l, a, s, n, dh]
    butt-joint; [d, l, a, s, e, dh]
        d: screw diameter [mm]
        l: screw length [mm]
        s: screw spacing [mm]
        n: number of screws in a row [-]
        dh: head diameter [mm]
        e: distance screw head to CLT edge [mm]
    CLT: array of CLT properties [t_lamella, o_lamella, rho_CLT, rho_CLT_k]
        t_lamella: array of lamella thicknesses of the used CLT panel [mm]
        o_lamella: array of lamella orientations of the used CLT panel [degree]
        rho_CLT: mean density of the CLT [kg/m^3]
        rho_CLT_k: characteristic density of the CLT [kg/m^3]
    LVL: array of LVL properties [t_LVL, rho_LVL, rho_LVL_k]
        t_LVL: array of lamella thicknesses of the used CLT panel [mm]
        o_lamella: array of lamella orientations of the used CLT panel [degree]
        rho_CLT: mean density of the CLT [kg/m^3]
        rho_CLT_k: characteristic density of the CLT [kg/m^3]
        lvl_timber: LVL material 'Softwood' or 'Hardwood'
    """

    d_screw, l_screw, s_screw, n_screw, dh = (
        Screw[0][k] for k in
    [0, 1, 2, 3, 4])
    d_screw_v, l_screw_v, s_screw_v, e, dhv = (
        Screw[1][k] for k in
    [0, 1, 2, 3, 4])
    t_lamella, o_lamella, rho_CLT, rho_CLT_k = CLT[0], CLT[1], CLT[2], CLT[3]
    t_LVL, rho_LVL, rho_LVL_k, lvl_timber= LVL[0], LVL[1], LVL[2], LVL[3]

    # Determining screw lengths
    l_screw_LVL = t_LVL / np.sin(a_screw)
    l_screw_CLT = l_screw - l_screw_LVL

    l_screw_v1 = e / np.cos(a_screw)
    l_screw_v2 = l_screw_v - l_screw_v1

    # Würth schroeven; ETA-11/0190
    # Tables A.2.1, A.2.2 and A.2.3
```

```
    def tensile(d_screw):
        if d_screw == 6.0:
            Ft_screw = 12500
        elif d_screw == 7.0:
            Ft_screw = 15000
        elif d_screw == 8.0:
            Ft_screw = 21500
        elif d_screw == 10.0:
            Ft_screw = 26000
        elif d_screw == 12.0:
            Ft_screw = 41000
        return Ft_screw

    Ft_screw = tensile(d_screw)
    Ft_screw_v = tensile(d_screw_v)

    # A.2.3.2 Axial withdrawal capacity
    def withdrawal(d, l1, l2, rho1, rho2, angle, Type):
        # Determine kax
        if angle >= np.deg2rad(45):
            kax_1 = kax_2 = 1
        elif angle < np.deg2rad(45):
            if Type == 'Splice':
                kax_1 = 0.5 + 0.5 * np.rad2deg(angle) / 45
                kax_2 = 0.3 + 0.7 * np.rad2deg(angle) / 45
                if l1 >= min(20 * d, 4 * d / np.sin(np.deg2rad(45))):
                    kax_1 = 1 / (1.2 * np.cos(angle)**2 + np.sin(angle)**2)
                if l2 >= min(20 * d, 4 * d / np.sin(np.deg2rad(45))):
                    kax_2 = 1 / (1.2 * np.cos(angle)**2 + np.sin(angle)**2)
            if Type == 'Butt':
                kax_1 = kax_2 = 0.3 + 0.7 * np.rad2deg(angle) / 45
                if l1 >= min(20 * d, 4 * d / np.sin(np.deg2rad(45))):
                    kax_1 = 1 / (1.2 * np.cos(angle)**2 + np.sin(angle)**2)
                if l2 >= min(20 * d, 4 * d / np.sin(np.deg2rad(45))):
                    kax_2 = 1 / (1.2 * np.cos(angle)**2 + np.sin(angle)**2)

        # Determine fax,k
        kbeta_1 = kbeta_2 = 1.0
        rho_a1 = rho_a2 = 350
        if 5.5 <= d <= 7:
            faxk_1 = faxk_2 = 11.5
        elif 7.5 <= d <= 10:
            faxk_1 = faxk_2 = 11.0
        elif 10 < d:
            faxk_1 = faxk_2 = 10.0

        if Type == 'Splice':
            kbeta_1 = 1.5 * np.cos(angle)**2 + np.sin(angle)**2
            if 590 <= rho1 <= 750:
                rho_a1 = 730
                faxk_1 = 35.0

        # Axial withdrawal capacity of a single screw
        Fax_1 = kax_1 * faxk_1 * d * l1 / kbeta_1 * (rho1 / rho_a1)**0.8
        Fax_2 = kax_2 * faxk_2 * d * l2 / kbeta_2 * (rho2 / rho_a2)**0.8
        return Fax_1, Fax_2

    Fax_LVL, Fax_CLT = withdrawal(
```

```
        d_screw, l_screw_LVL, l_screw_CLT, rho_LVL_k, rho_CLT_k, a_screw, 'Splice')
    Fax_1, Fax_2 = withdrawal(
        d_screw_v, l_screw_v1, l_screw_v2, rho_CLT_k, rho_CLT_k, a_screw, 'Butt')

    # A.2.3.3 Head pull-through capacity
    def head(dh, rho1, t_LVL):
        if dh <= 25 and 590 <= rho1 <= 750 and t_LVL >= 40:
            fheadk = 40 - 0.5 * dh
        elif 12 <= t_LVL <= 20:
            fheadk = 8.0
        else:
            fheadk = 23.0

        Fhead = fheadk * dh**2 * (rho1 / 350)**0.8
        return Fhead

    Fhead_LVL = head(dh, rho_LVL_k, t_LVL)
    Fhead1 = head(dhv, rho_CLT_k, t_LVL)

    # Tensile strength of splice plate
    Ft_LVL = 26 * s_screw * t_LVL

    Ft_Rk_splice = [Fax_CLT, Fax_LVL, Fhead_LVL, Ft_screw, Ft_LVL]
    Ft_Rk_butt = [Fax_1, Fax_2, Fhead1, Ft_screw_v]

    return Ft_Rk_splice, Ft_Rk_butt
```

In [2]:
```
def SPAX_strength(Screw, CLT, LVL):
    """
    Returns Ft_Rk_splice and Ft_Rk_butt:
    Ft_Rk_splice = [Fax_CLT, Fax_LVL, Fhead_LVL, Ft_screw, Ft_LVL]:
    An array of characteristic strengths of different splice plate members [N]
        Fax_CLT: Axial withdrawal strength of the screw in the CLT member
        Fax_LVL: Axial withdrawal strength of the screw in the LVL member
        Fhead_LVL: Head pull-through strength of the screw in the LVL member
        Ft_screw: Tensile strength of the screw
        Ft_LVL: Tensile strength of the LVL
    Ft_Rk_butt = [Fax_1, Fax_2, Fhead2]:
    An array of characteristic strengths of different butt-joint members [N]
        Fax_1: Axial withdrawal strength in the CLT member without screw head
        Fax_2: Axial withdrawal strength in the CLT member with screw head
        Fhead2: Head pull-through strength of the screw in the CLT member

    Parameters:
    Screw: two arrays of screw properties for splice plate and butt-joint
    splice plate; [d, l, a, s, n, dh]
    butt-joint; [d, l, a, s, e, dh]
        d: screw diameter [mm]
        l: screw length [mm]
        s: screw spacing [mm]
        n: number of screws in a row [-]
        dh: head diameter [mm]
        e: distance screw head to CLT edge [mm]
    CLT: array of CLT properties [t_lamella, o_lamella, rho_CLT, rho_CLT_k]
        t_lamella: array of lamella thicknesses of the used CLT panel [mm]
        o_lamella: array of lamella orientations of the used CLT panel [degree]
        rho_CLT: mean density of the CLT [kg/m^3]
        rho_CLT_k: characteristic density of the CLT [kg/m^3]
    LVL: array of LVL properties [t_LVL, rho_LVL, rho_LVL_k]
        t_LVL: array of lamella thicknesses of the used CLT panel [mm]
        o_lamella: array of lamella orientations of the used CLT panel [degree]
        rho_CLT: mean density of the CLT [kg/m^3]
        rho_CLT_k: characteristic density of the CLT [kg/m^3]
        lvl_timber: LVL material 'Softwood' or 'Hardwood'
    """

    d_screw, l_screw, s_screw, n_screw, dh = (
        Screw[0][k] for k in
    [0, 1, 2, 3, 4])
    d_screw_v, l_screw_v, s_screw_v, e, dhv = (
        Screw[1][k] for k in
    [0, 1, 2, 3, 4])
    t_lamella, o_lamella, rho_CLT, rho_CLT_k = CLT[0], CLT[1], CLT[2], CLT[3]
    t_LVL, rho_LVL, rho_LVL_k, lvl_timber= LVL[0], LVL[1], LVL[2], LVL[3]

    # Determining screw lengths
    l_screw_LVL = t_LVL / np.sin(a_screw)
    l_screw_CLT = l_screw - l_screw_LVL

    l_screw_v1 = e / np.cos(a_screw)
    l_screw_v2 = l_screw_v - l_screw_v1

    # SPAX schroeven; ETA-12/0114
    # 3.1 Mechanical resistance and stability
```

```
def tensile(d_screw):
    if d_screw == 6.0:
        Ft_screw = 11000
    elif d_screw == 7.0:
        Ft_screw = 13000
    elif d_screw == 8.0:
        Ft_screw = 17000
    elif d_screw == 10.0:
        Ft_screw = 28000
    elif d_screw == 12.0:
        Ft_screw = 38000
    return Ft_screw

Ft_screw = tensile(d_screw)
Ft_screw_v = tensile(d_screw_v)

# 3.9 Mechanical resistance and stability
# Axial withdrawal capacity
def withdrawal(d, l1, l2, rho1, rho2, angle):
    # Determine kax (self defined)
    kax = 1 / (1.2 * np.cos(angle)**2 + np.sin(angle)**2)

    # Determine fax,k
    if 6.0 <= d <= 8.0:
        faxk = 12.0
    elif d == 10.0:
        faxk = 11.5
    elif d == 12.0:
        faxk = 11.0

    # Axial withdrawal capacity of a single screw
    Fax_1 = kax * faxk * d * l1 * (rho1 / 350)**0.8
    Fax_2 = kax * faxk * d * l2 * (rho2 / 350)**0.8
    return Fax_1, Fax_2

Fax_LVL, Fax_CLT = withdrawal(
    d_screw, l_screw_LVL, l_screw_CLT, rho_LVL_k, rho_CLT_k, a_screw)
Fax_1, Fax_2 = withdrawal(
    d_screw_v, l_screw_v1, l_screw_v2, rho_CLT_k, rho_CLT_k, a_screw)

# Head pull-through capacity
def head(dh, rho1, t_LVL):
    if dh <= 16:
        fheadk = 27 - dh
    elif 16 <= dh <= 32:
        fheadk = 11 - 0.2 * (dh - 16)
    elif dh > 32:
        dh = 32
        fheadk = 11 - 0.2 * (dh - 16)
    if 12 <= t_LVL <= 20:
        fheadk = 8.0

    Fhead = fheadk * dh**2 * (rho1 / 350)**0.8
    return Fhead

Fhead_LVL = head(dh, rho_LVL_k, t_LVL)
Fhead1 = head(dhv, rho_CLT_k, t_LVL)
```

```
    # Tensile strength of splice plate
    Ft_LVL = 26 * s_screw * t_LVL

    Ft_Rk_splice = [Fax_CLT, Fax_LVL, Fhead_LVL, Ft_screw, Ft_LVL]
    Ft_Rk_butt = [Fax_1, Fax_2, Fhead1, Ft_screw_v]

    return Ft_Rk_splice, Ft_Rk_butt
```

In [3]:
```
def Rothoblaas_strength(Screw, CLT, LVL):
    """
    Returns Ft_Rk_splice and Ft_Rk_butt:
    Ft_Rk_splice = [Fax_CLT, Fax_LVL, Fhead_LVL, Ft_screw, Ft_LVL]:
    An array of characteristic strengths of different splice plate members [N]
        Fax_CLT: Axial withdrawal strength of the screw in the CLT member
        Fax_LVL: Axial withdrawal strength of the screw in the LVL member
        Fhead_LVL: Head pull-through strength of the screw in the LVL member
        Ft_screw: Tensile strength of the screw
        Ft_LVL: Tensile strength of the LVL
    Ft_Rk_butt = [Fax_1, Fax_2, Fhead2]:
    An array of characteristic strengths of different butt-joint members [N]
        Fax_1: Axial withdrawal strength in the CLT member without screw head
        Fax_2: Axial withdrawal strength in the CLT member with screw head
        Fhead2: Head pull-through strength of the screw in the CLT member

    Parameters:
    Screw: two arrays of screw properties for splice plate and butt-joint
    splice plate; [d, l, a, s, n, dh]
    butt-joint; [d, l, a, s, e, dh]
        d: screw diameter [mm]
        l: screw length [mm]
        s: screw spacing [mm]
        n: number of screws in a row [-]
        dh: head diameter [mm]
        e: distance screw head to CLT edge [mm]
    CLT: array of CLT properties [t_lamella, o_lamella, rho_CLT, rho_CLT_k]
        t_lamella: array of lamella thicknesses of the used CLT panel [mm]
        o_lamella: array of lamella orientations of the used CLT panel [degree]
        rho_CLT: mean density of the CLT [kg/m^3]
        rho_CLT_k: characteristic density of the CLT [kg/m^3]
    LVL: array of LVL properties [t_LVL, rho_LVL, rho_LVL_k]
        t_LVL: array of lamella thicknesses of the used CLT panel [mm]
        o_lamella: array of lamella orientations of the used CLT panel [degree]
        rho_CLT: mean density of the CLT [kg/m^3]
        rho_CLT_k: characteristic density of the CLT [kg/m^3]
        lvl_timber: LVL material 'Softwood' or 'Hardwood'
    """

    d_screw, l_screw, s_screw, n_screw, dh = (
        Screw[0][k] for k in
    [0, 1, 2, 3, 4])
    d_screw_v, l_screw_v, s_screw_v, e, dhv = (
        Screw[1][k] for k in
    [0, 1, 2, 3, 4])
    t_lamella, o_lamella, rho_CLT, rho_CLT_k = CLT[0], CLT[1], CLT[2], CLT[3]
    t_LVL, rho_LVL, rho_LVL_k, lvl_timber= LVL[0], LVL[1], LVL[2], LVL[3]

    # Determining screw lengths
    l_screw_LVL = t_LVL / np.sin(a_screw)
    l_screw_CLT = l_screw - l_screw_LVL

    l_screw_v1 = e / np.cos(a_screw)
    l_screw_v2 = l_screw_v - l_screw_v1

    # Rothoblaas schroeven; ETA-11/0030
    # 3.1 Mechanical resistance and stability
```

```
    def tensile(d_screw):
        if d_screw == 6.0:
            Ft_screw = 11300
        elif d_screw == 7.0:
            Ft_screw = 15400
        elif d_screw == 8.0:
            Ft_screw = 20100
        elif d_screw == 9.0:
            Ft_screw = 25400
        elif d_screw == 10.0:
            Ft_screw = 31400
        elif d_screw == 11.0:
            Ft_screw = 38000
        elif d_screw == 12.0:
            Ft_screw = 33900
        return Ft_screw

    Ft_screw = tensile(d_screw)
    Ft_screw_v = tensile(d_screw_v)

    # 3.9 Mechanical resistance and stability
    # Axial withdrawal capacity
    def withdrawal(d, l1, l2, rho1, rho2, angle, Type):
        # Determine kax
        if angle >= np.deg2rad(45):
            kax_1 = kax_2 = 1
        elif angle < np.deg2rad(45):
            if Type == 'Splice':
                kax_1 = 0.5 + 0.5 * np.rad2deg(angle) / 45
                kax_2 = 0.3 + 0.7 * np.rad2deg(angle) / 45
            if Type == 'Butt':
                kax_1 = kax_2 = 0.3 + 0.7 * np.rad2deg(angle) / 45

        # Determine fax,k
        kbeta_1 = kbeta_2 = 1.0
        if rho2 < 440:
            rho_a1 = rho_a2 = 350
            faxk_1 = faxk_2 = 11.7

        if Type == 'Splice':
            kbeta_1 = 1.5 * np.cos(angle)**2 + np.sin(angle)**2
            if lvl_timber == 'Hardwood' and rho1 <= 590:
                rho_a1 = 350
                faxk_1 = 7 * 10**-4 * rho1**1.6 * d**-0.34
            elif 590 <= rho1 <= 750:
                rho_a1 = 730
                faxk_1 = 29.0
            elif 460 <= rho1 <= 550:
                rho_a1 = 500
                faxk_1 = 15.0

        # Axial withdrawal capacity of a single screw
        Fax_1 = kax_1 * faxk_1 * d * l1 / kbeta_1 * (rho1 / rho_a1)**0.8
        Fax_2 = kax_2 * faxk_2 * d * l2 / kbeta_2 * (rho2 / rho_a2)**0.8
        return Fax_1, Fax_2

    Fax_LVL, Fax_CLT = withdrawal(
        d_screw, l_screw_LVL, l_screw_CLT, rho_LVL_k, rho_CLT_k, a_screw, 'Splice')
```

```
    Fax_1, Fax_2 = withdrawal(
        d_screw_v, l_screw_v1, l_screw_v2, rho_CLT_k, rho_CLT_k, a_screw, 'Butt')

    # Head pull-through capacity
    def head(dh, rho1, t_LVL, Type):
        if Type == 'Splice':
            if lvl_timber == 'Softwood':
                rho1 = min(rho1, 380)
                rho_a1 = 500
                fheadk = 20.0
            elif lvl_timber == 'Hardwood':
                rho1 = min(rho1, 590)
                rho_a1 = 730
                fheadk = 50
        elif Type == 'Butt':
            rho_a1 = 350
            fheadk = 10.5
        if 12 <= t_LVL <= 20:
            fheadk = 8.0

        Fhead = fheadk * dh**2 * (rho1 / rho_a1)**0.8
        return Fhead

    Fhead_LVL = head(dh, rho_LVL_k, t_LVL, 'Splice')
    Fhead1 = head(dhv, rho_CLT_k, t_LVL, 'Butt')

    # Tensile strength of splice plate
    Ft_LVL = 26 * s_screw * t_LVL

    Ft_Rk_splice = [Fax_CLT, Fax_LVL, Fhead_LVL, Ft_screw, Ft_LVL]
    Ft_Rk_butt = [Fax_1, Fax_2, Fhead1, Ft_screw_v]

    return Ft_Rk_splice, Ft_Rk_butt
```

In [4]:

```python
def Mrd_calc(Ft, t_lamella, o_lamella, fc0, fc90, T, panel_width=1000):
    """
    Calculate the design bending moment capacity Mrd for a CLT connection.

    Parameters:
    - Ft: Tensional force (N per meter width)
    - t_lamella: List of lamella thicknesses (mm)
    - o_lamella: List of lamella orientations (0 or 90 degrees)
    - fc0: Compression strength parallel to grain (N/mm²)
    - fc90: Compression strength perpendicular to grain (N/mm²)
    - T: Distance panel face to tensional force (mm)

    Returns:
    - Mrd: Design bending moment resistance (Nmm/m)
    - z: Lever arm (mm)
    - xr: Resultant compression force location (mm from top)
    """
    t1 = t_lamella[0]
    h_clt = sum(t_lamella)
    Ft = Ft / panel_width

    # Select appropriate compressive strength based on orientation
    fc_top = fc90 if o_lamella[0] == 0 else fc0

    F1 = fc_top * t1  # Force taken by top lamella (per mm width)

    if Ft <= F1:
        x = Ft / fc_top
        xr = x / 2
    else:
        F2 = Ft - F1
        fc_next = fc90 if o_lamella[1] == 0 else fc0
        h2 = F2 / fc_next

        x1 = t1 / 2
        x2 = t1 + h2 / 2
        x = t1 + h2
        xr = (F1 * x1 + F2 * x2) / Ft

    z = h_clt - T - xr
    Mrd = z * Ft * panel_width  # in Nmm/m

    return Mrd, z, xr, x
```

In [5]:
```python
def Ft_calc(screw_type, screw, CLT, LVL):
    # Dictionary mapping screw type to their strength functions
    strength_functions = {
        "SPAX": SPAX_strength,
        "Würth": Wurth_strength,
        "Rothoblaas": Rothoblaas_strength
    }

    # Get the appropriate strength function
    try:
        strength_func = strength_functions[screw_type]
    except KeyError:
        raise ValueError(f"Unsupported screw type: {screw_type}")

    # Call the function and extract the values
    values_splice = strength_func(screw, CLT, LVL)[0]
    values_butt = strength_func(screw, CLT, LVL)[1]

    return values_splice, values_butt
```

Appendix J: Site visit

The panel-to-panel connection has been tested in a lab to determine the strength and stiffness of the connection. However, executing a connection in a regulated lab environment, often on a small scale, is not a realistic comparison to the challenges a connection can cause on a real building site. In Warmenhuizen, a small village in the Netherlands, a project is being developed at the time of writing of this report. This project is innovative because of the use of both the Spider and TC FUSION connection as developed by Rothoblaas. The TC FUSION is a wet panel-to-panel connection that incorporates concrete and steel rebars to create a moment-resisting connection between two timber panels, see figure J.1. Besides panel-to-panel connection, the connection can also be used to rigidly connect a CLT panel to a reinforced concrete element [51].

Figure J.1: The concept of the TC FUSION connection [51]

The subject of this master thesis is a different connection type. However, due to the fact that both connection are a panel-to-panel connection, challenges on site can be similar. This was the incentive to take a look on site and discus these challenges with the executive party. First of all the reaction on the building system itself was quite positive. The quantity of free height that is gained with this system is rated very high. After removing the temporary supports the building is expected to look very spacious and elegant. Figure J.2 shows the natural impression the timber column supporting the timber floor gives. The most important challenges are construction speed, torque failure, labour intensity, levelling of plates and multiple contractors involved.

Construction speed
The use of the TC FUSION connection once again limits the speed of the production process. The temporary supports are needed until the concrete is hardened enough to be a structural component of the floor system. For buildings with few floors the temporary supports can be continued to the next floor. The placing of these supports still can be a time consuming occupation, so the process is still delayed. This is of course not a large issue for the connection subject of this thesis. After installing all screws, the connection is fully operational and temporary supports can be removed.

Torque failure
Specifically for timber to steel connections the torque failure of the screw was mentioned as a challenge. This failure type can occur when there is a sudden change in load. Mainly when connecting steel to timber the screw experiences a sudden change in loading when the head of the screw reaches the steel plate. In this project this was mainly challenging when connecting the Spiders, see figure J.3. The executive party on this building site is very experienced in timber construction, so by already knowing this challenge, the right precautions were taken. This is

done mainly by instructing the workers on site to be careful when tightening the screws and use a limitation on the strength of the screwdriver being used. An interesting addition to the possible torque failure of the screw, is the fact that the screw could also have failed without showing clear signs. The head of the screw can be twisted of the rest of the screw just enough to have no structural value, but not enough to be twisted of completely and by this showing its failure.

When creating a panel-to-panel connection as the one proposed in this thesis, the connection is timber-to-timber. However, as stated in the discussion, the use of a steel plate in the connection is not ruled out. It is even a very promising option to increase the strength and stiffness of the splice plate connection. If this adjustment is made, the torque failure of the screw becomes an additional challenge. This is not an insurmountable problem, but the workers on site should be informed on the effects of a failed screw in the connection. It should also be included on the engineering side of the process. A screw can, however careful the workers on site are, still fail and not been noticed as mentioned before. In the connection design this should be included in the safety margins.

Labour intensity
The TC FUSION connection is on site not immensely more labour intensive than a normal post-and-beam system. The novelty of the connections of course poses some additional challenges, but when this type of building system becomes more common also some skill is developed. On the other hand, the work off-site, in the production factory, becomes very labour intensive. The screws in the narrow face of the CLT panel, visible in figure J.4, have to be placed there manually. This is an enormous amount of screws that have to be installed precisely in the right place in the factory.

A splice plate connection is not advantageous regarding the labour needed. It is even arguably a more labour intensive connection on site. Where most of the labour for the TC FUSION connection can be made off-site, most of the work for the splice plate connection has to be done on site. The executive party on site also mentioned that placing screws overhead is harder and more labour intensive than working above the plates. To reduce the work that has to be done on site, it is advised to connect the LVL plate already to one of the CLT panels. This way the work on site is literally reduced by half. The other screws should already be pre-drilled in the LVL plate under the right angle, this is already common practice solid timber construction. Another option to ensure the screw is under the right angle, is the use of angled washers. The effect of washers will be investigated further. This will however reintroduce the risk of torque failure as mentioned before.

Levelling of plates
In Warmenhuizen the combination of a TC FUSION and Spider connection was produced for the first time ever. As with every innovation, progress comes with a trial and error process. The connection is checked in a lab and has been tested a lot of times, on site unexpected challenges can still occur. In this specific combination of connections a very specific challenge arose. To place the CLT panel on the spider connection it has to be lowered very precisely in a vertical way and horizontally very little inaccuracy is possible. The TC FUSION connection on the other hand needs some horizontal freedom in movement to make sure the screws from the plates do not collide. This challenge arose on site and was solved by tilting the column a little to create this horizontal degree of freedom.

The splice plate connection does not need this horizontal degree of freedom. A secondary challenge is for both the TC FUSION and splice plate connection relevant, namely the levelling of the plates. Before placing the CLT panels, the temporary supports were placed by another contractor. The degree of accuracy for the placement of the panels and thus the levelling of the connection depends a lot on the temporary supports. The plates themselves are also not perfectly

straight and this, in combination with small deviations in the temporary supports, can cause small dilations between the panels. In figure J.5 this is also noticed on site in Warmenhuizen. When working with timber as a construction material this is 'part of the deal'. For the splice plate connection the model is based on a compression point at the top of the first longitudinal layer in the panel, see figure 3.8. If the plates are not perfectly aligned, a small rotation is needed in the connection to reach this compression point. This rotation means an additional deflection and there are limits to the allowable deflection of the floor. This has two implications:

- The rotational stiffness model should include the effects of a dilation between the top of the panels.
- When removing the temporary supports a small, but instantaneous, deflection will occur. This is also the case with other materials, freely translated from Dutch: "the floor has to be startled".

Multiple contractors
When working with multiple construction materials, there is a chance multiple contractors are involved in the building process. This is also the case in Warmenhuizen and poses a little additional challenge in the project management. One contractor provides and assembles all timber element in the structure, where a secondary contractor provides the concrete part of the TC FUSION connection. The splice plate connection has a little advantage in that area, only a timber supplier is required. The placement of temporary supports plays a crucial role in ensuring the successful execution of on-site construction. Because this is often done by a separate contractor, the rules regarding accuracy should be specified very clearly in advance.

Besides these main challenges, there were some additional point of interest that are relevant to mention. First the remark was made it is often common practice to use equal screws as much as possible. Even if the engineer specifies smaller screws in a certain connection, the supplier uses larger screws of another connection, of course only if the larger screws are of equal constructive value. No one prefers to spend time distinguishing between different screw types on a construction site. Secondly there were some interesting structural adjustments to process the forces inside the point supported floors. A reinforcing rib was placed over the columns on the roof, this was just a locally thicker panel to withstand the larger forces. Also an edge beam was incorporated on the panel close to the spider connection.

Figure J.2: Timber columns in point supported floor

Figure J.3: Spider connection

Figure J.4: TC Fusion connection

Figure J.5: Plate dilation

Figure J.6: Overview structure